THE INFLUENCE OF URBAN MORPHOLOGY ON SENSIBLE HEAT FLUX AND CONVECTIVE RAINFALL DISTRIBUTIONS OVER GREATER MANCHESTER

MARIA DA GRAÇA DIAS CARRAÇA

Centre for Environmental Systems Research (CESR)
Research Institute for the Built and Human Environment (BuHu)
School of Environment and Life Sciences
University of Salford, Salford, UK

Submitted in Partial Fulfilment of the Requirements of the Degree of Doctor of Philosophy, September 2008

Contents

Contents i

List of Figures vii

List of Tables xxi

Acknowledgements xxiv

Abstract xxv

Chapter 1. Introduction 1

Chapter 2. The atmospheric boundary layer 7

2.1 Overview 7

2.1.1 The ABL sublayers 7

2.1.2 The diurnal cycle of the ABL 11

2.1.3 Stability and Convection 15

2.1.4 Entrainment and surface heat flux 18

2.2 Thermal and mechanical modifications of the boundary layer over urban areas 19

2.2.1 The urban boundary layer 19

2.2.2 Thermal modifications of the ABL: the Heat Island 20

2.2.3 The impact of the surface roughness 31

2.2.4 Dispersion of urban pollution 34

Chapter 3. Previous studies of the impact of urban areas on precipitation 37

3.1 Introduction 37

3.2 Observational studies **38**

3.3 Numerical studies **40**

3.4 Satellite studies **45**

3.5 Climatological studies **46**

3.6 The role of urban aerosols on precipitation **47**

3.7 On the effects of urban areas in numerical mesoscale forecast models **50**

3.8 Concluding remarks **51**

Chapter 4. Modelling the surface sensible heat flux **53**

4.1 Energy and water balance for urban and rural canopies **53**

4.1.1 Control volume approach 53

4.1.2 Water balance 55

4.1.3 Energy balance 56

4.1.4 Recent studies on surface energy balance over urban areas 62

4.2 Parameterisation of turbulent fluxes in the atmospheric inertial sublayer **65**

4.2.1 Introduction 65

4.2.2 Turbulent flow and some statistics 66

Reynolds averaging *67*

Covariances as measures of turbulent fluxes *67*

4.2.3 K-closure of the governing equations for the ABL 69

4.2.4 Mean profiles and similarity in a stationary and horizontally-uniform ABL 71

The logarithmic profile law in the neutral inertial sublayer *72*

Monin–Obukhov scales for the inertial sublayer *76*

Monin and Obukhov flux-profile relations for the (non-neutral) inertial sublayer *78*

Analitycal forms for the universal functions *82*

Chapter 5. Formulation for a model of surface sensible heat flux for Greater Manchester 84

5.1 Model overview 84

5.2 Bulk trasfer equation for surface sensible heat flux 87

Bulk transfer equation- aerodynamic surface temperature approach 87

Bulk transfer equation- radiometric surface temperature approach 89

The parameter kB^{-1} 90

5.3 Stability correction functions 91

5.4 The surface roughness parameterization- z_D, z_{0M} and z_{0H} 92

5.4.1 Overview 92

5.4.2 Zero-plane displacement length, z_D, and roughness length for momentum, z_{0M} - the Raupach's (1994) morphometric method 95

5.4.3 Tables of typical values for z_D and z_{0M} 98

5.4.4 Roughness length for heat z_{0H} - the Brutsaert (1982) method 104

5.5 Model tests 106

5.5.1 Sensitivity tests of the numerical model 107

Data 107

Results 108

5.5.2 Experiments on spatial variations of urban roughness 113

Chapter 6. A georeferenced database for surface roughness parameters over Greater Manchester 115

6.1 Introduction 115

6.2 Data sets 116

6.3 Estimates of the mean surface elements height (z_H), frontal area index (λ_F), and other morphologic parameters of the urban surface 117

6.4 Mapping morphologic parameters over a sample area of Greater Manchester. 119

6.4.1 Identification of land-use categories for a preliminary classification 119

6.4.2 A simple data analysis based on the tiles atributes, for a sample area 122

6.4.3 A simple data analysis by land-use category, for a sample area 126

6.5 Assessment of the frontal area index (λ_F) and of the derived height-normalized values of zero-plane displacement (z_D/z_H), for the sample area 129

6.5.1 Comparison between the estimates of frontal area index (λ_F) obtained from the CR data and values derived from Grimmond and Oke's (1999a) conceptual curve ... 129

6.5.2 Comparison between the estimates of height-normalized values of zero-plane displacement (z_D/z_H) obtained from Raupach's (1994, 1995) equation and from Grimmond and Oke's (1999a) conceptual curve 132

6.6 Establishement of the land-use categories for Greater Manchester. 134

6.7 Mapping the surface roughness parameters over a rectangular grid of 1x1km^2 resolution, for the Greater Manchester study area (24 x 24 km^2) 138

6.7.1 Tests of mapping morphologic surface parameters over a rectangular grid taking a sample area 138

6.7.2 Mapping the surface roughness parameters over a rectangular grid of 1x1km^2 resolution, for the Greater Manchester study area (24 x 24 km^2) 140

6.8 Concluding remarks 144

Chapter 7. Application of the model to Greater Manchester: simulations of surface sensible heat flux 147

7.1 The study domain 148

7.2 Study days 149

7.3 Observations 150

Air temperature, wind, and surface temperature 150

Note on local versus satellite radiometric surface temperature observations ... 158

Sensible heat flux *159*

7.4 Model input data over the entire study domain 161

7.5 Surface sensible heat flux model estimates versus observations 162

7.5.1 Case study 2 May 2004 162

Model results for the entire study domain *162*

Other simulations *164*

7.5.2 Case studies of 14 and 21 June 2004 168

Model results for the entire study domain *168*

7.6 Model estimates of the roughness length for sensible heat flux, z_{0H}, and excess resistance for heat $kB^{-1} = \ln(z_{0M}/z_{0H})$ 171

7.7 Testing the impact of surface heterogeneity - Model sensitivity tests to changes in the surface roughness and surface temperature 176

7.8 Concluding remarks 180

Chapter 8. Applications of the model in Greater Manchester to imply convective initiation. 182

8.1 Relationship of sensible heat flux to thermal forcing 182

8.2 Case study 21 June 2004 185

8.3 Concluding remarks 191

Chapter 9. Summary, conclusions and future work 193

9.1 Formulation for a model of surface sensible heat flux for Greater Manchester 193

The model *193*

Model limitations *195*

Results of preliminary model simulations *197*

9.2 Application of the model of surface sensible heat flux to Greater Manchester 198

Application of the model 198

The surface temperature, air temperature and wind data 199

The surface morphologic database, and model estimates of the roughness parameters zero-plane displacement length, z_D, and roughness length for momentum, z_{0M} 200

9.3 Model results of surface sensible heat flux for Greater Manchester. Model estimates of roughness length for heat, z_{0H}, and roughness lengths ratio (z_{0M}/z_{0H}) 202

9.4 Applications of the model in Greater Manchester to convective initiation ... 203

9.5 Implications for city development 205

9.6 Future work 206

Appendix 1. Thermal properties of common materials 208

Appendix 2. Surface morphologic parameters for a sample area and for the entire study domain 209

Appendix 3. Pressure maps and satellite images for the study days 212

Appendix 4. Photographs from the observational sites 214

Appendix 5. The 6 August 2003 and the 7 December 2003 217

References 219

List of Figures

Figure 1.1 . - Urban and rural populations of more developed regions and less developed regions, 1950-2030 [from World Urbanization Prospects, United Nations, 2004]. 1

Figure 2.1- Definition sketch showing orders of magnitude of the height of the atmospheric boundary layer (ABL) and its sublayers; the vertical scale is in metres. 8

Figure 2.2 - The boundary layer in high pressure regions over land consists of three major parts: a very turbulent mixed layer; a less turbulent residual layer containing former mixed layer air; and a nocturnal stable boundary layer of sporadic turbulence.(After Stull, 1988). 12

Figure 2.3 - Typical atmospheric profiles of the virtual potential temperature (θ_v), wind speed (u) and water vapour mixing ratio (q) over land in midlatitudes during cloudless conditions [from www.met.rdg.ac.uk/ ~swrhgnrj/ teaching/ MTMG49/ 1.1_introduction.doc, University of Reading, Boundary Layer Meteorology and Micrometeorology notes on-line, download on 2008]. 13

Figure 2.4 - Non-local static stability characterisation for various hypothetical virtual potential temperature θ_v profile. Dotted lines denote parcel movement (after Stull, 1988). 17

Figure 2.5 *The potential temperature and heat flux profiles assumed in the "jump" model (from Pielke, 2001).* 18

Figure 2.6 - Schematic of the urban boundary layer including its vertical layers and scales (after Oke, 1997; from Piringer et al., 2002). UBL stands for Urban Boundary Layer, and UCL for Urban Canopy Layer. 20

Figure 2.7 - UHI characteristics. (a) Cross-sections of air temperatures measured within the UCL (urban canopy layer) and surface temperatures (e.g., as observed by a remote sensor) under ideal heat island conditions during (i) nighttime and (ii)

daytime. T represents temperature in ^{0}C. (b) Plan view of spatial patterns of air temperature, which make up the nighttime UHI. (from Voogt, 2002) 22

Figure 2.8 - Typical diurnal variation of urban and rural air temperature under clear skies and weak air flow. The UHI is produced by the difference between cooling rates. [Redrawn from Oke, 1987; from http://www.urban-climate.org/UHI_Canopy.pdf, download on 2008; International Association for Urban Climate (IAUC) Teaching Resources] 23

Figure 2.9 - Urban Heat Island intensity plotted against the logarithm of city population. Different symbols are used for cities in different climate zones. Solid lines are the corresponding linear regression lines. Regression coefficients are different for different city morphologies (North American and European cities) and climates (temperate, tropical hot/dry, and tropical hot/humid) (from Chow and Roth, 2006). 26

Figure 2.10 - Daily variation of humidity on 30 fine summer days in and near Edmonton, Alberta (after Hage, 1975; from Oke, 1987). 28

Figure 2.11 - Schematic of thermally induced circulation and dust dome over an urban area under calm or light winds (after Lowry, 1967; from Arya, 2001). 29

Figure 2.12 - Sketch of the urban boundary layer showing the urban plume and schematic profiles of potencial temperature (Θ), during fine weather for a windy (a) day, and (b) night (after Oke, 1982; from Oke, 1987). 30

Figure 2.13 - (a) Surface temperature (K) boundary condition (after Draxler, 1986). (b) Model calculated wind vectors at a height of 50m (after Draxler, 1986). 30

Figure 2.14 - Effect of terrain roughness on the wind speed profile near the ground; the height zg is the top of the boundary layer above which the mean horizontal wind speed ū is approximately constant with the height (i.e. surface drag is negligible). (After Davenport, 1965; from Oke, 1987.) 32

Figure 2.15 - Effects of roughness change on the wind. Dashed lines are parallel extensions of the gradient wind direction. Arrow lengths approximately proportional to near-surface wind speed. The broad arrow represents the geostrophic wind. (After Oke, 1987). 32

Figure 2.16 - Flow regimes associated with different urban geometries (after Oke, 1987). 33

Figure 2.17 - The influence of building air flow on pollution dispersion (after Oke, 1987). 34

Figure 2.18 - Typical plume patterns, under different atmospheric stability conditions given by the potential temperature (θ) profile (graph on the left-hand side of each picture) (from Oke, 1987). 36

Figure 2.19 - Possible plume behaviour in the vicinity of a city at night with clear skies and light winds (from Oke, 1987). 36

Figure 3.1 - RAMS results for the evolution of urban heat island, moisture, and winds, for the first model level (48 m), on 8 Jun 1999. Temperature (ºC) is shaded, water vapor mixing ratio (g kg^{-1}) is contoured at intervals of 1 g kg^{-1}, and wind (m s^{-1}) vectors are plotted. There is evidence of moist convergence in the urban environment. The circle represents the approximate location of St. Louis. (After Rozoff et al., 2003; from Shepherd, 2005)..... 44

Figure 4.1- Schematic representation of the fluxes involved in the balances of (a) water and (b) energy of an urban ground-building-air volume (after Oke,1987). 54

Figure 4.2- Average diurnal variation of the surface energy balance terms (in W/m^2), at three sites in and around Basel. (▬) ΔQ_S is the variation of energy storage, (▬) Q_H is the sensible heat flux, (▬) Q_E is the latent heat flux, and (—) Q^* is the radiative flux. It represents average days for the observation period from June 10 to July 10, 2002 (including all sky conditions), at (a) an urban site (Sperrstrasse, Basel), (b) a suburban site (Allschwil) and (c) a rural site (Village Neuf). CET stands for Central Europe Time (UTC+1),[After Christen et al., 2003a; adaped from Fisher et al., 2005]. 60

Figure 4.3- Comparison of sensible heat flux (in W/m^2) measured using sonic anemometers on 15 m masts at Coleshill synoptic station (rural site) and at the Dunlop Tyres Ltd factory site (within Birmingham) plotted by N. Ellis. Results are averages by hour of day. The period covered was from 10 UTC on 7 July 2000 to 17 UTC on 28 July 2000, during the Birmingham campaign [From Middleton and Thomson, 2002] 61

Figure 4.4- Observed surface energy balance fluxes (in W/m^2) for two observation periods (days 172-178, June 21-26 2001) at the Marseille city centre site (ESCOMPTE). Data are ensemble means for the period including the canopy storage heat flux, ΔQ_S, determined as the residual of the observed terms (Q^*, Q_H,

and Q_E). Note that ΔQ_S peaks before solar noon and is negative about 2 hours before the net all-wave radiation flux Q*. [Adapted from Mestayer et al., 2005] 61

Figure 4.5 - Definition of layers involved in the study of urban climates at the local scale relative to the "box" (control volume) modeled by LUMPS (Local-Scale Urban Meteorological Parameterization Scheme). The lateral (or third) dimension of the box, not shown, is also 10^2–10^4 m. The top of the "box" is within the inertial sublayer, and the bottom is at the depth at which there is no net heat exchange over the time period of interest [from Grimmond and Oke, 2002]..... 65

Figure 4.6 - Generalized mean (spatial and temporal) wind velocity (u) profile in a densely developed urban area including the location of sublayers of the surface layer (inertial sublayer and roughness sublayer, RSL, and urban canopy layer, UCL). The measures on the height scale are the mean height of the roughness elements (z_H), the roughness sublayer (z_r, or the blending height), the roughness length for momentum (z_{0M}) and zero-plane displacement length (z_D). The dashed line represents the wind profile extrapolated from the inertial sublayer, and the solid line represents the actual wind profile [from Oke, 2006]..... 74

Figure 5.1- Geographical location of Greater Manchester. **(a) (Left)** Image of Major Land Cover Types for Great Britain [from COoRdinate INformation on the Environment, CORINE, Land Cover European Environment Agency, http://www.eea.europa.eu/, 2002]. [Red] indicates urban fabric, natural vegetated areas are [green], the rest are agro-foretry areas mainly. **(b) (Top- right)** Image of Land Use; [dark yellow] area represents populated place; the black rectangle limits the area of interest, which has 24x24 km^2 and is centred at the co-ordinates (-2.18, 53.43) [from NIMA- National Imagery and Mapping Agency, U.S. Geological Survey, http://www.usgs.gov/ 2002]. **(c) (Bottom- right)** Image generated from Digital Terrain Elevation Data [NIMA- National Imagery and Mapping Agency, U.S. Geological Survey, http://www.usgs.gov/ 2002]. 85

Figure 5.2- Cross-sectional representation of the surface layer showing roughness lengths for momentum and heat and the resistances between different levels. The zero-plane displacement level is omitted for simplicity. For some surfaces, $T = T_0 = T_R$ may be possible. Symbols are defined in the text. (After Voogt and Grimmond, 2000). 88

Figure 5.3- Relation between height-normalized values of zero-plane displacement and roughness length for momentum, and the packing density of roughness elements. Conceptual representation of the relation between height-normalized values of zero-plane displacement, z_D/z_H [z_d/z_H], and roughness length for momentum, z_{0M}/z_H [z_0/z_H], and the packing density of roughness elements (a) using λ_P and (b) using λ_F to describe density. Shaded areas are the reasonable zones or envelopes referred to in the text. Mean values of observed for f_d ($\overline{f_d} = \overline{z_D/z_H} = 0.67$) and f_0 ($\overline{f_0} = \overline{z_{0M}/z_H} = 0.10$) over land surfaces are also represented. The vertical dashed lines show the range of real-city roughness densities ($0.1 < \lambda_P < 0.62$, $0.05 < \lambda_F < 0.47$). Limits of flow regimes are schematised along the top. [From Grimmond and Oke, 1999a.] 94

Figure 5.4- Definition of surface dimensions used in morphometric analysis. The element portrayed has the characteristic mean dimensions, spacing, and total lot area (A_T) of the urban array. Using these measurements, the following nondimensional ratios are defined to characterise the morphometry: 95

Figure 5.5- Order of magnitude of roughness length for momentum, z_{0M} (m), for typical terrain types (from Stull, 1988). 99

Figure 5.6 - Photographs of the physical nature of urban morphometry representing examples of the four urban roughness categories in **Table 5.4**. Urban Terrain Zones (UTZ) codes are from Ellefsen (1990-91): (a) Do3, (b) Do3, (c) Do4, (d) Dc3, (e) Do2, (f) A5, (g) A2, (h)A1, (i) Dc2, (j) Dc1, (k) Dc1, and (l) Dc8. [After Grimmond and Oke, 1999a.] 103

Figure 5.7- Comparison between experimental and theoretical results on ln (z_{0M}/z_{0H}), for heat transfer (solid curves), and ln (z_{0M}/z_{0E}), for evaporation from wet surfaces (dash curves), plotted versus roughness Reynolds number. The curves represent theoretical results. The numbered points represent experimental results: 1 is short grass, 2 medium length grass, 3 bean crop, 4 savannah scrub, 5 and 6 pine forest (horizontal bars represent Re_* range and vertical bars the standard deviation). Also some experimental data points are superimposed on the theoretical curve for evaporation from wet grass. [Adapted from Brutsaert, 1982.] 105

Figure 5.8 - Results of model sensitivity tests (for z_D , z_{0M}, z_{0H},..., L, u_*, Q_H, and r_H) using the input values discussed in the text (**Table 5.5**) and indicated in the top

box. Each curve (A, B, C, D, E) relates to a different input variable, λ_F, z_H, u, T_R, or T_a, while all others are kept constant. The x coordinate relates to the variability range defined by j in **Table 5.5**. [♦] refer to the left y-axis, [▲] refer to the right y-axis. (Continued on next page.) 109

Figure 5.9 - Iteration output values for points: **(a)** C7- C9; **(b)** D1, D9 **(c)** D10, D11. 112

Figure 5.10 - Preliminary model results showing the impact of the wind speed, vertical temperature gradient and surface roughness on the surface sensible heat flux. **(a)** Surface sensible heat flux results, Q_H, of a modelling experiment for two vertical temperature gradients (filled and open symbols). Each point represents a complete model run using a specific set of input values (z_S, z_H, u, T_R, T_a, and λ_F), which are indicated on the graph. Here, points A, B, and C relate to the urban area represented in (b). **(b)** Schematic representation of the typical distribution of roughness over an urban area loosely resembling a part (5x5 km^2) of Greater Manchester. 113

Figure 6.1 - Distribution of buildings over a zone of Greater Manchester. Distribution of buildings, obtained from CR data, covering an area of 2.5km x 5km of Salford and Manchester. The axes labels represent the U. K. National grid co-ordinates of the area of interest (Ordnance Survey national grid system of eastings and northings), X: 380000m - 385000 m; Y: 398000m- 400500m. The legend shows the values of the buildings mean height associated with the different colours... 119

Figure 6.2 - Preliminary mapping over Grid A. Mean buildings height (m) estimated for each tile of Grid A, indicated by the number placed over each tile. Different tile colours refer to different categories, as shown on the legend. The thin black lines indicate a grid of 500m resolution discussed later. Heavy black lines show the area covered by Grid B (**Figure 6.3**)..... 121

Figure 6.3 - Preliminary mapping over Grid B. Mean buildings height (m) estimated for each tile of Grid B, indicated by the number placed over each tile. Different tile colours refer to different categories, as shown on the legend. The thin black lines indicate a grid of 500m resolution. 121

Figure 6.4 - Statistics of CR data on each tile of Grid A: mean buildings height, and fraction of built up area (plan area index). 123

Figure 6.5 - Statistics of CR data on each tile of Grid B: mean buildings height, and fraction of built up area (plan area index). 123

Figure 6.6 - Fraction of built up area (Plan area index), λ_P, over (a) Grid A and (b) Grid B. 124

Figure 6.7 - Frontal area index, λ_F, over (a) Grid A and (b) Grid B. 125

Figure 6.8 - Statistics of CR data for each category derived for Grids A and B. (a) Mean buildings height (m), and (b) their standard deviations; (c) Mean buildings area (m^2), and (d) their standard deviations (see Appendix 2, **Table A2.1**). The labels placed above the black bars refer to the categories defined for Grid B, while the legends on the X axis refer to the categories defined for Grid A. 126

Figure 6.9 - Fraction of built up area (plan area index) for each category. Estimates of the fraction of built up area performed over Grids A and B, based on the statistics of CR data for each category (see Appendix 2, **Table A2.1**). The labels placed above the black bars refer to the categories defined for Grid B, while the legends on the X axis refer to the categories defined for Grid A. 127

Figure 6.10 - Mean buildings area and fraction of built up area (plan area index) versus mean buildings height for each category, based on Grid A (purple) and Grid B (black). 128

Figure 6.11 - Categories distribution. Percentage of each category for a sample area covering a zone of Salford and Manchester over (a) a tile of 2.5km x 5km, using Grid A of **Figure 6.2** (b) a tile of 2 km x 2 km, using Grid B of **Figure 6.3**. 129

Figure 6.12 - Frontal area index, plan area index and buildings height. Estimates of the frontal area index for each tile of Grid A, **[▱ λ_F]** based on CR data set statistics and **[▰ λ_F_G&O]** using the conceptual curves of Grimmond and Oke (1999a). Mean buildings height **[♦ z_H]** and plan area index **[▱ λ_P]** for each tile of **Figure 6.2** and **Figure 6.6a** are also shown. The urban category associated to each tile is indicated by the label of the horizontal axis. 130

Figure 6.13 - Frontal area index versus plan area index, λ_P, for Grid A. Estimates of λ_F are obtained from the CR data set and **λ_F_G&O** are given by the conceptual curves of Grimmond and Oke (1999a). 131

Figure 6.14 - Height-normalized values of zero-plane displacement (z_D/z_H) versus frontal area index, for the range of λ_F values observed over the sample area (Grid

A). **[z_D/z_H_G&O]** are given by the Grimmond and Oke (1999a) conceptual curve (**Figure 5.3b**), and **[z_D/z_H_Ra,model]** by the Raupach (1994, 1995) model equation 5.4.4. The vertical dashed line shows the lower limit of real-city frontal area index ($0.05 < \lambda_F < 0.47$) and envelopes contained by the curved dashed lines define the reasonable limits outlined in (**Figure 5.3b**), after Grimmond and Oke (1999a). 133

Figure 6.15 - Mean buildings height over the sample area, using a rectangular grid. The mean buildings height (m) for each cell of the rectangular grid is indicated by the number placed over each cell. Different cell colours refer to different classes of mean building height (m), as shown on the legend. 138

Figure 6.16 - Plan area index over the sample area, using a rectangular grid. The plan area index,λ_P, for each cell is indicated by the number placed over each cell. Different cell colours refer to different classes of λ_P, as shown on the legend... 139

Figure 6.17 - Frontal area index over the sample area, using a rectangular grid. The frontal area index, λ_F, for each cell is indicated by the number placed over each cell. Different cell colours refer to different classes of λ_F, as shown on the legend. 139

Figure 6.18 - Illustration of the procedure used to identify and mark the different categories over the entire study domain. Arc View software is used, and based essentially on the map and aerial photograph layers (created from images available in www.multimap.com) it was possible to draw the polygonal grid. The number centred in each square cell (1x1 km^2) gives the U.K. National grid coordinates (in km) of the cell inferior left corner; the first three digits are the latitudinal coordinate and the last three are the longitudinal coordinate**.** 141

Figure 6.19 - Fraction of urbanised area for the Greater Manchester study domain. The coordinates X and Y are the U.K. National Coordinates. The total study area is 24 x 24 km^2 and the area of each grid square 1x1 km^2. The legend on the right-hand side refers to the values of the fraction of urbanised area..... 142

Figure 6.20 - Roughness data for the Greater Manchester study domain shown in Figure 6.19. The coordinates X and Y are the U.K. National Coordinates. The total study area is 24 x 24 km^2 and the area of each grid square 1x1 km^2. (a) Mean building height, z_H, for each cell in the study domain. The legend on the right-

hand side refers to the values of z_H expressed in m. (b) Mean frontal area index, λ_F, for the same study area. The legend on the right-hand side refers to the values of λ_F. Statistics of z_H and λ_F over the entire study domain are shown in **Table A2.2** of the Appendix 2. 142

Figure 6.21 - Model estimates of roughness parameters for the Greater Manchester study domain shown in **Figure 6.19**. The total study area is 24 x 24 km^2 and the area of each grid square 1 km^2. (a) Zero-plan displacement height, z_D , for each domain cell. The legend on the right-hand side refers to the values of z_D expressed in m. (b) Roughness height for momentum, z_{0M}, for each domain cell. The legend on the right-hand side refers to the values of z_{0M} expressed in m. Statistics of z_D and z_{0M} over the entire study domain are shown in **Table A2.2** of the Appendix 2. 143

Figure 6.22 - (a) Zero plan displacement length, z_D, and roughness length for momentum, z_{0m}, as functions of the surface roughness elements height, z_H. (b) Zero plan displacement length, z_D, versus roughness length for momentum, z_{0M}. Each line represents the fitted linear function between a pair of variables resulting from linear regression. R is the linear correlation coefficient. 144

Figure 7.1 - Relief in the Manchester region obtained from the Land-Form PANORAMA product provided by the Ordnance Survey, UK [http://www.ordnancesurvey.co.uk/]. The white square delimits the Greater Manchester study area of 24x24km^2. The coordinates X and Y are the U.K. National Grid Coordinates. The legend on the right-hand side refers to the values of the height above sea level expressed in metres. 148

Figure 7.2 *- Location of the urban observational sites in the Greater Manchester study domain [adapted from the aerial photographs available in www.multimap.com]: (a) Private AWS in Salford, (b) Thursfield Street (SALFEX field campaign), (c) Telford Building (experiment at Salford University), and (d) Sackville Building in central Manchester (observations from the University of Manchester University Atmospheric Science Research Group). The red lines indicate the georeferenced grid used in the present study, with cells of 1km x 1km. The UK National Coordinates of the lower-left and upper-right corners of the 6x5 km^2 area represented in this figure are (379000, 397000) and (385000, 402000), respectively.* 152

Figure 7.3 - Radiometric surface temperature, T_R, from satellite imagery (MODIS Terra/ Aqua) over Greater Manchester,**(a)** on the 2nd May 2002, at 11:45 UTC, under scattered cloud conditions,**(b)** on the clear sky day of 14th June 2004, at 12:50 UTC, and **(c)** on the 21st June 2004, at 13:00, under scattered cloud conditions. The total study area is 24 x 24 km^2 and the area of each grid square is 1 km^2. The grey areas are either missing data due to the mapping technique or areas of clouds. The legend on the right-hand side of each figure refers to the values of the temperature expressed in K. The coordinates X and Y are the U.K. National Coordinates, and the location of the **S**ALFEX site, the **P**rivate AWS at Salford**,** the **T**elford Building at the University of Salford, the Sackville Building at the **U**niversity of Manchester, and the Manchester **Airport** are indicated. Also statistics of T_R (K) over the entire study domain are shown. 154

Figure 7.4 - Radiometric surface temperature, T_R, air temperature, T_a, (a) and wind speed, u, (b) near the surface over Greater Manchester around 12 UTC on some clear sky days (dates on x-axis). T_R is derived from MODIS Terra/Aqua satellite data. T_a and u were obtained from several sources as indicated on the top legends. T_{Rmax} is the highest surface temperature value observed in a 1km^2 cell of the 24x24 km^2 Greater Manchester study domain. The data refer to a particular hour of the day (see **Figure 7.4a**) depending on the time of the satellite overpass available for each specific day. The values of T_R presented in this figure were extracted from images similar to the examples given in **Figure 7.3**. 155

Figure 7.5 - Air temperature (a) and wind observations (b) on the 2nd May 2002, from different sources over Greater Manchester: the synoptic AWS at Manchester airport (■), the private AWS situated in Salford (■), and the SALFEX campaign. The blue lines (—) represent 10min averages of the ultrasonic measurements at 11m during the SALFEX campaign. The figure also shows two sets of SALFEX radiosonde observations starting at 11:38 UTC (●) (at levels: 16, 20, 27, 37, 45 m) and 13:34 UTC (○) (at levels: 6, 14, 23, 31, 41 m); for each sounding, the highest temperature and the lowest wind speed shown are the values extrapolated for the 0 m level. 156

Figure 7.6 - Air temperature (a) and wind (b) observations on the 14 and 21 June 2004 from different sources over Greater Manchester: the synoptic AWS at Manchester airport (▰), the private AWS situated in Salford (▰), the experiment setup on the

roof of the Sackville Building, from the University of Manchester Atmospheric Science Research Group (—), and the experiment setup on the roof of the Telford Building at the University of Salford- (— and —). 157

Figure 7.7 - Observations on the 14th (a) and 21st (b) June 2004, at 20m height, on the roof of Telford building at the University of Salford (10 min averages): wind speed (u —) and virtual temperature (T_v —) from a CSAT3 sonic anemometer, and air temperature (T_a —) from a fine wire thermocouple. Q_{H_Tv} (▰) and Q_{H_Ta} (▰) are estimates of the sensible heat flux using 10 min averaged covariances between the observed vertical wind component and temperature. Q_{H_Tv} uses the virtual temperature values and Q_{H_Ta} the air temperature. These two estimates are similar. 160

Figure 7.8 - Model estimates of surface sensible heat flux, Q_H, on the 2nd May 2002, at 11:45 UTC, under scattered cloud conditions, for the Greater Manchester study area (24x24 km^2) shown in **Figure 7.3a**. The grey areas are either missing data due to the mapping technique or areas of clouds. The legend on the right-hand side of each figure refers to the values of Q_H expressed in W/m^2. The locations of the **S**ALFEX site, the **P**rivate AWS at Salford and the Manchester **Airport** are indicated by letters. Statistics over the entire study domain for the model estimates of Q_H (W/m^2) are shown on the bottom of the figure. 163

Figure 7.9 - Model estimates of surface sensible heat flux, Q_H, using different input data sets (T_R, T_a, u, z_S, z_H and λ_F) as presented in **Table 7.6**. The corresponding model outputs for the Monin-Obukhov variable ζ, friction velocity u_*, the stability correction functions for momentum and sensible heat, Ψ_M and Ψ_H, the Monin-Obukhov length, L, and the resistance to heat transfer between the surface and the measurement level , R_H, are shown as well. In all model runs z_H=5.1m and λ_F= 0.07. The graph is divided in five parts, showing the model outputs for five different surface temperature input values, T_R. For each surface temperature six different situations have been considered; the values of the input variables (T_a, u, and z_S) for the six cases are shown on the bottom of the graph. The model estimates represented by single lines are read on the right-hand axis, and the estimates represented by dots on left-hand axis. 166

Figure 7.10 - Model estimates of surface sensible heat flux, Q_H, using different input data sets (T_R, T_a, u, z_S, z_H and λ_F), as presented in **Table 7.7**. The corresponding model outputs for ζ, u_*, Ψ_M, Ψ_H, L, and R_H, are shown as well. Here the model runs are similar to those shown in the **Figure 7.9**, except that now the input roughness parameters are z_H=8m and λ_F= 0.13. The model estimates represented by single lines are read on the right-hand axis, and the estimates represented by dots on left-hand axis. 167

Figure 7.11 - Model estimates of surface sensible heat flux, Q_H, around 13 UTC, (a)on the clear sky day of 14th and (b) on the 21st June 2004, under scattered cloud conditions, for the Greater Manchester study area (24x24 km^2) shown in **Figure 7.3**. The grey areas are either missing data due to the mapping technique or areas of clouds. The legend on the right-hand side of each figure refers to the values of Q_H expressed in W/m^2. The locations of the Private AWS at Salford **P**, the Telford Building at Salford University **T**, University of Manchester **U**, and Manchester **Airport** are indicated. Statistics over the entire study domain for the model estimates of Q_H (W/m^2) are shown on the bottom of the figure..... 169

Figure 7.12 - Model estimates of surface sensible heat flux, Q_H, around 13 UTC, on (a) 14th and (b) 21st June 2004, for z_S=20 m and z_S=30m versus the same model estimates for z_S=45m shown in **Figure 7.11**. The statistical parameter R is the Pearson linear correlation coefficient..... 170

Figure 7.13 - Model estimates of log(z_{0H}) for the case studies, on the (a) 2nd May 2002, and (b) 14th and (c) 21st June 2004, around midday, for the Greater Manchester study area (24x24 km^2). These estimates are related to the model results of sensible heat flux shown on **Figure 7.11**. Grey areas are as in **Figure 7.11**. . Statistics over the entire study domain, for the model estimates of log(z_{0H}) are shown on the bottom of the figures..... 172

Figure 7.14 - Model estimates of kB^{-1}= ln(z_{0M}/z_{0H}) on the (a)2nd May 2003, and (b) 14th and (c) 21st June 2004, around midday, for the Greater Manchester study area (24x24 km^2). These values are related with the model results of sensible heat flux shown on **Figure 7.11**. Grey areas are as in **Figure 7.11**. Statistics over the entire study domain, for the model estimates of kB^{-1} are shown on the bottom of the figures..... 173

Figure 7.15 - Model estimates of surface sensible heat flux, Q_H (W/m^2), at a level z_S=45 m, using for all the domain cells the input values presented on the top of each figure, and (a) the spatial distributions of the roughness parameters z_H and λ_F for Greater Manchester shown in **Figure 6.20**, and (b) the spatial distribution of the surface temperature T_R from the satellite imagery over Greater Manchester on 2May 2002 at 11:45 UTC shown in **Figure 7.3a**..... 177

Figure 7.16 - Model estimates of surface sensible heat flux, Q_H (W/m^2), at a level z_S=45 m, using for all the domain cells the input values presented on the top of each figure: (a) using the spatial distributions of the roughness parameters z_H and λ_F for Greater Manchester shown in **Figure 6.20**, and (b) using the spatial distribution of the surface temperature T_R from the satellite imagery over Greater Manchester on 14 June 2004 at 12:50 UTC shown in **Figure 7.3b**..... 178

Figure 7.17 - Model estimates of Q_H (W/m^2), at a level z_S=45 m, using for all the domain cells the input values presented on the top of each figure: (a) using the spatial distributions of the roughness parameters z_H and λ_F for Greater Manchester shown in **Figure 6.20**, and (b) using the spatial distribution of T_R from the satellite imagery over Greater Manchester on 21 June 2004 at 13:00 UTC shown in **Figure 7.3c**. 178

Figure 8.1 - The synoptic pressure field and frontal positions over the UK and surrounding area at 12:00 UTC on 21st June 2004..... 186

Figure 8.2 - Satellite images over North West England on 21st June 2004 (MODIS, Bands 7-2-1, 5min, 500m) (a) Terra/ MODIS, 11:15 UTC (b) Aqua/MODIS, 13:00 UTC. The red line delimits the Greater Manchester study area of 24x24km^2. Note there are slight differences in projection between (a) and (b). The Mersey and Dee estuaries can just be seen on the left-hand side of the images. 186

Figure 8.3 - Surface sensible heat flux, Q_H, at 13:00 UTC and rainfall rate (mmh^{-1}) in the afternoon, on 21st June 2004, shown in a sequence of five images from the Hameldon Hill C-band radar located some 24km north of the centre of Manchester, North West England. These images are an example of the radar product used in this work (instantaneous rainfall rate image, every 5 min, with 2x2 km^2 spatial resolution)..... 187

Figure 8.4 - Hovmoller diagrams of rainfall rate (mmh^{-1}) on 21st June 2004 derived from the Hameldon Hill C-band radar located some 24km north of the centre of

Manchester, North West England (a) 06:00-11:00 UTC and (b) 12:00-17:00 UTC. The coordinates represent distance along a 7km wide swath running through the city centre in the direction of the westerly cell movement and the abscissa represents time. Some small spurious areas of rain remain where the removal of radar ground clutter echoes has been incomplete. The time of the satellite images shown in **Figure 8.2** are indicated by the vertical arrows next to the time axis. These diagrams were produced using IDL (Interactive Data Language) software. 188

Figure A2.1 - Comparison of two surface data products. Samples (2x2 km^2) of digitised georeferenced data over the same area of Greater Manchester.....209

Figure A3.1 - The synoptic pressure field and frontal positions, and satellite images, over the UK and surrounding area, for three study days. (Continued on the next page.).....212

Figure A4.1 - Location of the urban observational sites in the Greater Manchester study domain.....214

Figure A4.2 - Photographs taken in the afternoon, on the roof of Telford Building at Salford University, during the experiment of May - June 2004.....215

Figure A4.3 - Photograph taken on 28 June 2004, at Salford University, front of Peel Building. It shows the infrared thermometer (IMPAC IN5 Plus) and respective equipment used to measure the surface temperature.....216

Figure A4.4 - SALFEX site at Thrusfield Street in Salford (Northwestward view)..216

Figure A4.5-Sackville Building in Central Manchester,seen from Portland Tower..216

Figure A5.1 - The synoptic pressure field and frontal positions, and satellite images, over the United Kingdom and surrounding area, for two days: (a) 6 August 2003 and (b) 7 December 2003.....217

Figure A5.2 - Radiometric surface temperature, T_R, from satellite imagery (MODIS Aqua) over Greater Manchester, (a) on the clear sky day of the 6 August 2003, at 12:55 UTC, and (b) on the 7 December 2003, at 12:40, under scattered cloud conditions.....218

List of Tables

Table 2.1 - Simple classification scheme of urban heat island types (after Oke, 1995) 24

Table 2.2 - Commonly hypothesised causes of the canopy layer heat island (after Oke, 1982; from Oke, 1987). 25

Table 2.3 - Commonly hypothesised causes of the urban boundary layer heat island (after Oke, 1982; from Oke, 1987). 25

Table 4.1 - Ranges of average daily maximum values of net radiation and fluxes in North American cities at the Multicity Urban Hydrometeorological Database-MUHD. One salient feature of urban sites is that the storage heat flux is as significant as the sensible heat flux, which is different from typical rural sites where it is much less. [after Grimmond and Oke, in Piringer et al., 2002] (from Fisher et al., 2005). 64

Table 4.2 - Interpretation of the Monin-Obukhov Length L with respect to atmospheric stability (after Seinfeld and Pandis, 1998). 78

Table 5.1 - Vertically integrated forms of the universal stability functions for momentum and for heat, $\Psi_H(\zeta)$ and for $\Psi_M(\zeta)$, used in the model for surface sensible heat flux. The corresponding local stability functions, $\phi_M(\zeta)$ and $\phi_H(\zeta)$, are also shown. In these formulations it is assumed that k=0.4. 91

Table 5.2 - Typical roughness lengths for momentum (z_{0M}) of homogeneous surface types (from Wieringa, 1993). 100

Table 5.3 - Typical roughness and other aerodynamic properties of homogeneous zones in urban areas, ordered by height and density: mean roughness heights (z_H), zero-plane displacement ($z_d \equiv z_D$), roughness length for momentum ($z_0 \equiv z_{0M}$), aerodynamic conductance for momentum transport (g_{aM}) and drag coeficient (C_D) (from Grimmond and Oke, 1999a). 100

Table 5.4 - Typical nondimensional roughness properties of homogeneous zones in urban areas, ordered by urban density and flow regime: plan area index, λ_P, street

canyon aspect ratio, λ_S, and the coefficients f_d and f_0. Urban Terrain Zones (UTZ) codes are from Ellefsen (1990-91)[After Grimmond and Oke, 1999a.] 102

Table 5.5 - Values of the variables used in the model sensitivity test: frontal area index (λ_F), surface elements height (z_H) wind speed (u), surface temperature (T_R) and air temperature (T_a) . In all cases, the measurement height has been taken as z_S = 20m. 108

Table 6.1 - Preliminary land-use classifications for Greater Manchester. Land-use categories identified over Grid A and Grid B. 122

Table 6.2 - Roughness parameters for each land-use category. Mean buildings height (z_H), plan area index (λ_P), frontal area index (λ_F), normalised zero plan displacement height estimated (z_D/z_H)(e) estimated from λ_F values shown on this table using equation 5.4.4, and mean horizontal plan area of the buildings, respectively. 135

Table 6.3 - *Greater Manchester categories and Ellefsen (1990/91) UTZ. Categories defined for Salford and Manchester (first column) and Urban Terrain Zones (UTZ) of Ellefsen (1990/91). Mean buildings height (in storey and metre tiles, considering that one storey is about 3.5 m height); total of roof area in each UTZ; area of the UTZ; fraction of roof area. The values underlined refer to the Greater Manchester Categories (from* ***Table 6.2****); all the other values are for the UTZ of Ellefsen (1990/91).* 136

Table 7.1- Summary of the observational of air temperature and wind data sources. 151

Table 7.2 - Sensible heat flux observed on the 2nd May 2002, around 12 UTC, in Thursfield Street, Salford, using a sonic anemometer at 11m. 160

Table 7.3 - Sensible heat flux observed on the 14 and 21 June 2004, around 13 UTC, on the roof of Telford Building at 20m, at the University of Salford (from **Figure 7.7**). 161

Table 7.4 - Model input data used over the entire study domain for the three case studies. 162

Table 7.5 - Model results of sensible heat flux, Q_H, and respective input data sets, for two domain cells in the nearer neighbourhood (southeast/ east) of the cell of interest where SALFEX observational equipment was installed. Also shown in the last column are the minimum and maximum values of Q_H estimated over the entire study area. The values in bold are represented in **Figure 7.8**. 164

Table 7.6 - Model estimates of surface sensible heat flux, Q_H, and respective input data sets. In all cases z_H=5.1m and λ_F= 0.07..... 166

Table 7.7 - Model estimates of surface sensible heat flux, Q_H, and respective input data sets. In all cases z_H=8m and λ_F= 0.13..... 167

Table 7.8 - Summary of the model input data used over the entire study domain for the model sensitivity tests to the surface roughness and surface temperature. 177

Table A1.1 - Thermal properties of natural materials.....208

Table A1.2 - Thermal properties of materials used in building and urban construction.....208

Table A2.1 - Data analysis results. Statistics of CR data for each category performed over grids A and B (build up area, buildings height, buildings area, and total area for each category).....210

Table A2.2 - Statistics over the entire study domain for the roughness parameters z_H(m), ☒$_F$, z_D (m) and z_{0M} (m), shown in Figure 6.20 and Figure 6.21.....211

Acknowledgements

I would like to thank Professor Chris Collier for the guidance of my research work and his valuable comments during the progress of this thesis. I am especially grateful for his enormous patience in the moments I most needed encouragement. He always encouraged me giving sage advice in his friendly manner.

I would like to thank Dr. Fay Davies for her assistance in developing some computer codes and for her comments especially at the writing up stage. I greatly appreciate her patience in reading my work and her friendship.

I am thankful to Dr. Karen Bozier and Dr. Gavin Robbins for their help in gathering some atmospheric observations at Salford University.

Thanks are also due to the *University of Manchester Atmospheric Science Research Group* for the provision of urban meteorological data, the *Met Office* (through the *British Atmospheric Data Centre*) for the provision of rainfall radar data, and the *Environmental Agency* for the provision of digitised georeferenced data of the surface elements height for Greater Manchester. The SALFEX experiment was in collaboration with the Met Office and the University of Reading, and I would like to thank them for the SALFEX data used in this thesis.

I acknowledge the earlier financial assistance of *Fundação Eugénio de Almeida*, which encouraged me to do my Ph.D. studies abroad.

I am grateful to Professora Ana Maria Silva for supporting my application to Salford University and for her suggestions.

I acknowledge the support of the *Department of Physics of the University of Évora* and the *Geophysics Centre of Évora* that facilitated my stay in England.

This Ph.D. study was funded by the Portuguese Foundation for Science and Technology (FCT) under doctoral grant SFRH/BD/4771/2001, through the Operational Programme for Science and Innovation 2010 (POCI 2010).

Abstract

Human activities, and alterations of the nature and morphology of the land surface, perturb the land surface- atmosphere balances of energy, mass and momentum. These changes lead to modifications of the atmospheric boundary layer which affect weather processes. Specifically, urban areas have been documented to change temperature distributions, wind patterns and air quality. They can also impact the development of clouds and precipitation in and around cities.

Among the causes ascribed to the modification of convective precipitation induced by urbanisation, most studies suggest that the atmospheric destabilisation associated with the heat island and surface roughness is the most significant, more so than microphysical or moisture enhancement. However the relative importance of these mechanisms remains unclear.

The present work reports an investigation of the effects of urban surface heterogeneity on the distribution of sensible heat flux and its impact on convective precipitation, in Greater Manchester. A simple numerical scheme is formulated to derive fields of surface sensible heat flux for a range of wind and temperature values over the urban area. This involves the derivation and mapping of urban surface morphologic characteristics such as the height of buildings and the frontal area index. Comparisons are made with previously published morphologies derived for other urban areas. The sensible heat flux values from the numerical procedure are compared to direct independent measurements for a number of days. The sensible heat flux field and the rainfall field measured using a C-band radar are compared. The possible influences of the urban morphology on the rainfall distribution, and the eventual initiation of convective cells by the sensible heat flux input generated over buildings in Manchester city centre, are discussed.

Chapter 1. Introduction

The industrial revolution led to a rapid development of urban areas that has continued through the last 200 years or so. Over the last 50 years, there was a significant growth of the world's urban population (see **Figure 1.1**), and it continues to grow faster than the total population of the world. Recent estimates of the United Nations (2004) indicate that about 48% of the world's population lived in urban areas in 2003, and this proportion is expected to rise to 61% by 2030, while for the rural population a slight decline is anticipated in the same period. Almost all the world's population growth expected in the next 30 years will be concentrated in the urban areas.

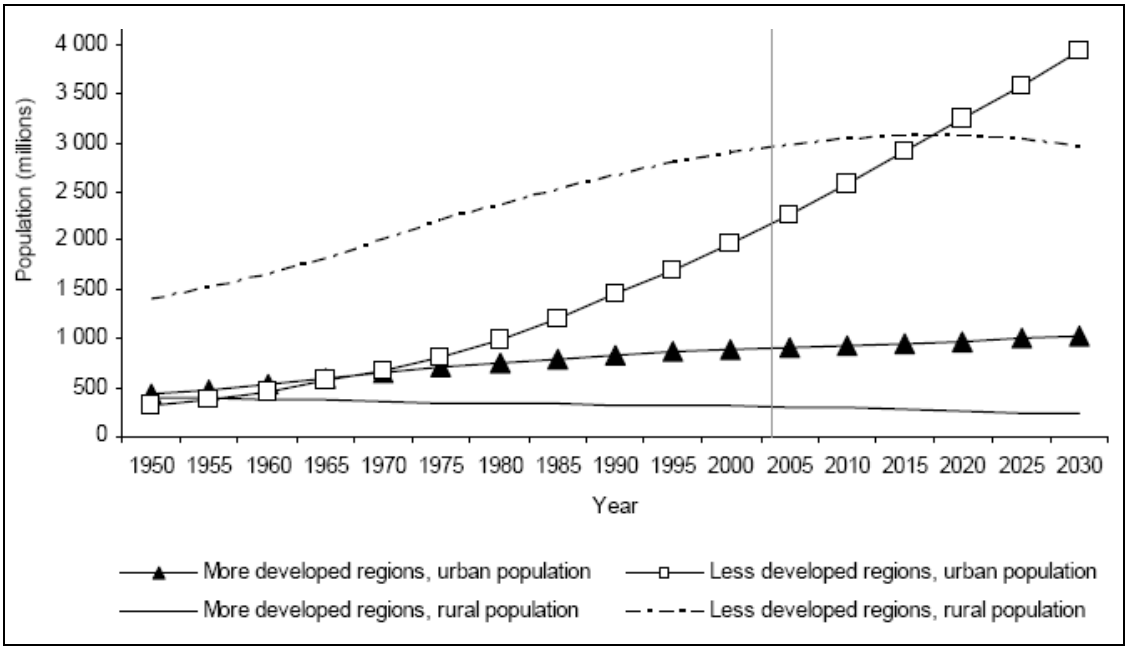

Figure 1.1 *. - Urban and rural populations of more developed regions and less developed regions, 1950-2030 [from World Urbanization Prospects, United Nations, 2004].*

The process of urbanisation did not affect in the same way all regions of the world. Urbanisation is very advanced in the more developed regions (Europe, Northern

America, Australia/New Zealand and Japan), where 74% of the population lived in 2003 in urban areas, a figure projected to increase to 82% by 2030. In Europe, for example, during this period the fraction of the population living in urban areas is expected to rise from 73% to 80%. On the other hand, in the less developed regions (Africa, Asia (excluding Japan), Latin America and the Caribbean, Melanesia, Micronesia and Polynesia) the proportion of urban population is lower, 42% in 2003, but is expected to attain 57% by 2030 (United Nations, 2004). Population growth will be particularly rapid in the urban areas of less developed regions (**Figure 1.1**).

It is important to mention that, in spite of the trend towards the concentration of the population in large metropolitan areas, this has not yet resulted in a decline in the size of smaller cities. In 2003, the majority of all urban residents (25% of the world's population) lived in relatively small urban settlements with fewer than 500,000 residents, while just 4% of the world's population resided in mega-cities (urban conurbations of 10 million persons or more) (United Nations, 2004). In the more developed regions, in 2003 nearly 40% of the population lived in small urban settlements, which is about twice that in the less developed regions. Taking into account the present scenario of the urban population, and in spite of the particular attention that has to be paid to the problems associated with the large metropolitan areas, it is very important not to neglect the comparatively smaller cities. The development of all urban areas, with their specific problems, should be studied.

The speed and the scale of the world's urban population growth pose formidable challenges to the individual countries as well as to the world community. Monitoring these developments and creating sustainable urban environments remain crucial issues on the international development agenda (United Nations, 2004).

Although presently urban areas only cover approximately 0.2% of the earth's land surface, the spatial coverage and density of cities are expected to rapidly increase in the future. Urban environments have impacts at all scales from local to global by changing atmospheric composition, impacting components of the water cycle, and modifying the carbon cycle and ecosystems. However, our understanding of the role of urbanisation on the total Earth's climate system is incomplete. More observational and modelling work is required to improve basic understanding of how urban zones impact the weather and climate (Shepherd, 2005; Collier, 2006; Pielke *et al*., 2006, 2007).

Urbanisation, which includes residential, commercial and industrial developments, brings about significant changes in the land use and land cover. Urbanisation causes essential differences in the characteristics of the land-atmosphere interface from those of the surrounding rural areas. For example, urban construction materials store heat and form an impermeable surface, leading in general to a warmer and drier surface and increasing runoff. The block like geometry of the buildings creates the possibility of radiation trapping and air stagnation on the streets (canyons), and causes atmospheric uplift and a very rough surface that generates air turbulence. On the other hand, additional heat and water are released into the atmosphere from anthropogenic sources associated with urban activities. Moreover, the increase of air pollution affects the air quality and atmospheric radiative processes, and supplies additional cloud condensation nuclei (Oke, 1987; Arya, 2001; Roth, 2002; Arnfield, 2003; Jin and Shepherd, 2005; Collier, 2006).

The human activities and the alteration of the nature and morphology of the land surface (i.e., its radiative, thermal, aerodynamic, moisture and other thermodynamic properties) perturb the land surface-atmosphere balances of energy, mass (water vapour, cloud condensation nuclei and other atmospheric constituents) and momentum, leading to the modification of the atmospheric boundary layer and affecting the weather processes (as discussed further in Chapter 2). Urban areas have been documented to affect temperature distributions, wind patterns and air quality (the urban heat island is probably the effect more widely discussed). Furthermore, urban areas can also impact the development of clouds and precipitation in and around cities, in particular the enhancement of convective precipitation downwind urban areas has been broadly observed (Chapter 3). Some numerical studies show, for example, the impact of the surface sensible heat flux and roughness of urban surfaces on convective rain (Thielen *et al*., 2000, Shepherd, 2002, Rozoff *et al.*, 2003, and Shepherd, 2005).

Among the causes ascribed to the modification of convective precipitation induced by urbanisation (Shepherd *et al.*, 2002), most studies suggest that dynamic forcing (destabilisation associated with the heat island and surface roughness) is the most significant (Baik *et al.*, 2001; Guo *et al.*, 2006), more so than microphysical or moisture enhancement. Urban areas modify boundary layer processes mostly through the production of an urban heat island, and by increasing turbulence through locally enhanced roughness. However the relative importance of these mechanisms remains

unclear (Collier, 2006; Guo *et al*., 2006; Shepherd and Burian, 2003; Shepherd, 2005). Further studies are necessary to investigate urban effects on convective precipitation in cities located in different geographic and climatic conditions, and to characterise the physical processes involved in urban-induced precipitation (Guo *et al*., 2006; Shepherd, 2005). Convection is an important factor of the weather in the United Kingdom, since a considerable percentage of precipitation is produced by convective clouds (Bennett *et al.*, 2006; Hand *et al*, 2004; Hand, 2005; Shaw, 1962; Wilby, 2001).

The principal aim of this research is to develop a numerical model of the urban atmospheric boundary layer that can be used to estimate surface sensible heat flux across a large urban area. This requires the following objectives: (i) to specify the characteristics of the buildings in the urban area, which for this work is part of Greater Manchester encompassing the centres of Manchester and Salford, and (ii) to perform sensitivity tests investigating how the model performs under particular conditions. A further objective is to investigate the influence of the urban area on the distribution of convective precipitation by comparison of the distribution of surface sensible heat flux with observations of rainfall made using weather radar located to the north of the study area.

A simple numerical scheme, based upon several published systems, principally Grimmond and Oke (1999a) and Voogt and Grimmond (2000), and developed to derive fields of surface sensible heat flux for a range of wind and temperature values over an urban area, is used to explore the impact of urban surface heterogeneity. The objective is to apply the model to the Manchester urban area for convective daytime summer conditions. These are conditions for which we anticipate that the urban morphology will modify the distribution of sensible heat flux, and influence convective developments (Hand *et al*, 2004; Hand, 2005; Wilby, 2001). The model is formulated for a large part of Greater Manchester, in a study area of 24 × 24 km^2, with a grid resolution of 1 × 1 km^2, where the bulk equations are used and the model parameters are specified as averages over each grid square. Input meteorological variables used in the model are the radiometric surface temperature (satellite skin temperature), T_R, the air temperature, T_a, and the wind velocity, u. Model roughness parameters are the zero-plane displacement length, z_D, roughness length for momentum, z_{0M}, and roughness length for heat, z_{0H}. Morphologic methods are adopted

to estimate the zero-plane displacement length and the roughness length for momentum as a function of the surface elements height, z_H, and the frontal area index, λ_F. Chapter 4 concerns the modelling of turbulent fluxes on the atmospheric surface layer, providing the background basis of the numerical model of surface sensible heat flux that will be used, and a detailed description of the formulation of the model is given in Chapter 5. The sensitivity of the surface sensible heat flux to the different model input parameters, surface temperature, air temperature, wind velocity, mean building height, and frontal area index, has been investigated for a range of typical input values. Also simulations with a schematic urban morphology used to investigate the impact of different types of building arrays, have been carried out and discussed here.

To implement the model, surface morphology as well as meteorological data needed to be obtained for the Greater Manchester study area. Thus an urban surface characterisation in terms of some morphologic aspects, such as the fraction of the built up area, the surface elements height, z_H, and the frontal area index, λ_F, has been carried out during this project. A surface morphologic database for Greater Manchester was developed from analysis of digitised surface elements data, aerial photography, maps and field surveys, and the surface roughness parameters zero-plane displacement length, z_D, and roughness length for momentum, z_{0M}, were estimated for the entire study domain (see Chapter 6).

Finally, the model of surface sensible heat flux is implemented over Greater Manchester study area (Chapter 7) for three study days (on 2 May 2002, 14 and 21 June 2004), using observational values of air temperature, wind speed, and surface temperature derived from satellite imagery, at around midday, and the spatial distribution of surface roughness parameters zero-plane displacement length and roughness length for momentum, obtained in Chapter 6. The resulting surface sensible heat flux fields so obtained are examined in order to look for any patterns that may indicate areas of increased heat flux, which might be related to convective initiation downwind the urban area. It is found that the urban area produces considerable spatial variation in surface sensible heat flux, with particularly high values in the city centre, and the lowest values in rural areas.

Subsequently (Chapter 8), the sensible heat flux field over Greater Manchester previously derived (in Chapter 7) for the 21 June 2004 study day, is compared with

integrated rainfall rate field derived from a C-band radar. Convective cells are observed to initiate downwind of the centre of the city occupied by high rise buildings. In order to demonstrate that our hypothesis is well founded, here we relate the differences of surface sensible heat flux, between the Greater Manchester urban area and its rural surroundings, to values of thermal forcing, which may eventually trigger convective initiation. The methodology adopted is comparable to that of Baik e*t al.* (2001), used to evaluate the impact of the nocturnal excess of surface radiative flux over an urban area, compared with its rural surroundings, on convective initiation downwind the city.

In this way, the model-generated distribution of sensible heat flux over Greater Manchester is applied to investigate if the presence of the city may trigger convective initiation. The eventual initiation of convective cells by the sensible heat flux input generated by the high-rise buildings in the city centre is discussed.

In Chapter 9 conclusions and future work are presented. Major urban development and regeneration have been planned in several regions of the UK and elsewhere. The modification of the morphology of the cities expected in the future poses new challenges in various knowledge fields, from building design and city planning to meteorology.

Chapter 2. The atmospheric boundary layer

In this chapter, a general presentation of the *Atmospheric Boundary Layer* (ABL) is made in order to provide the context within which the later research is presented. First, a flat, uniform, and homogeneous atmospheric boundary layer is assumed, and special attention is paid in the evolution of the ABL during the diurnal cycle over the land surface. Then, the modification of the ABL due to the presence of an urban area will be discussed; the impact of both the urban heat island and the increased roughness on the boundary layer structure will be considered, as well as some aspects of urban pollution.

2.1 Overview

2.1.1 The ABL sublayers

The troposphere, where most weather phenomena occur, extends from the earth's surface up to an average altitude of 11 km. The whole troposphere suffers the influence of the surface characteristics, but in general only the lowest couple of kilometres are directly modified by the surface. The Atmospheric Boundary Layer (ABL) can be defined as the bottom layer of the troposphere that is directly influenced by the presence of the earth's surface, and responds to surface forcings with a time scale of about an hour or less (Stull, 1988). These forcings include frictional drag, evaporation and transpiration, heat transfer, pollutant emission, and terrain induced flow modification.

The ABL is characterised by turbulent mixing generated by frictional drag as the atmosphere moves over the surface of the Earth, and by the rising thermals from the heated earth's surface. The ABL receives much of its heat and all of its water through turbulent processes. The ABL is capped by a statically stable layer of air or *temperature inversion.* The height of the ABL ranges from hundred metres, in

statically stable situations, to a few kilometres, in convective conditions, depending upon the strength of the surface-generated turbulent mixing (Oke, 1987) (**Figure 2.1**). In general the ABL is thinner in high-pressure regions than in low-pressure regions. In low-pressure regions the ABL extends from the ground to large altitudes throughout the troposphere, and it is difficult to determine the top of the ABL for these situations. Thus, in these cases, cloud base is normally used as an arbitrary limit for ABL studies (Stull, 1988).

The bottom of the ABL (10%) is called the *surface layer* (**Figure 2.1**); by day it may extend to a height of about 50 m, but at night when the turbulence decreases, the ABL becomes thinner and it may be only a few metres in depth. Above the surface layer there is the *outer layer*, often referred to as the *mixed layer,* which extends to the top of the ABL.

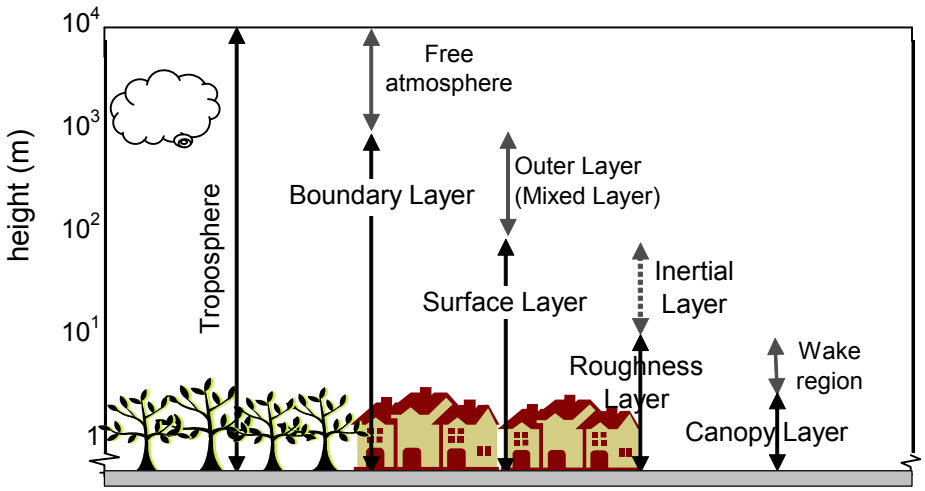

Figure 2.1*- Definition sketch showing orders of magnitude of the height of the atmospheric boundary layer (ABL) and its sublayers; the vertical scale is in metres.*

The *surface layer* may be divided in two main layers, the *roughness layer* and the *inertial layer* (Stull, 1988; Oke, 1987; Brutsaert, 1982). Near the surface is the *roughness layer*, whose depth depends upon the nature, dimensions and arrangement of the surface roughness elements. In this region the air flow is strongly affected by the individual surface elements (i.e., grass, trees, buildings, etc.) and, thus, it is very irregular. Within the *roughness layer* ducting and trapping of airflow and multiple reflections of radiation may occur. The *roughness layer* includes the *canopy layer* (Oke *et al.*, 1989; Raupach *et al.*, 1991) which extends from the surface to the top of

the surface elements, and a turbulent wake region above, where the wakes from the individual roughness surface elements are distinguishable.

The *roughness sublayer* extends from the surface up to a height at which the influence of individual roughness elements on the flow is "mixed up" by turbulence (Raupach *et al.,* 1991; Rotach, 1999), and the flow can be considered horizontally homogeneous. This remaining part of the surface layer, above the roughness layer, is usually called *inertial sublayer*.

Within the roughness sublayer there is greater spatial variability of temporally averaged atmospheric fluxes than within the inertial sublayer; these fluxes are chaotic in the roughness sublayer but become approximately invariant in the inertial sublayer (Grimmond and Oke, 2002).

The inertial sublayer is subjected to the average effect of the surface, in terms of momentum and heat budgets, and the individual wakes are not important. Within the *inertial layer* the vertical wind profile is approximately logarithmic and the Monin-Obukhov Similarity Theory (MOST) is assumed to be valid (Oke, 1987, 2006; Rotach *et al.*, 2005 ; Brutsaert, 1982; Stull, 1988; Garratt, 1992; Kaimal and Finningan, 1994; Arya, 2001). This will be discussed further in Chapter 4.

In most applications over urban areas simple relationships, based only on the average building height (z_H), are used to determine the height of the roughness layer (z_r) (Rotach, 1999). Rule-of-thumb estimates and field measurements indicate that the top of the roughness layer can be as low as $1.5z_H$ at densely built, closely spaced, and homogeneous sites, but greater than $4z_H$ in low density areas (Grimmond and Oke, 1999a; Rotach, 1999; Christen *et al*. 2003b). Thus, an instrument placed below z_r, in the roughness layer, may register microclimate anomalies but above that, in the inertial layer, it 'sees' a blended, spatially-averaged signal that is representative of the local scale (Oke, 2006).

In direct contact with the surface there is a thin layer of few centimetres where molecular transport dominates over turbulent transport. This layer is called *micro-layer, interfacial layer or laminar layer* (Stull, 1988; Oke, 1987; Brutsaert, 1982).

Above the ABL is the *free atmosphere*, which is usually non turbulent, or sporadically turbulent. Above the ABL the effects of surface friction are absent so the wind is governd by the strength and orientation of the horizontal pressure gradient force and by the Coriolis force. At the *free atmosphere*, the wind is approximately

geostrophic, that is, the horizontal Coriolis force nearly balance the horizontal pressure gradient force. The geostrophic wind is parallel to the isobars with low pressure to the left in the Northern Hemisphere and to the right in the Southern Hemisphere (Garratt, 1992).

As the surface is approached, friction reduces the wind speed and, thus, the Coriolis force, which depends on the wind speed, latitude an air density. The geostrophic balance of forces is broken, and the wind direction changes so that it cuts the isobars at an increasingly large angle the nearer is to the surface. Thus, as the surface is approached the wind direction changes, in an anti-clockwise manner in the Northern Hemisphere, and clockwise in the Southern Hemisphere. The deviation of the wind vector from the geostrophic wind vector is called *backing* or *veering* angle. At the same elevation, the surface roughness alterations modify the wind speed and consequently alter the backing (or veering*)* angle. Therefore, as wind flows from one surface to another of different roughness, both the wind speed and direction are altered (**Figure 2.15**). In addition, the wind direction can also change due to alterations of atmospheric stability, because it affects the vertical transport of momentum (Oke, 1987). Alterations of the wind direction observed over cities have been attributed to the rural- urban surface differences (see Chapter 3).

The *Ekman spiral* (Garratt, 1992; Holton, 1992; Stull, 1988) is a mathematical description of the wind profile in the atmospheric boundary layer, and it is frequentely used to model the wind in the *outer layer*. In this idealized description it is stated that the wind speed is zero at the surface, due to friction, and the wind becomes geostrophic at large distances above the surface, where friction is negligible. In this context, the lowest level at which the wind becomes geostrophic (geostrophic wind level) may be considered to be the top of the ABL. In practice it is observed that the geostrophic wind level is often between 1 and 2 km, and it is assumed that this indicates the upper limit of frictional influence of the earth's surface. According to the Ekman spiral description, below the geostrophic wind level the deviation of the wind vector from the geostrophic wind vector diminishes upward at an exponential rate. The wind blows across the isobars toward low pressure, at an angle that is a maximum at the surface and does not exceed 45°.

2.1.2 The diurnal cycle of the ABL

During fair weather over land, the ABL has a marked diurnal cycle (Oke, 1987; Stull, 1988), which is sketched in **Figure 2.2**. Soon after sunrise the ground surface radiation budget becomes positive and the surface temperature rises. The air near the surface becomes hotter than the air above and the vertical gradient of the air temperature generates an upward turbulent sensible heat flux through the surface layer. A turbulent *mixed layer* starts to grow in depth, and the stable layer of the previous night successively erodes until it is eliminated by mid-morning. This *mixed layer* is characterised by intense mixing in a statically unstable situation where thermals of warm air rise from the ground. The convectively driven *mixed layer* is capped by a statically stable *entrainment zone,* also called an *inversion layer,* which acts as lid to the rising thermals and confines the domain of turbulence. The *mixed layer* grows principally through entrainment at the top of the layer, and reaches its maximum height of about 1 to 2 km in the afternoon (Oke, 1987; Stull, 1988).

Near sunset, solar radiation rapidly decreases and, due to long wave radiation emission, the Earth's ground surface begins to cool to a temperature below that of the air above, the surface radiation budget turns negative, and the thermals cease to form. There is an air temperature gradient directed towards the surface, and so downward sensible heat flux. As the night progresses, a ground-based radiation inversion develops above the ground surface, and the bottom of the atompheric *boundary layer* is transformed into a statically stable *nocturnal boundary layer* (Oke, 1987). With the change in the surface sensible heat flux, the primary source of turbulence in the ABL is removed and so the turbulence rapidly decays. Only roughness generated turbulence persists near the surface (Oke, 1987), and the *nocturnal boundary layer* height may shrink to less than 100 m. The NBL layer is usually strongly stable and there is no mixed layer near the surface. Above the inversion a neutral or weakly stable layer exists, the *residual layer*, as a remnant of the previous day's mixed layer (Oke, 1987). As opposed to the *daytime mixed layer*, which has a clearly defined top, the *nocturnal stable boundary layer* has a poorly defined top that smoothly blends into the residual layer above (Stull, 1988).

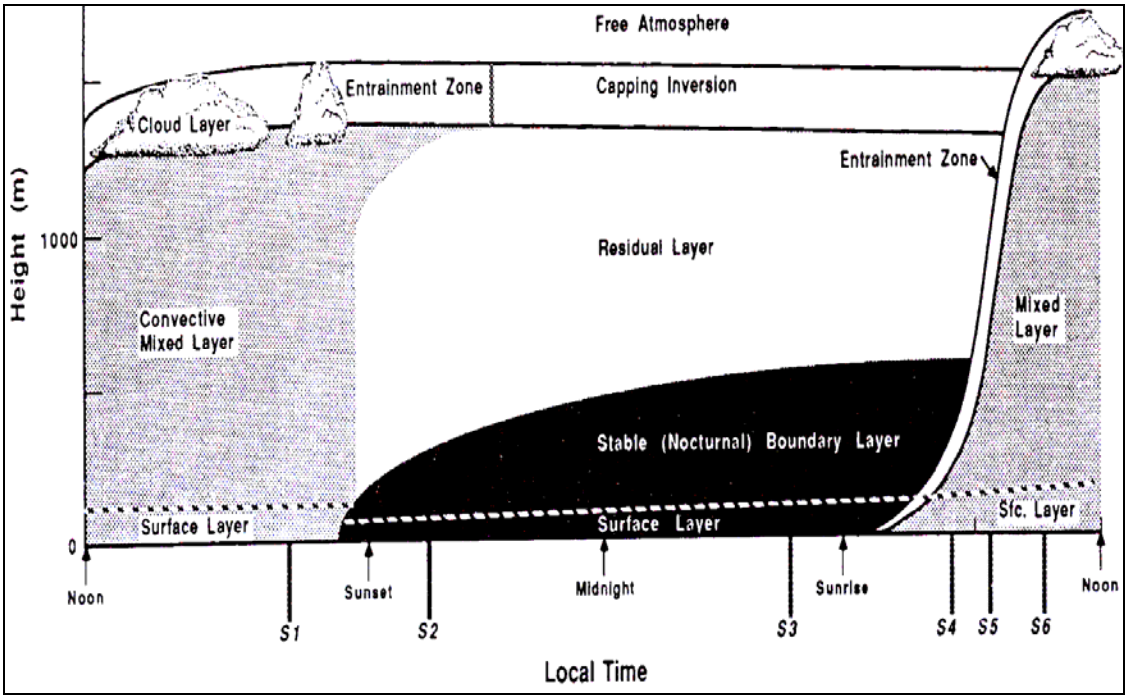

Figure 2.2 *- The boundary layer in high pressure regions over land consists of three major parts: a very turbulent mixed layer; a less turbulent residual layer containing former mixed layer air; and a nocturnal stable boundary layer of sporadic turbulence.(After Stull, 1988).*

Typical daytime and night time atmospheric profiles of potential temperature (θ), wind speed (u) and water vapour mixing ratio (q) over land in midlatitudes during cloudless conditions, are shown in **Figure 2.3**.

Before going further, it is important to define some atmospheric variables. The *potential temperature* (θ) of an air parcel is defined as the temperature which the unsatured parcel would have if it were expanded or compressed adiabatically from its existing pressure and temperature (p, T) to a standard pressure p_0 (generally taken as 1000 mb). The *virtual temperature* (T_v) is the temperature that dry air must have in order to have the same density as the moist air at the same temperature. The *virtual potential temperature* (θ_v) of an air parcel is defined as the temperature which the unsatured parcel would have if it were expanded or compressed adiabatically from its existing pressure and virtual temperature (p, T_v) to a standard pressure p_0 (generally taken as 1000 mb). Further discussion about these variables (θ, T_v, and θ_v) and the respective atmospheric vertical profiles related to atmospheric stability are presented in

a number of publications (Wallace and Hobbs, 1977; Stull, 1988; Tsonis, 2002; Pielke, 2001; Arya, 2001).

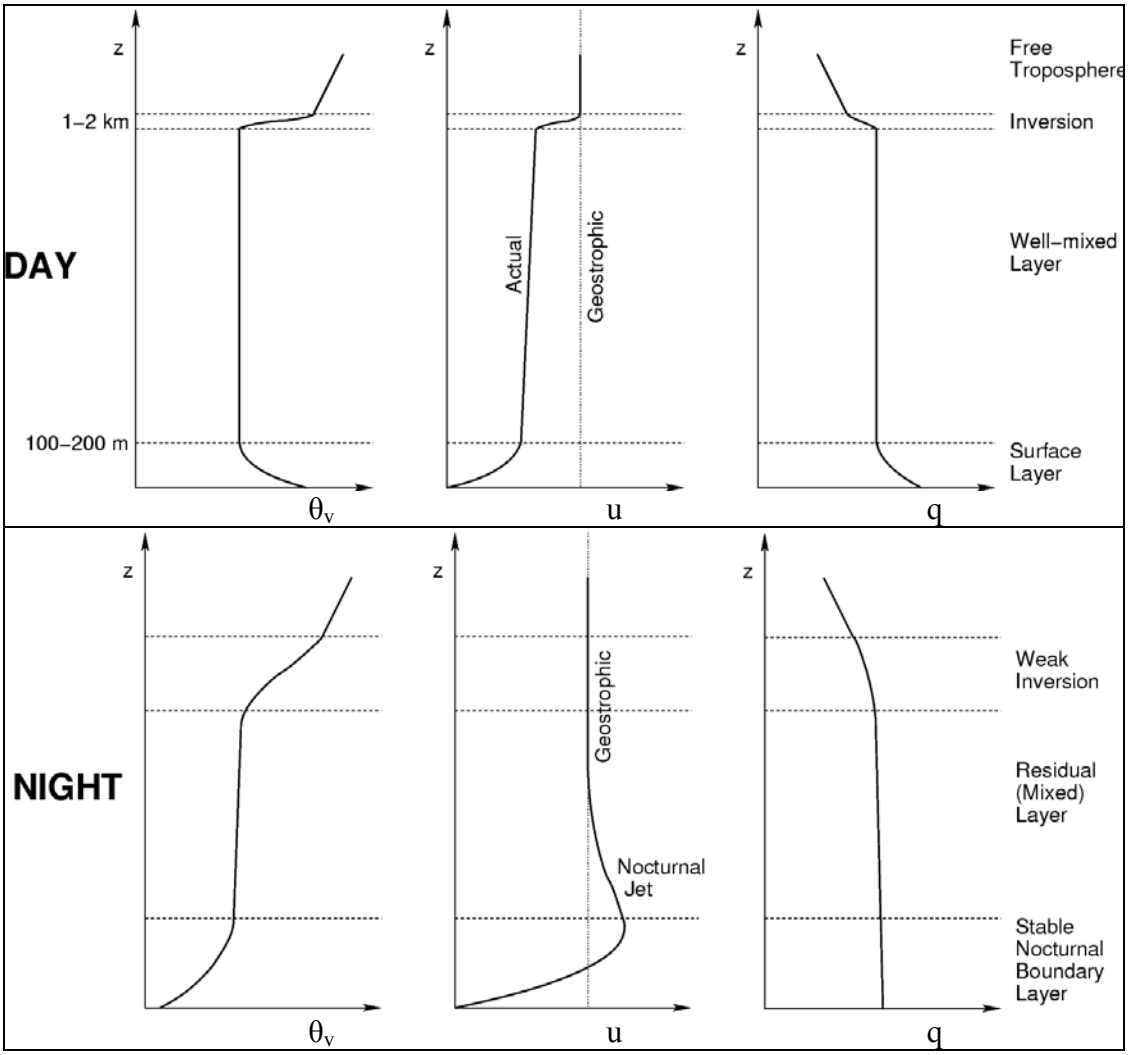

Figure 2.3 *- Typical atmospheric profiles of the virtual potential temperature (θ_v), wind speed (u) and water vapour mixing ratio (q) over land in midlatitudes during cloudless conditions [from www.met.rdg.ac.uk/ ~swrhgnrj/ teaching/ MTMG49/ 1.1_introduction.doc, University of Reading, Boundary Layer Meteorology and Micrometeorology notes on-line, download on 2008].*

The turbulence in a typical daytime boundary layer tends to mix uniformly temperature, wind speed, moisture and other properties throughout the ABL in the vertical. The resulting daytime vertical profiles of virtual potential temperature (θ_v) wind speed (u), and water vapour mixing ratio (q, mass of water vapour per unit mass of dry air), and are sketched in **Figure 2.3 (DAY)**, for the time indicated by flag S1 in

Figure 2.2. In **Figure 2.3 (Day)** the structure of the atmospheric boundary layer is clearly evident. The *surface layer* is often charaterised by a superadiabatic profile, and virtual potential temperature profiles are nearly adiabatic in the middle portion of the mixed layer (Stull, 1988). Abrupt changes in these profiles occur at the top of the mixed layer where the capping inversion often inhibits the upward transport of surface effects (Oke, 1987). Water vapour mixing ratio tends to decrease with height due to the evaporation of soil and plant moisture from below, and the entrainment of drier air from above. The moisture decrease across the top of the mixed layer is very pronounced, and is often used together with potential temperature profiles to identify the mixed layer top from radiosoundings (Stull, 1988). Winds are subgeostrophic throughout the mixed layer. The middle portion of the mixed layer frequently has nearly constant wind. Wind speed decrease towards zero near the ground, resulting in a wind speed profile that is nearly logarithmic with height in the inertial sublayer (Arya, 2001; Stull, 1988).

Figure 2.3 (NIGHT) represent atmospheric profiles for the time indicated by flag S3 in **Figure 2.2.** Typical night time temperature profiles often show an inversion aloft (at the top of the the residual layer) as well as a lower ground-based radiation inversion (Oke, 1987). The surface vertical profiles of temperature, and eventualy humidity, reverse sign because the surface is now a sink for heat and water vapour. The wind profile may exibit a maximum located near the top of the *nocturnal stable boundary layer,* which is termed *low level nocturnal jet*. It arises because the stability of the surface inversion decouples the air above it from the frictionl influence of the surface (Oke, 1987; Stull, 1988).

The preceding decription of the diurnal cycle of the ABL only relates to horizontal, spatially uniform terrain in fine weather. This ideal picture can be considerably broken up by weather systems whose wind and cloud patterns are not tied to surface features or to the daily heating cycle (Oke, 1987). Threfore, stable boundary layers also can form during the day, as long as the underlying surface is colder than the air. These situations often occur during warm air advection over a cold surface, such as after a warm frontal passage or near shorelines (Stull, 1988). Also, overcast conditions can reduce insolation at ground level leading, consequently, to a decrease of the intensity of thermals. Under these conditions the mixed layer may exhibit slower

growth during the day, and may even become non-turbulent or neutrally-stratified (Stull, 1988).

On the other hand, over oceans, the boundary layer depth varies relatively slowly in space and time, because the sea surface temperature changes little over the diurnal cycle. Most changes in boundary layer depth over oceans are caused by synoptic and mesoscale processes and vertical motion and advection of different air masses over the sea surface (Stull, 1988).

2.1.3 Stability and Convection

The principal agents of transport and mixing in the mixed layer are *thermals*. These are rising masses of warm air that originate over especially warm surface zones. If surface winds are moderate a surface hump (hills or islands, for example) can act as a trigger for thermals. Favoured sites which act as sources for thermals are relatively dry areas, such as bare soil, rock, asphalt or sands, and Sun-facing slopes. The hot air at the surface forms a flattened bubble until the instability becomes sufficient to cause it to start to rise. The thermal grows in size as it rises due to entrainment of surrounding air. The size of the thermal depends on the dimensions of the source area, and the rate of rise upon the degree of instability. The thermal may cease to rise because (i) it has lost buoyancy by mixing, (ii) its moisture condenses into cloud and the extra turbulence due to the release of latent heat causes even greater mixing or because (iii) it reaches an inversion (Oke, 1987).

As the tops of the thermals reach greater and greater depths they might reach their *lifting condensation level* if sufficient moisture is present, resulting in fair-weather cumulus clouds, which may occur during the course of the day (Stull, 1988). Whether cumulus clouds remain relatively small or undergo significant vertical development (possibly leading to precipitation or a severe storm) is largely dependent upon the strength of any capping inversion and the stability of the air above the ABL (Bennett *et al.*, 2006).

The dominant process in the lower atmosphere is convection. A major control on the type and extent of convective activity is the vertical temperature structure as express in the concept of stability. Atmospheric stability may be viewed as the relative

tendency for an air parcel to move verticaly, and can be evaluated in terms of the temperature lapse rate. For example, considering the eventual vertical motion of an unsaturated air parcel, parcel theory gives a criterion of static stability of the atmosphere, in terms of the environment virtual potential temperature lapse rate, $\partial\theta_v/\partial z$ (e.g., Arya, 2001; Pielke, 2001; Tsonis, 2002):

unstable, when $\left(\frac{\partial\theta_v}{\partial z}\right) < 0$; neutral, when $\left(\frac{\partial\theta_v}{\partial z}\right) = 0$; stable, when $\left(\frac{\partial\theta_v}{\partial z}\right) > 0$ (2.1)

As illustrated in **Figure 2.4**, the measurement of the local lapse rate alone is insufficient to determine the static stability, i.e., there are many situations where the local definition fails (Stull, 1988 ; Arya, 2001). A determination of static stability is possible if the virtual potential temperature θ_v profile over the whole ABL is known, as sketched in **Figure 2.4**. A definition of atmospheric static stability based on the knowledge of convection or measurements of buoyancy flux is presented by Stull (1988). For a further discussion on the issue of atmospheric stability, see for example Wallace and Hobbs (1977), Holton (1992), Pielke (2001), and Tsonis (2002).

The boundary layer structure is directly influenced by the surface heat and moisture fluxes. Once the surface energy budget is altered, fluxes of heat, moisture, and momentum within the planetary boundary layer are directly affected (Segal *et al.*, 1989). The interaction between the Earth's surface and the atmosphere is critically important with respect to the development of cumulus convective rainfall (Pielke, 2001). Weather forecasters use a variety of indices, derived from the vertical profile of thermodynamic variables in the atmosphere, to assess the potential for such rainfall. These indices have been developed to measure the susceptibility of a given temperature and moisture atmospheric profiles to the occurrence of deep convection. Particularly useful measures are the convective inhibition energy (CINE) and the convective available potential energy (CAPE) as they provide information on whether or not convection will occur and on how severe a storm might become, respectively (Holton, 1992). Some of these parameters, which are referred to within the present text, are defined in the published literature (e.g., Musk, 1988; Holton, 1992 ; Pielke, 2001; Tsonis, 2002).

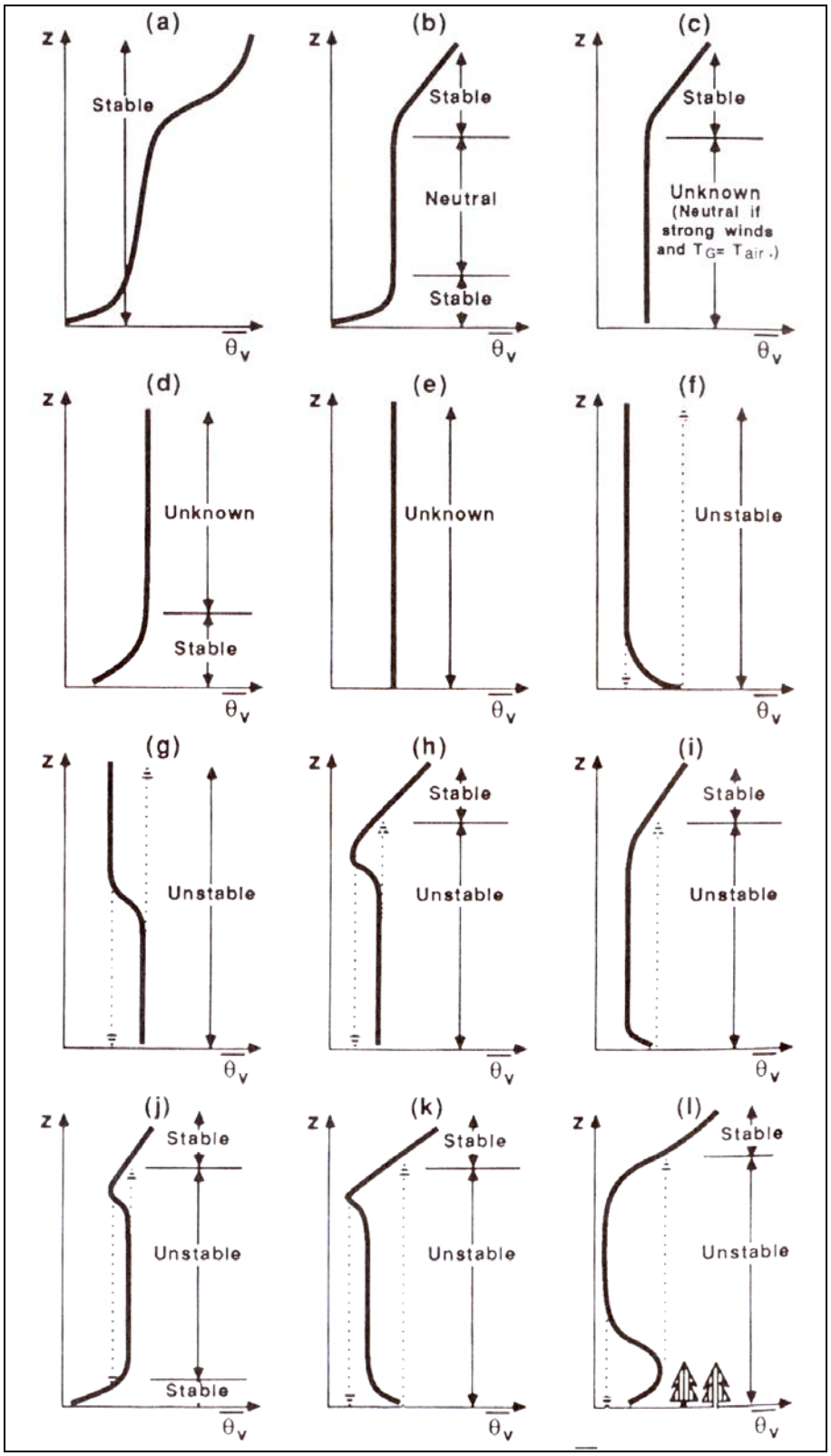

Figure 2.4 *- Non-local static stability characterisation for various hypothetical virtual potential temperature θ_v profile. Dotted lines denote parcel movement (after Stull, 1988).*

2.1.4 Entrainment and surface heat flux

Figure 2.5 illustrates an idealization of the vertical structure of the convective boundary layer, where the surface heat flux Q_H, depth of the layer z_i, and temperature stratification just above z_i determine the vertical profile of temperature and heat flux.

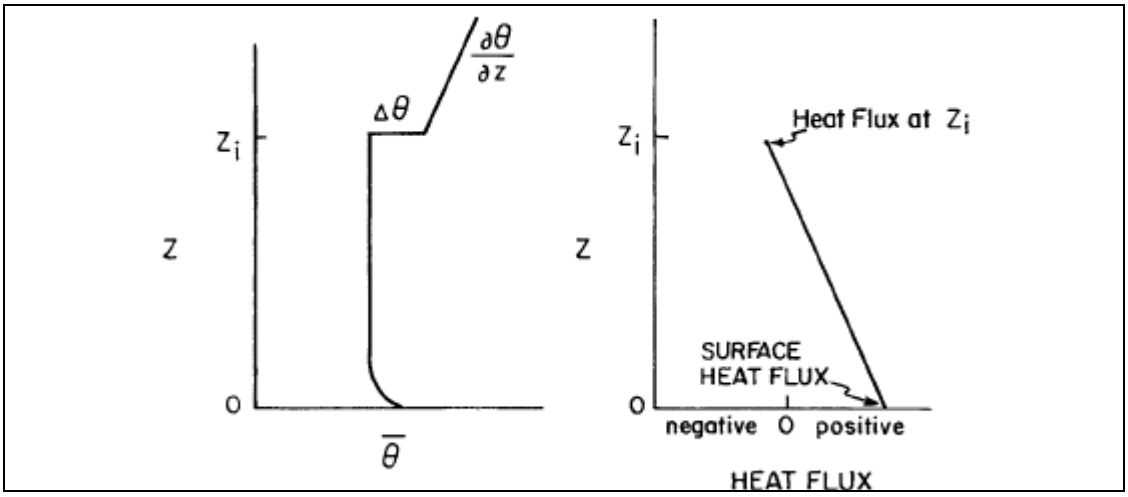

Figure 2.5 *The potential temperature and heat flux profiles assumed in the "jump" model (from Pielke, 2001).*

In the absence of large-scale wind flow, Pielke (2001) suggest the use of Deardorff (1974) equation to estimate the growth rate of z_i ,

$$\frac{\partial z_i}{\partial t} \sim Q_H^{2/3} z_i^{-4/3}. \qquad (2.2)$$

The entrainment of air from above z_i to heights below z_i is given by

$$Q_{H z_i} \sim -\alpha Q_H, . \qquad (2.3)$$

where α (=0.2) is the entrainment coefficient. The rate of growth of the boundary layer during the day, and the ingestion of free atmospheric air into the boundary layer, are therefore both dependent on the surface heat flux Q_H. McNider and Kopp (1990) discuss how the size of thermals generated from surface heating are a function of z_i, Q_H, and height within the boundary layer.

A simplified form of the prognostic equation can be used to illustrate how temperature change is related to the surface heat flux Q_{Hs} (Pielke, 2001),

$$\frac{\partial\theta}{\partial t} = \frac{\partial}{\partial z}\left(\frac{Q_H}{\rho c_p}\right), . \qquad (2.4)$$

where ρ is the air density and c_p is the specific heat at constant pressure. Integrating from the surface to z_i and using the mean value theorem of calculus yields

$$\frac{\partial\theta}{\partial t} = \frac{1}{z_i \rho c_p}\left[Q_{Hs} - Q_{Hz_i}\right] = \frac{1.2}{z_i \rho c_p} Q_{Hs}, \qquad (2.5)$$

where equation (2.3) with α=0.2 has been used. Using this equation, it is possible to estimate that, for a boundary layer of 1 km deep, a surface heat flux of 100 W m^{-2} produces a heating rate of 2 ^{o}C over 6 hours.

2.2 Thermal and mechanical modifications of the boundary layer over urban areas

2.2.1 The urban boundary layer

In comparison with the surrounding landscape the urban surface is usually rougher, warmer, and possibly drier (Roth, 2002). As air flows from the countryside to the city, an internal boundary layer develops downwind from the leading-edge of the city (**Figure 2.6a**). Above the internal boundary layer flow characteristics are the same as in approach flow at the same height above the surface. The urban boundary layer (UBL) is that portion of the atmospheric boundary layer above the canopy whose climate characteristics are modified by the presence of a city at the surface.

The layers of the UBL can be described in the same terms as discussed in **Section 2.1.1.** Thus the region of the UBL between the rooftops and the ground is known as the *urban canopy layer* UCL. Within this region we find the urban canyons, ducting and trapping of airflow, and multiple reflections of radiation (**Figure 2.6b** and **Figure 2.6c**). Above that is the *turbulent wake layer*, where the wakes from the individual buildings and surface patterns can be discerned. Still higher is the *urban inertial sublayer*, where the momentum and heat budgets feel the average effect of the urban area, but where individual wakes are not important. Finally, the urban *outer layer* extends to the top of the urban boundary layer.

The atmospheric boundary layer is more complex over urban than rural areas. In general, the urban roughness sublayer has a much larger vertical extension compared to rural areas occupying the first tens of metres above the surface. (Grimmond and Oke, 2002).

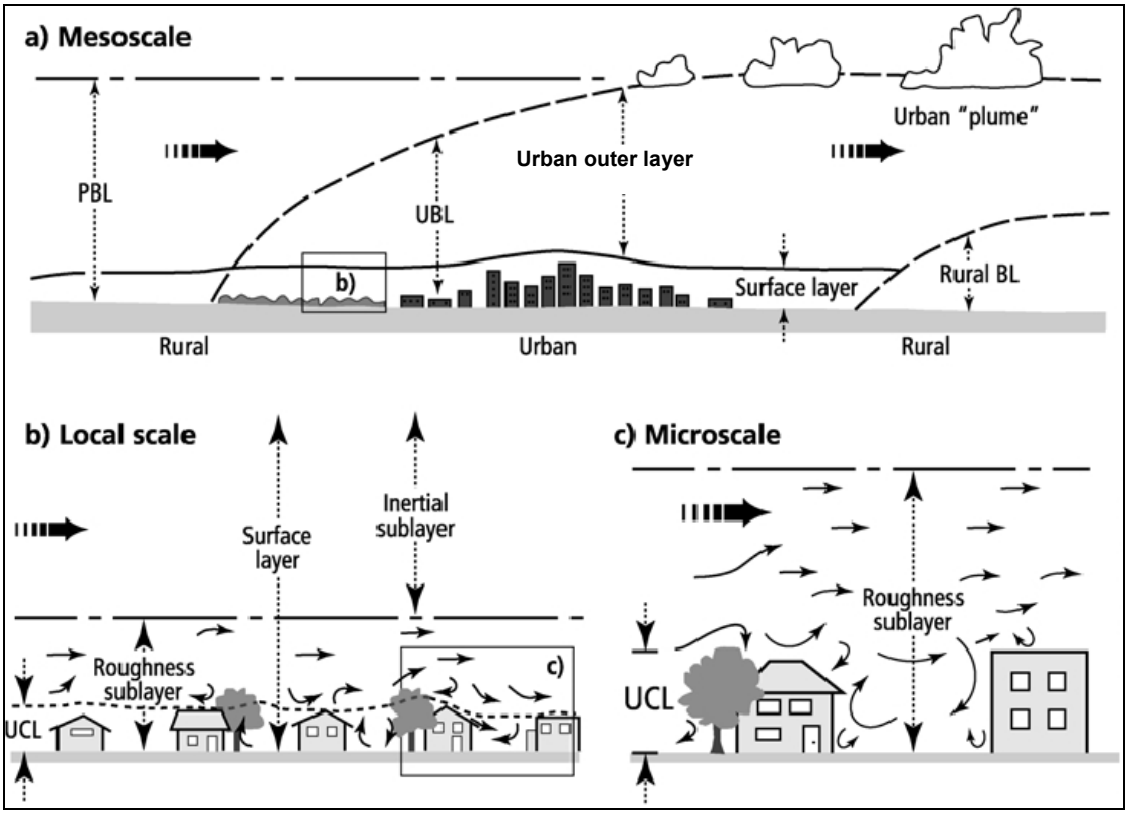

Figure 2.6 *- Schematic of the urban boundary layer including its vertical layers and scales (after Oke, 1997; from Piringer et al., 2002). UBL stands for Urban Boundary Layer, and UCL for Urban Canopy Layer.*

2.2.2 Thermal modifications of the ABL: the Heat Island

The most frequently observed and best documented climatic effect of urbanisation is the increase in surface and air temperature over the urban area, as compared to rural surroundings (Arya, 2001; Roth, 2002). This phenomena is termed urban heat island (UHI), because the pattern of isotherms forms an island shaped pattern. The actual pattern for a given city depends on the configuration of the urbanized area, but typically a large gradient of air temperature forms near the urban–rural boundary followed by a more gradual rise to the city core (**Figure 2.7**). The UHI

intensity (ΔTu-r) (**Figure 2.8**) is defined as the maximum difference in the urban peak temperature and the rural background temperature). Under reasonably stationary synoptic weather conditions, the air heat island intensity shows a pronounced diurnal variation with a minimun value around midday and a maximum value around or before midnight. UHIs in the air are largest at night with a maximum in the city core and may even be negative by day. Thus, the greatest air temperature differences between urban and rural areas are usually observed during the night (**Figure 2.8**). In many cases, heat from the city is sufficient to maintain a shallow convective mixed layer at night, even while a substantial stable boundary layer has developed over the surrounding countryside (**Figure 2.12**).

Within the built-up area, the pattern is influenced locally by surface features such as parks, water bodies and more or less densely built-up areas of the city, as well as topographical features such as hills (**Figure 2.7**) (Roth, 2002). The spatial pattern of isotherms loosely follows the urbanized area, but may show evidence of being transported (advected) downwind. The topographic setting of the city (e.g., a coastline or valley location) may add further complexity to the spatial characteristics of the UHI, as topographic effects (e.g., sea breezes) interact with urban effects. (Voogt, 2002)

The urban heat island (UHI) arises from differences in urban/rural cooling rates, i.e. less cooling in the city and it is most pronounced at night under clear skies and light winds. Although the UHI is most apparent after sunset the UHI induced circulation is more clearly observed during the daytime than nighttime because of the urban–rural pressure gradient and vertical mixing during daytime hours (Shepherd and Burian, 2003).

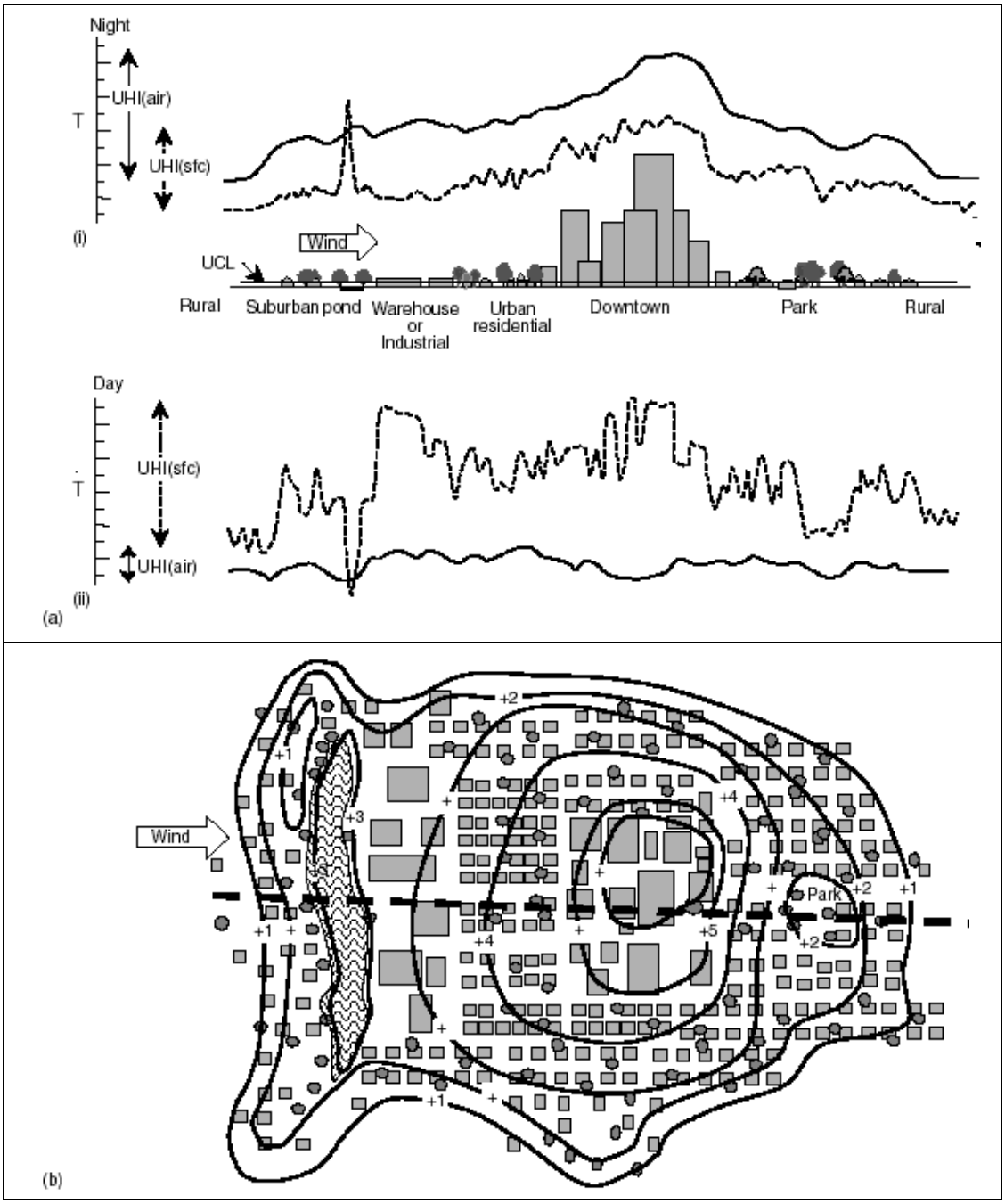

Figure 2.7 - *UHI characteristics. (a) Cross-sections of air temperatures measured within the UCL (urban canopy layer) and surface temperatures (e.g., as observed by a remote sensor) under ideal heat island conditions during (i) nighttime and (ii) daytime. T represents temperature in* ^{0}*C. (b) Plan view of spatial patterns of air temperature, which make up the nighttime UHI. (from Voogt, 2002)*

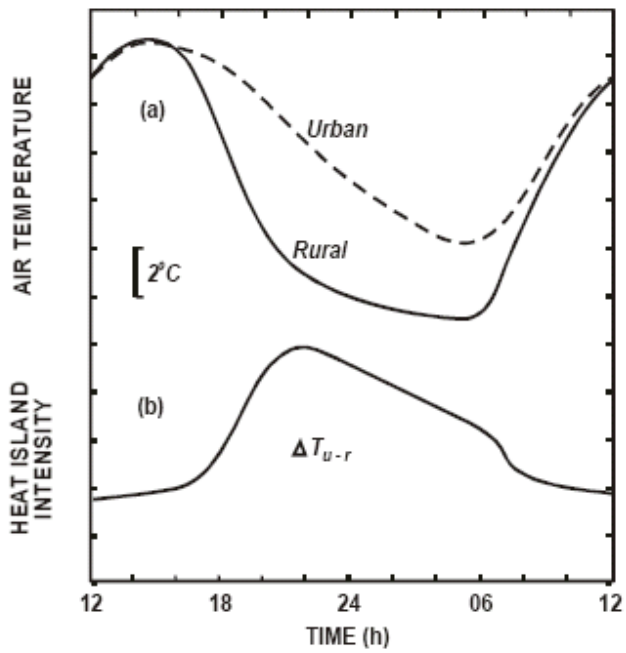

Figure 2.8 *- Typical diurnal variation of urban and rural air temperature under clear skies and weak air flow. The UHI is produced by the difference between cooling rates. [Redrawn from Oke, 1987; from http://www.urban-climate.org/UHI_Canopy.pdf, download on 2008; International Association for Urban Climate (IAUC) Teaching Resources]*

The UHI most often refers to the increase of air temperature, in the near-surface layer of the atmosphere within cities relative to their surrounding countryside. Observations of most UHIs are derived from air temperature measurements made within the canopy layer. More recently, remote sensors operating in the thermal infrared wavelength region and mounted on aircraft or satellites have been used to observe the surface UHI, with high spatial resolution (Voogt, 2002). The surface temperature is very sensitive to changes in surface conditions, and therefore shows much greater spatial variability and temporal variation between day and night, than does air temperature (**Figure 2.7a**). Thus, although surface and air temperature heat islands are related, they are not the same, and care should be taken to distinguish between them. (Voogt, 2002)

Note that remote sensing measurement systems, such as radiometers, detect radiation emitted and reflected by the surface, rather than temperature directly, so their output is often termed the apparent surface temperature. This temperature may be

substantially different from the "true" surface temperature because of the preferential view of horizontal surfaces by the sensor, reduced transmission of radiation to the sensor by the atmosphere, and the reflectivity of the surface in the waveband of the sensor. (Voogt, 2002)

It is important to recognize that several types of UHIs can be defined depending on their location and height within the urban environment and on the measurement method (**Table 2.1**). They are related, but the processes involved in their genesis are different and so are their temporal dynamics (Roth, 2002).

Oke (1995) considered separately the UHI of the urban canopy layer and the UHI of the rest urban boundary layer above. The mechanisms that cause the thermal modification of both regions of the urban boundary layer above are listed in **Table 2.2** and **Table 2.3**, respectively. The region above the canopy layer is warmed by energy entering through its lower boundary, such as anthropogenic heat emanating from the building roofs, chimneys and industrial stacks, or energy transported upwards form the canopy layer. On the other hand, it is also possible that heat is added to the urban boundary layer from above, because both by day and by night the urban layer is often capped by an inversion and, hence, there is warmer air aloft. The action of urban-generated turbulence may erode the base of the inversion and mix this warmer air downwards in the process of convective entrainment. The detailed structure of urban temperature profiles tends to support this idea of dual heat convergence from below and above.

Table 2.1 *- Simple classification scheme of urban heat island types (after Oke, 1995)*

UHI type	Location
Air temperature UHI:	
- Urban canopy layer heat island	Found in the air layer beneath roof-level.
- Urban boundary layer	Found in the air layer above roof-level; can be advected downwind with the urban plume.
Surface temperature UHI	Different heat islands according to the definition of “surface” used (e.g. bird’s-eye view = 2-D vs. true 3-D surface vs. ground = road).
Sub-surface UHI	Found in the ground beneath the surface.

Table 2.2 *- Commonly hypothesised causes of the canopy layer heat island (after Oke, 1982; from Oke, 1987).*

Altered energy balance terms leading to positive thermal anomaly	Features of urbanisation underlying energy balance changes
- Increased absorption of short-wave radiation	Canyon geometry - increased surface area and multiple reflection
- Increased long-wave radiation from the sky	Air pollution - greater absorption and re-emission
- Decreased long-wave radiation loss	Canyon geometry- reduction of sky view factor
- Anthropogenic heat source	Building and traffic heat losses
- Increased sensible heat storage	Construction materials - increased thermal admittance
- Decreased evapotranspiration	Construction materials - increased "water-proofing"
- Decreased total turbulent heat transport	Canyon geometry - reduction of wind speed

Table 2.3 *- Commonly hypothesised causes of the urban boundary layer heat island (after Oke, 1982; from Oke, 1987).*

Altered energy terms leading to a positive thermal anomaly	Features of urbanisation underlying energy changes
- Anthropogenic heat source.	Chimney and stack releases.
- Increased sensible heat input-entrainment from below.	Canopy heat island - increased heat flux from canopy layer and roofs.
- Increased sensible heat input-entrainment from above.	Heat island, roughness - increased turbulent entrainment.
- Increased absorption of short-wave radiation.	Air pollution - increased aerosol absorption.

The intensity of an urban heat island depends on many factors, such as the size of the city and its energy consumption, geographical location, season, time of the day, and synoptic weather conditions (Arya, 2001).

Some attempts have been made to correlate the maximum nocturnal heat island intensity (based on air temperatures at 10m above ground level) with population (considered as representative of the city size and energy consumption), (**Figure 2.9**). Cities with a population of about 1000 people have been observed to have maximum temperature excesses (compared to the surrounding rural area) of 2 to 3 ^{0}C, while cities of a million or more inhabitants have been known to generate excesses of 8 to 12 ^{0}C (Oke, 1982; Katsoulis and Theoharatus, 1985).

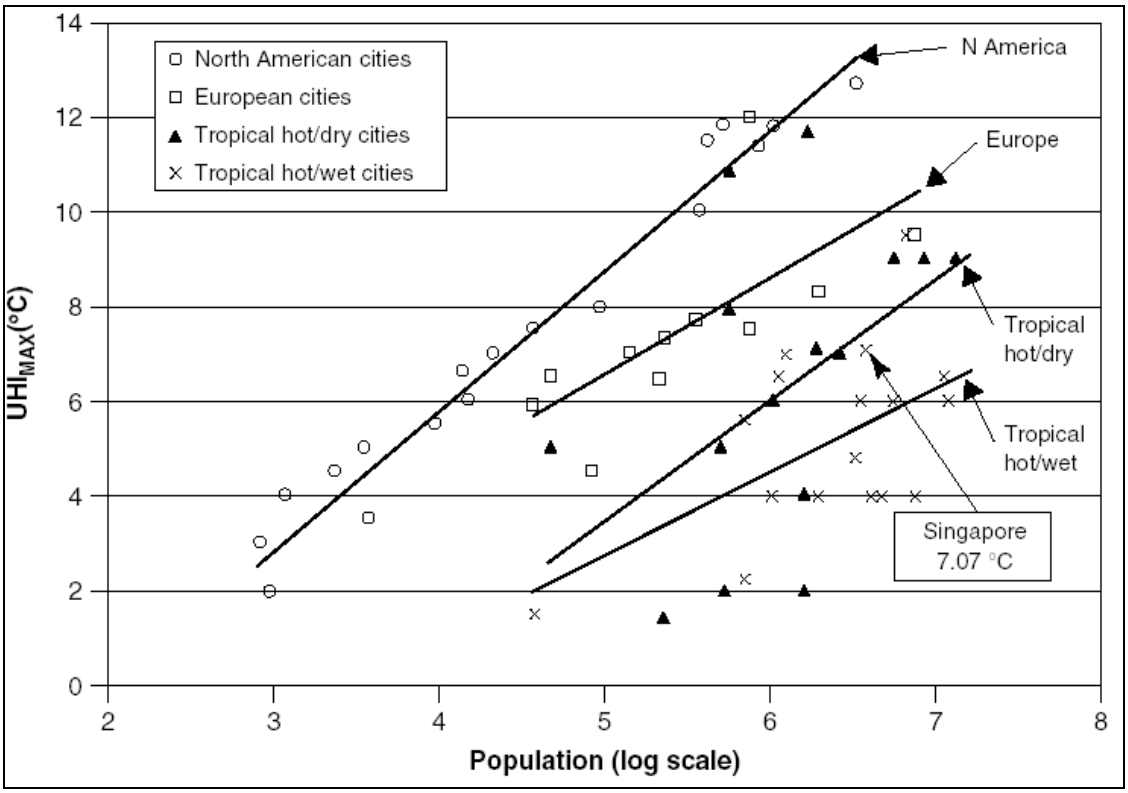

Figure 2.9 *- Urban Heat Island intensity plotted against the logarithm of city population. Different symbols are used for cities in different climate zones. Solid lines are the corresponding linear regression lines. Regression coefficients are different for different city morphologies (North American and European cities) and climates (temperate, tropical hot/dry, and tropical hot/humid) (from Chow and Roth, 2006).*

The use of city population alone is not very satisfactory in explaining the maximum intensity of urban heat island. A much stronger correlation was obtained between the maximum heat island intensity and the geometry of the street canyons in the city centre, as characterised by the average building height to width (H/W) ratio. The following regression relationship has been obtained from the data from 31 cities in North America, Europe, and Australia (Oke, 1987; Arya, 2001):

$$\Delta T_{u\text{-}r} = 7.54 + 3.97 \ln (H/W) \qquad (2.6)$$

Urban geometry and density of development influence physical processes such as the trapping of both incoming solar and outgoing longwave radiations, the amount of anthropogenic heat release, and turbulent transports.

Temporal and spatial characteristics of the urban heat island of Lódz, Poland, have been investigated by Klysik and Fortuniak (1999). The results indicated that in Lódz the factor of the building development compactness, high percentage of artificial surfaces, very narrow streets (H/W >1) in a compact area of a few square kilometres play a more important role than the size of the city in forming a strong UHI.

Unger *et al*. (2001) examine the connection between the built-up urban surface and near-surface air temperature, for the city of Szeged, Hungary. From this study it came to light that the shape of the seasonal mean UHI profile is independent of the seasonal weather conditions and it is determined only by the urban surface factors. More results about the role of land-use parameters (built-up ratio, sky view factor and building height) in the spatial development of UHI in Szeged are presented by Bottyan and Unger (2002).

For example, Kim and Baik (2002) studied the maximum urban heat island intensity in Seoul, Korea, using data from two meteorological observatories (an urban site and a rural site) during the period of 1973–96. Four predictors considered in this study were the maximum UHI intensity for the previous day, wind speed, cloudiness, and relative humidity. The previous-day maximum UHI intensity is positively correlated with the maximum UHI, and the wind speed, cloudiness, and relative humidity are negatively correlated with the maximum UHI intensity. Among the four predictors, the previous-day maximum UHI intensity appeared to be the most important. The relative importance among the predictors varies depending on time of day and season.

The available information concerning humidity in the urban boundary layer suggests that urban/rural differences have a similar sign to those in the canopy, and may be detected up to 1 km above the city, and in the downwind plume (Oke, 1987). Mid-latitudes studies suggests that the urban canopy air is usually drier by day, but slightly more moist by night. This pattern is more evident during summer weather, as illustrated in **Figure 2.10**.

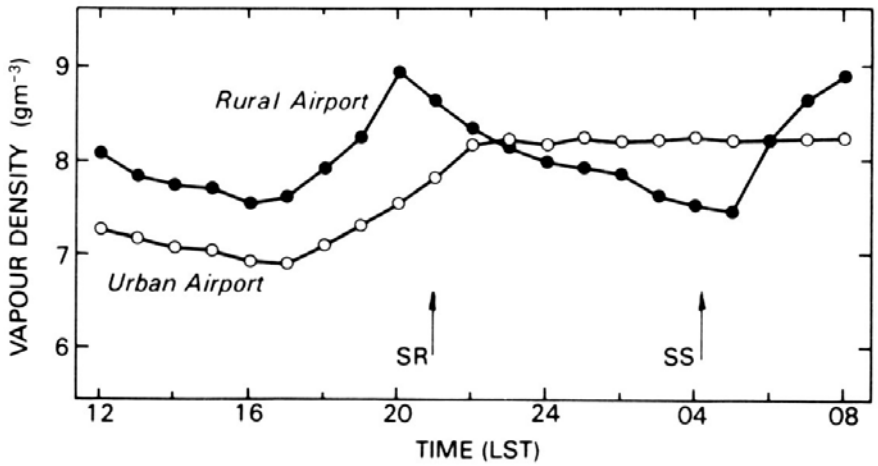

Figure 2.10 *- Daily variation of humidity on 30 fine summer days in and near Edmonton, Alberta (after Hage, 1975; from Oke, 1987).*

The traditional view of cities is of hot dry areas compared to their rural surroundings has developed partly because there is little water available for moisture fluxes on buildings or road surfaces (Arya, 2001). However, there may be large areas of urban environments which contain vegetation and hence have access to the store of moisture in the soil. Observational experiments have shown that the moisture fluxes can be a significant term in the energy balance within suburban areas (Grimmond and Oke, 1995; Best and Clark, 2002). Narita *et al*. (2002) and Honjo *et al.* (2002) presented results of micro-climatological observations of cool-island phenomena in an urban park; the observations were performed in and around the large green space "Shinjyuku Gyoen" in Tokyo during summertime.

The high resolution mesoscale version of the Met Office Non-Hydrostatic Unified Model has been used (Best and Clark, 2002) to assess the impacts on the surface layer heat island and the boundary layer structure over a city. Results of this study, applied to the Reading and London urban areas, show that the ratio of urban fraction to vegetation fraction within a city influences the size of the urban heat and dry islands. Similar results are found for both specific and relative humidity, with increasing urban fractions reducing the humidity and resulting in a dry surface layer island. The boundary layer structure is significantly altered by the presence of an urban fraction.

The urban heat island exerts strong influences on both the mean flow and turbulence structure of the urban boundary layer. The thermal anomaly represented by

the city affects the approaching air flow by altering the local pressure field, modifying the stability, and increasing turbulence. The magnitude of such influences depend upon the strengths of the gradient flow and the urban heat island.

With calm or very weak winds and a strong urban heat island, a thermally induced circulation system may develop over the urban area and its rural surroundings. This circulation is essentially caused by the rising of warm air over the city and sinking of cold air over the surrounding countryside. The near-surface air from the rural surroundings converges toward the thermal low pressure that forms over the city, while at upper levels the air flow diverges away from the city. **Figure 2.11** depicts a schematic of thermally induced circulation and dust dome over an urban area.

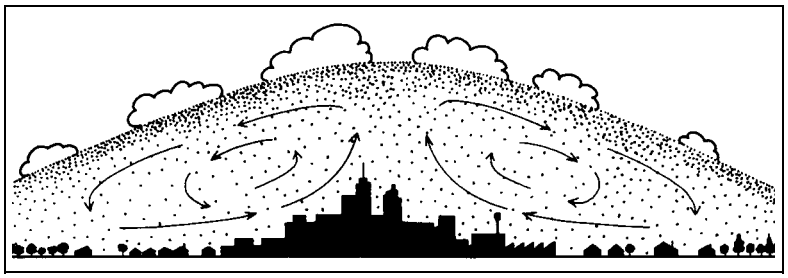

Figure 2.11 *- Schematic of thermally induced circulation and dust dome over an urban area under calm or light winds (after Lowry, 1967; from Arya, 2001).*

In the presence of a mean wind speed, excesses of temperature and pollutants, and deficits of humidity are carried downwind in a "urban plume" (Oke, 1982; Hanna, *et al.*, 1987; Stull, 1988). These plumes are as wide as the city, and can be transported hundreds of kilometres downstream (**Figure 2.12**).

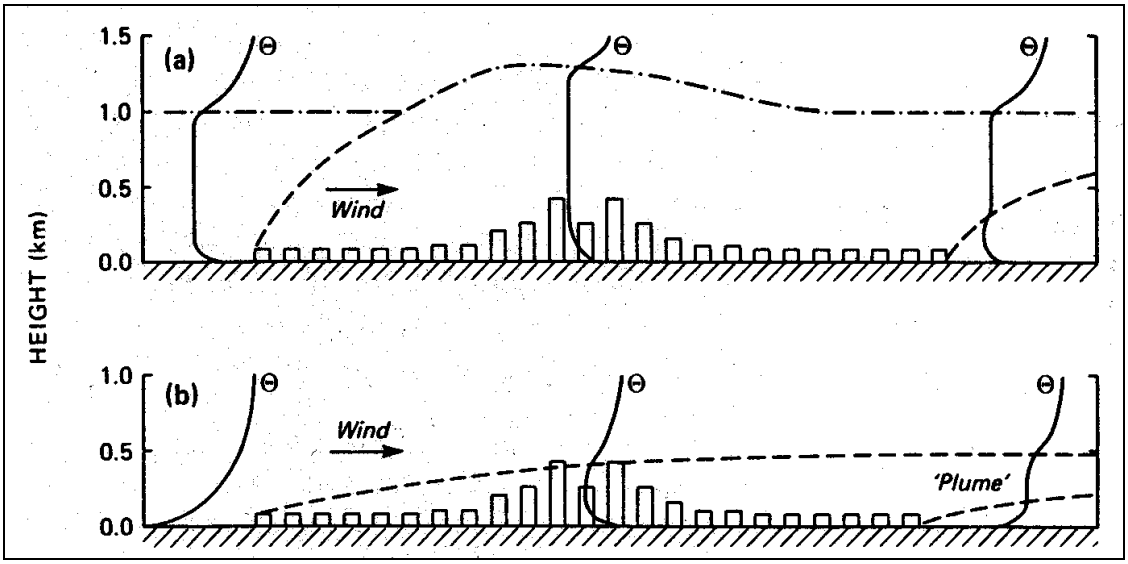

Figure 2.12 *- Sketch of the urban boundary layer showing the urban plume and schematic profiles of potencial temperature (Θ), during fine weather for a windy (a) day, and (b) night (after Oke, 1982; from Oke, 1987).*

Enhanced urban turbulence at night due to warm surface conditions can create counter-rotating vortices on opposite sides of the city (Draxler, 1986) as shown in **Figure 2.13**.

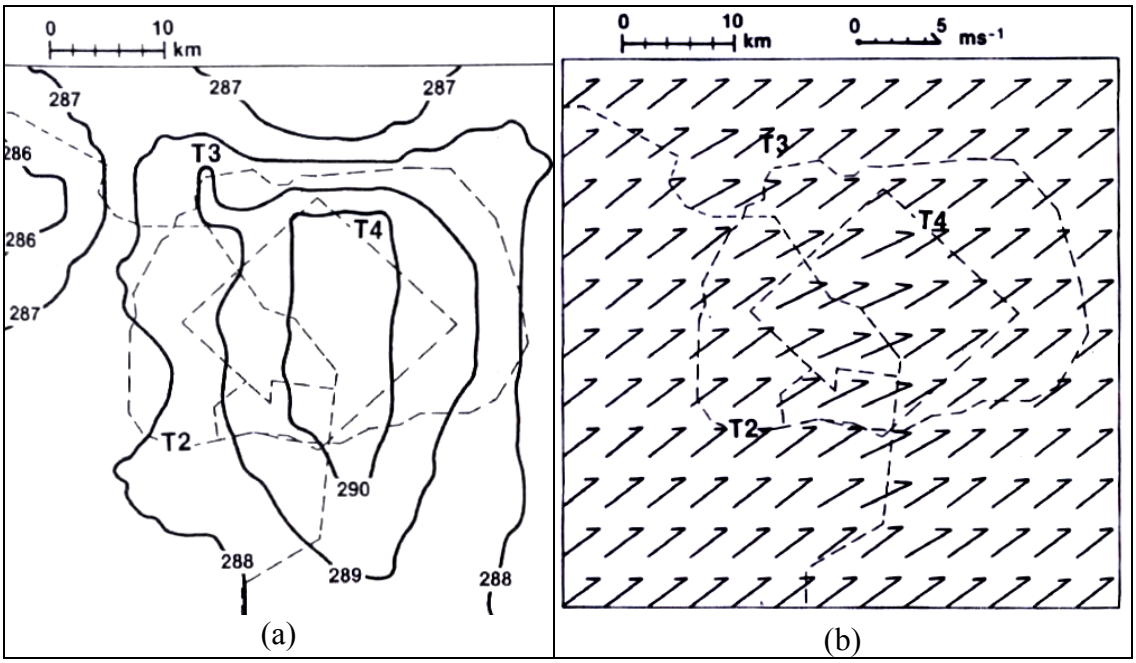

Figure 2.13 *- (a) Surface temperature (K) boundary condition (after Draxler, 1986). (b) Model calculated wind vectors at a height of 50m (after Draxler, 1986).*

Balling and Cerveny (1987) noted an increase in wind speed over the city at night, which they suggested was due to local urban horizontal temperature gradients and enhanced vertical mixing with the faster flow aloft.

In contrast to rural areas the urban atmosphere does not experience a strong diurnal variation in stability. Both by day and by night the urban atmosphere is well mixed, which tends to destroy strong temperature gradients. Therefore neither strong instability or stability are observed. In rural areas a typical nocturnal strong stability near the ground causes a decoupling from the upper air flow and high winds are found aloft. In urban areas, however, the existence of a nocturnal mixing layer facilitates vertical exchanges of horizontal momentum and thus higher surface wind speeds are found (Oke, 1987).

Thermal modification of the urban boundary layer occurs as cooler rural air traverses across the warmer city. During the day the influence of a large city may extent up to 0.6-1.5 km, virtually extending throughout the entire planetary boundary layer (**Figure 2.12a**). This is possible because the normal daytime convection is augmented by both mechanical and thermal convection from the rougher, warmer city. At night the urban heat island may contract to a depth of only 0.1 to 0.3 km (Oke, 1987) because the bulk of the planetary boundary layer is stable and this suppresses vertical transfer. Nevertheless the combination of urban warmth at the surface and increased forced convection is capable of eroding the stability of rural air as it advects over the city (**Figure 2.12b**).

2.2.3 The impact of the surface roughness

In the absence of any topography, the roughness elements of a city are mainly its buildings. These relatively tall, sharp-edged and inflexible objects make cities the roughest of all aerodynamic atmosphere boundaries. The increased drag and turbulence due to the increased surface roughness results in a deeper zone of frictional influence within which wind speeds are reduced in comparison with those at the same height in the country (**Figure 2.14**). Under strong wind conditions, and therefore weak urban heat island, the mechanical effects of increased surface roughness usually dominate over the thermal effects.

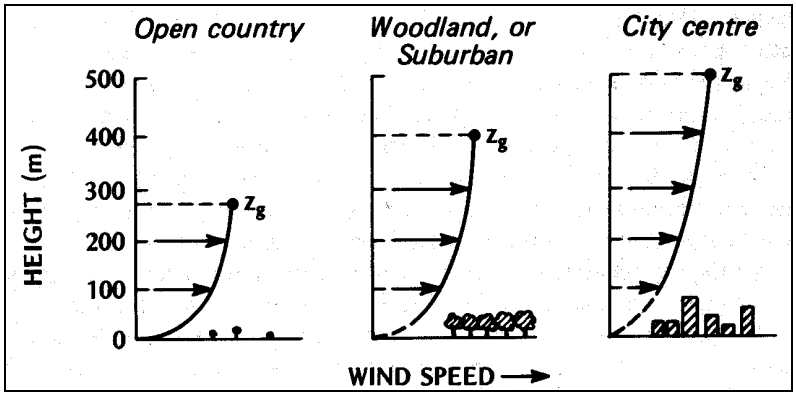

Figure 2.14 *- Effect of terrain roughness on the wind speed profile near the ground; the height zg is the top of the boundary layer above which the mean horizontal wind speed ū is approximately constant with the height (i.e. surface drag is negligible). (After Davenport, 1965; from Oke, 1987.)*

The local slowing of the air flow causes it to converge over the city (**Figure 2.15**), and it is accompanied by uplift. This vertical motion in addition to that induced by heat island effect may be sufficient to cause the urban boundary layer to "dome" up over the city by about 250 m in the daytime (see **Figure 2.11**). Downwind of the city the return to less rough rural surfaces results in subsidence but an elevated "plume" of raising air may persist for tens of kilometres.

Modifications of the wind direction across and downwind of significantly large cities can be observed, because of the deflecting effect of the Coriolis force associated to the changes of wind speed (see Hunt *et al*., 2004). In the Northern Hemisphere this would produce anti-clockwise turning for southward moving air and clockwise turning for northward moving air (**Figure 2.15**).

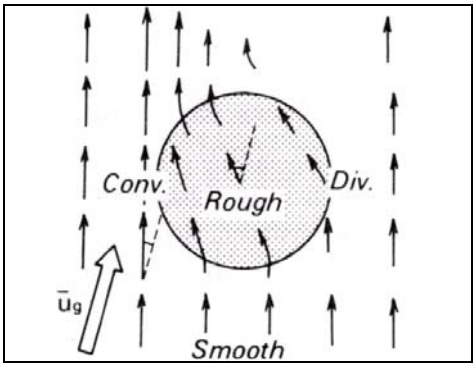

Figure 2.15 *- Effects of roughness change on the wind. Dashed lines are parallel extensions of the gradient wind direction. Arrow lengths approximately proportional to near-surface wind speed. The broad arrow represents the geostrophic wind. (After Oke, 1987).*

At the urban canyon scale, knowledge of the wind around buildings is of importance to the dispersion of atmospheric pollutants and to the safety and comfort of the occupants and nearby pedestrians. It is also useful in order to protect against wind damage and to economise on wind-related maintenance and running costs.

In an urban area, the flow pattern around the buildings depends upon the geometry of the building array, especially the building height to width ratio- H/W (where H is the mean building height and W is the along-wind spacing). **Figure 2.16** shows some examples of flow regimes associated with different urban geometries; **Figure 2.17** illustrates the influence of air flow around buildings on pollution dispersion.

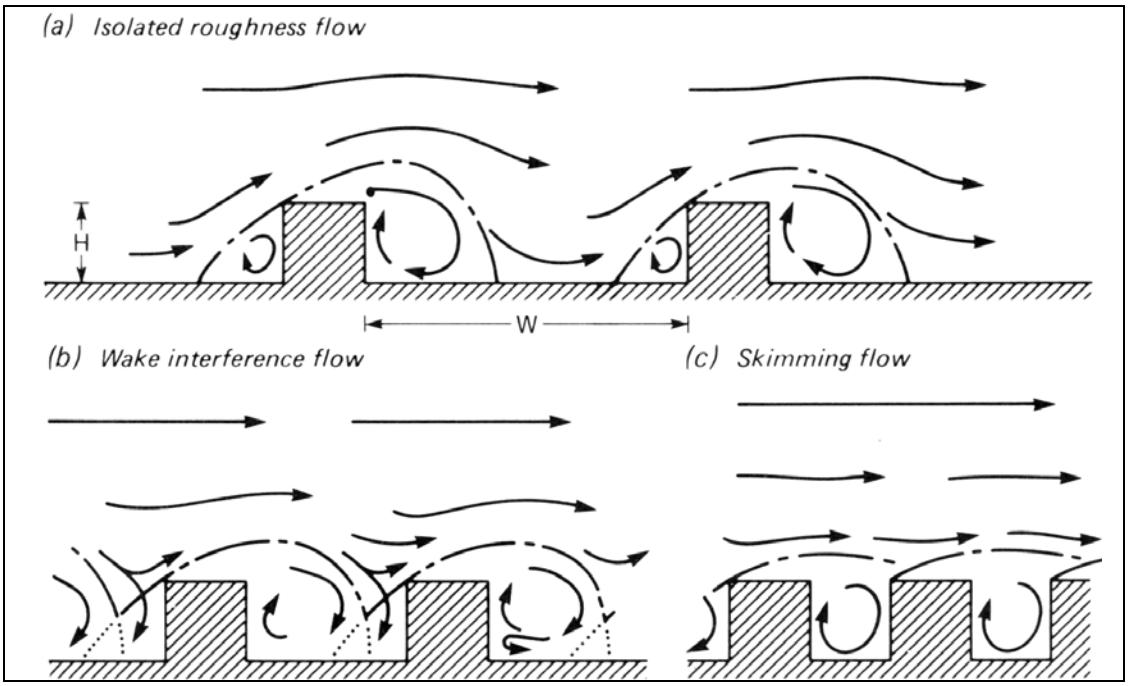

Figure 2.16 *- Flow regimes associated with different urban geometries (after Oke, 1987).*

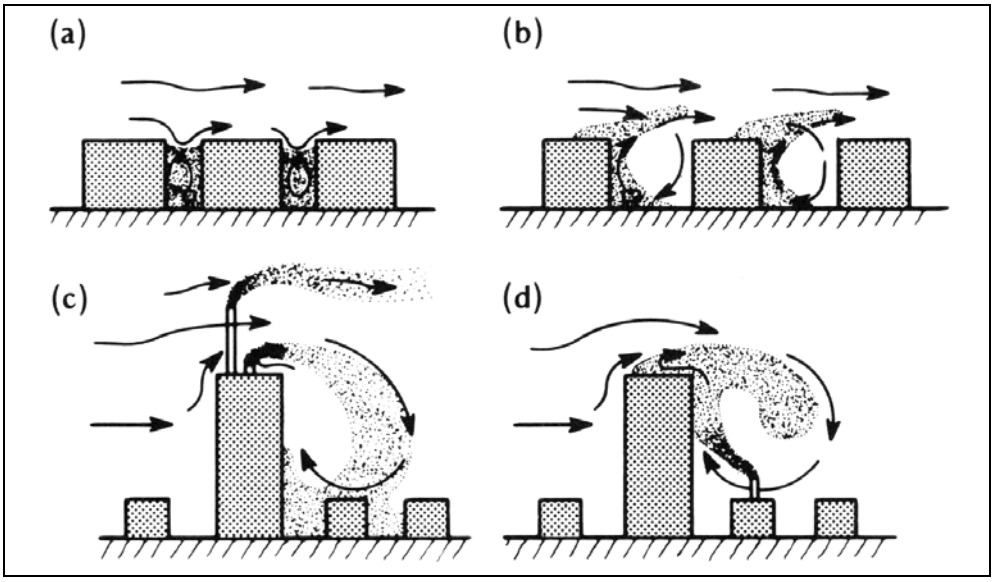

Figure 2.17 *- The influence of building air flow on pollution dispersion (after Oke, 1987).*

2.2.4 Dispersion of urban pollution

This section was included here for completeness, but this subject is beyond the scope of the research reported in this thesis, although aerosols are thought to impact urban precipitation which is discussed in Chapter 3. The issue of *Air Pollution, Meteorology and Dispersion* is explored by Arya (1999), and Seinfeld and Pandis (1998), for example. For a further review see Oke (1987) on which the following is based.

The atmospheric flow (mean wind and turbulence) controls the dispersion of pollutants on many scales. The horizontal dispersion in the atmospheric boundary layer depends largely on the wind field. The wind direction governs the general trajectory of the pollutants, and the wind speed determines both the distance of downwind transport of pollutants and the dilution of pollutants due to the elongation of the pollutant plume. On the other hand, the turbulence controls the extent of the pollutants dispersion in the cross wind direction. The wind speed and the surface roughness determine also the intensity of mechanical turbulence.

The vertical transport of pollutants in the atmospheric boundary layer is largely controlled by the predominant stability conditions of the atmosphere, and therefore the vertical profile of the atmospheric temperature. Free convection is an important

process of diffusing pollutants, and the upper limit of the vertical extent of the pollutants dispersion is the deepth of the mixed layer ABL. Strong atmospheric instability and a deep mixed layer ABL are good conditions for pollutant dispersion, and are typical of sunny day time conditions, specially in summer. On the other hand, the worst conditions for dispersion of pollutants occur when there is a temperature inversion and the atmospheric boundary layer is stable. This situation tends to suppress atmospheric turbulence, the upward motion is reduced, and pollutants released into the atmosphere at low levels tend to remain there. *Smog* refers to locally high concentrations of pollutants in stagnant, stable air, and forms when stable or sinking air masses inhibit the dispersion of pollutant emissions.

Note that, by definition, an atmospheric inversion occurs when warm air overlies cooler air. The atmospheric temperature inversion can be caused by air cooling from below (e. g., radiative cooling), air warming from above (e.g., in a anticyclone, in the lee of mountains, in convection cells between clouds), or advection of warmer or cooler air (e.g., frontal inversion, which occurs in a cold front, caused by cold air wedging warmer air, or in a warm front, caused by warm air over-riding colder air) (McIlveen, 1998).

As it is illustrated in **Figure 2.18** from Oke (1987), it is common to classify the pollution plumes into five basic types according to their dispersion patterns, which depend on the atmospheric stability conditions. **Figure 2.19** shows how some pollution plumes generated in the vicinity of a city may behave at night with clear skies and light winds, namely it illustrates the importance of the location of the pollution source for the occurence of the undesirable fumigation effect.

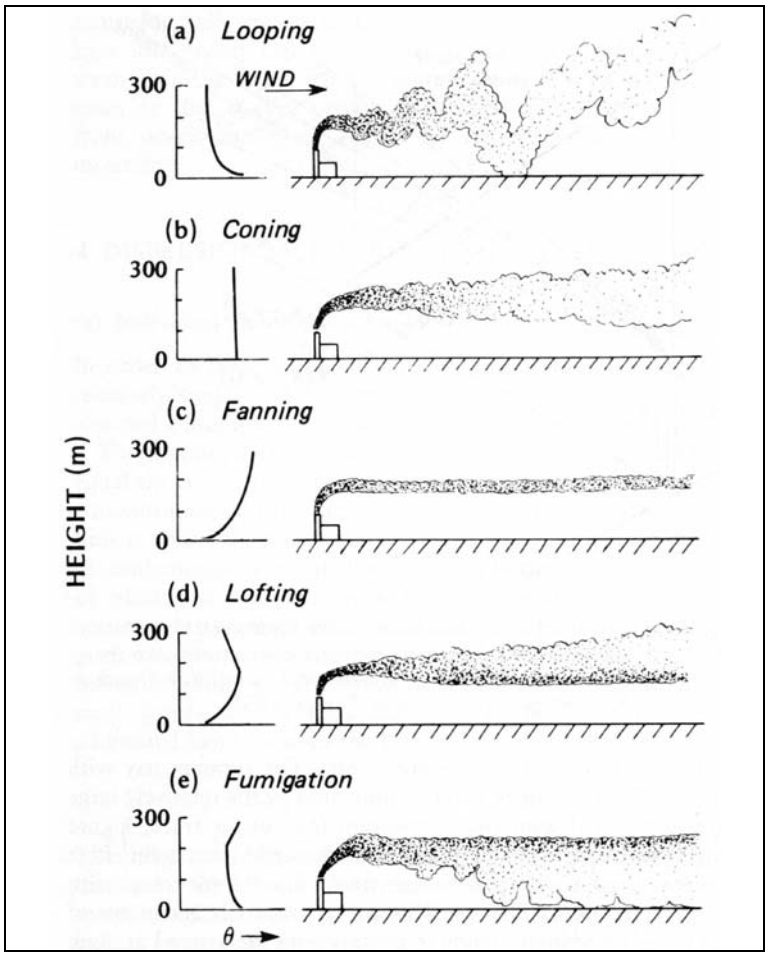

Figure 2.18 *- Typical plume patterns, under different atmospheric stability conditions given by the potential temperature (θ) profile (graph on the left-hand side of each picture) (from Oke, 1987).*

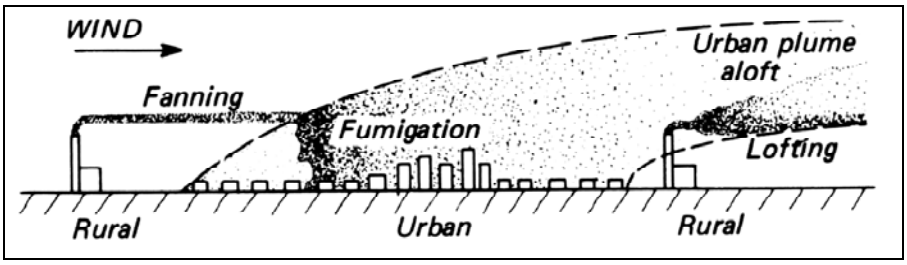

Figure 2.19 *- Possible plume behaviour in the vicinity of a city at night with clear skies and light winds (from Oke, 1987).*

Chapter 3. Previous studies of the impact of urban areas on precipitation

3.1 Introduction

There is renewed debate on how urban areas might affect precipitation (Shepherd and Jin, 2004; Shepherd, 2005). Possible mechanisms for urban areas to impact on precipitation or convection include one or a combination of the following: 1) enhanced convergence due to increased surface roughness in the urban areas (e.g., Changnon *et al.,* 1981; Bornstein and Lin, 2000; Thielen e*t al.,* 2000), 2) destabilisation due to UHI-thermal perturbation of the boundary layer and resulting downstream translation of the UHI circulation or UHI-generated convective clouds (e.g., Shepherd *et al.,* 2002; Shepherd and Burian, 2003), 3) enhanced aerosols in the urban environment for Cloud Condensation Nuclei (CCN) sources (e.g., Diem and Brown, 2003; Molders and Olson, 2004), or 4) bifurcating or diverting of precipitating systems by the urban canopy or related processes (e.g., Bornstein and Lin, 2000; Loose and Bornstein, 1977). It has also been hypothesized that urban areas serve as moisture sources needed for convective development (e.g., Dixon and Mote, 2003).

To date, there is no conclusive answer to what mechanism dominates urban-induced precipitation processes or what is the relative role of each mechanism. Furthermore, how the urban environment modifies these processes is also poorly understood (Shepherd, 2005).

Recent reviews of the current investigations on urban-induced rainfall are presented by Thielen *et al.* (2000), Shepherd (2005), Collier (2006), and Pielke *et al*. (2007). In this chapter some previous studies of the impact of urban areas on the precipitation are examined, particularly those exploring the modification of the precipitation fields by the Urban Heat Island (UHI) and the urban surface roughness. Also the suppression of rain by urban aerosols is discussed, which remains a matter of some controversy.

3.2 Observational studies

A tendency for thunderstorm formation over large cities rather than the rural environment has been noted as early as the 1920s. Most of the studies related to urban-induced precipitation emerged during a period of rapid global urban growth and observable changes in rainfall trends, and early investigations on the 1960s-1970s found evidence of warm seasonal rainfall increases over and downwind of major cities (Shepherd, 2005). The Metropolitan Meteorological Experiment (METROMEX) was an extensive study that took place in the 1970s in the United States to further investigate modification of mesoscale and convective rainfall by major cities (Changnon *et al.*, 1977; Huff, 1986). This experiment established the causes of urban-induced cloud changes, the reality and magnitude of warm-season rainfall increases, and the types of increases in storm activity such as more thunderstorms, lightning, hail and damaging surface winds (Changnon *et al*., 1981). In general, results from METROMEX shown that urban effects lead to increased precipitation during the summer months. An enhancement of rainfall frequencies over and downwind of urban areas was observed. Rainfall enhancement was observed for the urban area itself and at a distance of 40 km downwind of the city centre. METROMEX results also suggested that areal extent and magnitude of urban and downwind precipitation anomalies were related to size of the urban area (Changnon, 1992). In METROMEX studies, the increased precipitattion was attributed mostly to the modifications of the airflow due to the heat island and the increased roughness. The possibility that the presence of increased giant CCN concentrations originating from the urban area could also play a role in the precipitation processes was not excluded.

Frequentelly refered to papers on the METROMEX related studies are Changnon *et al.*, 1977; Huff, 1986; Huff and Vogel, 1978; Changnon, 1979; Changnon *et al.,* 1981; Braham *et al.*, 1981; Changnon *et al.,* 1991; Changnon, 1992.

More recent studies have continued to validate and to extend the findings from pre- and post-METROMEX investigations.

Loose and Bornstein (1977) investigated the effects of New York City on regional flow patterns using obervational data and numerical simulations. The study showed that urban areas may significantly affect synoptic scale fronts. Most fronts

slow down when moving over the urban area. The retardation of the fronts was interpreted as being a result of the increased surface frictional drag applied to the front by the increased surface roughness of the city as compared to that of its surrounding environs. In cases of well developed heat island an increase of the frontal speed was observed in the region over the downwind part of the urban area. The increase in frontal speed was attributed to the horizontal presure gradients associated with the UHI.

Bornstein and LeRoy (1990) found that New York City affects both summer daytime thunderstorm formation and movement. During conditions with nearly calm regional flows, the NYC UHI initiated convective activity, thus producing a radar echo frequency maximum over the City. Moving thunderstorms, however, bifurcated and moved around the city due to a building-barrier-induced divergence effect. During such conditions, radar echo maxima were thus produced on both lateral edges of the City and downwind of the city, while a minimum was located over the city itself.

Jauregui and Romales (1996) observed that the daytime heat island seemed to be correlated with intensification of rain showers during the wet season (May-October) in Mexico City. They also presented an analysis of historical records showing that frequency of intense rain showers has increased in recent decades in correlation with the growth of the city. Selover (1997) found similar results for moving summer convective storms over Phoenix, Arizona.

Tumanov *et al.* (1999) studied the influences of Bucharest, Romania, on weather and climate. Estimates of the urban heat island are presented based upon ground level air temperature measurement in a few representative points in Bucharest (May-December 1994). The intensity of the effect is analysed versus synoptic mesoscale patterns. Other effects of the urban area on some atmospheric parameters, particularly on cloud systems and precipitation, using radar images, are presented too. Several types of behaviour could be identified for the cloud systems approaching the city depending on the characteristics of the air masses. One of them consists of a front dislocating while passing the city, and being reshaped after crossing it. Another behaviour is the enhancement of the precipitation amounts over the city. Both of these phenomena could be seen on radar images.

Bornstein and Lin (2000) examined network data for Atlanta for the summer of 1996. The cases studies carried out showed that the UHI may induce a convergence

zone that initiated storms downwind of the city. It was concluded that storms approaching Atlanta may diverge around the peripheries of the city.

In 2000 the U.S. Weather Research Program panel concluded that more observational and modelling research is needed in the area of urban-induced rainfall anomalies (Dabberdt *et al.,* 2000).

3.3 Numerical studies

In terms of modelling research, several studies have addressed the evolution and impact of the urbanisation on the environment, but very few have focused on the impact of precipitation processes.

Recently, investigators have begun to explicitly address the impact of urban surfaces on rainfall processes (Thielen and Gadian, 1997; Thielen *et al.*, 2000; Baik *et al.*, 2001 and Baik *et al.*, 2002; Rozoff *et al.*, 2002; Craig and Bornstein, 2002; Shepherd, 2002; Shepherd *et al.*, 2002).

Thielen and Gadian (1997) presented a numerical study of the influence of topography and urban heat island effects on the outbreak of convective storms under unstable meteorological conditions. Analysis of observational data of convective storms in Northern England suggested that the particular combination of effects such as sea breezes, elevated terrain and the presence of large cities has an influence on the initiation and development of convective storms.

To study the importance of these effects for the development of convection, a cloud physics model was initialised with the topography and surface characteristics of Northern England. The model enabled inclusion of three principal influences: sea breezes, topography and urban heat islands. The results suggested that the presence of the Pennines, a north–south orientated ridge, could influence the initiation of convection due to its long sun-facing slopes, and to a lesser degree forced lifting along the slopes.

The inclusion of urban heat island effects produces enhanced and prolonged convection, particularly downwind of the major urbanised areas (Manchester and Bradford/Leeds). According to the authors, in the case of Manchester this favoured the outbreak of cells, in the vicinity of the Forest of Trawden (at a distance of about 50 km

norwest of Manchester). Since the predominating wind directions in the area are south, westerly, enhancement of convection and rainfall downwind of the area of Manchester could thus result in increased frequency of storms in the Central Pennines (Forest of Trawden, Forest of Pendle and Forest of Rossendale). Results of this study thus seem to support the observation of an increased likelihood of storms particularly in the Central Pennines. However, the authors mentioned that the parameterisation of the soil characteristics was very simple and based on one single parameter only. In order to confirm the results, it is suggested that new simulations, on a higher resolution and including a more realistic coupling of soil and atmosphere, should be undertaken.

Thielen *et al.* (2000) used a mesoscale meteorological model to address the influence of urban surfaces on the development of convective precipitation. The results showed that sensible heat fluxes and enhanced roughness can have considerable influence on convective rainfall. A sensitivity study was performed to assess the impact of variations of the individual parameters on the development of precipitation. Results showed that variations in the surface parameters, especially sensible heat flux, affect the development of precipitation over Paris, France. Thielen *et al.* (2000) also reported that rainfall was focused over and 60–80 km downwind of the urban area in the ‘‘urban’’ model simulation.

Sensitivity experiments indicated that on a relatively short time scale (of less than 4 h), it is mainly the surface sensible heat fluxes and subsequent buoyancy variations that influence the rainfall development. The influences of local changes in the surface latent heat fluxes are comparatively slow acting, and do not show significant effects within the 4 h of simulation. On the other hand, changes in the roughness length modify the precipitation patterns significantly downwind of the urban surface. The effects develop only after 2–3 h of simulation, and seem to be a function of the height of the roughness lengths. In combination with a variable sensible heat flux, the buoyancy forces dominate the precipitation development. Similar conclusions could be drawn for those simulations that include topography. Because the topographical gradients are small, the artificially induced heat islands through urbanisation remain the dominant surface forcing. Overall, the numerical results seem to confirm observations, such as those from the METROMEX experiment, that the frequency distribution of rain-bearing cells is enhanced over urban areas, and that precipitation can be enhanced by the presence of urban areas (Thielen *et al*. 2000).

Baik *et al.* (2001) in a two-dimensional numerical study investigated dry and moist convection forced by an urban heat island, using the Advanced Regional Prediction System (ARPS) mesoscale model. Various heating amplitudes, representing the intensity of the urban heat island, were used with a uniform basic-state wind speeds, and basic-state relative humidity. Results of moist simulations demonstrate that the downwind updraft cell induced by the urban heat island can initiate moist convection and result in surface precipitation in the downstream region when the basic-state thermodynamic conditions are favourable. Model results showed that as the urban heat island intensity increases, the time required for the first cloud water (or rainwater) formation decreases and its horizontal location is closer to the heating centre. It is also shown that for the same basic-state wind speed and heat island intensity a stronger dynamic forcing, i. e., a stronger downwind updraft, is needed to trigger moist convection in less favourable basic-state thermodynamic conditions. A study of Han and Baik (2006) extends the previous one (Baik *et al.* 2001) and investigates urban heat island induced circulation and convection in three dimensions theoretically and numerically.

Craig and Bornstein (2002) used Project Atlanta data and MM5 model (fifth-generation Pennsylvania State University– National Center for Atmospheric Research Mesoscale Model) to investigate an UHI initiated convection case over Atlanta. Model simulations for a case study indicated that the UHI induced convergence and convection. It was also shown that when Atlanta roughness lengths, thermal properties, and building barrier were removed from the simulations, an area of precipitation was eliminated, thus suggesting its urban origin.

Shepherd (2002) employed a convective- mesoscale model to (a) determine if an UHI thermal perturbation can induce a dynamic response to affect rainfall processes and (b) quantify the impact of the following three factors on the evolution of rainfall: urban surface roughness, magnitude of the UHI temperature anomaly, and physical size of the UHI temperature anomaly. The Advanced Regional Prediction System (ARPS) model was used. An urban area of 30 km was defined in the initial land surface parameters of the model. In the control experiment, the initial model profiles are based on the classical, idealized UHI distribution of temperature, roughness, and vegetation in an urban area (Shepherd, 2002). Sensitivity tests suggested that roughness exerts a control on the amount and timing of urban-induced precipitation

that falls directly over the city. Namely, when the variation in temperature was removed from the experiment, the precipitation is found over the city. In this case, where the variation in roughness is the primary forcing, results indicate enhanced low-level convergence preceding convective development over the city. The results are consistent with other previous studies, and suggest that roughness length promotes increased forcing through focusing lowlevel convergence, mainly over the city. Results also show a tendency for experiments with increased roughness length to initiate convection 10-25 minutes earlier than the control experiment. In experiments, where only the UHI thermal perturbation was generating the forcing that ultimately led to precipitation, it was apparent that the primary precipitation region is 20-30 km downwind of the urban center. Other experiments, showed that the magnitude of the surface UHI didn't seem to affect significantly the distribution and location of precipitation, but a downwind region of precipitation was significantly greater for a greater magnitude UHI than the smaller magnitude UHI. This result was attributed to larger boundary layer destabilization resulting in more vigorous meso-circulations. Results of sensitivity tests suggested also that smaller cities tend to produce a maximum in rainfall downwind of the city while larger cities produce a maximum in rainfall over and slightly downwind of the center of the city.

Rozoff *et al.* (2003) used the Regional Atmospheric Modelling System (RAMS) (Cotton *et al.* 2003), with Land Ecosystem–Atmosphere Feedback-2 (LEAF-2) (Walko *et al.* 2000) and the Town Energy Budget (TEB) (Masson, 2000) surface parameterisations, to examined a 1999 storm case in St. Louis and determine the role of the urban surface convergence mechanisms on initiating deep, moist convection. A major conclusion derived from these experiments is that the UHI has a substantial effect on the modelled storms. The simulated UHI caused a mesoscale circulation with surface winds directed toward the city. Resulting convergence produced enhanced boundary layer convection, triggering storms in the moist and unstable environment. It has been found that surface convergence on the leeward side of the urban heat island plays a key role in initiating convection downwind of the city (**Figure 3.1**).

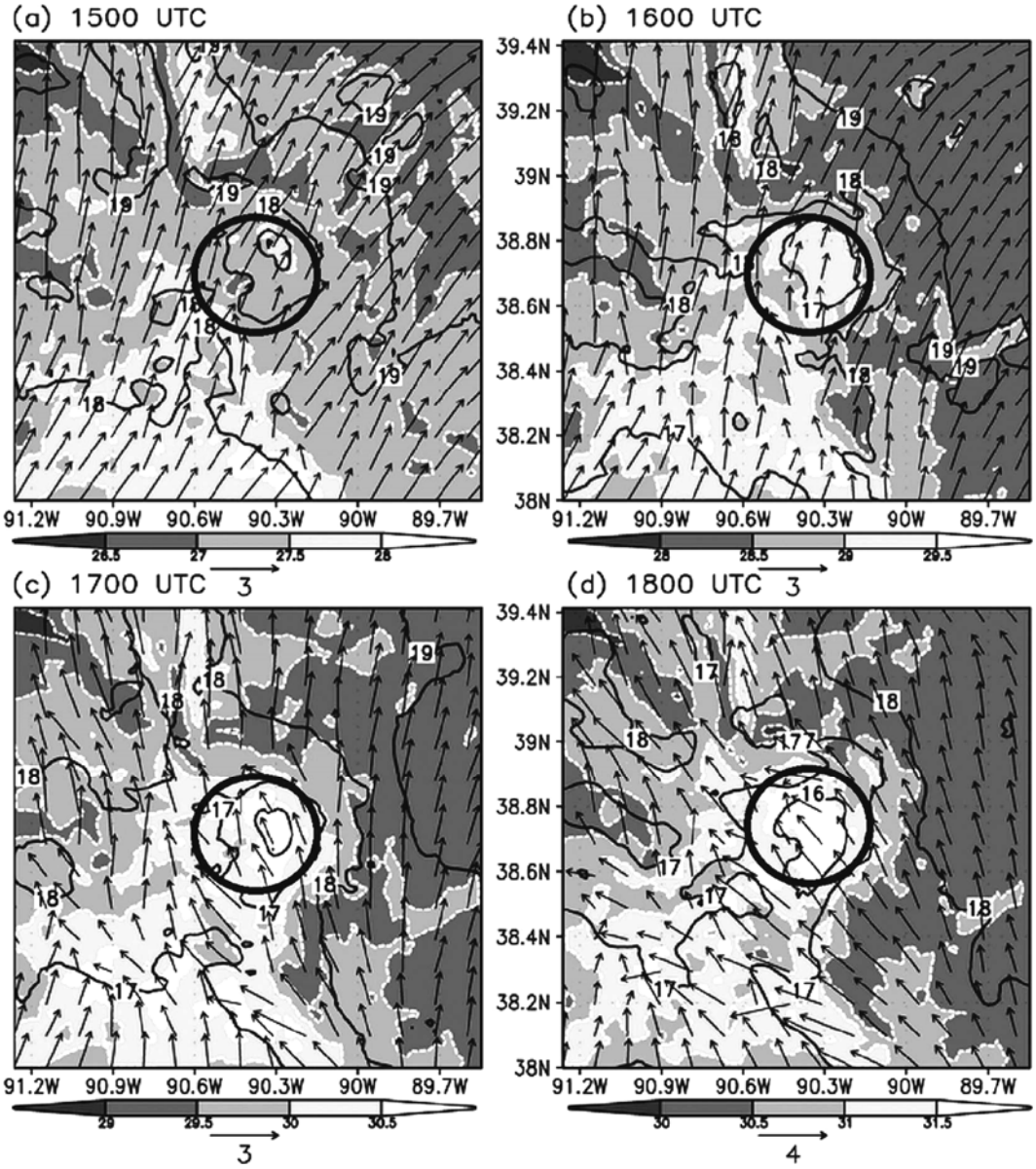

Figure 3.1 *- RAMS results for the evolution of urban heat island, moisture, and winds, for the first model level (48 m), on 8 Jun 1999. Temperature (ºC) is shaded, water vapor mixing ratio (g kg^{-1}) is contoured at intervals of 1 g kg^{-1}, and wind (m s^{-1}) vectors are plotted. There is evidence of moist convergence in the urban environment. The circle represents the approximate location of St. Louis. (After Rozoff et al., 2003; from Shepherd, 2005).*

Molders and Olson (2004) found evidence of enhanced precipitation over and downwind of high latitude cities like Fairbanks, Alaska. Their mesoscale model simulations (with MM5) indicated that urban land use, aerosols, and moisture sources had statistically significant impacts on downwind precipitation.

Shepherd (2005) shows results for a case day study in Houston area, using a modified version of the fifth-generation Pennsylvania State University– National Center for Atmospheric Research Mesoscale Model (MM5). On the case day (25–26 July 2001) weak large scale forcing was in place and mesoscale forcing (e.g., sea breeze, urban circulation) was dominant. The urban surface was included in the model by modifying albedo, surface emissivity, roughness length, and vegetation parameters in the land classification. Results for "no urban" and "urban" model simulations were compared. Simulations results for the 300-m wind field, surface fluxes, cloud water, and rainwater (Shepherd, 2005; Figure 9) show that the "urban" run produced convection that the "no urban" run does not feature. It was also evident that urban Houston creates a convergent zone that interacts with the sea-breeze circulation. Radar observations for the day confirmed that heavier rainfall was observed over the city of Houston and just to the north of the city. A cross section of equivalent potential temperature and vertical velocity model results (Shepherd, 2005; Figure 10) also indicated how the boundary layer responds in the "urban" and "no urban" cases; the "urban" boundary layer is deeper and includes vertical velocity features.

There is increasing evidence that large coastal cities, like Tokyo, Japan, and Houston can influence weather through complex urban land use– weather – climate feedbacks (Shepherd, 2005). Kusaka *et al.* (2000) and Ohashi and Kida (2002) present reviews of the urban–coastal impacts of Tokyo on mesoscale-convective circulations.

3.4 Satellite studies

The study of Shepherd *et al.* (2002) established the possibility of using satellite-based rainfall estimates for examining rainfall modification by urban areas on global scales and over long time periods. Their results illustrated that the spaceborne precipitation radar system could identify anomalously high rainfall rates downwind of major cities. Data of 15-month (spanning three years- 1998-2000) from the Tropical Rainfall Measuring Mission (TRMM) satellite's precipitation radar were employed to identify warm-season rainfall patterns around five American cities. It was founded that the average percentage increase in mean rainfall rate in a hypothesised “downwind maximum impact area” over an “upwind control area” was 28.4% with a range of 14.6

to 51%. The typical distance from the urban centre of the downwind rainfall rate anomaly was 30-60 km, consistent with earlier studies. This fact provided confidence that urban rainfall effects are detectable by TRMM satellite estimates (Shepherd *et al.*, 2002).

To validate the satellite observations, Shepherd and colleagues carried out the 2004 Studies of Precipitation Anomalies from Widespread Urban Land Use (SPRAWL) discussed in (Shepherd *et al.,* 2004). The goal of SPRAWL was to obtain a database of urban-induced thunderstorms and associated mesoscale and synoptic conditions. Such cases are being analysed and simulated using coupled atmosphere–land surface models (Shepherd, 2005).

Shepherd and Burian (2003) used data from the first satellite-based precipitation radar aboard the Tropical Rainfall Measuring Mission (TRMM) and ground-based rain gauges to examine rainfall anomalies in Houston area. The authors hypothesized that dynamic processes related to the urban heat island and enhanced mechanical turbulence in cities interacting with the sea-bay breeze produce a preferred region for convective development in the metropolitan Houston area and regions downwind.

3.5 Climatological studies

Takahashi (2003) presented evidence confirming previous literature studies that identified an increase in the frequency of occurrence of heavy rainfall in the Tokyo area in recent decades.

The study by Fujibe (2003) linked increase surface convergence over the urban area to enhanced convection over major Japanese cities like Tokyo.

Inoue and Kimura (2004) used National Oceanic and Atmospheric Administration (NOAA) satellite images to show that the frequency of low-level clouds is enhanced over the Tokyo metropolitan area in the early afternoon. They suggested that low-level clouds form at the top of thermals in the mixed layer enhanced by stronger sensible heat flux in the urban area.

Changnon (2003) analyzed a database of freezing-rain occurrences during the period of 1945– 2000 and found that freezing-rain occurrences in large cities are

decreased by 10%–30% because of the heat island. The cities in his study included Chicago, Illinois; New York City; St. Louis; and Washington, D.C.

Diem and Brown (2003) found that anthropogenic activities in the arid Phoenix area appear to have positively affected summer precipitation totals in downwind areas, particularly the Lower Verde basin. This study offered no conclusive evidence of a possible cause, but they suggested that the responsible enhancement mechanisms may include increased transfer of water vapour to the atmosphere due to irrigation, increased convergence due to urban roughness and irrigation-induced circulations, and increased urban aerosols serving as CCN.

Dixon and Mote (2003) investigated the patterns and causes of Atlanta UHI-initiated precipitation. The study revealed the importance of urban-related moisture sources for convective processes. The key result of this study was that UHI-induced precipitation soundings showed much higher dew-points (as much as 5°C) below 550 hPa than average days. Also, airmass analysis showed that these events were more frequent under the most humid air masses rather than the ones with the greatest UHI intensities.

Burian and Shepherd (2005) analysed data from a dense rain gauge network, i.e., 19 raingauges located within and nearby Houston, to quantify the impact of urbanization of the Houston metropolitan area on the local diurnal rainfall pattern. Diurnal rainfall distribution and enhance afternoon rainfall amounts were observed. Results show statistically significant enhancement of rainfall in the Houston area in the post-urban time period, and demonstrate the changes to the diurnal rainfall pattern in the Houston urban area compared with surrounding areas, which corroborate the results found for St Louis (Huff and Vogel, 1978) and Phoenix (Balling and Brazel, 1987).

3.6 The role of urban aerosols on precipitation

Most of the studies mentioned in the previous sections focused on dynamic forcing mechanisms of precipitation related to the urban land use and did not consider the cloud microphysics mechanisms, namely the role of the aerosols on the initiation of precipitation.

The processes of precipitation formation depend on the presence of aerosols in clouds, specifically Cloud Condensation Nuclei (CCN) and Ice Nuclei (IN) (Pruppacher and Klett, 1997; Toon, 2000). The three major sources of aerosols in the atmosphere are desert dust, smoke from biomass burning, and anthropogenic air pollution, which are recognised as sources of large concentrations of small CCN. They lead to the formation of clouds constituted by high concentration of small droplets, which increases cloud albedo and tends to suppress precipitation (Rosenfeld, 2000). Rosenfeld *et al.* (2001) acknowledged that short lived convective clouds are the more sensitive to the impact of aerosols on precipitation, because the rate of cloud water conversion into precipitation has to compete with the rate of cloud water loss due to mixing and evaporation with the ambient air. Consequently, large-scale synoptically forced cloud systems, which are typically longer lived, are less vulnerable to the impact of smoke and dust on the precipitation.

Space-borne (Coakley *et al.*, 1987) and aircraft (Radke *et al.*, 1989) measurements of ship tracks in marine stratocumulus clouds provided the first evidence that effluents from ship chimneys change cloud microstructure by redistributing their water into a larger number of smaller droplets. Conclusive evidence that smoke from burning vegetation suppresses precipitation was obtained by Rosenfeld (1999) with the observations of the Tropical Rainfall Measuring Mission (TRMM) satellite launched on November 1997.

Instrumentation on board of weather satellites revealed numerous ship track–like features in clouds over land, created by major urban and industrial pollution sources Rosenfeld (2000). Pollution tracks from Turkey, Canada, and Australia were analysed. As remarked by Rosenfeld (2000), the satellite data provided evidence connecting urban and industrial air pollution to the reduction of precipitation, allowing the identification of both the sources and the affected clouds. The simultaneous spaceborne measurements over large areas of cloud microphysics, cloud water, and precipitation made it possible to relate the precipitation to cloud microstructure. Rosenfeld (2000) observed that urban and industrial aerosols may suppress rain and snow by providing large concentrations of small CCN, which lead to large quantities of small cloud droplets. In addition he explained that in these circumstances the clouds must grow to greater depth and colder cloud top temperatures for the initiation of

precipitation. Thus, it means that precipitation would be suppressed when aerosols are introduced into relatively shallow and short-lived clouds.

Borys *et al.* (2000, 2003) provided evidence that pollution can also suppress precipitation in winter orographic clouds. It was shown that pollution increases the concentration of CCN and of cloud drops, leading to the formation of smaller cloud drops. The reduced drop size leads to a less efficient riming process, to smaller ice crystals, smaller fall velocities, and smaller amounts of snowfall.

In contrast to the debate about urban aerosols suppressing rainfall, Diem and Brown (2003) partially attributed precipitation enhancement downwind Phoenix to increased CCN due to pollution, although they recognized that increased humidity from irrigation systems and flow convergence induced by the urban surface were probably the dominant factors.

In a more recent study Givati and Rosenfeld (2004) analysed precipitation records in regions downwind pollution centres and compared them to regions unaffected by these pollution sources. Two different geographical areas of similar topography were chosen for this study, California and Israel. The statistical results in both locations showed that on the upslope of the mountain and the mountain top, both downwind of the pollution regions, precipitation is reduced. This decrease was attributed to increase in droplet concentrations and the decrease in droplet size. On the other hand, farther downwind and on the lee side of the mountain, the amount of precipitation increased. The authors explained this increase by the fact that the smaller cloud particles need a longer time to grow, allowing the winds aloft to carry them over the mountain top. In addition it was observed that over the whole track of the clouds the integrated rainfall amount was reduced.

On the other hand, Andreae *et al*. (2004) presented evidence that polluted or smoky clouds over Amazon might invigorate precipitation processes. They reported that the high concentrations of cloud drops reduce the efficiency for growth by collection. In this case the drops continue to grow by condensation and reach higher altitudes and lower temperatures where ice can form. Since these clouds are deeper they could produce lightning, hail, and heavy rain.

Shepherd and Jin (2004) reported Rosenfeld suggestion that urban aerosols act to delay conversion of cloud water into precipitation. Precipitation processes are delayed to greater heights in the clouds, respectively delaying the downdraft and

allowing the clouds to invigorate further. In dry and unstable conditions, this causes reduced precipitation due to very low precipitation efficiency, and in tropical and moist subtropical conditions, enhanced storm vigor (increased updrafts, rainfall, lightning). The additional cloud water and strong updraft induces enhanced electrical activity as observed in Houston by Orville *et al.* (2001) and in Louisiana by Steiger and Orville (2003).

Molders and Olson (2004) investigated the impact of urban growth and release of aerosols, moisture, and heat on precipitation for Fairbanks, Alaska. Results of this study showed that a significant enhancement in precipitation occurred downwind of Fairbanks when more but smaller aerosols were considered in the numerical simulations. The authors attributed the enhancement of precipitation to shifts in the cloud microphysical processes. However, in their study visible changes in precipitation were also found when urban land surfaces and moisture were altered.

An important conclusion from recent work is that aerosols can have large impacts on the precipitation processes in clouds and can enhance or suppress precipitation depending on cloud type, seasonality, climate regime, or orographic profile of the urban area. Also, although the role of urban aerosols on precipitation remains unclear, there is agreement in both the UHI-dynamics arguments and aerosol–microphysics arguments for precipitation variability in urban environments (Shepherd, 2005, Shepherd and Jin, 2004).

3.7 On the effects of urban areas in numerical mesoscale forecast models

Existing soil models are mostly designed and validated for rural surfaces. However, in mesoscale numerical models, with grid lengths of a few kilometres, urban areas can represent a considerable fraction of the model domain and should not be neglected (Thielen *et al.,* 2000).

Urban areas modify boundary layer processes. As a consequence, larger scale meteorological processes can also be affected by the presence of cities. Although the importance of the lower boundary for mesoscale models has been discussed for some time, detailed representation of the surface heat and moisture fluxes has only recently

(in the 1990s) been included in mesoscale numerical modelling (Thielen *et al*., 2000). According to Thielen *et al*. (2000), the principal reasons for this are that the heat and moisture transfers at the surface depend on a variety of surface characteristics (i.e., heat capacity, permeability, porosity) as well as vegetation parameters (i.e., type of plant, leaf surface, root density), for which explicit data are mostly not available. The definition of representative parameters for mesoscale model grid dimensions is difficult because of the heterogeneity of urban surfaces and the turbulent nature of the air flow.

A recent paper of Bornstein and Craig (2002) provides a history of the various techniques used in numerical mesoscale models to reproduce the effects of urban areas on simulated boundary layer thermodynamic and dynamic fields.

Shepherd (2005) makes a synopsis of recent modelling studies on the impact of urban areas on precipitation. The author highlight the importance of the numerical modelling as it enables controlled experiments to characterize the physical processes involved in urban precipitation processes. According to the author, the relatively few number of numerical model studies present in the literature is due to several factors, such as a poor or nonexistent representation of urban surface parameters, oversimplified or inadequate representation of wet microphysical processes, lack of ability to represent aerosol fields in models, a relative downturn in urban-precipitation research (and funding) in the decade or so following the METROMEX era, and limitations in computing capabilities for fully coupled atmosphere–land modeling systems with explicit microphysical, dynamical, aerosol, and land surface processes.

Masson (2006) presents a review of the recent work on the urban surface modelling and the meso-scale impact of cities.

3.8 Concluding remarks

Guo *et al*. (2006) indicated that one important reason for researchers to eventually obtain different results of urbanization effect on convective precipitation is due partly to the difficulty to separate local topographic and atmospheric circulation effects from urban effects, since most studied cities are located in the different climatic and geographic conditions and have different regional circulation, and also possibly

have different urban aerosol emissions. Thus, further experimental studies are necessary to investigate urban effect on convective precipitation in cities located in different geographic and climatic conditions. In addition, the numerical modelling studies are particularly important resources because they enable controlled experiments to characterise the physical processes involved in urban-induced precipitation (Guo *et al*., 2006; Shepherd, 2005), and separate the typically urban-induced effects from the climatic and geographic influences.

More observational and modelling work is required to improve basic understanding of weather and climate impacts in the urban zone. This is particularly important since local-scale anthropogenic changes in weather and climate have a proportionally larger impact on the global population when they are associated with increases in population density. Recent international meetings in Lodz, Poland (2003), and Vancouver, British Columbia, Canada (2004), highlighted the importance of understanding the role of the urban environment on the Earth's climate system (Shepherd and Jin, 2004).

Chapter 4. Modelling the surface sensible heat flux

This chapter concerns the modelling of turbulent fluxes on the atmospheric surface layer, providing the background basis of the surface sensible heat flux model that will be implemented later in the present study. In section 4.1, the surface energy and water balances over urban (and rural) areas are discussed, as well as the importance of the surface sensible heat flux for the surface energy balance. In this context, the control volume approach is presented. Also some results of previous studies on surface energy balances over urban areas are discussed. In section 4.2, the parameterisation of the sensible heat flux and other turbulent fluxes in the atmospheric surface sublayer is considered. The flux-profile equations for the inertial layer, and the stability correction functions for momentum, sensible heat and water vapour fluxes are presented; surface roughness parameters, such as zero-plane displacement length, roughness length for momentum, sensible heat, and water vapour, are defined.

4.1 Energy and water balance for urban and rural canopies

4.1.1 Control volume approach

To model urban-induced phenomena, momentum, energy and water balances of the urban and rural canopies must be represented (Arya, 2001). Urban canopies are complex because they present a large diversity of size, shape, composition, and arrangement of the surface elements including buildings, streets, trees and parks. Although is not acceptable to neglect this diversity when studying the environment within the canopy, it is reasonable to do so when discussing the whole building-air volume. Thus, a useful approach in describing an urban energy balance is to consider an imaginary box or control volume, whose top is set above the roof level and its base at a certain depth in the ground. More specifically, the control volume extends from a depth in the ground below which energy exchanges are negligible, during the time

period relevant to the process under investigation, to an atmospheric level where the vertical heat exchange divergence is negligible (in the constant flux layer or inertial sublayer) (Oke, 1988; Arya, 2001; Arnfield, 2003). Using the control volume approach, it is possible to ignore the canopy elements as individual energy sources and sinks and avoid questions related to their complex spatial arrangement. The control volume approach can also be used to study the water balance at the surface.

A schematic representation of the fluxes involved in the balances of water and energy of an urban ground-building-air control volume is illustrated in **Figure 4.1a** and **Figure 4.1b**.

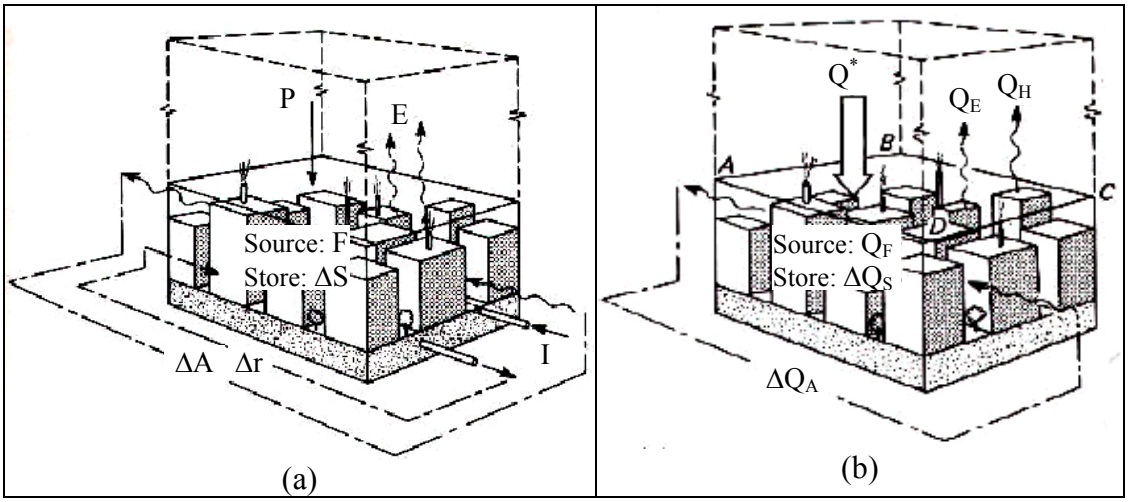

Figure 4.1- *Schematic representation of the fluxes involved in the balances of (a) water and (b) energy of an urban ground-building-air volume (after Oke,1987).*

The control volume approach may also be applied to describe surface flux balances over rural areas. The water and energy balances of a ground-building-air volume or of a ground-vegetation-air volume, can be expressed by the equations (4.1.1) and (4.1.2), respectively.

The water and energy balances of an urban control volume with that of a corresponding volume in the surrounding countryside will be compared in a qualitative way. To simplify the question, both control volumes are considered to exist in an extensive homogeneous area, in order that the advection (ΔA and ΔQ_A) may be neglected. Consequently, only vertical fluxes averaged over the plane ABCD (**Figure 4.1b**), and any internal storage changes have to be taken into consideration (Oke, 1987; Arya, 2001, Piriger and Joffre, 2005).

4.1.2 Water balance

According to the control volume concept presented above, the water balance for a volume extending from about roof level (in the inertial atmospheric sublayer) to the depth in the ground where no significant net exchange of water takes place during the time period relevant to the process under investigation can be expressed as (Grimmond and Oke, 1991; Arnfield, 2003)

$$p + F + I = E + r + \Delta S + \Delta A \quad [kg.m^{-2}.s^{-1}] \qquad (4.1.1)$$

where p is precipitation, F is the water vapour released due to anthropogenic activities (such as combustion), I is the piped water supply of the city (from rivers or reservoirs), E is evapotranspiration, r is runoff, ΔA is the net horizontal advection of moisture (water droplets and vapour) through the sides of the control volume, and ΔS is the net water storage change within the volume (in air, trees, buildings, soil, etc.) during the time period considered.

The water balance is linked to the energy balance, equation (4.1.2), through the evapotranspiration term, which is proportional to the latent heat flux: $Q_E = L_v E$, where L_v is the latent heat of vaporization of water (Oke, 1987; Arnfield, 2003).

In general, the water input to an urban area is greater than in its rural surroundings, because the precipitation contribution (p) is augmented by both the piped water supply (I) and the water release due to combustion (F), for which there are no rural counterparts, except in case of irrigation (Oke, 1987).

On the other hand, evapotranspiration (E) and water storage (ΔS) are expected to be lower in the urban area than in its surrounding countryside. This is because of land cover differences, particularly the replacement of vegetation by relatively impervious materials. Although the complex surface of the urban fabric presents a large rain interception area it appears that the low infiltration, characteristic of urban materials, compensate this effect (Oke, 1987).

The runoff (r) is greater in the urban area, where part of this is due to the discharge of a fraction of the piped water supply (I) as waste water, via sanitary sewers. Also the urban surfaces waterproofing and artificial runoff routing (e.g. storm sewers) contribute largely for the excess of urban runoff compared to the rural

situation (Oke, 1987). In older cities, such as Manchester, storm runoff is carried in the sanitary sewers, these systems being known as combined sewer systems.

4.1.3 Energy balance

According to the control volume approach previously discussed in **section 4.1.1,** the equation for the Surface Energy Balance (SEB) is (Oke, 1988; Arnfield, 2003)

$$Q* + Q_F = Q_H + Q_E + \Delta Q_S + \Delta Q_A \ [J.m^{-2}.s^{-1}] \qquad (4.1.2)$$

where $Q*$ is net all-wave radiation, Q_F represents energy releases within the control volume due to anthropogenic activities (e.g. combustion), Q_H and Q_E are vertical turbulent fluxes of sensible and latent heat, respectively, ΔQ_S is energy storage variation within the control volume (in air, trees, buildings, ground, etc.) and ΔQ_A is horizontal energy advection (sensible and latent heat) through the sides of the control volume. Due to the different values of heat capacities for air and solid materials (see Table A1.1, Apendix 1), in practice the variations in energy storage ΔQ_S can normally be associated to the total conductive heat flux (Q_G) for all air–solid interfaces within the control volume (Arnfield, 2003; Arya, 2001).

As discussed by Piringer and Joffre (2005), in experimental data analysis, when flux measurements are carried out in the inertial layer, the urban Surface Energy Balance (SEB) is usually derived from measured terms, $Q*$, Q_H, and Q_E, each one implicitly including part of the energy released from anthropogenic activities, Q_F, and is expressed as (Grimmond and Oke, 1999b)

$$Q* = Q_H + Q_E + \Delta Q_S \ [J.m^{-2}.s^{-1}] \qquad (4.1.3)$$

where the terms $Q*$, Q_H, Q_E and ΔQ_S represent essentially the same as in equation (4.1.2), but their values may reflect the efect of the energy released from anthropogenic activities. The estimates of the storage term, ΔQ_S, in cities are generally determined as a residual in an energy balance of other terms that are directly observed ($Q*$, Q_H, and Q_E) (Grimmond and Oke, 1999b, 2002; Kanda, 2007). Also, equation (4.1.3) assumes that the surface is of sufficient horizontal extent that advection (ΔQ_A) may be considered negligible.

The *anthropogenic heat flux* is a most typical urban energy component as it is generally absent over rural or natural surfaces (Piringer and Joffre, 2005). In urban areas the addition of the anthropogenic heat flux, Q_F, makes available more energy for partitioning. The anthropogenic heat flux is a significant component of the energy balance of any large city. The value of Q_F depends on the *per capita* energy use in the urban area and its population density. The relative importance of the anthropogenic heat flux in the surface energy balance has been estimated for a number of cities in different seasons (Oke, 1987, 1988; for a review see Arnfield, 2003, and Kanda, 2007). The largest values of the ratio Q_F/ Q^* were found in densely populated cities in middle and high latitudes and in the winter season. Annually averaged values of Q_F/ Q^* for large cities vary between 0.2 (Los Angeles) and 3 (Moscow) with a more typical value of 0.35 (Arya, 2001). For a particular city, the anthropogenic heat flux displays large temporal (both seasonal and diurnal) and spatial variations. In all cases, the city centre appears as the primary heat source, although there may be other localised "hot spots" in industrial areas (Arya, 2001). Numerical simulations showed that the indirect impact of Q_F on the regional temperature is up to 1.0 ^{0}C even in Tokyo (e.g, Ichinose *et al.*, 1999; Kanda, 2007). Investigations of day-of-week variations suggested that maximum and minimum temperatures on weekdays are statistically higher than those on weekends. Weekday *versus* weekend differences in temperature were at most 1.0 ^{0}C, indirectely showing the impact of Q_F, (Fujibe, 1987,1988a, b; Gordon, 1994; Simmonds and Keay, 1997; Kanda, 2007).

Analysis of the radiative energy balance of mid-latitude cities suggests that, in spite of the observed differences in atmospheric turbidity, and in the temperature, albedo, and emissivity between urban and rural surfaces, and although urbanisation alters every component flux of the radiation budget, the net effect on urban-rural radiation differences is small. Apparently the changes in radiative inputs and outputs occur in such a way that they counterbalance each other (Oke, 1987; Piringer and Joffre, 2005; Kanda, 2007). In urban areas the attenuation due to atmosphere pollution reduces the incoming shortwave radiation (see Oke, 1982, 1987, 1988, and Arnfield, 2003, for reviews; Kanda, 2007). However this decrease is partially balanced by decreased upward shortwave radiation due to a lower urban albedo, resulting in a small difference of net shortwave radiation between rural and urban areas. A similar offset exists in urban areas for downward and upward longwave radiation. Due to the

increased emissions from gaseous and particulate atmospheric pollutants, the incoming longwave radiation is greater in urban areas, but the outgoing longwave radiation is also greater because of the higher surface temperatures of urban areas. These balancing relationships between the radiative components result in small differences in the net radiation, Q^*, between rural and urban areas (Kanda, 2007).

The heat storage term, ΔQ_S, is an important term in the urban canopy energy balance. The greater storage of the urban system is not simply due to differences in thermal properties. A comparison of the thermal properties of soil and urban materials used in building and construction (see **Table A1.1** and **Table A1.2,** Appendix 1) does not reveal the required differences (Oke, 1987). The reason for greater urban storage may be attributed to the insulation provided by rural vegetation coverage, the greater surface area for absorption due to the urban geometry, and the reduced latent heat flux due to relative dryness of urban materials. Thus the building and urban ground-covering materials thermal properties, such as large heat capacities and thermal condutivities, and the increase in the thermally active volume forced by the complex tree dimensional geometry, both allow additional heat storage into buildings (Kanda, 2007). The urban vertical constructions provide shade and radiation trapping. Buildings have not only horizontal but also vertical and/or skewed orientations, which strongly alter the radiative transfers and energy budget. Intercomparison of measured $\Delta Q_S/Q^*$ at various urban and suburban sites (Grimmond and Oke, 1995, 1999b; Christen and Vogt, 2004; Kanda, 2007) showed that as vegetation cover fraction increased, $\Delta Q_S/Q^*$ decreased. Numerical studies (Arnfield and Grimmond, 1988; Kanda, 2007) and outdoor experiments using scale models (Pearlmutter *et al.*, 2005; Kanda, 2007) suggest that surface geometry does influence $\Delta Q_S/Q^*$; radiation absortion and heat storage are higher in building arrays with deeper canyons (Kanda, 2007).

Large amounts of ΔQ_S during daytime are balanced by a large release of ΔQ_S during the night. Nocturnal values of $\Delta Q_S/Q^*$ in cities are generally 0.9 to 1.3 (Grimmond and Oke, 1999a; Christen and Vogt, 2004; Moriwaki and Kanda, 2004; Kanda, 2007). The nocturnal release of ΔQ_S is often larger than the radiative loss of Q^*, and the excess energy sustains the upward sensible and latent heat fluxes even at night.

In the urban canopy a large portion of the available energy is transferred to the atmosphere as sensible heat flux, Q_F, because of the increased surface temperatures and enhanced turbulence. In general, in dry weather conditions, the impervious nature of urban surfaces reduces the water availability for evaporation, and the latent heat flux, Q_E, is relatively small. Altough the Bowen ratio ($\beta=Q_H/Q_E$) tends to be large in urban areas, locally the situation can be very different, for example over green parks (Oke, 1987; Arya, 2001). Urban parks, especially if irrigated, may act as oases, because they are moisture sources in an generally dry area. Also, in an urban area, following heavy rain the sensible heat to all wave radiation ratio Q_H/Q^* may drop to approximately 20%, while at the end of a drying period it may be 65% even at a suburban site (Oke, 1987; Arnfield, 2003; Piringer and Joffre, 2005). The moisture availability is one of the more important controlling factors of urban climate. The wetness parameter gradually decreases with the elapsed time after precipitation (Morywaki and Kanda, 2006; Kanda, 2007).

An illustration of the diurnal variation of the surface energy balance is is shown in **Figure 4.2** (after Christen *et al.*, 2003a; *in* Fisher *et al.*, 2005). It shows results of observations for an urban site (Basel, Switzerland) and that of its surroundings. Similar results were found in other studies, namely by Cleugh and Oke (1986), for Vancouver (see Oke, 1987).

Probably the most important difference is the lower evapotranspiration in the city leading to a preferential partition of energy into sensible forms (Q_H and ΔQ_S), and therefore a warming of the urban environment. The sensible heat appears to be largely stored in the urban surface in the morning, and released to the atmosphere in the late afternoon and evening (**Figure 4.2a** and **b**). In general, in the day time the net radiation input is greater in the urban than in the rural case, but this is almost entirely counterbalanced by a greater loss at night (Oke, 1987).

Urban and suburban results (**Figure 4.2a** and **b**) show that the turbulent sensible heat flux, Q_H, is the primary way of dissipating the daytime net radiation excess. Sensible heat storage, ΔQ_S, is also a significant term in the balance. A particular characteristic of the suburban site is the delay of the surface sensible heat flux curves, Q_H, which remain positive after sunset. So, this continued warming of the atmosphere, due to the upward turbulent sensible heat flux, may be important in the growth of the urban heat island that occurs in the same period (Oke, 1987; Fisher *et*

al., 2005). At night, the turbulent terms are small and the net radiative transfer is mostly supplied from storage (Oke, 1987). Suburban results (**Figure 4.2b**) show that the latent heat flux (due to evapotranspiration), Q_E, is also a large term in surface energy balance , showing that water is still considerably available in spite of the waterproofing effects of urban development.

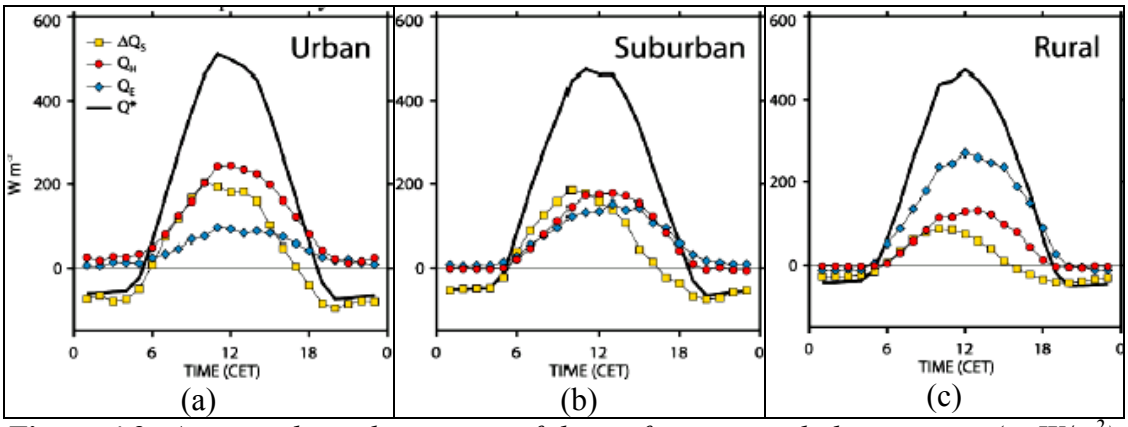

***Figure 4.2**- Average diurnal variation of the surface energy balance terms (in W/m²), at three sites in and around Basel. (-■-) ΔQ_S is the variation of energy storage, (-■-) Q_H is the sensible heat flux, (-■-) Q_E is the latent heat flux, and (–) Q^* is the radiative flux. It represents average days for the observation period from June 10 to July 10, 2002 (including all sky conditions), at (a) an urban site (Sperrstrasse, Basel), (b) a suburban site (Allschwil) and (c) a rural site (Village Neuf). CET stands for Central Europe Time (UTC+1),[After Christen et al., 2003a; adaped from Fisher et al., 2005].*

In order to give an idea of the variation of the magnitude of the surface fluxes for different locations, surface flux measurements over other european cities, such as Marseille (**Figure 4.4**) and Birmingham (**Figure 4.3**), are also shown. Note that in general the results cannot be directly extrapolated to different cities due to land use, climatological and urban metabolism differences.

Comparison of **Figure 4.3** with **Figure 4.2** shows similar diurnal variation of sensible heat flux over the observational (urban and rural) sites of Basel and Birmingham, however the magnitude of the fluxes is higher in Basel. Also the diurnal variation of surface energy fluxes for Marseille city centre **Figure 4.4** and for the urban site in Basel **Figure 4.2** is the same, but in this case the surface energy balance involves greater amounts of energy in Marseille.

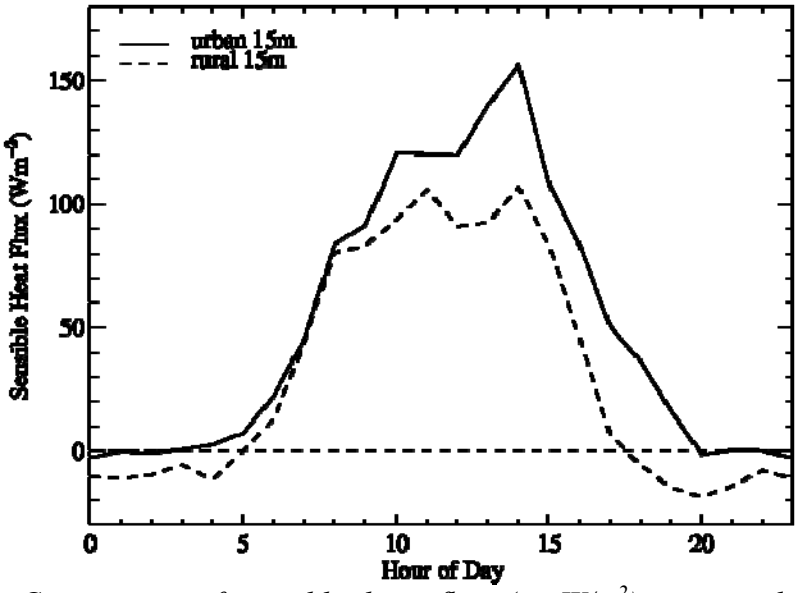

Figure 4.3- *Comparison of sensible heat flux (in W/m^2) measured using sonic anemometers on 15 m masts at Coleshill synoptic station (rural site) and at the Dunlop Tyres Ltd factory site (within Birmingham) plotted by N. Ellis. Results are averages by hour of day. The period covered was from 10 UTC on 7 July 2000 to 17 UTC on 28 July 2000, during the Birmingham campaign [From Middleton and Thomson, 2002]*

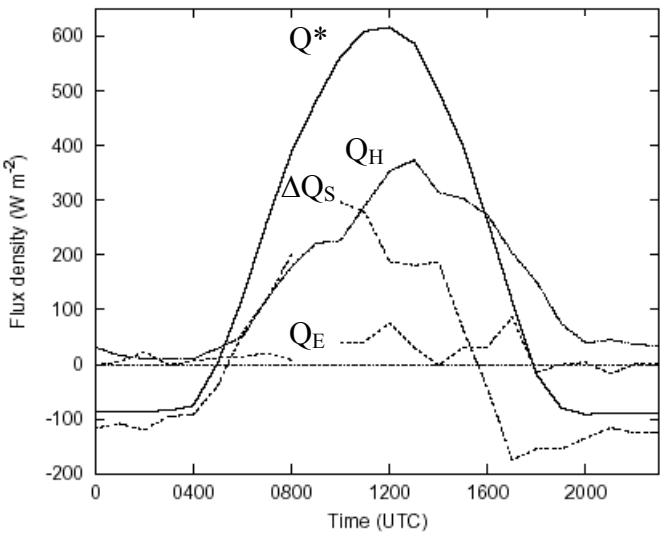

Figure 4.4- *Observed surface energy balance fluxes (in W/m^2) for two observation periods (days 172-178, June 21-26 2001) at the Marseille city centre site (ESCOMPTE). Data are ensemble means for the period including the canopy storage heat flux, ΔQ_S, determined as the residual of the observed terms (Q^*, Q_H, and Q_E). Note that ΔQ_S peaks before solar noon and is negative about 2 hours before the net all-wave radiation flux Q^*. [Adapted from Mestayer et al., 2005]*

4.1.4 Recent studies on surface energy balance over urban areas

With the objective of understanding exchange processes over urban areas, a number of field campaigns have been implemented during the last few decades. Data on surface energy exchanges in urban environments have been collected to represent cities with different building materials and architectural styles, as well as for conditions where direct energy release from human activities is more significant.

Initially campaigns took place in North American cities (Oke, 1988; Grimmond and Oke, 1999b, 2002; Piringer *et al.*, 2002), being followed by several experimental studies examining the surface energy balance in European cities [see for example, (Klysik, 1996; Offerle *et al.,* 2005, 2006), Lodz, Poland; (Dupont *et al.*, 1999), ECLAP experiment, French acronym for ‘‘Etude de la Couche Limite dans l’Agglome´ ration Parisienne’’, Paris, France; (Holmer and Eliasson, 1999), Sweden; (Jauregui *et al.*, 2002), Barcelona, Spain; (Christen *et al.,* 2002, 2003; Christen and Vogt, 2004; Rotach *et al*., 2005), BUBBLE, the Basel UrBan Boundary Layer Experiment, Switzerland; (Grimmond *et al.,* 2002; Mestayer *et al*., 2005), ESCOMPTE, French acronym for Expérience sur Site pour Contraindre les Modèles de Pollution Atmosphérique et de Transport d’Émissions, Marseille, France; (Ellis and Middleton, 2000a, b, c; Middleton *et al*., 2002), Birmingham field experiments, UK.].

In Fisher *et al.* (2005) new developments and results initiated by, or accessible to, COST 715 members are briefly summarised (COST is the French acronym, for "European Cooperation in the Field of Scientific and Technical Research"). A more complete review of the problem together with analyses of recent experimental data can be found in a separate report (COST 715- Working Group 2) by Piringer and Joffre (2005). Piringer and Joffre (2005) present a set of recent experimental campaigns providing relevant meteorological, turbulence and urban features data for European urban and sub-urban conditions. According to the authors such data can be used for testing and validating parameterisation schemes and models. The campaigns considered were the following: BUBBLE, Switzerland, 2001/2002; the field campaign UBL-ESCOMPTE over Greater Marseille area, France, 2001; the Birmingham field experiments, UK, , 1998, 1999, 2000; the Bologna experiment, Italy, 2001/2002; the Cracow and Katowice experiments, Poland, 2002, 2003; the Helsinki experiment,

Finland, 2002; the CALRAS (Comprehensive Alpine Radiosonde) data set, Alpine area, 1991-1999; the ATHIBLEX/MEDCAPHOT experiments in Athens, 1994; the experiments in Copenhagen area and surroundings, Oresund, Jaegtvej and Jaegersborg, Denmark, since ~1980; the Hannover measurements, Germany, in the framework of the project VALIUM, 2001- 2003.

Recent parameterisation and modelling of the surface energy balance, are also discussed in these COST 715 reports (i.e, Fisher *et al.*, 2005; Piringer and Joffre, 2005). Namely, with LUMPS- Local-scale Urban Meteorological Pre-processing Scheme (Grimmond and Oke, 2002); the French SUBMESO model, SM2-U, (Guilloteau and Dupont, 2002); the TEB/ISBA - Town Energy Balance and Interaction Soil-Biosphere-Atmosphere scheme (Noilhan and Planton, 1989; Masson, 2000); the FVM - Finite Volume Model (Martilli *et al.*, 2002); the ARPS (Advanced Regional Prediction System) and OHM (Objective Hysteresis Model) for Paris; the ADMS model for Birmingham and London; and the Cracow model. Implications of surface energy balance results for Numerical Weather Prediction NWP modelling for European cities are also discussed.

The experimental and numerical studies undertaken by COST 715 led to some important conclusions and recommendations reported by Fisher *et al.* (2005). It was found that the diurnal variation of the surface energy balance terms, obtained during some major field experiments in European Cities, agree with previous observations over North American cities (Oke, 1988; Grimmond and Oke, 1999b, 2002). The available observations of urban heat fluxes demonstrate significant perturbation of the surface energy balance (partitioning into sensible, latent, and storage heat fluxes) compared to the rural surroundings (see, for example, **Figure 4.2**, showing the diurnal variation of the surface energy balance over Basel region, and similar results of Cleugh and Oke (1986), in (Oke, 1987), for Vancouver). In particular the sensible heat flux remains directed upwards throughout the night, sustained by large releases of heat stored in the urban fabric during the previous day (Fisher *et al.*, 2005). As expected, given the lack of vegetation cover at most urban sites, the latent heat fluxes are small, and the Bowen ratio ($B= Q_H /Q_E$) is therefore larger than 1 (**Table 2.1**).

Table 4.1 *- Ranges of average daily maximum values of net radiation and fluxes in North American cities at the Multicity Urban Hydrometeorological Database- MUHD. One salient feature of urban sites is that the storage heat flux is as significant as the sensible heat flux, which is different from typical rural sites where it is much less. [after Grimmond and Oke, in Piringer et al., 2002] (from Fisher et al., 2005).*

Parameter	**Range (W m^{-2})**
Net all-wave radiation Q*	< 400 - 650
Latent heat flux Q_E	10 - 235
Sensible heat flux Q_H	120 - 310
Storage heat flux ΔQ_S	150 - 280
Average daytime Bowen ratios Q_H/Q_E:	(dimensionless)
residential sites	1.2 - 2
during irrigation ban Vancouver	~ 2.8
light industrial site	~ 4.4
city centre	~ 9.8

4.2 Parameterisation of turbulent fluxes in the atmospheric inertial sublayer

4.2.1 Introduction

The inertial sublayer is usually studied within the framework of Monin-Obukov Similarity Theory (MOST) (e.g., Fisher *et al*, 2001; Kanda, 2007; Kanda *et al*., 2007). This will form the basis of the model to be used later in the present study to derive fields of sensible heat flux over the urban area and to explore the impact of the urban surface heterogeneity. In this section the flux-profile relationships are presented for wind, temperature, and eventually other relevant quantities such as specific humidity in the inertial sublayer of the atmospheric boundary layer. As will be discussed, these relationships were not derived by the solution of the transport equations, rather they were arrived at by invoking similarity, through the application of dimensional analysis.

Figure 4.5 illustrates the structure of the urban ABL highlighting the important region within the surface layer close to the ground to be modelled, which involves the control volume concept defined in section 4.1.1. As it will be seen in the following chapters, in the present work the dimensions of the control volume are similar to those presented in **Figure 4.5**, namely the horizontal extension of the domain cells have a size of 1x1 km^2.

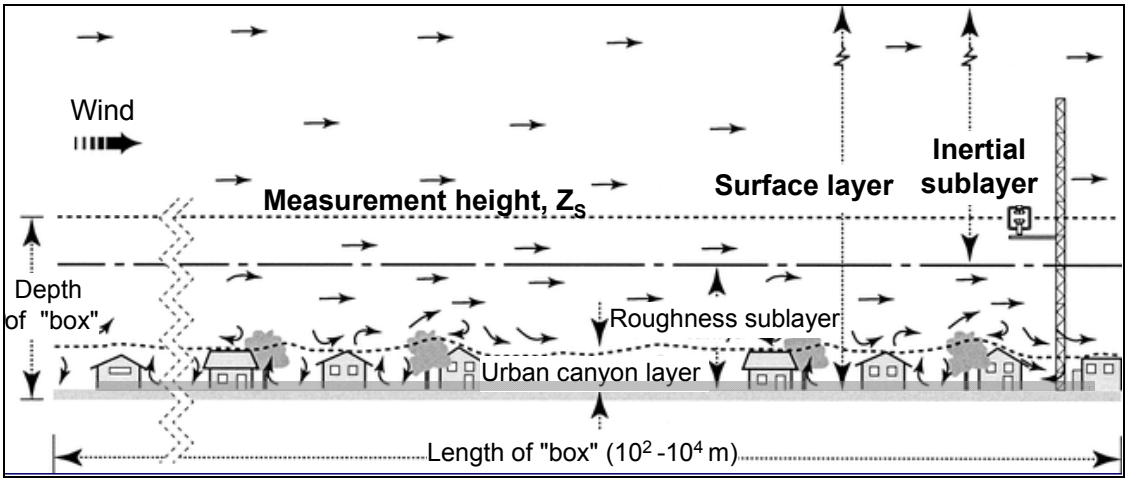

Figure 4.5 *- Definition of layers involved in the study of urban climates at the local scale relative to the "box" (control volume) modeled by LUMPS (Local-Scale Urban Meteorological Parameterization Scheme). The lateral (or third) dimension of the box, not shown, is also 10^2–10^4 m. The top of the "box" is within the inertial sublayer, and the bottom is at the depth at which there is no net heat exchange over the time period of interest [from Grimmond and Oke, 2002].*

The urban boundary layer is characterised by stronger turbulence as compared to the upwind rural boundary layer. The increased turbulence is a result of the increased production of turbulent kinetic energy over an urban area due to increases in both the shear and buoyancy production terms in the turbulent kinetic energy equation (Brutsaert, 1882; Stull, 1988; Garratt, 1992). Turbulent variances, fluxes and other statistics in the inertial layer of the urban boundary layer, however, follow the same similarity scaling and display similar structure as turbulence in the homogeneous ABL for the same values of stability and other similarity parameters (Oke, 1995; Arya, 2001).

However the applicability of the MOST over urban areas has been questioned. Note that in cities building heights and their spatial variability can be large enough to break down the separation of the inertial sublayer, from the roughness sublayer underneath it, and from the region the above (Rotach, 1999). Therefore the inertial sublayer may not exist over cities and consequently the MOST is not applicable, because the theory assumes that turbulence statistics should follow universal functions that are independent of surface roughness (Roth, 2000; Kanda, 2007). In addition a city with high-rise buildings can provide a large obstacle to the mesoscale flow field, and barrier effects on precipitation or sea breezes, for example, may be observed. In these extreme cases, conventional roughness treatments fail (Kanda, 2007), and the MOST is not applicable.

4.2.2 Turbulent flow and some statistics

The turbulent nature of the atmospheric boundary layer (ABL) is one of its most remarkable and important features. Due to the complexity of the turbulent flow a description of the flow at all points and time is not feasible. The random nature of turbulence makes deterministic description difficult. Consequently, any study of turbulent flows (either in the form of observations or solution of the conservation equations) is directed towards describing their statistical characteristics, usually in terms of moments and spectra (Garratt, 1992). In the present study the former approach is considered.

Reynolds averaging

The statistical approach usually involves separating the turbulent from the nonturbulent parts of the flow, followed by averaging to provide a statistical descriptor, using Reynolds decomposition and averaging techniques (Stull, 1988). It is assumed that any process, s (x,y,z,t), can be decomposed into a mean component, $\bar{s}$, and a turbulent component or fluctuation, s',

$$s = \bar{s} + s' \qquad (4.2.1)$$

where an overbar denotes an average, and a prime denotes a deviation from the average. Thus, for atmospheric variables, one has, for example

$$\begin{aligned} u &= \bar{u} + u' \qquad v = \bar{v} + v' \qquad z = \bar{z} + z' \\ \theta &= \bar{\theta} + \theta' \qquad q = \bar{q} + q' \qquad c = \bar{c} + c' \end{aligned} \qquad (4.2.2)$$

where u, v, and z are the wind components, θ is the potential temperature, q is the specific humidity, and c is the concentration of an atmospheric constituent (e. g. aerosol, pollutant, or water vapour).

Covariances as measures of turbulent fluxes

In boundary layer meteorology, turbulent fluxes of momentum, heat, and mass (moisture, pollutants, etc.) are of major importance.

In fluid dynamics the transport of a variable per unit area per unit time, (i.e., a dynamic flux, or simply flux), divided by the average air density (ρ), or in the case of heat flux, divided also by specific heat of air at constant pressure (c_p), is termed kinematic flux. The kinematic flux has the same units as velocity times the variable being transported. Kinematic fluxes are more closely related to meteorological variables that can be easily measured (such as temperature and wind) than are the associated dynamic fluxes. Thus, for convenience the ABL fluxes can be presented in kinematic form. This procedure is acceptable because the atmospheric boundary layer is usually relatively thin so that the density, and specific heat of air at constant pressure changes, across it can be neglected in comparison to changes of the other meteorological variables (Stull, 1988).

Also, in order to simplify fluxes description, the flux of a certain quantity ($\overline{u.s}$) can be split into three components, a vertical component and two horizontal components. In addition, as described previously, the fluxes can also be split into mean

and turbulent parts. Using Reynolds decomposition and averaging techniques, the kinematic flux of a quantity *s* in a direction *j* is given by (Kaimal and Finnigan, 1994)

$$\overline{u_j.s} = \overline{u_j}.\overline{s} + \overline{u_j's'} \qquad (4.2.3)$$

where $\overline{u_j.s}$ is the kinematic flux in direction j, $\overline{u_j}.\overline{s}$ is the kinematic flux associated with the transport by the mean flow (i.e., advection), in the direction j, and $\overline{u_j's'}$ is the flux associated with turbulence transport, also in the direction j. An overbar denotes an average, and a prime denotes a deviation from the average. Statistically, kinematic turbulent fluxes are covariances. Accordingly, the kinematic fluxes of heat, moisture, u-momentum and v-momentum, in the vertical direction, are respectively given by

$$\overline{w.\theta} = \overline{w}.\overline{\theta} + \overline{w'\theta'} \qquad (4.2.4)$$

$$\overline{w.q} = \overline{w}.\overline{q} + \overline{w'q'} \qquad (4.2.5)$$

$$\overline{w.u} = \overline{w}.\overline{u} + \overline{w'u'} \qquad (4.2.6)$$

$$\overline{w.v} = \overline{w}.\overline{v} + \overline{w'v'} \qquad (4.2.7)$$

The two last fluxes are also the x-direction kinematic flux of w-momentum, and the y-direction kinematic flux of w-momentum, respectively.

It is important to recognise that the mean vertical wind component is negligible ($\overline{w}$~0) throughout most of the ABL, except where convection occurs. As a result, the vertical advective fluxes are usually negligible compared to the vertical turbulent fluxes in the ABL. On the other hand, this approximation is not applicable in the horizontal direction, where relatively strong mean horizontal winds and turbulence can cause fluxes of comparable magnitudes (e.g, Garratt, 1992).

In the present work (**Chapter 7**) measurements of turbulent surface sensible heat flux are obtained from the covariances of the observations of the vertical wind component, w, and virtual temperature, T_v, using a sonic anemometer, i.e.

$$Q_H \cong \rho c_p \overline{w'T_v'} \cong \rho c_p \overline{w'T'} \qquad (4.2.8)$$

Note that in view of the smallness of the dry adiabatic lapse rate, $\Gamma_d \sim 9.8$ K km^{-1}, for most practical purposes in the surface layer the potential temperature, θ, appearing in the equations may be replaced by the temperature, T (Brutsaert, 1982). For the definition of virtual and potential temperatures, and the discussion of the respective

atmospheric vertical profiles and atmospheric stability, see for example (Wallace and Hobbs, 1977), (Stull, 1988), (Pielke, 2001) and (Tsonis, 2002).

4.2.3 K-closure of the governing equations for the ABL

The set of equations governing the atmospheric flow consists of the three equations for the conservation of momentum (the Navier-Stokes equations), an equation for the conservation of mass (the continuity equation), an equation for the conservation of thermal energy (the thermodynamic or enthalpy equation), an equation for the conservation of water vapour (the humidity equation) and the equation of state (the gas law). This system of seven basic equations (an equation for liquid water or ice is omitted here) describes the spatial and temporal (x, y, z, t) dependence of the atmospheric variables u (longitudinal velocity component), v (transverse velocity component), w (vertical velocity component), ρ (air density), T (absolute temperature), q (specific humidity) and p (pressure) (Brutsaert, 1982; Stull, 1988; Garratt, 1992; Kaimal and Finningan, 1994; Arya, 2001).

The Reynolds number, Re, is defined as

$$Re = UL/\nu = \rho UL/\mu \qquad (4.2.9)$$

where U is a characteristic velocity, L is a characteristic length, ρ is the density of the fluid, ν is the kinematic viscosity and μ is the dynamic viscosity of the fluid. The Reynolds number can be interpretated as the ratio of the inertial to the viscous forcings in the Navier–Stokes equations (Stull, 1988). It is used to identify and predict different flow regimes, such as laminar or turbulent flow. Laminar flow occurs at low Reynolds numbers, where viscous forces are dominant, and is characterized by smooth, constant fluid motion, while turbulent flow, on the other hand, occurs at high Reynolds numbers and is dominated by inertial forces, which tend to produce random eddies, vortices and other flow fluctuations. Large Reynolds numbers indicate very turbulent flow, which usually occurs within the atmosphere, where typically $Re \sim 10^7$ in the ABL (Garratt, 1992; Stull, 1988).

Analytical solutions of the equations for the conservation of momentum, energy and water vapour are generally not possible, and numerical solutions for large Reynolds number flow (typically greater than 10^4 to 10^6) are impracticable (Garratt, 1992; Kaimal and Finningan, 1994). Therefore ABL studies address statistical

considerations, averaged flow fields represented by Reynolds averaged equations, and the simplified ABL equations termed the Boussinesq equations (see for example Brutsaert, 1982; Stull, 1988; Garratt, 1992; Kaimal and Finningan, 1994). However the application of the averaging operator to these equations results in the appearance of new (unknown) terms, such as the covariances $\overline{u_j'\theta'}$, $\overline{u_j'q'}$, and $\overline{u_i'u_j'}$, which are interpreted as turbulent fluxes. It is impossible to *close* the equation set, that is there will always be more unknowns than equations. This is termed the closure problem, and the higher-order moment terms must be parameterised in terms of known quantities. The closure approximation is named after the highest-order moments retained in the problem. For example, if only mean (first order moment) equations are to be solved, and the covariance (second order moment) terms parameterised, the closure is termed first order.

A first order closure scheme (K-closure) (Garratt, 1992; Kaimal and Finningan, 1994; Arya, 2001) uses eddy transfer coefficients, K_s, to relate any turbulent flux to the local mean gradient of the quantity *s* being transported. That is, for any quantity, the turbulent fluxes (or covariances) can be written in terms of the following flux-gradient relation:

$$\overline{u_j's'} = -K_s \frac{\partial \bar{s}}{\partial x_j} \qquad (4.2.10)$$

which, for K_s positive, implies downgradient flow.

In general one is concerned with vertical transfer in the ABL, as represented by the turbulent terms of the simplified mean equations in a stationary and horizontally-uniform ABL (Garratt, 1992; Arya, 2001), so that the vertical fluxes for the quantities u, v, θ and q are given by

$$\frac{\tau_{xz}}{\rho} = \overline{u'w'} = -K_M \frac{\partial \bar{u}}{\partial z} \qquad (4.2.11)$$

$$\frac{\tau_{yz}}{\rho} = \overline{v'w'} = -K_M \frac{\partial \bar{v}}{\partial z} \qquad (4.2.12)$$

$$\frac{Q_H}{\rho c_p} = \overline{w'\theta'} = -K_H \frac{\partial \bar{\theta}}{\partial z} \qquad (4.2.13)$$

$$\frac{E}{\rho} = \overline{w'q'} = -K_E \frac{\partial \bar{q}}{\partial z} \qquad (4.2.14)$$

where K_M, K_H and K_E are the eddy transfer coefficients for momentum, heat and water vapour, respectively, τ_{xz} and τ_{yz} represent the vertical flux of each momentum horizontal component, Q_H the sensible heat flux, and E is the evapotranspiration. First order closure transfers the problem of the unknown covariances to that of specifying the eddy transfer coefficients. Formulations for K are discussed, for example, in (Garratt, 1992). Note that the K-closure scheme proposes gradient-transport relations for the turbulent fluxes in analogy with the classical laws of molecular transport of properties, namely, Newton's law of viscosity, Fourier's law of heat conduction and Fick's law of mass diffusion, respectively (Arya, 2001).

4.2.4 Mean profiles and similarity in a stationary and horizontally-uniform ABL

In atmospheric boundary layer studies, where complexity of turbulence prevents solutions of the governing equations, i.e. due to the closure problem, it is common practice to rely on empirical relationships between meteorological variables based on observations (Beljaars, 1992). Similarity theory provides the framework to organize and group the experimental data, and is used in virtually all ABL schemes that have been developed for atmospheric models. The procedure starts with the identification of the relevant physical parameters, then dimensionless groups are formed from these parameters, and finally experimental data are used to find functional relations between dimensionless groups of variables (Beljaars, 1992). The procedures are simple in principle (the Buckingham Pi dimensional analysis method; see e.g. Stull, 1988), but require experience and intuition in practice. The judgment of which parameters are important is a crucial aspect of the analysis (Beljaars, 1992).

In this context, it is advantageous to consider different parts of the boundary layer (surface layer, outer layer, etc.) and different atmospheric stability conditions (neutral, very unstable, etc.) separately, to simplify the problem and to limit the number of dimensionless groups that are relevant at the same time. In this section equations for atmospheric variable profiles, such as wind and temperature, in the inertial sublayer are presented.

As discussed in previous chapters, the inertial sublayer (**Figure 4.5**) is the lower part of the boundary layer above the roughness obstacles, which is sufficiently close to the ground surface that the effect of the Coriolis force is negligible, but it is far enough from the surface that both viscosity of the air and the structure of the individual roughness elements have no effect on flow (Brutsaert, 1982). In the published literature a dynamic layer (not shown in **Figure 4.5**) is often mentioned. This is defined as the fully turbulent region in the lower part of the inertial layer, where also the effect of buoyancy force due to density stratification is negligible (Brutsaert, 1982). Under diabatic conditions, i. e., with density stratification of the air, this layer may extend over only a few metres or less, whereas under conditions of neutral stability the dynamic sublayer occupies the entire inertial sublayer.

It has been verified experimentally that in the neutral inertial layer the vertical profiles of the mean wind speed, mean temperature, mean specific humidity and concentration of other constituents of the air, provided they are released or absorbed uniformly at the surface, are all logarithmic functions of the height above the surface (Brutsaert, 1982). However, in the non-neutral inertial layer, the logaritmic law for the vertical profiles of atmospheric variables is no longer valid. This is because besides the factors governing the turbulent transfer in the neutral inertial layer, the stability of the atmosphere, that is, the effect of the buoyancy resulting from the effective vertical density gradient, must be considered. In the following subsections the vertical profiles of atmospheric variables (such as wind, temperature and humidity) in the neutral and non-neutral inertial layer will be discussed.

The logarithmic profile law in the neutral inertial sublayer

The logarithmic wind profile law was developed in the late 1920s and it was introduced into meteorology by Prandtl (1932) and one of the simplest derivations is that of Landau and Lifshitz (1959) (Brutsaert, 1982). The approach is based on dimensional analysis, and it consists of noting that in plane -parallel flow (stationary, over a flat and horizontally uniform surface) an increase of the mean velocity in the z-direction, $\partial \bar{u} / \partial z$, is evidence of a downward momentum flux and a sink at the surface. Thus, the mean velocity gradient in a fluid of density ρ is determined by the shear stress at the surface, τ_0, and the distance from the surface, z. These variables can

be combined into a single dimensionless parameter, the von Karman's constant k=0.4, as follows (Brutsaert, 1982)

$$\frac{u_*}{z\left(\partial \bar{u} / \partial z\right)} = k \qquad (4.2.15)$$

where u_* is the friction velocity defined by (see next subsection)

$$u_* = \left|\tau_0/\rho\right|^{1/2} \qquad (4.2.16)$$

The logarithmic wind profile equation is derived from integration of equation **(4.2.15**), namely

$$\bar{u}_2 - \bar{u}_1 = \frac{u_*}{k} \ln\left(\frac{z_2}{z_1}\right) \qquad (4.2.17)$$

where the subscripts refer to two levels within the neutral inertial sublayer. Alternatively, one can write (Brutsaert, 1982)

$$\bar{u} = \frac{u_*}{k} \ln\left(\frac{z}{z_{0M}}\right), \quad \text{for } z >> z_{0M} \qquad (4.2.18)$$

where the integration constant z_{0M} is the height at which the wind speed becomes zero, and it is referred to as roughness length for momentum. Graphically (**Figure 4.6**), z_{0M} may be visualised as the zero velocity intercept of the logarithmic curve resulting from a plot of mean velocity data versus elevation in the neutral inertial sublayer (e.g, Stull, 1988).

Except for flexible obstacles or water waves, the value of roughness length for momentum, z_{0M}, is theoretically independent of the flow, and only a function of the nature of the surface (i. e., the geometry, size and arrangement of the surface roughness elements) (Brutsaert, 1982). In Chapter 5 some published tables of typical values of z_{0M} for some homogeneous terrain types, are shown.

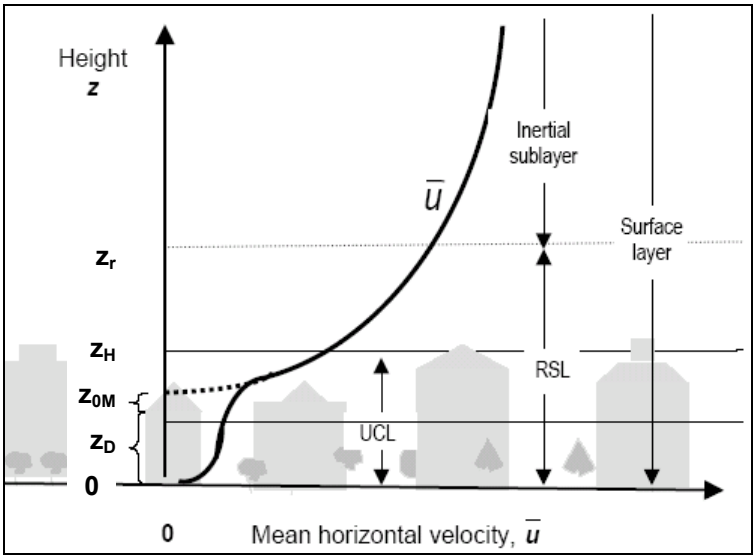

Figure 4.6 - *Generalized mean (spatial and temporal) wind velocity (u) profile in a densely developed urban area including the location of sublayers of the surface layer (inertial sublayer and roughness sublayer, RSL, and urban canopy layer, UCL). The measures on the height scale are the mean height of the roughness elements (z_H), the roughness sublayer (z_r, or the blending height), the roughness length for momentum (z_{0M}) and zero-plane displacement length (z_D). The dashed line represents the wind profile extrapolated from the inertial sublayer, and the solid line represents the actual wind profile [from Oke, 2006].*

In the case of rough surfaces there is some uncertainty concerning the reference level z=0 as used in equation **(4.2.15)**. To minimise this difficulty, it is common practice to define z=0 as the level of the bases of the roughness elements, and to allow for a shift in reference level for the coordinate used in the similarity formulation (Brutsaert, 1982). Accordingly, instead of equation **(4.2.15)** one has

$$\frac{u_*}{(z - z_D)(\partial \bar{u} / \partial z)} = k \qquad (4.2.19)$$

where z_D is termed zero-plane displacement height. Thus, upon integration, one has

$$\bar{u} = \frac{u_*}{k} \ln\left(\frac{z - z_D}{z_{0M}}\right), \quad \text{for } z >> z_{0M} \qquad (4.2.20)$$

The dimensional approach used to derive equation **(4.2.19)** can be extended to derive expressions for the temperature profile and those of other quantities, such as specific humidity q, or the concentration of other atmospheric constituents (Brutsaert,

1982). Thus, just like equation **(4.2.19)**, the following dimensionless ratios have been found to be approximately invariant:

$$\frac{\overline{w'\theta'}}{u_*(z-z_D)\left(\frac{\partial\bar{\theta}}{\partial z}\right)} = -k_H \qquad (4.2.21)$$

and

$$\frac{\overline{w'q'}}{u_*(z-z_D)\left(\frac{\partial\bar{q}}{\partial z}\right)} = -k_E \qquad (4.2.22)$$

where θ is potential temperature and q is specific humidity, and $k_H = a_H k$ and $k_E = a_E k$ are the von Karman constants for sensible heat (Q_H) and water vapour (E) fluxes. In practice it is reasonable to assume that $k_H = k_E = k = 0.4$ (Brutsaert, 1982; Hogstron, 1988; Andreas *et al.*, 2006), so that $a_H = a_E = 1$.

Integration of equations **(4.2.21)** and **(4.2.22)** between two levels, z_1 and z_2, in the neutral inertial sublayer produces

$$\bar{\theta}_1 - \bar{\theta}_2 = \frac{\overline{w'\theta'}}{ku_*}\ln\left(\frac{z_2 - z_D}{z_1 - z_D}\right) \qquad (4.2.23)$$

and

$$\bar{q}_1 - \bar{q}_2 = \frac{\overline{w'q'}}{ku_*}\ln\left(\frac{z_2 - z_D}{z_1 - z_D}\right) \qquad (4.2.24)$$

The vertical integration of equations **(4.2.21)** and **(4.2.22)** between the surface and some height z gives

$$\bar{\theta}_s - \bar{\theta} = \frac{\overline{w'\theta'}}{ku_*}\ln\left(\frac{z - z_D}{z_{0H}}\right), \quad \text{for } z >> z_{0H} \qquad (4.2.25)$$

and

$$\bar{q}_s - \bar{q} = \frac{\overline{w'q'}}{ku_*}\ln\left(\frac{z - z_D}{z_{0E}}\right), \quad \text{for } z >> z_{0E} \qquad (4.2.26)$$

where z_{0H} is the roughness length for sensible heat, and z_{0E} is the roughness length for water vapour. Equations (4.2.25) and (4.2.26) can also be writen in the follwing form, respectively,

$$\bar{\theta}_s - \bar{\theta} = \frac{Q_H}{ku_*\rho c_p}\ln\left(\frac{z - z_D}{z_{0H}}\right), \quad \text{for } z >> z_{0H} \qquad (4.2.27)$$

and

$$\bar{q}_s - \bar{q} = \frac{E}{ku_*\rho}\ln\left(\frac{z - z_D}{z_{0E}}\right), \quad \text{for } z >> z_{0E} \qquad (4.2.28)$$

The integration constant z_{0H} (or z_{0E}) can be seen as the level above z_D where the potential temperature $\bar{\theta}$ (or the specific humidity $\bar{q}$) would assume its surface value if the logarithmic profile were extrapolated downward outside its actual range of validity; it is the zero intercept of (θ_s-θ) (or q_s-q) data measured in the neutral inertial sublayer and plotted versus (z-z_D).

Monin–Obukhov scales for the inertial sublayer

Monin–Obukhov Similarity Theory (MOST) (1954) is the basic similarity hypothesis for the stationary horizontally homogeneous inertial sublayer (e.g., Fisher *et al*, 2001; Kanda, 2007; Kanda *et al*., 2007). Empirical evidence from field experiments over flat terrain points to an inertial sublayer where the structure of turbulence is determined by a few key parameters as proposed by Monin and Obukhov (1954). These key parameters are the height z above the surface, the buoyancy parameter (g/θ) (ratio of inertia and buoyancy forces; see Stull, 1988), the kinematic surface stress (τ_0/ρ), and the surface temperature flux $Q_H/(\rho c_p) = (\overline{w'\theta'})_s$ (Beljaars, 1992; Kaimal and Finnigan, 1994). In these expressions *g* is gravitational acceleration, θ is potential temperature, τ_0 is turbulent stress at the surface, ρ is air density, Q_H is the sensible heat flux at the surface, c_p is the specific heat of air at constant pressure, and $(\overline{w'\theta'})_s$, the covariance of vertical velocity *w* with potential temperature near the surface, is the kinematic sensible heat flux.

These parameters can be used to define a set of dimensional scales for the inertial sublayer, such as, a velocity scale (the friction velocity), a temperature scale, a humidity scale, a length scale (the Obukhov length), and the height above ground scale, as follows (Beljaars, 1992; Kaimal and Finnigan, 1994).

The turbulent momentum flux acts like a shear stress and is called the Reynolds stress, τ. During situations where turbulence is generated or modulated by wind shear near the ground, the magnitude of the surface Reynolds' stress, τ_0, proves to be an important scaling variable (Beljaars, 1992). The total vertical flux of horizontal momentum, τ_0, near the surface is given by

$$\tau_0 = \left[\tau_{xz}{}^2 + \tau_{yz}{}^2\right]^{1/2} \qquad (4.2.29)$$

where τ_{xz} and τ_{yz} represent the vertical flux of each momentum horizontal component,

$$\tau_{xz} = -\rho\overline{u'w'}_s \text{ and } \tau_{yz} = -\rho\overline{v'w'}_s \qquad (4.2.30)$$

or, if the x-coordinate axis is aligned with the horizontal wind, u,

$$\tau_0 = -\rho\overline{u'w'}_s \qquad (4.2.31)$$

Based on these equations, a velocity scale termed friction velocity, u_*, is defined as

$$u_*^2 = \left[\overline{u'w'}_s^2 + \overline{v'w'}_s^2\right]^{1/2} \qquad (4.2.32)$$

or, if the x-coordinate axis is aligned with the horizontal wind, u,

$$u_* = \left[\overline{u'w'}_s\right]^{1/2} \qquad (4.2.33)$$

so that

$$u_* = \left|\tau_0/\rho\right|^{1/2} \qquad (4.2.34)$$

where τ_0 is the Reynolds stress at the surface, ρ the air density. The reference wind velocity u_* is a measure of turbulent surface stress (see Kaimal and Finnigan, 1994).

Other key scales for the surface sublayer are then defined, such as (Beljaars, 1992; Kaimal and Finnigan, 1994)

the temperature scale,

$$\theta_* = -(\overline{w'\theta'})_s / u_* \qquad (4.2.35)$$

the humidity scale,

$$q_* = -\overline{w'q'}_s / u_* \qquad (4.2.36)$$

the length scale, the Obukhov length,

$$L = u_*^2\theta / kg\theta_* \text{ or } L = -u_*^3\theta / kg(\overline{w'\theta'})_s \text{ or } L = -\frac{\rho c_p u_*{}^3\theta}{kgQ_H} \qquad (4.2.37)$$

and the height above ground scale, *z*.

The Obukhov length can be interpreted as the height ($z = |L|$) of the dynamic sublayer (Brutsaert, 1982), being where the production of turbulent kinetic energy (see Stull, 1998; Garratt, 1992) is dominated by the dynamic terms associated to the vertical gradients (shear) of horizontal wind components.

The Obukhov length, L, may also be generalised to take into account the buoyancy effect of the water vapour flux, usually achieved by replacing Q_H in the

expression for L by (Q_H+0.07Q_E). In most cases it is not necessary to consider this degree of refinement, although this is not valid when $Q_H << Q_E$, which is not unusual over the oceans for example (Dyer, 1974).

The Obukhov length, L, has the opposite sign to the surface sensible heat flux, Q_H. Thus L is positive for stable and negative for unstable atmospheric conditions, and tends to infinity in the case of neutral stability. By definition L can have values in the range $-\infty \leq L \leq +\infty$ but values of L smaller in magnitude than about 1 m are rare, and the practical range on L is 1 to 1000 m (Middleton, 1995). In the UK the sensible heat flux, Q_H, is usually in the range -50 to 200 W m^{-2} and the friction velocity, u_*, is typically 0.05 to 0.5 m s^{-1} (Middleton and Thomson, 2002). The Obukhov length is positive and small in stable conditions with light winds at night, is negative and small (of order -10m) on strongly convective days, is of order -100 m on windy days with some solar heating, and tends to infinity in the neutral case with purely mechanical turbulence (Middleton and Thomson, 2002). **Table 4.2** after Seinfeld and Pandis (1998) also summarises an interpretation of the Obukhov length with respect to atmospheric stability.

Table 4.2 *- Interpretation of the Monin-Obukhov Length L with respect to atmospheric stability (after Seinfeld and Pandis, 1998).*

L		Stability Condition
Small negative	-100 m < L < 0	Very unstable
Large negative	-10^5 m $\leq L \leq$ -100 m	Unstable
Very large (positive or negative)	$\lvert L \rvert > 10^5$ m	Neutral
Large positive	10 m $\leq L \leq 10^5$ m	Stable
Small positive	0 < L < 10 m	Very stable

Monin and Obukhov flux-profile relations for the (non-neutral) inertial sublayer

Monin and Obukhov (1954) introduced the stability parameter ζ [for z_D=0], that accounts for the effect of the buoyancy resulting from the effective vertical density gradient (Brutsaert, 1982),

$$\zeta=(z-z_D)/L \qquad (4.2.38)$$

where *z* is height above the surface, z_D the zero plane displacement height and *L* is the Obukhov length. The atmospheric stability may be characterised by the Monin-Obukhov parameter, ζ, which is zero for statically neutral stability, is positive for

stable and negative for unstable conditions, in a typical range of 1 to 5, or −5 to −1, respectively.

According to Monin and Obukhov similarity theory (1954), various atmospheric parameters and statistics, such as gradients, variances, and covariances, when normalized by appropriate powers of the scaling factors (for example, u_*, ✓$_*$, q_*, L and z), become universal functions of the stability parameter ζ (Kaimal and Finnigan, 1994).

The so called flux-gradient or flux-profile relations relate the vertical turbulent flux of a quantity to the vertical gradient/profile of the mean value of that quantity, usually applied in the inertial layer of the ABL. In the horizontally homogeneous and stationary inertial sublayer, where the turbulent fluxes are approximately constant with the height, the profile of a variable *s* can be expressed as

$$\frac{\partial \bar{s}}{\partial x_j} = -\frac{s_*}{kz}\phi_s(\zeta) \text{ or } \frac{\partial \bar{s}}{\partial x_j} = -\frac{\overline{u_j's'}}{ku_*z}\phi_s(\zeta) \qquad (4.2.39)$$

The integrated form of the atmospheric profile for the variable *s* is given by

$$\bar{q} - \bar{q}_S = \frac{\overline{u_j's'}}{ku_*}\left[\ln\left(\frac{z - z_D}{z_{0S}}\right) - \Psi_S(\zeta)\right] \qquad (4.2.40)$$

with

$$\Psi_S(\zeta) = \int_{z_{0S/L}}^{\zeta} [1 - \phi_S(\zeta)]\frac{d\zeta}{\zeta} \qquad (4.2.41)$$

Thus, in the inertial sublayer the turbulent fluxes are expressed as functions of the average vertical gradients and universal functions which depend on the surface roughness (z_{0S}) and atmospheric stability.

Note that for the atmospheric inertial sublayer, the Monin-Obukhov similarity theory (1954) allows the eddy transfer coefficient K_s [see equation (4.2.10)] for any property (s) to be specified in terms of a range of flow properties (Garratt, 1992),

$$K_s = ku_*z/\phi_s(\zeta) \qquad (4.2.42)$$

where k is the van Karman's constant, u_* the friction velocity, z the height above the zero-plane displacement, $\phi_s(\zeta)$ the appropriated universal function, ζ (=z/L) the Monin-Obukhov stability parameter and L the Obukhov length.

MOST flux-profile relations for wind, temperature, and specific humidity are represented as, respectively,

$$\frac{\partial \bar{u}}{\partial z} = \frac{-\overline{w'u'}_s}{kzu_*}\phi_M(\zeta) \text{ or } \frac{\partial \bar{u}}{\partial z} = \frac{u_*}{kz}\phi_M(\zeta) \qquad (4.2.43)$$

$$\frac{\partial \bar{\theta}}{\partial z} = -\frac{\overline{w'\theta'}_s}{kzu_*}\phi_H(\zeta) \text{ or } \frac{\partial \bar{\theta}}{\partial z} = \frac{\theta_*}{kz}\phi_H(\zeta) \qquad (4.2.44)$$

$$\frac{\partial \bar{q}}{\partial z} = -\frac{\overline{w'q'}_s}{kzu_*}\phi_v(\zeta) \text{ or } \frac{\partial \bar{q}}{\partial z} = \frac{q_*}{kz}\phi_E(\zeta) \qquad (4.2.45)$$

where u is the horizontal wind speed, θ is the potential temperature, q is the specific humidity, u_* is friction velocity, θ_* is the temperature scale, and q_* is the humidity scale. $\phi_M(\zeta)$, $\phi_H(\zeta)$ and $\phi_E(\zeta)$ are the universal functions for momentum, sensible heat and water vapour, respectively. The universal functions, $\phi(\zeta)$, have a value of nearly 1 for neutral atmospheric stratification, range over $0 < \phi(\zeta) < 1$ for unstable stratification, and $\phi(\zeta) > 1$ for stable stratification. For strong stability ($\zeta >> 1$) the universal functions are nearly constant.

The integrated profiles with respect to height can be written as extensions of the logarithmic profiles to non-neutral conditions. When the surface values ($u=0$, $\theta=\theta_s$ and $q=q_s$) are used, these profiles can be written as (Brutsaert, 1982; Arya, 2001)

$$\bar{u} = \frac{\overline{w'u'}_s}{ku_*}\left[\ln\left(\frac{z - z_D}{z_{0M}}\right) - \Psi_M(\zeta)\right] \qquad (4.2.46)$$

$$\bar{\theta}_s - \bar{\theta} = \frac{\overline{w'\theta'}_s}{ku_*}\left[\ln\left(\frac{z - z_D}{z_{0H}}\right) - \Psi_H(\zeta)\right] \qquad (4.2.47)$$

$$\bar{q}_s - \bar{q} = \frac{\overline{w'q'}_s}{ku_*}\left[\ln\left(\frac{z - z_D}{z_{0E}}\right) - \Psi_E(\zeta)\right] \qquad (4.2.48)$$

where z_{0M}, z_{0H} and z_{0E} are the roughness lengths for momentum, sensible heat and water vapour (defined on the basis of logaritmic profile). Ψ_M ,Ψ_H and Ψ_E are universal functions, for momentum, heat and vapour, related to the local universal funtions ϕ_M , ϕ_H and ϕ_E , respectively, as

$$\Psi_M(\zeta) = \int_{z_{0M/L}}^{\zeta} [1 - \phi_M(\zeta)] \frac{d\zeta}{\zeta}$$
$$\Psi_H(\zeta) = \int_{z_{0H/L}}^{\zeta} [1 - \phi_H(\zeta)] \frac{d\zeta}{\zeta} \qquad (4.2.49)$$
$$\Psi_E(\zeta) = \int_{z_{0E/L}}^{\zeta} [1 - \phi_E(\zeta)] \frac{d\zeta}{\zeta}$$

The values of ζ [=(z-zd)/L] in all the above equations must be large as compared to (z_{0M}/L). Specially, over a very rough surface these relations cannot be expected to be valid if this condition is not satisfied (Brutsaert, 1982).

Equations (4.2.46) - (4.2.48) can be written in the form:

$$\tau = ku_*\rho \frac{\bar{u}}{\left[\ln\left(\frac{z - z_D}{z_{0M}}\right) - \Psi_M(\zeta)\right]} \qquad (4.2.50)$$

$$Q_H = ku_*\rho c_p \frac{\bar{\theta}_s - \bar{\theta}}{\left[\ln\left(\frac{z - z_D}{z_{0H}}\right) - \Psi_H(\zeta)\right]} \qquad (4.2.51)$$

$$E = ku_*\rho \frac{\bar{q}_s - \bar{q}}{\left[\ln\left(\frac{z - z_D}{z_{0E}}\right) - \Psi_E(\zeta)\right]} \qquad (4.2.52)$$

Flux- profile relations, e.g. (4.2.40), allow the fluxes in the inertial sublayer to be determined from measurements at some height z.

Under neutral conditions, when $|\zeta| \ll 1$ (but $z-z_D \gg z_{0M}$), the universal functions become (Brutsaert, 1982; Beljaars, 1992)

$$\phi_M = \phi_H = \phi_E = 1 \qquad (4.2.53)$$

and

$$\Psi_M = \Psi_H = \Psi_H = 0 \ , \quad \zeta = 0 \qquad (4.2.54)$$

so, the flux-profile relations turn into logarithmic profiles. The universal functions are also termed stability correction funtions.

The forms of the universal functions are not given by the Monin–Obukhov theory, but must be determined.

Analitycal forms for the universal functions

There is no consensus on the form the analytical universal functions, $\phi(\zeta)$, should take. The forms used have been obtained from experimental data. An overview of these formulations can be found in, for example, (Dyer, 1974), (Brutsaert, 1982), and (Hogstrom, 1988). The generally accepted forms of the universal stability correction functions for momentum and heat, $\phi_M(\zeta)$ and $\phi_H(\zeta)$, are defined on the basis of various micrometeorological experiments (Arya, 2001) as

$$\text{Unstable conditions, } \zeta<0 \quad \begin{cases} \phi_M = (1-\beta_M\zeta)^{-1/4} \\ \phi_H = \alpha_H(1-\beta_H\zeta)^{-1/2} \\ \phi_v = \alpha_E(1-\beta_E\zeta)^{-1/2} \end{cases} \qquad (4.2.55)$$

$$\text{Stable conditions, } \zeta\geq 0 \quad \begin{cases} \phi_M = 1+\beta_M\zeta \\ \phi_H = \alpha_H + \beta_H\zeta \\ \phi_E = \alpha_E + \beta_E\zeta \end{cases} \qquad (4.2.56)$$

where α_H, α_E, β_M, β_H and β_E are empirical constants, for momentum, heat and vapour flux-profile functions, respectively.

The vertically integrated forms of the stability functions for momentum, $\Psi_M(\zeta)$, heat, $\Psi_H(\zeta)$, and vapour, $\Psi_E(\zeta)$, expressed using the equations **(4.2.55)** and **(4.2.56)** have the following form (Paulson, 1970; Businger *et al.*, 1971; Dyer, 1974; Brutsaert, 1982; Arya, 2001):

$$\zeta<0 \quad \begin{cases} \Psi_M(\zeta) = 2\ln\left(\frac{1+x}{2}\right) + \ln\left(\frac{1+x^2}{2}\right) - 2\tan^{-1}(x) + \frac{\pi}{2} \\ \Psi_H(\zeta) = 2\ln\left(\frac{1+x^2}{2}\right) \\ \Psi_E(\zeta) = 2\ln\left(\frac{1+x^2}{2}\right) \end{cases} \qquad (4.2.57)$$

where $x = (1-\beta\zeta)^{1/4}$ (4.2.58)

$$\zeta\geq 0 \quad \begin{cases} \Psi_M(\zeta) = -\beta_M\zeta \\ \Psi_H(\zeta) = -\beta_H\zeta \\ \Psi_E(\zeta) = -\beta_E\zeta \end{cases} \qquad (4.2.59)$$

where β represents β_M, β_H, or β_v, depending on the flux-profile functions (for momentum, heat or vapour, respectively) they are related to. Although the log-linear

function appears to be suitable to describe moderately-stable conditions when $0< \zeta<1$, there is still no agreement on the values of its parameters and on the form of the ϕ functions for very stable conditions, when $\zeta>1$ (Brutsaert, 1982; Beljaars and Holtslag, 1991).

Many empirical formulations have been proposed for the stability correction functions. In the present study, following Voogt and Grimmond (2000), the general form of the expressions for stability functions given by equations (4.2.55)-(4.2.59) (Arya, 2001) is assumed. The equations used to model the surface sensible heat flux are the vertically integrated forms of the universal stability functions, Ψ_M for momentum and $\Psi_H(\zeta)$ for heat, presented in Table 5.1 of Chapter 5. The Hogstrom (1988)- modified Dyer (1974) formulation is used for $\Psi_H(\zeta)$, and for $\Psi_M(\zeta)$ under unstable atmospheric conditions; and the Ulden and Holtslag (1985) formulation is used for Ψ_M under moderately-stable conditions.

Chapter 5. Formulation for a model of surface sensible heat flux for Greater Manchester

In this chapter a description of the formulation of the numerical model of surface sensible heat flux for Greater Manchester is given. In section 5.1 a summary of the model is presented. The bulk transfer equation for surface sensible heat flux used in the model is discussed in section 5.2, and the particular stability correction functions adopted here are specified in section 5.3. Section 5.4 explains the methods that will be implemented in the present study to determine the surface roughness parameters necessary to model the surface sensible heat flux. In section 5.5 results of model sensitivity tests, for a range of typical wind speed and temperature input values, are discussed. In this section, modelling experiments on spatial variations of urban roughness, based on some synthetic situations, are also discussed.

5.1 Model overview

In this chapter a numerical scheme, to be used in the present research, is presented, based upon several published systems, principally Voogt and Grimmond (2000) and Grimmond and Oke (1999a), and developed to derive fields of surface sensible heat flux for a range of wind speeds and temperatures over an urban area.

The model is formulated initially for Greater Manchester (**Figure 5.1**), in a study area of 24km x 24km, with a grid resolution of 1km x 1km, where the bulk equations will be used and the model parameters are specified as averages over each grid square.

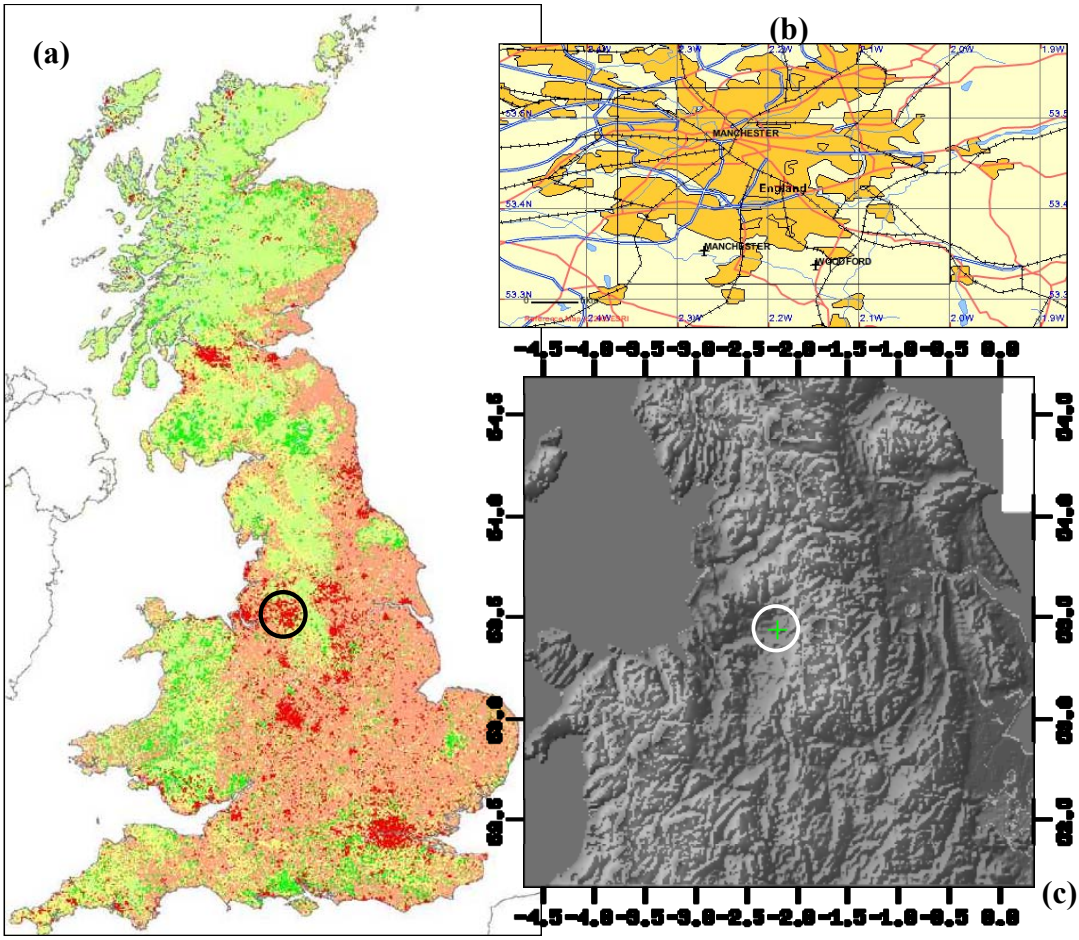

Figure 5.1- *Geographical location of Greater Manchester.* ***(a) (Left)*** *Image of Major Land Cover Types for Great Britain [from COoRdinate INformation on the Environment, CORINE, Land Cover European Environment Agency, http://www.eea.europa.eu/, 2002]. [Red] indicates urban fabric, natural vegetated areas are [green], the rest are agro-foretry areas mainly.* ***(b) (Top- right)*** *Image of Land Use; [dark yellow] area represents populated place; the black rectangle limits the area of interest, which has 24x24 km^2 and is centred at the co-ordinates (-2.18, 53.43) [from NIMA- National Imagery and Mapping Agency, U.S. Geological Survey, http://www.usgs.gov/ 2002].* ***(c) (Bottom- right)*** *Image generated from Digital Terrain Elevation Data [NIMA- National Imagery and Mapping Agency, U.S. Geological Survey, http://www.usgs.gov/ 2002].*

The surface sensible heat flux, Q_H, over the urban area is calculated by a resistance-type formulation using the difference between the satellite radiometric surface temperature, T_R, and air temperature, T_a, (Voogt and Grimmond, 2000):

$$Q_H = \rho \; c_p \frac{(T_R - T_a)}{r_H} \qquad (5.1.1)$$

$$r_H = \frac{1}{k\,u_*}\left[\ln\left(\frac{z_S - z_D}{z_{0M}}\right) - \Psi_H\right] + \frac{1}{k\,u_*}\ln\left(\frac{z_{0M}}{z_{0H}}\right) \qquad (5.1.2)$$

$$L = \frac{-u_*^{\,3}\rho c_p T_a}{kgQ_H} \qquad (5.1.3)$$

$$u_* = k\,u\left[\ln\left(\frac{z_S - z_D}{z_{0M}}\right) - \Psi_M\right]^{-1} \qquad (5.1.4)$$

Here, the parameter g (= 9.8 m s^{-2}) is the acceleration of gravity, ρ (=1.2 kg m^{-3}) is the air density, c_p (=1004 J kg^{-1} K^{-1}) is the specific heat of the air at constant pressure, k (= 0.4) is the von Karman's constant. In this formulation, Q_H is the surface sensible heat flux, r_H is the resistance to heat transfer from a surface at the temperature T_R to an atmospheric level z_S at the temperature T_a, u is the wind speed at the level z_S, L is the Monin-Obukhov length, u_* is the friction velocity, z_D is the zero-plane displacement length, z_{0M} is the roughness length for momentum, z_{0H} is the roughness length for heat, Ψ_M and Ψ_H are the stability correction functions for momentum and heat, respectively.

Stability corrections for momentum and heat, Ψ_M and Ψ_H, used in our model are shown in section 5.3. The Hogstrom (1988)- modified Dyer (1974) equations are used to calculate Ψ_M, when L<0, and Ψ_H. Ulden and Holtslag (1985) equation is used to calculate Ψ_M, when L>0.

Q_H, u_* and L (or the stability functions) are determined from equations (5.1.1)- (5.1.4) solved by an iterative procedure.

Input meteorological variables used in the model are the surface and air temperatures, T_R and T_a, and the wind velocity, u. T_a and u are typically measured several metres above the surface, at the measurement height, z_S, in the inertial sub-layer where the Monin-Obukhov Similarity Theory is valid. This will form the basis of the model to be used later to explore the impact of the heterogeneity of the urban canopy.

As discussed in section **4.1.1**, a useful approach in describing an urban energy budget is to consider a near-surface active layer or control volume, whose top is set at, or above, the roof level and its base at the depth of zero net ground heat flux over the chosen period of interest (Oke, 1987). In our case, the top is set at the measurement height z_S, in the inertial sub-layer.

The model input roughness parameters are the mean surface elements height, z_H, and the frontal area index, λ_F. For each domain cell, z_H and λ_F are calculated from the area-weighted averages of the correspondent values for each land use category present. Basically, over built areas z_H and λ_F are derived from analysis of surface form according to the methodology reported by Grimmond and Oke (1999a) (section **5.4**), while for natural surfaces these roughness parameters are estimated using reference tables given in the literature (Grimmond and Oke, 1999a, Wieringa, 1993, Brutsaert, 1982, Grimmond *et al*, 1998). The zero-plane displacement length, z_D, and the roughness length for momentum, z_{0M}, are estimated as a function z_H and λ_F, using Raupach's (1994, 1995) morphometric method [equations (5.4.4)- (5.4.6)]. The roughness length for heat, z_{0H}, is determined as a function of z_{0M}, using the formulation proposed by Brutsaert (1982) for bluff-rough surfaces [equations (5.4.7)- (5.4.8)]. These formulations are presented in section **5.4**.

To implement the model, besides the meteorological data, surface morphology data need to be obtained for the study area. A surface morphologic database for Greater Manchester has being developed from analysis of digital elevation data, aerial photography, maps and field surveys. The roughness parameters, z_H and λ_F, were estimated from digitised georeferenced data of the surface elements provided by the Environment Agency and the Cities Revealed User Group. This will be detailed in Chapter 6.

5.2 Bulk trasfer equation for surface sensible heat flux

Bulk transfer equation- aerodynamic surface temperature approach

The turbulent transport of sensible heat between a surface and the atmosphere can be parameterised by a resistance-type formulation. The local-scale surface sensible heat flux, Q_H, can be calculated from the bulk transfer equation (Voogt and Grimmond, 2000)

$$Q_H = \rho \; c_p \frac{(T_0 - T_a)}{r_{ah}} \; [= C_H \; u \, (T_0 - T_a)] \qquad (5.2.1)$$

where

$\rho \equiv$ air density (=1,2 kg m^{-3})

$c_p \equiv$ specific heat of the air, at constant pressure (=1004 J kg^{-1} K^{-1})

$C_H \equiv$ exchange coefficient for heat

$u \equiv$ wind speed at the level z_s

$T_a \equiv$ air temperature at the level z_s

$T_0 \equiv$ aerodynamic surface temperature (temperature extrapolated, via the logarithmic profile, down to a surface that is at the height $z_D + z_{0H}$).

$r_{ah} \equiv$ aerodynamic resistance for heat (resistance from a height $z_D + z_{0H}$, having an aerodynamic temperature T_0 , to the height z_s in the lower atmosphere)

$z_D \equiv$ zero-plan displacement length

$z_{0H} \equiv$ roughness length for heat

$z_s \equiv$ level above the surface, at the inertial layer, where the wind speed, u, and the air temperature, T_a, are measured.

Figure 5.2 represents schematically the roughness lengths for momentum and heat and the resistances between different levels of the surface layer.

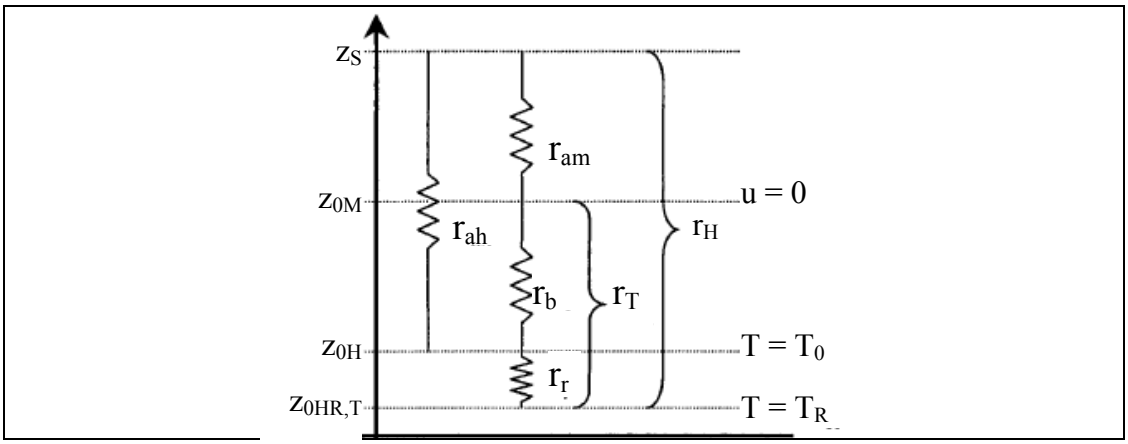

Figure 5.2*- Cross-sectional representation of the surface layer showing roughness lengths for momentum and heat and the resistances between different levels. The zero-plane displacement level is omitted for simplicity. For some surfaces, $T = T_0 = T_R$ may be possible. Symbols are defined in the text. (After Voogt and Grimmond, 2000).*

The classical aerodynamic resistance to heat transfer, r_{ah}, is given by Verma (1989) (compare to equation 4.2.42 of section 4.2.5):

$$r_{ah} = r_{am} + r_b = \frac{1}{k\,u_*}\left[\ln\left(\frac{z_S - z_D}{z_{0M}}\right) - \Psi_H\right] + \frac{1}{k\,u_*}\ln\left(\frac{z_{0M}}{z_{0H}}\right) \qquad (5.2.2)$$

where r_{ah} is the aerodynamic resistance for heat, r_{am} is the aerodynamic resistance for momentum, r_b is the bulk aerodynamic excess resistance; z_{0M} is the roughness length

for momentum [$z_D + z_{0M}$ is the level at which the wind speed extrapolates to zero via the logarithmic wind profile]; k (= 0.4) is the von Karman's constant, Ψ_M (ζ) and Ψ_H (ζ) are the stability correction functions for momentum and heat, and the Monin-Obukov variable ζ is given by $\zeta = (z_S - z_D)/L$. The Monin-Obukhov length, L, and the friction velocity, u_*, presented in Chapter 4, are expressed by equations (5.1.3) and (5.1.4) respectively.

Note that McIlveen (1992, 1998) gives the following relationship

$$\Delta\theta = \frac{Q_H}{\rho c_p k u_*} \ln(z_2/z_1) \qquad (5.2.3)$$

where $\Delta\theta$ is the lapse of potential temperature between heights z_1 and z_2. Taking typically values of u_* (0.3 ms^{-1}) and Q_H (100 Wm^{-2}) (corresponding to fairly strong surface heating), it follows that the potential temperature lapse between the base of the surface boundary layer and the screen level (say heights 1 cm and 1.5m, respectively) is 5 ^oC. For typically values, taking the surface temperature, T_S, and the screen temperature, T_a, one can consider the following approximate formulation (Fox, 1998).

$$T_a = T_S - 0.05 Q_H \qquad (5.2.4)$$

Bulk transfer equation- radiometric surface temperature approach

To implement equation (5.2.1), both the surface temperature and the roughness length for heat are needed, which are difficult to measure. Usually a radiometric surface temperature, T_R, is measured rather than the aerodynamic surface temperature, T_0, so that the sensible heat flux can be calculated (Stewart *et al.*, 1994) by

$$Q_H = \rho\ c_p \frac{(T_R - T_a)}{r_H} \qquad (5.2.5)$$

Here the resistance r_H is given by

$$r_H = r_{ah} + r_r \qquad (5.2.6)$$

where r_H is resistance to heat transfer from a surface at T_R and r_r is excess of resistance.

Under unstable conditions, $T_R > T_0$, frequently; as a result, this requires that $r_H > r_{ah}$ (Voogt and Grimmond, 2000). This can be represented algebraically by adding an excess resistance to r_{ah}, namely, $r_H = r_{ah} + r_r$ (**Figure 5.2**).

The parameter kB^{-1}

The resistance r_b which is defined by equation (5.2.2) accounts for the fact that the transfer of heat to, or from, a surface encounters more aerodynamic resistance than does momentum. The excess resistance for heat is expressed commonly in terms of the dimensionless parameter kB^{-1}, which is a term of equation (5.2.2). The aerodynamic definition is

$$kB^{-1} = \ln\left(\frac{z_{0M}}{z_{0H}}\right) \qquad (5.2.7)$$

$$r_b = B^{-1}u_*^{-1} \qquad (5.2.8)$$

Typically, formulation (5.2.5) is used rather than (5.2.1). Replacing the term r_{ah} in equation (5.2.6) by the value presented in equation (5.2.2) it is possible to write

$$r_H = r_{am} + r_b + r_r = r_{am} + r_T \qquad (5.2.9)$$

$$r_H = \frac{1}{k\,u_*}\left[\ln\left(\frac{z_s - z_D}{z_{0M}}\right) - \Psi_H\right] + \frac{1}{k\,u_*}\ln\left(\frac{z_{0M}}{z_{0HR,T}}\right) \qquad (5.2.10)$$

where r_T represents the resistance between z_{0M} and the surface. Furthermore, Ψ_M and Ψ_H, which should be included in r_b, are rarely incorporated (Voogt and Grimmond, 2000). Thus, the excess of resistance for heat expressed in terms of kB^{-1} is redefined as

$$kB^{-1}\Big|_{R,T} = \ln\left(\frac{z_{0M}}{z_{0HR,T}}\right) \qquad (5.2.11)$$

$$r_T = B^{-1}\Big|_{R,T} u_*^{-1} \qquad (5.2.12)$$

Here the subscripts R and T make explicit the dependence of the results on the use of radiometric temperatures and the method for calculating the resistance.

In the present model for estimating the surface sensible heat flux, the radiometric surface temperature approach is used, which is expressed in terms of equations (5.2.5) and (5.2.10), the Monin-Obukhov length, L, and the friction velocity, u_*. However, for, simplicity the subscripts R and T that express the dependence of the results on the use of radiometric temperatures and the method for calculating the resistance, will be omitted; thus the symbols z_{0H} and kB^{-1} will be used instead of $z_{0HR,T}$ and $kB^{-1}\Big|_{R,T}$. This formulation is summarized in the overview of section **5.1** by equations (5.1.1)-(5.1.4).

5.3 Stability correction functions

In the present study, following Voogt and Grimmond (2000), the general form of the expressions for stability functions given by equations (4.2.55)- (4.2.59) is assumed. The equations used to model the surface sensible heat flux are the vertically integrated forms of the universal stability functions, Ψ_M for momentum and $\Psi_H(\zeta)$ for heat, presented in Table 5.1, where $\zeta=(z_S-z_D)/L$. The Hogstrom (1988)- modified Dyer (1974) formulation is used for $\Psi_H(\zeta)$, and for $\Psi_M(\zeta)$ when ζ <-0.1; for Ψ_M when $0.1< \zeta < 1$, the Ulden and Holtslag (1985) formulation is used. The corresponding local stability functions, $\phi_M(\zeta)$ and $\phi_H(\zeta)$, are also shown. Near neutral criteria are defined here as $|\zeta| < 0.1$, being $\phi_M= 1$, $\phi_H= 0.95$ and $\Psi_M= \Psi_M = 0$.

Table 5.1 *- Vertically integrated forms of the universal stability functions for momentum and for heat, $\Psi_H(\zeta)$ and for $\Psi_M(\zeta)$, used in the model for surface sensible heat flux. The corresponding local stability functions, $\phi_M(\zeta)$ and $\phi_H(\zeta)$, are also shown. In these formulations it is assumed that k=0.4.*

Moderately-stable conditions, $0.1<\zeta<1$		
$\phi_M = 1+5\zeta$ (5.3.1)	$\Psi_M = -5\zeta$ (5.3.2)	Ulden and Holtslag (1985)
$\phi_H = 0.95+4.5\zeta \Leftrightarrow$ $\phi_H = 0.95(1+4.74)\zeta$ (5.3.3)	$\Psi_H = -4.74\zeta$ (5.3.4)	Hogstrom (1988)- modified Dyer (1974)
Unstable conditions, ζ< -0.1		
$\phi_M = (1-15.2\zeta)^{-1/4}$ (5.3.5)	$\Psi_M(\zeta) = 2\ln\left(\frac{1+x}{2}\right)+\ln\left(\frac{1+x^2}{2}\right)-2\tan^{-1}(x)+\frac{\pi}{2}$ $x = (1-15.2\zeta)^{1/4}$ (5.3.6)	
$\phi_H = 0.95(1-15.2\zeta)^{-1/2}$ (5.3.7)	$\Psi_H(\zeta) = 2\ln\left(\frac{1+x^2}{2}\right)$ $x = (1-15.2\zeta)^{1/4}$ (5.3.8)	
Near neutral conditions, $|\zeta| < 0.1$		
$\phi_M = 1$ (5.3.9)	$\Psi_M=0$ (5.3.10)	
$\phi_H = 0.95$ (5.3.11)	$\Psi_H= 0$ (5.3.12)	

Note that when using Hogstrom (1988)- modified Dyer (1974) stability equations, the following aspects must be taken into consideration. (i) The universal funtions for momentum and heat have been determined for the stability range $-3 < |\zeta| < 1$ (Hogstrom,1988). (ii) The stability function analysis criteria were: reasonably steady-state conditions; $u_* \geq 0.1$ m/s, for the analysis of universal funtion for momentum; $u_* \geq 0.1$ m/s and $|Q_H| \geq 10$ W/m^2, for the analysis of universal funtions for heat (Hogstrom,1988).

5.4 The surface roughness parameterization- z_D, z_{0M} and z_{0H}

5.4.1 Overview

Cities have the largest values of zero-plane displacement and roughness length values compared to other surfaces (e.g.,Wieringa, 1993, Table VIII). As discussed by Grimmond and Oke (1999a) this fact has major implications for surface drag, momentum transport, the scales and intensity of turbulence, mass convergence (uplift) and divergence (subsidence). These phenomena affect the depths of the roughness sublayer, the shape of the wind profile and the type of flow found in the urban canopy layer (Angell *et al.,* 1973; Auer, 1981; Landsberg, 1981; Cermak *et al.,* 1995). Hence, accurate knowledge of the aerodynamic characteristics of cities is vital to describe, model, and forecast the behavior of urban winds and turbulence at all scales. Unfortunately, the ability to assign values of zero-plane displacement (z_D) and roughness length (z_{0M}) remains problematic. Two classes of approach are available:

1) *micrometeorological* (or *anemometric*) methods that use field observations of wind or turbulence to estimate aerodynamic parameters included in theoretical relations derived from the logarithmic wind profile, and;

2) *morphometric* (or *geometric*) methods that use algorithms that relate aerodynamic parameters to measures of surface morphometry.

Micrometeorological methods have the advantage that the characteristics of the surface do not need to be specified (the roughness elements can consist of any mix and be arranged in any pattern). The greatest disadvantages are the expense and difficulty involved in obtaining and operating a field site (especially installing a tower in a city to make the measurements), and the fact that, while in principle results can be obtained

for any wind direction, in practice appropriate conditions may not occur for all wind directions (e.g., Grimmond *et al.,* 1998).

Morphometric methods have the advantage that values can be implemented without need of tall towers and instrumentation. Further, if a spatially continuous database of the distribution of roughness elements is available then values can be computed for any wind direction surrounding the site of interest. They do, however, have the disadvantage that most are based on empirical relations derived from wind tunnel work that concern idealized flows over simplified arrays of roughness elements. In these simulations the flow is often relatively constant in direction, typically normal to the face of the surface elements, and the elements arrays are often regularly spaced (in rows or a staggered grid). These conditions differ from those in real cities, where wind direction is ever changing and, even if the street pattern is relatively regular, the size and shape of individual roughness elements (mainly buildings and trees) are not.

According to Grimmond and Oke (1999a), given the errors involved in *both* measurement and morphometric analysis and the lack of an overall standard, it is not possible to indicate which class of methods is more accurate. However it is noted that morphometric methods are relatively simple, are cost-effective, and yield values for all directions around a site and are therefore attractive. Grimmond and Oke (1999a) suggest that, if measurement is considered, turbulence-based approaches are favoured over those involving multilevel profiles of anemometers. On the other hand, if morphometric analysis is envisaged, the authors recommendations concerning which morphometric methods should be used include considerations such as

- ease of implementation (input requirements),
- applicability across the full range of typical urban morphometries,
- choice of descriptor of surface form (roughness density), and
- conformity with the suggested curves and envelopes of reasonableness drawn in **Figure 5.3**. **Figure 5.3** from Grimmond and Oke (1999a) shows a conceptual representation of the relation between height-normalized values of zero-plane displacement (z_D/z_H) and the packing density of roughness elements using the (a) plan area index λ_P and (b) frontal area index λ_F to describe density.

Moreover Grimmond and Oke (1999a) suggest that, if neither measurements nor morphometric analysis can be conducted, first-order estimates can be obtained from tables of typical values (section **5.4.3**).

In the present study over Greater the Manchester urban area a morphometric approach is used (sections **5.4.2**), and a surface data base for the morphologic parameters of interest is developed (see Chapter 6).

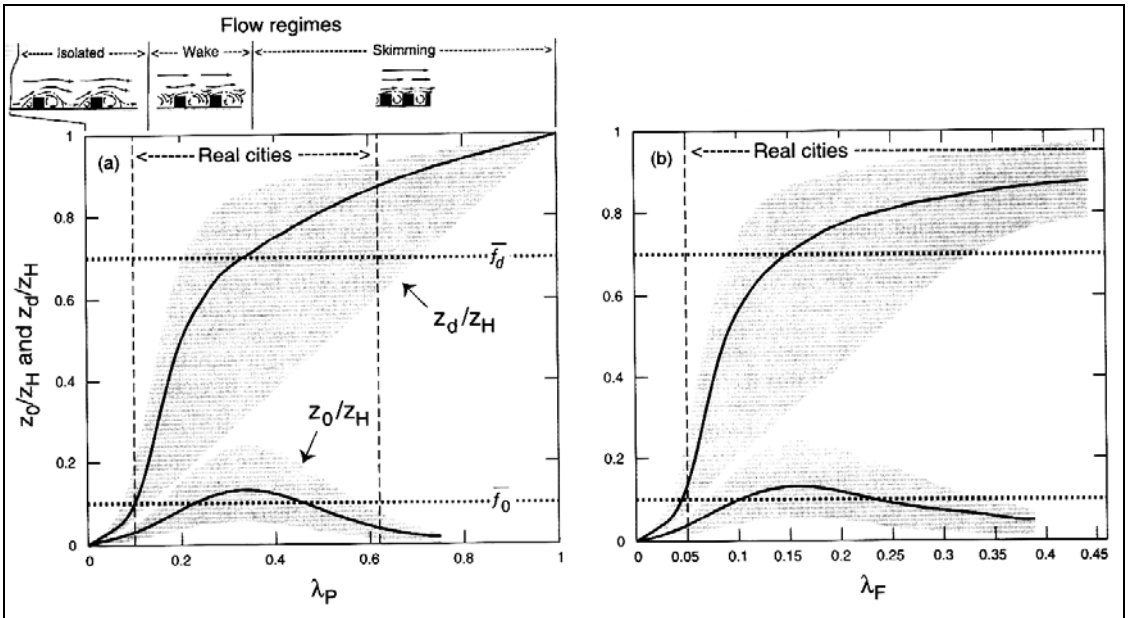

***Figure 5.3**- Relation between height-normalized values of zero-plane displacement and roughness length for momentum, and the packing density of roughness elements. Conceptual representation of the relation between height-normalized values of zero-plane displacement, z_D/z_H [z_d/z_H], and roughness length for momentum, z_{0M}/z_H [z_0/z_H], and the packing density of roughness elements (a) using λ_P and (b) using λ_F to describe density. Shaded areas are the reasonable zones or envelopes referred to in the text. Mean values of observed for f_d ($\overline{f_d} = \overline{z_D/z_H} = 0.67$) and f_0 ($\overline{f_0} = \overline{z_{0M}/z_H} = 0.10$) over land surfaces are also represented. The vertical dashed lines show the range of real-city roughness densities ($0.1 < \lambda_P < 0.62$, $0.05 < \lambda_F < 0.47$). Limits of flow regimes are schematised along the top. [From Grimmond and Oke, 1999a.]*

5.4.2 Zero-plane displacement length, z_D, and roughness length for momentum, z_{0M} - the Raupach's (1994) morphometric method

The dependence of the zero-plane displacement length (z_D) and roughness length for momentum (z_{0M}) on the size, shape, density, and distribution of surface elements has been studied using wind tunnels, analytical investigations, numerical modeling, and field observation (see reviews by Wieringa 1993; Bottema 1995a, b; 1997). Grimmond and Oke (1999a) considered a list of morphometric methods that, although not exhaustive, includes those commonly used plus three recently developed methods (Raupach, 1994; Bottema, 1995a–c; Macdonald *et al*., 1998). The methods differ in terms of the attributes of the roughness elements and/ or the weighting functions used. The authors outlined the morphometric methods and their similarities and differences, and conducted a sensitivity analysis of each. The dimensions used to characterize the surface geometry in the different methods are defined in **Figure 5.4**.

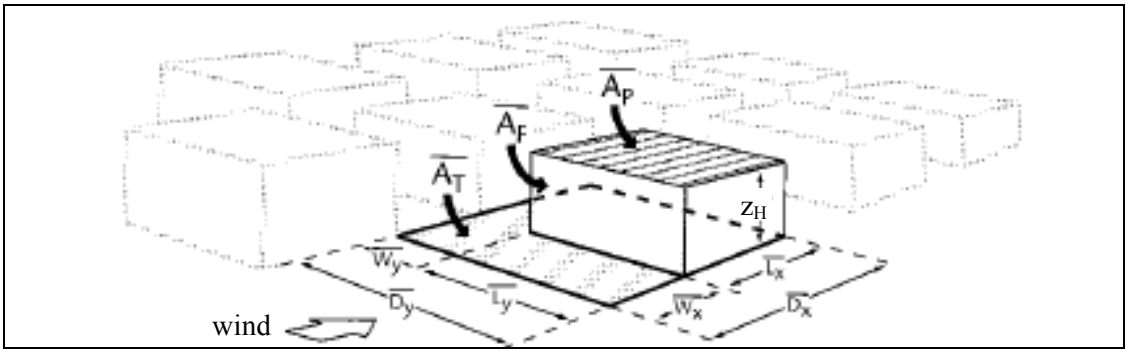

Figure 5.4*- Definition of surface dimensions used in morphometric analysis. The element portrayed has the characteristic mean dimensions, spacing, and total lot area (A_T) of the urban array. Using these measurements, the following nondimensional ratios are defined to characterise the morphometry:*

$\overline{\lambda_P} = \overline{A_P}/\overline{A_T} = \overline{L_x}\,\overline{L_y}/\overline{D_x}\,\overline{D_y}$, $\overline{\lambda_F} = \overline{A_F}/\overline{A_T} = \overline{z_H}\,\overline{L_y}/\overline{D_x}\,\overline{D_y}$, $\overline{\lambda_S} = \overline{z_H}/\overline{W_x} = \overline{z_H}/\overline{D_x} - \overline{L_x}$, and $\overline{\lambda_C} = \left[\overline{L_x}\,\overline{L_y} + 2\left(\overline{L_y}\,\overline{z_H}\right) + 2\left(\overline{L_x}\,\overline{z_H}\right)\right]/\overline{D_x}\,\overline{D_y}$ (a*fter Grimmond and Oke, 1999a).*

Figure 5.4 illustrates surface dimensions used in morphometric analyses. Based in these dimensions, the following nondimensional ratios are defined to characterise the morphometry: plan area index, λ_P, frontal area index, λ_F, street canyon aspect ratio, λ_S, and complete aspect (or three-dimensional) aspect ratio, λ_C. Note that, although in **Figure 5.4** the surface roughness element is drawn as building like, the

surface element is generic, representing all obstacles relevant to airflow. Similarly, the concept is not limited to a grid array. It could include scattered trees, differently shaped houses, and winding streets that are more typical of real cities.

The morphometric methods analised by Grimmond and Oke (1999a) can be divided into three sets: a simple height-based ‘‘rule of thumb’’ and two sets distinguished by the type of aspect ratio (non-dimensional area) used to describe the active surface presented to the flow. One of these sets uses the fraction of the plan surface area covered by roughness elements (λ_P), the other uses the frontal area index (λ_F) of the elements as ‘‘seen’’ by the oncoming wind.

The most common morphometric approach is a simple "rule of thumb", which assumes that z_D and z_{0M} are simply related to the mean height of the surface elements, $\overline{z_H}$:

$$z_D = f_d \overline{z_H} \qquad (5.4.1)$$

and

$$z_{0M} = f_0 \overline{z_H} \qquad (5.4.2)$$

where f_d and f_0 are empirical coefficients derived from observation. Garratt (1992) finds $f_d \sim 0.67$ and $f_0 \sim 0.10$ to be good overall mean values for land surfaces. Raupach *et al.* (1991) note that surveys of measured coefficients give $f_d \sim 0.64$ and $f_0 \sim 0.13$ for field crops and grass canopies and $f_d \sim 0.8$ and $f_0 \sim 0.06$ for forests.

Grimmond and Oke (1999a) found that the very simple "rule of thumb" works relatively well for both z_D and z_{0M}. However, because its formulation includes no recognition of density it cannot respond to the effects of packing. This deficiency becomes increasingly problematic for z_D because of the anticipated slope of the f_d curve with density (**Figure 5.3**). This is less of a problem for z_{0M} because of the behavior of the f_0 curve with density; but the formulation increasingly overestimates roughness at very high and very low densities and fails to pick up the roughness peak. Grimmond and Oke (1999a) recommend values of $f_0 \sim 0.1$ in urban areas, and for f_d values of 0.5 for low- density, 0.6 for medium- density, and 0.7 for high- density urban sites. The values of $f_d \sim 0.7$ and $f_0 \sim 0.1$ are sketched in **Figure 5.3**.

In the present study the surface roughness is described using the height of the surface roughness elements, $\overline{z_H}$, and frontal area index, $\lambda_F = \overline{A_F}/\overline{A_T}$, where $\overline{A_F}$ is the mean area of the surface elements facing the wind and $\overline{A_T}$ is the mean area of the

elements array (see **Figure 5.4**). For simplicity, the plan area index $\lambda_P = \overline{A_P}/\overline{A_T}$, where $\overline{A_P}$ is the mean plan horizontal area occupied by elements, can be used as a measure of density. The frontal area index, which combines mean height, breadth, and density of roughness elements, is defined as (see **Figure 5.4**).

$$\lambda_F = \overline{L_y}\,\overline{z_H}\rho_{el} = \overline{L_y}\,\overline{z_H}/(\overline{D_y}\,\overline{D_x}) \qquad (5.4.3)$$

where $\overline{L_y}$ is the mean breadth of the roughness elements perpendicular to the wind direction; ρ_{el} is the density [number (n) of roughness elements per unit area (ρ_{el} = n/A_T)]; $\overline{D_x}$ is the average inter-element spacing between element centroids, in the alongwind direction; $\overline{D_y}$ is the average inter-element spacing between element centroids, in the crosswind direction. Typical values of frontal area index, λ_F, are in the range 0.1- 0.25 for crops, about 1-10 for forests (Raupach *et al.* 1991), and 0.1-0.3 for urban areas, with individual sectors varying from 0.06 to 0.4 (Grimmond and Oke, 1999a).

In the present model of surface sensible heat flux, the zero-plane displacement length, z_D, and the roughness length for momentum, z_{0M}, are calculated as a function of the height of the surface roughness elements, z_H, and frontal area index, λ_F, using Raupach's (1994, 1995) method, which is one of the morphometric approaches recommended by Grimmond and Oke (1999a) for urban areas,

$$\frac{z_D}{\overline{z_H}} = 1 + \left\{ \frac{\exp\left[-\left(c_{d1}2\lambda_F\right)^{0.5}\right] - 1}{\left(c_{d1}2\lambda_F\right)^{0.5}} \right\} \qquad (5.4.4)$$

$$\frac{z_{0M}}{\overline{z_H}} = \left(1 - \frac{z_d}{\overline{z_H}}\right)\exp\left(-k\frac{u}{u_*} + \psi_h\right) \qquad (5.4.5)$$

Where

$$\frac{u_*}{u} = \min\left[\left(c_S + c_R\lambda_F\right)^{0.5}, \left(\frac{u_*}{u}\right)_{max}\right] \qquad (5.4.6)$$

and

$\psi_h \equiv$ roughness sublayer influence function,

$u \equiv$ wind speed

$u_* \equiv$ friction velocity

$c_S \equiv$ drag coefficient for the substrate surface at height z_H in the absence of roughness elements

c_R ≡ drag coefficient of an isolated roughness element mounted on the surface at height

z_H ≡ surface elements height

c_{d1} ≡ a free parameter.

Typical values specified by Raupach (1994), and used in our model, are: c_S=0.003 , c_R=0.3, $(u^*/u)_{max}$ = 0.3, ψ_h = 0.193, c_{d1} = 7.5. Raupach (1994) discusses the errors likely to be associated with these values and Bottema (1995b) considers their appropriateness in urban studies. Note that Raupach's (1994, 1995) method was initially designed for random building arrangements and sparse random canopies.

Raupach *et al.* (1991) note that complete specification of the roughness is likely to require other aspect ratios in addition to λ_F (for a further discussion see Grimmond and Oke, 1999a).

According to Grimmond and Oke (1999a), Raupach's (1994, 1995) method is one of the best three morphometric methods currently available. Input requirements are relatively simple and the method applies across the full range of roughness densities. The estimates of z_D and z_{0M} generated for North American cities mainly fall within the limits of acceptance (**Figure 5.3**) proposed by Grimmond and Oke (1999a).

The values of the roughness parameters, such as mean surface elements height (z_H) and frontal area index (λ_F), necessary to model the surface sensible heat flux over the Greater Manchester study domain, are summarized in **Table 6.2** of Chapter 6, for each land-use category. These include built-up areas, vegetated areas and water surfaces. Although the definitions illustrated in **Figure 5.4** are general and apply to permeable-rough surfaces covered with vegetation, in this case it is not easy from geometric analyse to assign values to z_H and λ_F. Thus, in the present work, while for urbanized zones z_H and λ_F are estimated mainly from the geometric dimensions of the surface elements (buildings), for permeable-rough surfaces with vegetation and water surfaces these values are extrapolated from reference tables in the published literature.

5.4.3 Tables of typical values for z_D and z_{0M}

Tables of typical roughness can be found in the published literature (e.g., Oke, 1987; Stull, 1988; Raupach *et al.*,1991; Garratt, 1992; Wieringa, 1993). **Figure 5.5**, from Stull (1988) and **Table 5.2** from Wieringa (1993), show roughness length for momentum, z_{0M}, for typical terrain types.

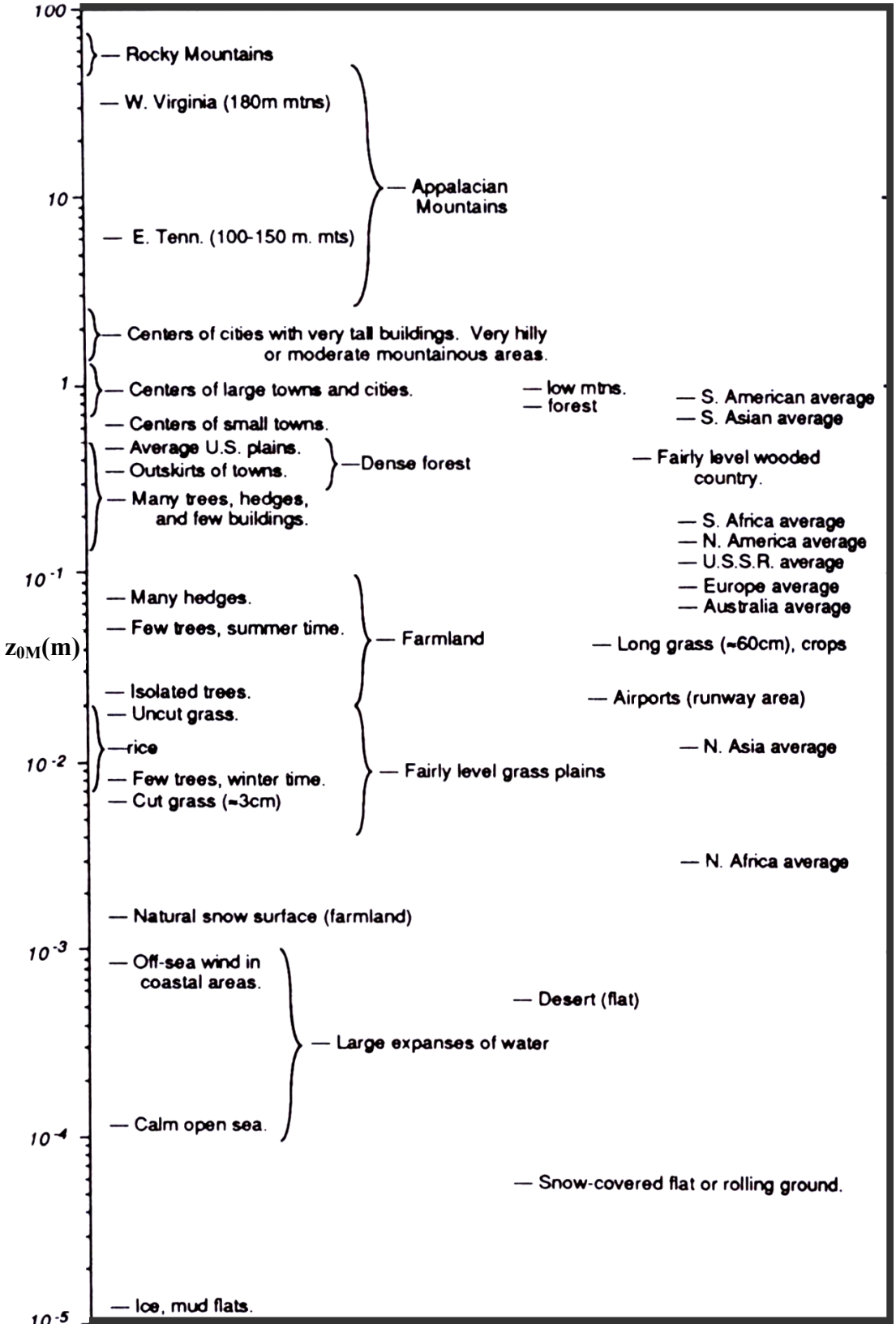

***Figure 5.5**- Order of magnitude of roughness length for momentum, z_{0M} (m), for typical terrain types (from Stull, 1988).*

Table 5.2 *- Typical roughness lengths for momentum (z_{0M}) of homogeneous surface types (from Wieringa, 1993).*

Surface type	Roughness length (m)	Number of references
Sea, loose sand, and snow	≈0.0002 (u-dependent)	17
Concrete, flat desert, tidal flat	0.0002-0.0005	5
Flat snow field	0.0001-0.0007	4
Rough ice field	0.001-0.012	4
Fallow ground	0.001-0.004	2
Short grass and moss	0.008-0.03	4
Long grass and heather	0.02-0.06	5
Low mature agricultural crops	0.04-0.09	4
High mature crops ("grain")	0.12-0.18	4
Continuous bushland	0.35-0.45	2
Mature pine forest	0.8-1.6	5
Tropical forest	1.7-2.3	2
Dense low buildings ('suburb')	0.4-0.7	3
Regularly-built large town	0.7-1.5	4

Table 5.3 *- Typical roughness and other aerodynamic properties of homogeneous zones in urban areas, ordered by height and density: mean roughness heights (z_H), zero-plane displacement ($z_d \equiv z_D$), roughness length for momentum ($z_0 \equiv z_{0M}$), aerodynamic conductance for momentum transport (g_{aM}) and drag coeficient (C_D) (from Grimmond and Oke, 1999a).*

Urban surface form	$\overline{z_H}$ (m)	$\overline{z_d}$[a] (m)	$\overline{z_0}$[a] (m)	$\overline{g_{aM}}$[b] (mm s^{-1})	$\overline{C_D}$[b] (× 10^{-2})
Low height and density					
Residential—one- or two-story single houses, gardens, small trees. Mixed houses and small shops. Warehouse, light industrial, few trees.	5–8	2–4	0.3–0.8	30–50	0.6–1.0
Medium height and density					
Residential—two- and three-story large or closely spaced, semidetached and row houses, large trees. Less than five-story blocks of flats with open surroundings. Mixed—houses with shops, light industry, churches, schools.	7–14	3.5–8.0	0.7–1.5	45–75	0.9–1.5
Tall and high density					
Residential—closely spaced < six-story row and block buildings or major facilities (factory, university, etc.), town center.	11–20	7–15	0.8–1.5	50–80	1.0–1.6
High-rise[c]					
Urban core or suburban nodes with multistory tower blocks in dense urban surroundings. Major institutional complexes.	>20	>12	>2.0	>90	>1.9

[a] Sites with above- (below-) average tree cover will have larger (smaller) z_d and z_0. Sites with deciduous tree cover will have 20%–30% smaller z_0 values during the leaf-off period. Smaller values are likely if the fetch direction is along a major road. Values greater than or less than these can arise because of the absolute height of the roughness elements.
[b] Assumes neutral stability, $z_r = 50$ m and $u = 5$ m s^{-1}.
[c] There are almost no measured values in this class; therefore, values have little support.

Table 5.3 from Grimmond and Oke (1999a) extends **Table 5.2** from Wieringa (1993) by recognizing four types of urban roughness terrain defined on the basis of the height and packing density of the roughness elements. **Table 5.3** associates each of these urban surface types with a typical range of mean roughness heights (z_H) and the corresponding range of values for the roughness-related parameters, such as zero-plane

displacement (z_D) and roughness length for momentum (z_{0M}). Values of aerodynamic conductance for momentum transport (g_{aM}) and drag coeficient (C_D), defined in Grimmond and Oke (1999a), but not discussed in the present work, are also presented in this table. Values in the high-rise building class of **Table 5.3** are without support from field data. Hence are largely based on morphometric estimates, theory, and intuition, and should therefore only be used as rough indications. Grimmond and Oke (1999a) suggest that it may even be argued that flow around such irregular arrays cannot conform with the requirements of equilibrium flow and the logarithmic law.

Grimmond and Oke (1999a) discuss the values presented in **Table 5.3** as follows. Comparing these urban z_{0M} values of **Table 5.3** with those of natural surfaces given by other tables of typical roughness confirms that cities and forests are near the top end of the scale. For example, broadly typical values of z_{0M} are for water, 0.0002m; short grass, 0.01m; crops, 0.1m; and forests, 1–2m. According to Grimmond and Oke (1999a), using the same measurement height ($z_s = 50$ *m)* and wind speed ($u = 5$ ms^{-1}) as specified in **Table 5.3**, these roughness lengths translate into the following values of aerodynamic conductance for momentum transport (g_{aM}): water, 5 mm s^{-1}; short grass, 11 mm s^{-1}; crops, 21 mm s^{-1}; and forests, 62–96 mm s^{-1} (e.g., Szeicz, 1974; Stewart, 1984). Therefore, with all other factors remaining the same, the drag exerted and the efficiency of above-roof diffusion and transport are greater over cities than for most rural surfaces except forests. The downtown cores of modern cities probably exceed forest values. Nevertheless, it should not be ignored that z_{0M} for the first urban category in **Table 5.3** (which occupies a considerable area of many cities) is not as large as that for a mature forest, and that only the fourth category of urban roughness can be called unusually rough. Notice also that within a single city it is possible to find almost a fourfold range of z_{0M}, g_{aM}, and C_D if the full range of morphometry classes are represented. Thus, Grimmond and Oke (1999a) hypothesize that, with all other factors remaining the same, greater roughness will be generated by cities compared to forests because the drag coefficient for sharp edged buildings is greater than for trees and their porosity to airflow is essentially zero. On the other hand, these features may be compensated for by the lower density of elements in a city.

For the medium and tall classes in **Table 5.3**, z_{0M} varies relatively little. According to Grimmond and Oke (1999a) this lack of variation is because, although skimming flow generates less roughness, this effect is partially compensated for by the

greater absolute height of the elements. The tall and medium classes are thus mainly differentiated by z_D.

Grimmond and Oke (1999a) also forward a simple scheme to aid users to obtain estimates of urban roughness parameters by using **Table 5.4** and **Figure 5.6** together. This approach avoids measuring multiple absolute dimensions and instead uses qualitative (essentially visual) assessment of urban form along with nondimensional roughness coefficients (f_d and f_0). The first three categories in the first column of **Table 5.4** broadly correspond to those combinations of roughness density that generate the isolated, wake interference, and skimming flow regimes, respectively, and the fourth category is urban morphometry that results in what might be called ‘‘chaotic flow.’’ While these densities can be quantified by use of aspect ratios, such as plan area index (λ_P) , frontal area index (λ_F) or street canyon aspect ratio (λ_S) (see **Figure 5.4**), it probably is much easier to classify urban morphometry from aerial photography (**Figure 5.6**), for example.

Table 5.4 *- Typical nondimensional roughness properties of homogeneous zones in urban areas, ordered by urban density and flow regime: plan area index, λ_P, street canyon aspect ratio, λ_S, and the coefficients f_d and f_0. Urban Terrain Zones (UTZ) codes are from Ellefsen (1990-91)[After Grimmond and Oke, 1999a.]*

Urban surface density—Flow regime	UTZ (urban terrain zones[a])	$\overline{\lambda_P}$[b]	$\overline{\lambda_S} = \overline{z_H}/\overline{W}$	$f_d = \overline{z_d}/\overline{z_H}$	$f_0 = \overline{z_0}/\overline{z_H}$
Low density—isolated flow					
Buildings and trees are small and widely spaced, e.g., modern single-family housing with large lots and wide roads; light industrial area or shopping mall with large paved or open space.	Do1, Do3–Do5	0.05–0.40	0.08–0.30	0.35–0.50	0.06–0.10
Medium density—wake interference flow					
Two- to four-story buildings and mature trees, elements of various heights occupy more than 30% surface area and create semienclosed spaces (street canyons, courtyards), e.g., closely spaced, large, and semidetached houses, blocks of apartments in open surroundings. Mixed houses with shops, light industry, churches, and schools.	A5, Dc3, Dc5, Do2	0.3–0.5	0.3–1.0	0.55–0.7	0.08–0.16[c]
High density—skimming flow					
Buildings and trees closely packed and of similar height, narrow street canyons, e.g., old town centers, dense row, and semidetached housing, dense factory sites.	A1–A4, Dc2, Dc4	0.5–0.8	0.65–2.00	0.60–0.85	0.07–0.12
High-rise—chaotic or mixed flow[d]					
Scattered or clustered tall towers of different heights jutting up from dense urban surroundings, e.g., modern city core, tall apartment, major institution.	Dc1, Dc8, Do6	>0.4	>1	0.50–0.70	0.10–0.20

[a] UTZ codes are from Ellefsen (1990–91).
[b] Plan areas of buildings only.
[c] Largest values likely to apply to midrange of λ_P and λ_S
[d] Unique distribution of major elements makes it difficult to generalize, except to expect that roughness is enhanced by addition of tall elements.

Figure 5.6 *- Photographs of the physical nature of urban morphometry representing examples of the four urban roughness categories in* ***Table 5.4****. Urban Terrain Zones (UTZ) codes are from Ellefsen (1990-91): (a) Do3, (b) Do3, (c) Do4, (d) Dc3, (e) Do2, (f) A5, (g) A2, (h)A1, (i) Dc2, (j) Dc1, (k) Dc1, and (l) Dc8. [After Grimmond and Oke, 1999a.]*

5.4.4 Roughness length for heat z_{0H} - the Brutsaert (1982) method

A number of methods are available to determine kB^{-1}(= ln (z_{0M}/z_{0H})). Voogt and Grimmond (2000) evaluate some approaches for an urban environment with little vegetation, and conclude that an appropriate kB^{-1} can be obtained by using the Brutsaert (1982) equation for bluff-rough situations. Hence, in the model for surface sensible heat flux used in the present study, the roughness length for heat, z_{0H}, is determined as a function of z_{0M}, using the formulation proposed by Brutsaert (1982) for bluff-rough surfaces

$$z_{0H} = z_{0M}\left[7.4\exp\left(-2.46\,\mathrm{Re}_*^{\,0.25}\right)\right] \qquad (5.4.7)$$

Here Re_* is the roughness Reynold's number, defined as

$$\mathrm{Re}_* = z_{0M}\frac{u_*}{\nu} \qquad (5.4.8)$$

where ν = 1.461 x10^{-5} m s^{-1} is the kinematic molecular viscosity and u_* the friction velocity. The roughness Reynold's number characterises hydrodynamically rough or smooth flow regimes (smooth, for Re_* <2). Equation (**5.4.7**) is shown in **Figure 5.7** as the solid line, for bluff-surfaces.

Figure 5.7 shows the variation of kB^{-1}= ln (z_{0M}/z_{0H}) for heat and kB^{-1}= ln (z_{0M}/z_{0E}) for mass transfer as a function of the roughness Reynold's number, for different types of surface cover. Brutsaert (1982) suggests that these values can be used for practical calculations, when no other information is available.

Several experimental and theoretical studies show that there is a pronounced dissimilarity between the bulk transfer properties for scalars at permeable-rough surfaces and those at bluff-rough surfaces. More specifically, they show that for heat (or mass transfer) at a vegetation cover the quantity kB^{-1} is relatively insensitive to changes in z_{0M} and that it depends only mildly on the friction velocity u_* (Brutsaert, 1982). The ratio (z_{0M}/z_{0H}) does not display as much change for most grassy or tree-covered surfaces as it does for surfaces with bluff roughness. Several results on kB^{-1} are summarized in **Figure 5.7** from Brutsaert (1982).

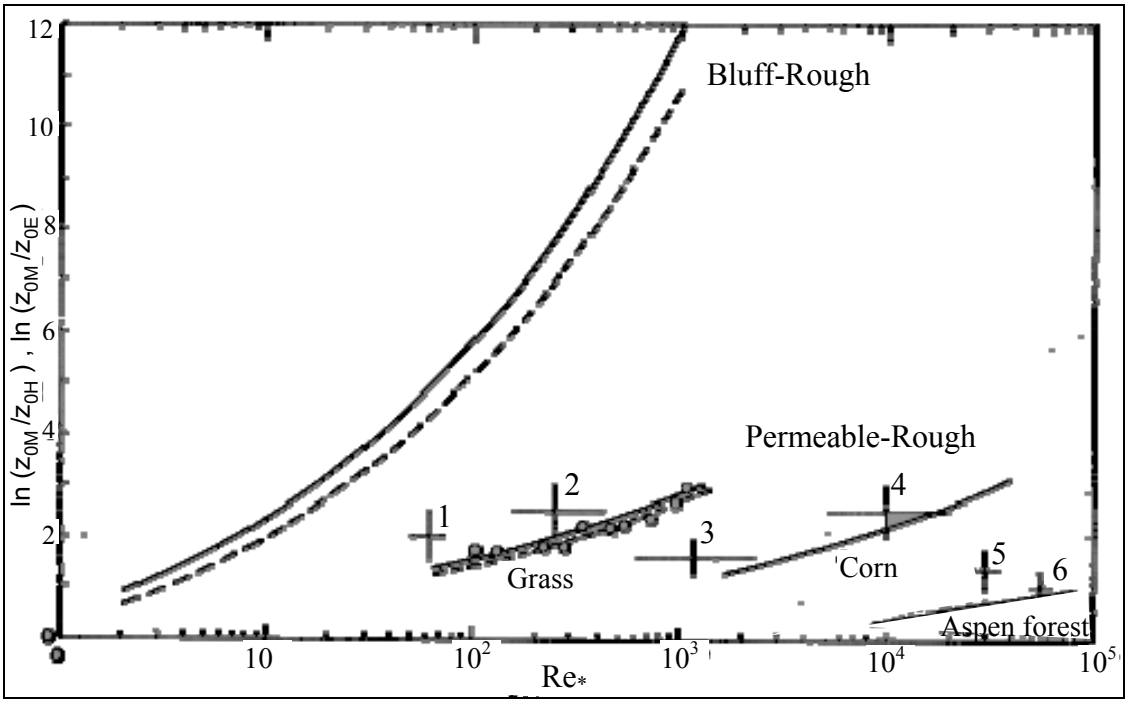

***Figure 5.7**- Comparison between experimental and theoretical results on ln (z_{0M}/z_{0H}), for heat transfer (solid curves), and ln (z_{0M}/z_{0E}), for evaporation from wet surfaces (dash curves), plotted versus roughness Reynolds number. The curves represent theoretical results. The numbered points represent experimental results: 1 is short grass, 2 medium length grass, 3 bean crop, 4 savannah scrub, 5 and 6 pine forest (horizontal bars represent Re* range and vertical bars the standard deviation). Also some experimental data points are superimposed on the theoretical curve for evaporation from wet grass. [Adapted from Brutsaert, 1982.]*

Figure 5.7 shows that in the rough domain over surfaces with bluff obstacles z_{0H} (and z_{0E}) are considerably smaller than z_{0M} (for $2<Re^*<1000$, $1<\ln(z_{0M}/z_{0H})<12$). According to Brutsaert (1982), this large difference in roughness is a manifestation of the dissimilarity between the transfer mechanisms of momentum and those of scalar properties right at the surface. Momentum transfer takes place not only as a result of viscous shear, but the roughness of obstacles also generates an effective form drag involving local pressure gradients. The transfer of the passive property at the wall is controlled primarily by molecular diffusion. This dissimilarity is also manifested by the difference in the bulk transfer coefficients.

Voogt and Grimmond (2000), in a study for a simple urban area found extremely small radiometric roughness lengths for heat (z_{0H}), ranging from 10^{-4} to 10^{-12} m. These small values have been found also by others, for example, Sugita and

Brutsaert (1990) and Malhi (1996). Voogt and Grimmond (2000) admitted that the values determined in their study are likely to be close to the extreme because of the lack of vegetation at the sites. The authors considered also that this small results suggest that similiarity theory is predicting physically unrealistic values to compensate for the inadequacy of the stability dependence of the exchange coefficient or aerodynamic resistance (as documented previously by Sun and Mahrt, 1995b).

Voogt and Grimmond (2000) conclude that, for the studied urban environment, a reasonable estimate for $kB^{-1}|_{R,T}$ appears to be about 20–27, which is larger than those observed over vegetated and agricultural surfaces and suggests extremely small z_{0H} values. This range represents the results obtained by three independent methods. The values determined from the bluff-rough curve given in Brutsaert (1982) provide the largest values of $kB^{-1}|_{R,T}$.

In a recent study, Kanda *et al.* (2007) found an empirical function between kB^{-1} and Re_* for urban sites, similar to equation (5.4.7) of Brutsaert (1982), but where the constant value of 2.46 is replaced by 1.49. The function was derived from the results of the Comprehensive Outdoor Scale Model (COSMO) experiments for urban climate, and showed reasonable agreement with the available data from three urban sites (Kanda *et al.*, 2007)- a light industrial area in Vancouver (Voogt and Oke, 1997; Voogt and Grimmond, 2000), a business district in Tokyo (Sugawara, 2001), and a densely built residential area in Tokyo (Moriwaki and Kanda, 2004, 2006).

5.5 Model tests

Previous sections describe how the model was specified, this section will outline how it was implemented and tested. Q_H, u_* and L were determined from equations (5.1.1)- (5.1.4) iteratively for a range of meteorological conditions. The stability correction functions used in the model are the vertically integrated forms of the universal stability functions, Ψ_M for momentum and Ψ_H for heat, presented in **Table 5.1**.

The meteorological parameters used in the model are the surface and air temperatures, T_R and T_a, and the wind velocity, u. T_a and u are typically measured several metres above the surface, at the measurement height,z_S, in the inertial sublayer.

The model input roughness parameters are the mean surface elements height, z_H, and the frontal area index, λ_F. The zero-plane displacement length, z_D, and the roughness length for momentum, z_{0M}, are estimated as a function z_H and λ_F, using Raupach's (1994, 1995) morphometric method [equations (5.4.4)- (5.4.6)]. The roughness length for heat, z_{0H}, is determined as a function of z_{0M}, using the formulation proposed by Brutsaert (1982) for bluff-rough surfaces [equations (5.4.7)- (5.4.8)].

Once the model was formulated, the numerical implementation was developed using FORTRAN code written by the author. The numerical model was then subjected to sensitivity tests using a range of typical values for each input variable (T_a , u , T_R, z_H, and λ_F) were carried out (section 5.5.1). Numerical experiments on the effects of spatial variations of urban roughness were also performed (5.5.2).

5.5.1 Sensitivity tests of the numerical model

Data

The sensitivity of the surface sensible heat flux (Q_H) to the different model parameters, wind speed (u), air temperature (T_a), surface temperature (T_R), surface elements height (z_H) and frontal area index (λ_F), has been investigated. The model was evaluated for the main situation of interest, namely atmospheric convective conditions over the Manchester region, which occur during daytime, typically in springtime and summer. The model was tested for a range of typical input values of each variable: $0.01 \leq \lambda_F \leq 0.47$; $0.5\text{m} \leq z_H \leq 12\text{m}$; $0.5\text{m/s} \leq u \leq 12\text{m/s}$; $274\text{K} \leq T_R \leq 320\text{K}$; $280\text{K} \leq T_a \leq 303\text{K}$, as shown in **Table 5.5**.

In order to simplify the analysis of the test results, the synthetic examples studied (a total of 120) were organised into 5 groups (A, B, C, D, E) in such a way that in each group the input values are the same for all variables, except for one of them as follows:

(A) z_H= 6 m, u= 1.5 m/s, T_R= 303 K, T_a= 293 K, and λ_F= 0.01, 0.03, …, 0.45, or 0.47;
(B) λ_F= 0.2, u= 1.5 m/s, T_R= 303 K, T_a= 293 K, and z_H= 0.5, 1.0, …, 11.5, or 12.0 m;
(C) λ_F= 0.2, z_H= 6 m, T_R= 303 K, T_a= 293 K, and u= 0.5, 1.0, …, 11.5, or 12.0 m/s;
(D) λ_F= 0.2, z_H= 6 m, u= 1.5 m/s, T_a= 293 K, and T_R= 274, 276, …, 318, or 320 K;
(E) λ_F= 0.2, z_H= 6 m, u= 1.5 m/s, T_R= 303 K, and T_a= 280, 281, …, 302, or 303 K.

In all cases, the measurement height has been taken as z_S = 20m.

Table 5.5 *- Values of the variables used in the model sensitivity test: frontal area index (λ_F), surface elements height (z_H) wind speed (u), surface temperature (T_R) and air temperature (T_a) . In all cases, the measurement height has been taken as z_S = 20m.*

i	A	B	C	D	E	A	B	C	D	E	A	B	C	D	E	A	B	C	D	E	A	B	C	D	E
j	λ_F					z_H (m)					u (m/s)					TR (K)					Ta (K)				
1	0.01	0.2	0.2	**0.2**	0.2	6	0.5	6	6	6	1.5	1.5	0.5	**1.5**	1.5	303	303	303	**274**	303	293	293	293	**293**	280
2	0.03	0.2	0.2	**0.2**	0.2	6	1	6	6	6	1.5	1.5	1	**1.5**	1.5	303	303	303	**276**	303	293	293	293	**293**	281
3	0.05	0.2	0.2	**0.2**	0.2	6	1.5	6	6	6	1.5	1.5	1.5	**1.5**	1.5	303	303	303	**278**	303	293	293	293	**293**	282
4	0.07	0.2	0.2	**0.2**	0.2	6	2	6	6	6	1.5	1.5	2	**1.5**	1.5	303	303	303	**280**	303	293	293	293	**293**	283
5	0.09	0.2	0.2	**0.2**	0.2	6	2.5	6	6	6	1.5	1.5	2.5	**1.5**	1.5	303	303	303	**282**	303	293	293	293	**293**	284
6	0.11	0.2	0.2	**0.2**	0.2	6	3	6	6	6	1.5	1.5	3	**1.5**	1.5	303	303	303	**284**	303	293	293	293	**293**	285
7	0.13	0.2	0.2	**0.2**	0.2	6	3.5	6	6	6	1.5	1.5	3.5	**1.5**	1.5	303	303	303	**286**	303	293	293	293	**293**	286
8	0.15	0.2	**0.2**	**0.2**	0.2	6	4	**6**	6	6	1.5	1.5	**4**	**1.5**	1.5	303	303	**303**	**288**	303	293	293	**293**	**293**	287
9	0.17	0.2	0.2	**0.2**	0.2	6	4.5	6	6	6	1.5	1.5	4.5	**1.5**	1.5	303	303	303	**290**	303	293	293	293	**293**	288
10	0.19	0.2	0.2	0.2	0.2	6	5	6	6	6	1.5	1.5	5	1.5	1.5	303	303	303	292	303	293	293	293	293	289
11	0.21	0.2	0.2	**0.2**	0.2	6	5.5	6	6	6	1.5	1.5	5.5	**1.5**	1.5	303	303	303	**294**	303	293	293	293	**293**	290
12	0.23	0.2	0.2	0.2	0.2	6	6	6	6	6	1.5	1.5	6	1.5	1.5	303	303	303	296	303	293	293	293	293	291
13	0.25	0.2	0.2	0.2	0.2	6	6.5	6	6	6	1.5	1.5	6.5	1.5	1.5	303	303	303	298	303	293	293	293	293	292
14	0.27	0.2	0.2	0.2	0.2	6	7	6	6	6	1.5	1.5	7	1.5	1.5	303	303	303	300	303	293	293	293	293	293
15	0.29	0.2	0.2	0.2	0.2	6	7.5	6	6	6	1.5	1.5	7.5	1.5	1.5	303	303	303	302	303	293	293	293	293	294
16	0.31	0.2	0.2	0.2	0.2	6	8	6	6	6	1.5	1.5	8	1.5	1.5	303	303	303	304	303	293	293	293	293	295
17	0.33	0.2	0.2	0.2	0.2	6	8.5	6	6	6	1.5	1.5	8.5	1.5	1.5	303	303	303	306	303	293	293	293	293	296
18	0.35	0.2	0.2	0.2	0.2	6	9	6	6	6	1.5	1.5	9	1.5	1.5	303	303	303	308	303	293	293	293	293	297
19	0.37	0.2	0.2	0.2	0.2	6	9.5	6	6	6	1.5	1.5	9.5	1.5	1.5	303	303	303	310	303	293	293	293	293	298
20	0.39	0.2	0.2	0.2	0.2	6	10	6	6	6	1.5	1.5	10	1.5	1.5	303	303	303	312	303	293	293	293	293	299
21	0.41	0.2	0.2	0.2	0.2	6	10.5	6	6	6	1.5	1.5	10.5	1.5	1.5	303	303	303	314	303	293	293	293	293	300
22	0.43	0.2	0.2	0.2	0.2	6	11	6	6	6	1.5	1.5	11	1.5	1.5	303	303	303	316	303	293	293	293	293	301
23	0.45	0.2	0.2	0.2	0.2	6	11.5	6	6	6	1.5	1.5	11.5	1.5	1.5	303	303	303	318	303	293	293	293	293	302
24	0.47	0.2	0.2	0.2	0.2	6	12	6	6	6	1.5	1.5	12	1.5	1.5	303	303	303	320	303	293	293	293	293	303

The input values are given by a matrix of 5 columns x 24 rows: $\lambda_F(i,j)$, $z_H(i,j)$, $u(i,j)$, $T_R(i,j)$, $T_a(i,j)$, with i= A, B,..., E, and j= 1, 2,.., 24 (**Table 5.5**). After model runs, a matrix of also 5 columns x 24 rows is obtained for each output parameter: $z_D(i,j)$, $z_{0M}(i,j)$, $z_{0H}(i,j)$,..., $L(i,j)$, $u_*(i,j)$, $Q_H(i,j)$, with i= A, B,..., E, and j = 1,2,.., 24 (the results for each output parameter are represented in a graph of **Figure 5.8**).

Note that, as shown in **Table 5.5**, the input values for the point (A,1), for example, are $\lambda_F(A,1)$= 0.01, $z_H(A,1)$ = 6m, u(A,1)= 1.5m/s, $T_R(A,1)$= 303K, $T_a(A,1)$= 293K, and the obtained output values for this point are $z_D(A,1)$, $z_{0M}(A,1)$, $z_{0H}(A,1)$,..., L(A,1), $u_*(A,1)$, $Q_H(A,1)$. On the other hand, in order to simplify the analysis of results, matrix points belonging to the same column (A, B, C, D or E) have the same input values for all variables, except for one. For example, points in column A just differ on the λ_F value [$\lambda_F(A,1)$ = 0.01, $\lambda_F(A,2)$ = 0.03, ..., $\lambda_F(A,24)$ = 0.47; $z_H(A,1)$ = ...= $z_H(A,24)$ = 6m; u(A,1) = ...= u(A,24) = 1.5m/s; $T_R(A,1)$ = ...= $T_R(A,24)$ = 303K; $T_a(A,1)$ = ...= $T_a(A,24)$= 293K], and points of column E just differ on the T_a value.

Results

Model output values for several parameters of interest were derived. **Figure 5.8** shows results of model tests for the roughness parameters (z_D, z_{0M}, z_{0H}), Monin-Obukhov variable ζ and length scale L, friction velocity u_*, stability functions for momentum and for heat, $\Psi_M(\zeta)$ and for $\Psi_H(\zeta)$, and for the sensible heat flux Q_H and resistance to heat transfer r_H, using the input values specified in the previous

subsection. Each point on the curves represents a complete model run using a specific set of input values, a total of 24 for each curve. Each curve relates one output parameter (e.g, Q_H) to one input variable (λ_F, z_H, u, T_R or T_a) all the other input variables are kept constant. For example, for the sensible heat flux graph (Q_H), curve A of **Figure 5.8** shows the variation of Q_H as λ_F increases from 0.01 to 0.47, at intervals of 0.02, while the value of all the other input parameters is the same for all the points of this curve (z_S = 20m, z_H=6m, u=1.5m/s, T_R=303K, T_a=293K). The x coordinate relates to the input parameters variability range defined in the previous subsection and defined by *j* in **Table 5.5**.

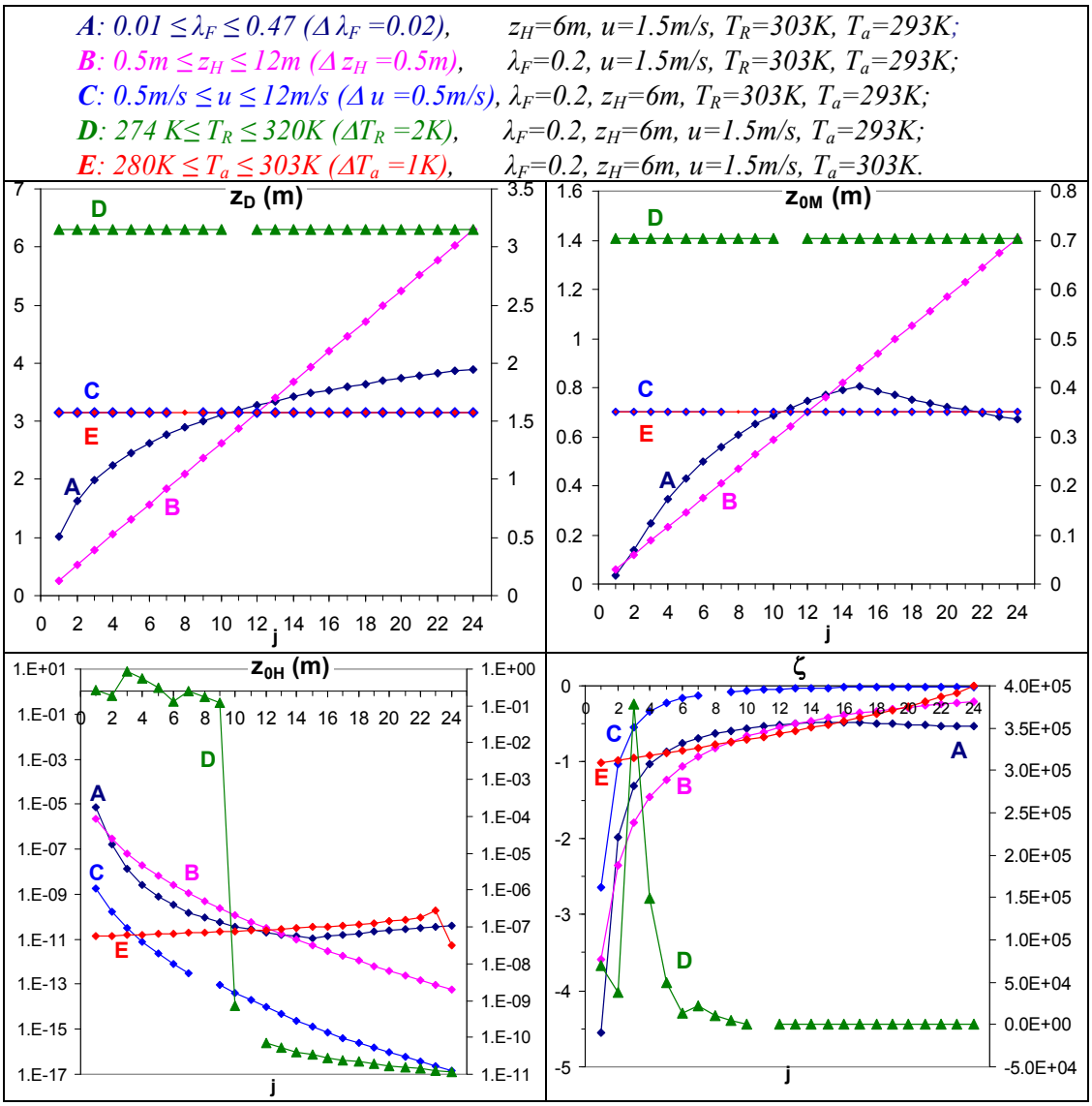

Figure 5.8 *- Results of model sensitivity tests (for z_D , z_{0M}, z_{0H},..., L, u_*, Q_H, and r_H) using the input values discussed in the text (**Table 5.5**) and indicated in the top box. Each curve (A, B, C, D, E) relates to a different input variable, λ_F, z_H, u, T_R, or T_a, while all others are kept constant. The x coordinate relates to the variability range defined by j in **Table 5.5**. [♦] refer to the left y-axis, [▲] refer to the right y-axis. (Continued on next page.)*

*(Continuation of **Figure 5.8**)*

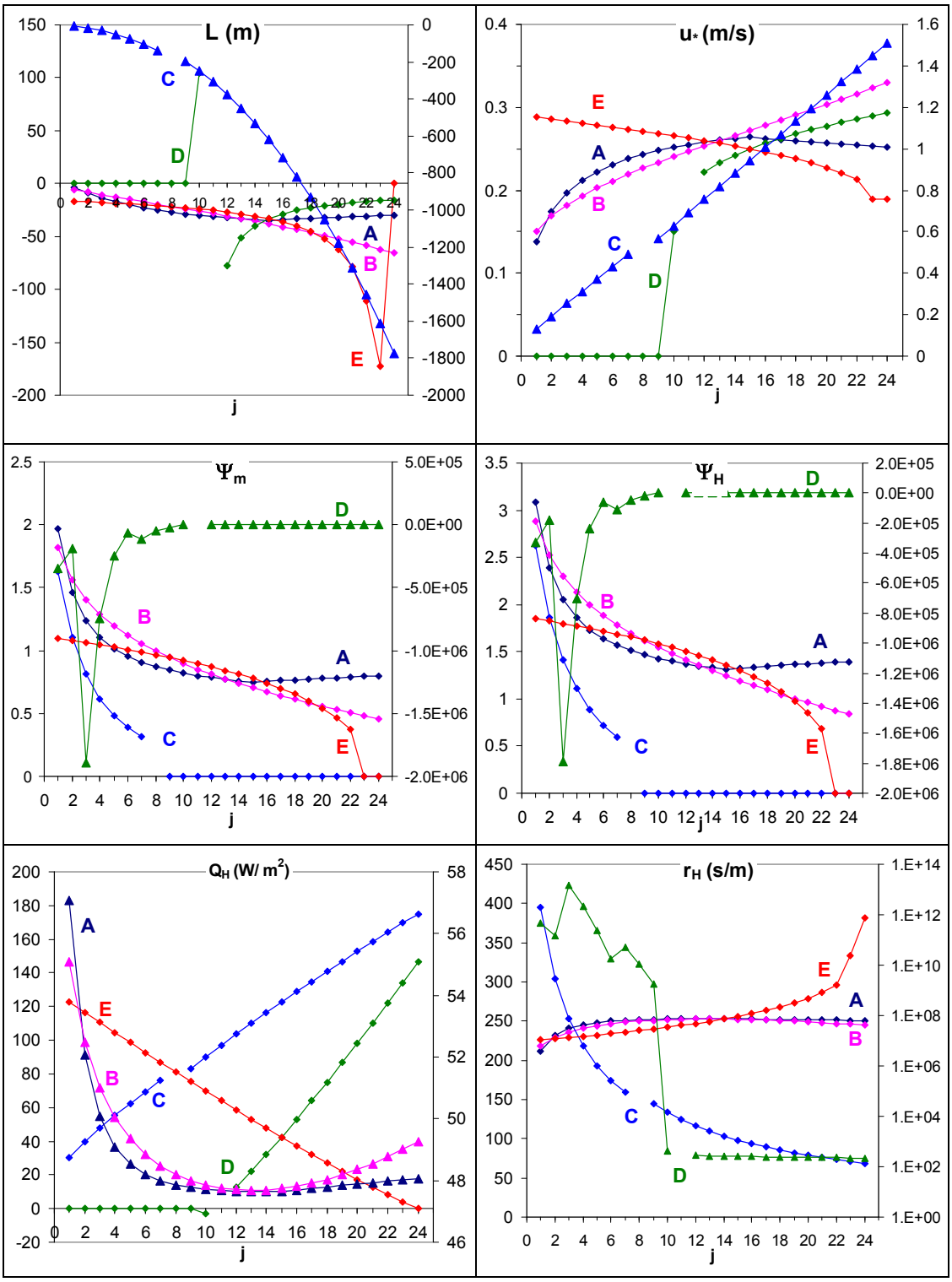

The model is capable of providing estimates of the surface sensible heat flux, Q_H, with a precision of $1x10^{-4}$ W/m^2 (the model iterations are terminated when this

value of precision is reached). If a higher precision is used, the computations are subject to larger truncation errors.

For the range of typical input values used, the model behaves reasonably for slightly stable to unstable conditions. However, as expected, the model fails for the stable conditions represented by points D1-D9, where the air temperature is superior to the surface temperature (T_a>T_R) and the measurement height z_S >>L. Also, the solution does not converge for points C8 and D11, which are cases where there is a discontinuity of the stability functions. These discontinuities are a consequence of the established criteria for being near neutral stability: $|\zeta=(z_S-z_D)/L| < 0.1$, where $\Psi_M= \Psi_H = 0$ (see **Table 5.1**). Case C8 is in an unstable- near neutral transition zone and D11 in a stable- unstable transition zone.

A discontinuity is also observed between points A15 and A16, in this case due to the different behaviour of the roughness parameter z_{0M} for values of $\lambda_F > 0.29$. The value λ_{Fmax} (=0.29) can be interpreted as the onset of "over-sheltering", the point at which adding further roughness elements merely shelters one another (Raupach, 1994). After this point the roughness z_{0M} is seen to decrease, yet the heat flux (Q_H) increases.

For each of the runs, a time sequence of the output values of Q_H, L, u_* , and ζ [=(z_S -z_D)/L] was plotted. **Figure 5.9a** shows the output for C7, C8 and C9 cases. This shows that for both C7 and C9 the solution converges after only approximately four iterations, and stable solutions for the model equation set are found. The run C8, as detailed above, shows that there is no unique solution to the equation set, and an oscillatory behaviour occurs. **Figure 5.9b** shows two cases for a very stable surface layer (D1 and D9), where the solution does not converge at all. **Figure 5.9c** shows a convergent solution for a slightly stable surface layer found in D10, whereas D11, the case discussed above, is non- convergent.

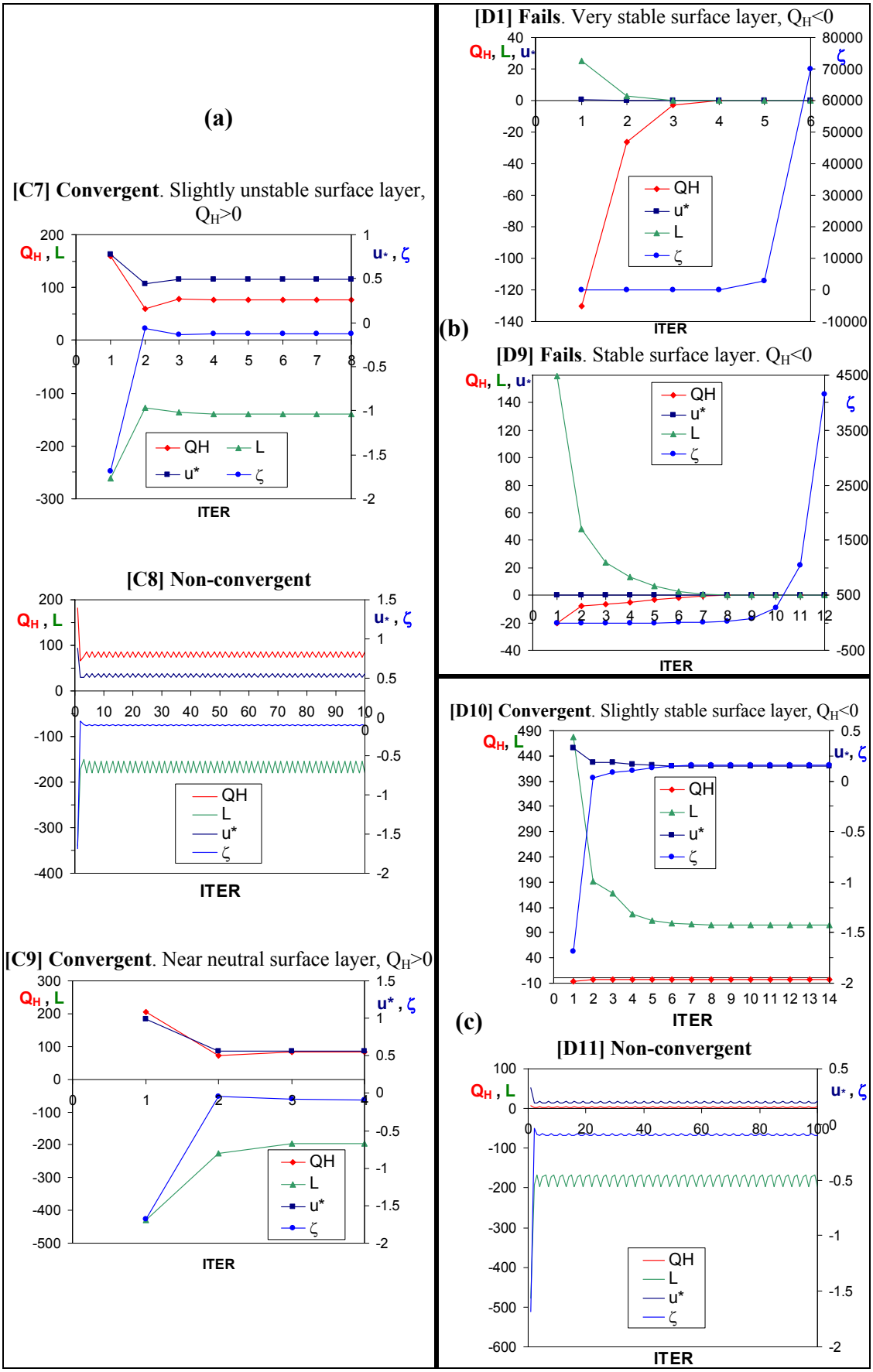

Figure 5.9 *- Iteration output values for points:* ***(a)*** *C7- C9;* ***(b)*** *D1, D9* ***(c)*** *D10, D11.*

5.5.2 Experiments on spatial variations of urban roughness

In order to more clearly identify the comparative impact of surface roughness *versus* local heating effects, some modelling experiments have been carried out **Figure 5.10a**. **Figure 5.10a** shows model results of surface sensible heat flux, Q_H, for a range of wind speeds (1.5, 3, 6, 10 and 12 m/s). For each wind speed situation, three frontal area index values have been considered (λ_F =0.10, 0.21 and 0.35), and for each of these cases four possible mean building height values (z_H = 34, 25, 15 and 6m) were used. In all the cases the measurement height was the same, z_S= 50m. This modelling experiment was carried out for two vertical temperature gradients (filled and open diamonds).

Also experiments with a schematic urban morphology were used to investigate the impact of different types of building arrays; three examples of typical urban situations (A, B and C) are described in **Figure 5.10b** and the corresponding points in **Figure 5.10a** are marked in red.

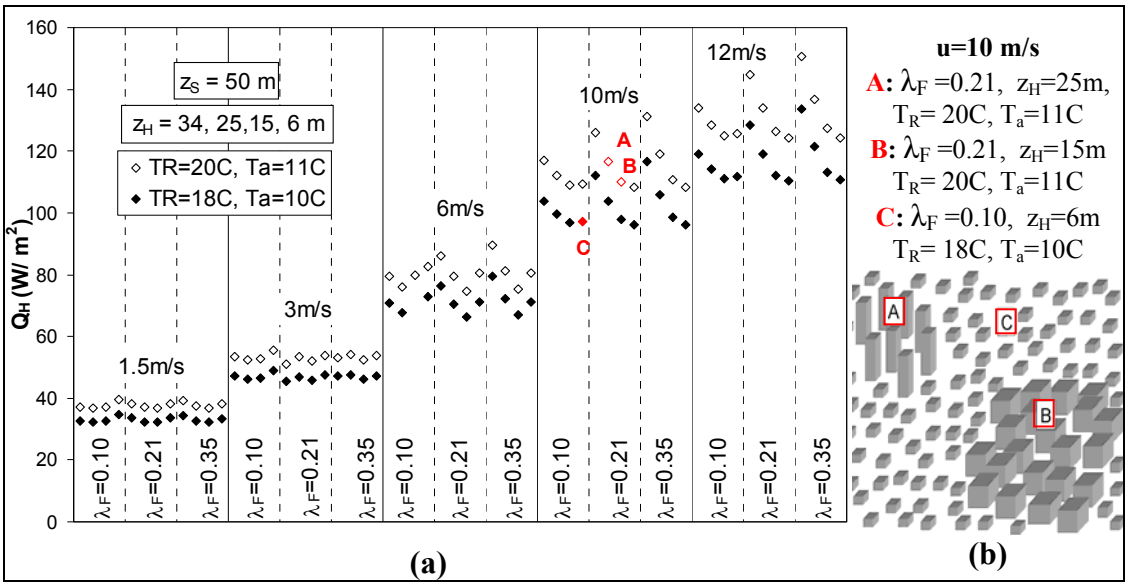

Figure 5.10 *- Preliminary model results showing the impact of the wind speed, vertical temperature gradient and surface roughness on the surface sensible heat flux.* ***(a)*** *Surface sensible heat flux results, Q_H, of a modelling experiment for two vertical temperature gradients (filled and open symbols). Each point represents a complete model run using a specific set of input values (z_S, z_H, u, T_R, T_a, and λ_F), which are indicated on the graph. Here, points A, B, and C relate to the urban area represented in (b).* ***(b)*** *Schematic representation of the typical distribution of roughness over an urban area loosely resembling a part (5x5 km^2) of Greater Manchester.*

The preliminary model results in **Figure 5.10a** show the impact of the wind speed, vertical temperature gradient (T_R-T_a) and roughness (z_H and λ_F) on the surface sensible heat flux, Q_H. Q_H increases with the wind speed and with the vertical temperature gradient (shown by the difference between the open and solid diamonds). Q_H also depends on the roughness, expressed by the parameters z_H and λ_F. This effect is most evident for the higher wind speeds.

The frontal area index (λ_F) has the most impact for high values of λ_F, in high wind speed cases and for tall buildings (high z_H). The greater the wind speed, the bigger the influence of the vertical temperature gradient and building heights on the surface sensible heat flux.

Considering the urban area represented in **Figure 5.10b**, it can be seen (**Figure 5.10a**) that the area of uniform low buildings (C) has a lower sensible heat flux than those areas (A and B) which have higher roughness. However, interestingly, the area of high rise buildings close together (A) produces almost the same sensible heat flux as the area (B) having lower buildings. So, in real cities it is possible that urban zones such as represented by B cause more impact on Q_H than those similar to A since they tend to cover much larger areas.

Chapter 6. A georeferenced database for surface roughness parameters over Greater Manchester

In this chapter information on urban morphology available for Greater Manchester in northwest England is analysed, and an approach to derive the roughness parameters needed to model the surface sensible heat flux is described. A surface morphologic database for Greater Manchester, developed from analysis of digitised georeferenced data of the surface elements height (*Cities Revealed Building Heights Data* and *Environment Agency* data), aerial photography, maps and field surveys, is described. Initially, data of a sample area of Greater Manchester are analysed. Then, land-use categories are established for Greater Manchester and reference morphologic parameters are attributed to each land-use category. The fraction of urbanised area and model surface morphologic parameters, such as the surface elements height (z_H) and frontal area index (λ_F), are estimated and mapped over a rectangular grid of 1km x 1km resolution, for the Greater Manchester study area. Using these values it was possible to obtain model estimates of the zero-plan displacement height (z_D) and roughness height for momentum (z_{0M}) for each domain cell.

6.1 Introduction

A fundamental methodological problem in hydroclimatological research is the definition of the characteristics of the urban surface and its representation in numerical models. For modelling studies of the atmospheric boundary layer, collection of information on the three-dimensional nature of the urban surface is vital. The urban surface-atmosphere interface is extremely complex, thereby defying simple description.

Grimmond and Souch (1994) presented a methodology which uses Geographic Information System (GIS) based techniques to represent the characteristics and morphology of the urban surface. The methodology can be used to describe a site objectively, model fluxes, or ensure spatial consistency between measured and

modelled data. The GIS based methodology of Grimmond and Souch (1994) consists of two parts: the development of a georeferenced database and a dynamic, objective means of sampling the database.

The procedure for the morphologic characterisation of the urban surface described in the present work builds upon the framework presented by Grimmond and Souch (1994). The methodology is applied to a zone (24x24 km^2) of Greater Manchester. In the present work, of the mapping of urban morphologic parameters, we need to be mindful of the nature of the investigation of the effects of urban surface roughness on the distribution of sensible heat flux. The results obtained are compared with values presented by Grimmond and Oke (1999a).

6.2 Data sets

For the present study an urban surface characterisation is needed in terms of some morphologic aspects, such as the mean height of the surface elements, z_H, and the frontal area index, λ_F, (see section 5.4.2). Furthermore, it is important to discuss the importance of knowledge of the surface material characteristics, both built and vegetative, and the distribution of water.

Digitised georeferenced data of the surface elements (*Cities Revealed Building Heights Data* and *Environment Agency* data), aerial photography, maps and field surveys, were used for the surface characterisation of Greater Manchester.

The commercial *Cities Revealed Building Height Data*, CR data, and the *Environment Agency* data of the height of surface elements, EA data, are supplied on an ArcView compatible file format.

The CR data, which were derived from high resolution aerial visible imagery and supplied by The GeoInformation Group [http://www.citiesrevealed.com/, 2002], provide information on the distribution of the buildings, their mean height and respective plan area.

The EA data, measured using airborne lidar [http://www.environment-agency.gov.uk/, 2002], provide information on the height of surface elements (e.g., trees and buildings) and permit the identification of water layers. However, these data files do not provide specific information on buildings.

On the contrary, CR data files just provide information on buildings, which are already delimited as polygons with a certain height and horizontal area. **Figure A2.1** of Appendix 2 compares data samples of the digitised georeferenced products CR and EA, over the same area of Greater Manchester.

EA data together with maps and aerial photos, allow mapping car parks, rivers, roads, railways, vegetated areas, buildings, etc... However, the buildings dimensions and distribution given by CR data are essential for a more expeditious calculation of the roughness parameters over urban areas, when using morphometric/geometric methods as outlined by Grimmond and Oke (1999a). Therefore, in the present work the different data products were taken into consideration together for the characterisation of the study area.

The data were mapped and analysed using GIS software ArcView.

6.3 Estimates of the mean surface elements height (z_H), frontal area index (λ_F), and other morphologic parameters of the urban surface

The surface morphologic parameters, such as the mean surface elements height ($\overline{z_H}$, or simply z_H) and frontal area index of the elements (λ_F), were estimated in order to derive the roughness parameters needed to model the surface sensible heat flux (section 5.4.2).

The mean buildings height, $\overline{z_H}$, and the plan area index, λ_P, for an urban homogeneous array, are direct results from the CR data statistics performed using ArcView. The fraction of built up area, i. e. the quotient between the total horizontal plan built area over an urban array and the total lot area of the urban array, is taken as an estimate of the roughness parameter λ_P - plan area index.

The frontal area index, λ_F, is calculated from the CR digitised data in the following way. Consider the equivalences (see section 5.4.2),

$$\lambda_P = \frac{\overline{A_P}}{\overline{A_T}} = \frac{A_P}{A_T} \quad \text{and} \qquad (6.3.1)$$

$$\lambda_F = \frac{\overline{A_F}}{\overline{A_T}} = \frac{A_F}{A_T}, \qquad (6.3.2)$$

where

$\overline{z_H}$ ≡ mean buildings height

A_T ≡ total lot area of the urban array

$\overline{A_T}$ ≡ mean lot area

A_P ≡ total plan built area over the urban array

$\overline{A_P}$ ≡ mean plan area of the buildings

λ_P ≡ plan area index

A_F ≡ total frontal area of the buildings over the urban array

$\overline{A_F}$ ≡ mean frontal area of the buildings

λ_F ≡ frontal area index

Taking equations (6.3.1) and (6.3.2), it is possible to write

$$\frac{\lambda_F}{\lambda_P} = \frac{\overline{A_F}}{\overline{A_P}} = \frac{A_F}{A_P} \quad \text{and} \qquad (6.3.3)$$

$$\lambda_F = \frac{\overline{A_F}}{\overline{A_P}} \lambda_P \qquad (6.3.4)$$

Therefore, the frontal area index can be estimated from the expression

$$\lambda_F = \frac{\overline{A_F}}{\overline{A_P}} \frac{A_P}{A_T} \qquad (6.3.5)$$

In this equation $\overline{A_P}$, A_P, and A_T are direct results from the CR data statistics performed using ArcView. The mean frontal area $\overline{A_F}$ is calculated using the approximation that buildings are rectangular parallelepipeds with a squared base, thus

$$\overline{A_F} = \overline{z_H} \sqrt{\overline{A_P}} \qquad (6.3.6)$$

Note that this calculation involves two important approximations. The buildings are approximated to rectangular parallelepiped and the frontal area index (λ_F) of the elements, as ‘‘seen’’ by the oncoming wind, is considered independent of the wind direction. On the other hand, in this first approach just the buildings were considered, instead of considering all surface roughness elements over the urban area. Although

the buildings are the obstacles more relevant to airflow over cities, other elements such as trees will be considered later.

6.4 Mapping morphologic parameters over a sample area of Greater Manchester.

6.4.1 Identification of land-use categories for a preliminary classification

In order to establish land-use categories for Greater Manchester and to attribute reference morphologic parameters to each land-use category, first an exploratory study has been carried out. The objective of this preliminary study is to find some typical values of surface parameters for Greater Manchester urban area, and test the mapping procedures before applying to the entire study domain. For the study described here, a sample area of Salford and Manchester considered to be representative of the Greater Manchester urbanised area has been selected. The distribution of the buildings over the test zone is mapped on **Figure 6.1**, where buildings are projected on the terrain level horizontal plan as obtained from CR data.

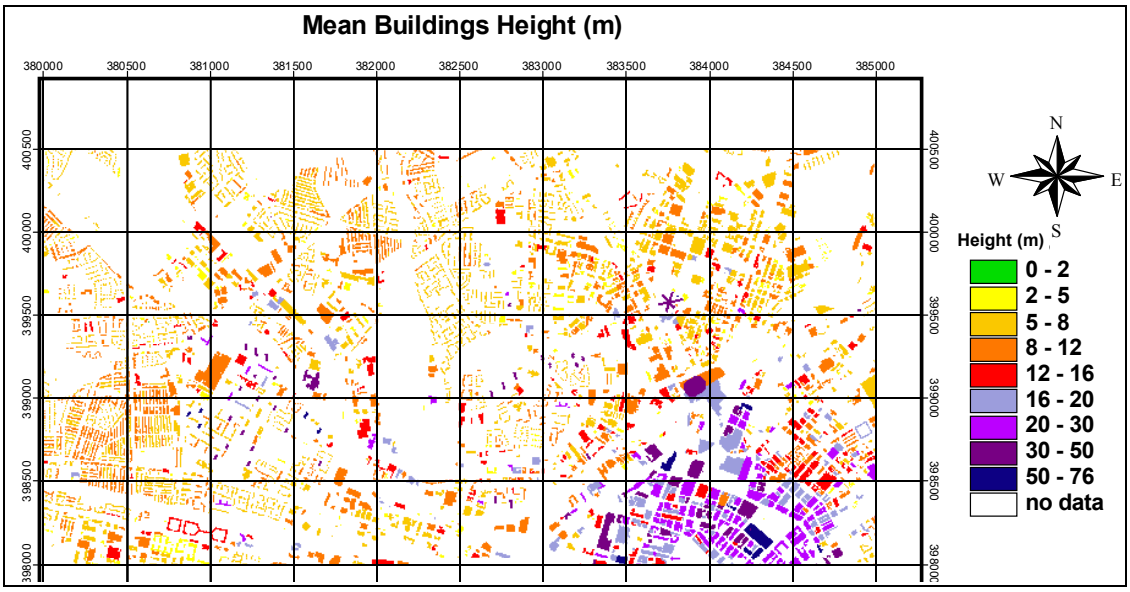

Figure 6.1 *- Distribution of buildings over a zone of Greater Manchester. Distribution of buildings, obtained from CR data, covering an area of 2.5km x 5km of Salford and Manchester. The axes labels represent the U. K. National grid co-ordinates of the area of interest (Ordnance Survey national grid system of eastings and northings), X: 380000m - 385000 m; Y: 398000m- 400500m. The legend shows the values of the buildings mean height associated with the different colours.*

Based on the CR data set layer, homogenous tiles in terms of surface morphology and surface cover were delimited, forming a non regular polygon grid (Grid A, **Figure 6.2**) over the area of interest. Each tile should be regarded as homogeneous with respect to the relevant characteristics at the scale of the problem (local scale, order of magnitude ~100 m). The aspects of the morphology used to define the tiles to be mapped were the buildings height, plan area and density, and street width.

Also identified are tiles as green zones, water surfaces, roads and railways. EA data, maps, aerial photographs and some field surveys at randomly chosen locations allow for checks of the three-dimensional nature of the urban surface and the distribution of built, vegetative or water cover zones. The tiles were grouped according to their similarity and classified in terms of some land-use categories (Grid A, **Figure 6.2**). The names of the categories were essentially selected on the basis of the research of Ellefsen (1990/91) and partly summarised in **Table 6.3**. The classifications were selected by comparing the aerial photographs and the land use data set with the classifications by Ellefsen (1990/91) shown in **Table 5.4** and **Figure 5.6**. For the classifications that matched the published definitions these classifications are used. For those classifications that were different, a new classification was defined as close to the published definitions as possible (see **Table 6.3**).

In order to test the adequate size of the delimited tiles, another grid similar to that described above, but where more attention has been paid to the details on the local scale, was produced (Grid B, **Figure 6.3**). Naturally, in this case the designed tiles are smaller. Note that because of micro-scale heterogeneity the choice of boundaries may change a site description (Grimmond and Souch, 1994).

The different tiles identified over the sample area in this preliminary analyses are mapped in **Figure 6.2** (Grid A) and **Figure 6.3** (Grid B). The mean buildings height and land-use category are indicated for each tile. A summary of land-use categories is given in **Table 6.1**.

Figure 6.2 and **Figure 6.3** show part of Manchester city centre (Centre, in dark blue) and its peripheral streets (CentreP, in purple), where the mean buildings height is relatively high (see also **Figure 6.1**). The Salford Precinct zone, with some tall blocks and relatively low residential houses, is also evident in **Figure 6.2** (CentreN, in pink). Residential areas of high rise buildings (ResH, in red) are market as well. The larger

green areas are urban parks. Note that the residential areas (Res, in yellow), of typically low buildings, and the mix zones (Res_mix, in orange), of low residential and commercial/ industrial buildings, occupy an extensive fraction of the urban area. The river Irwell (Canal, in bright blue) and a main railway (RailW, in black) are marked in **Figure 6.3**.

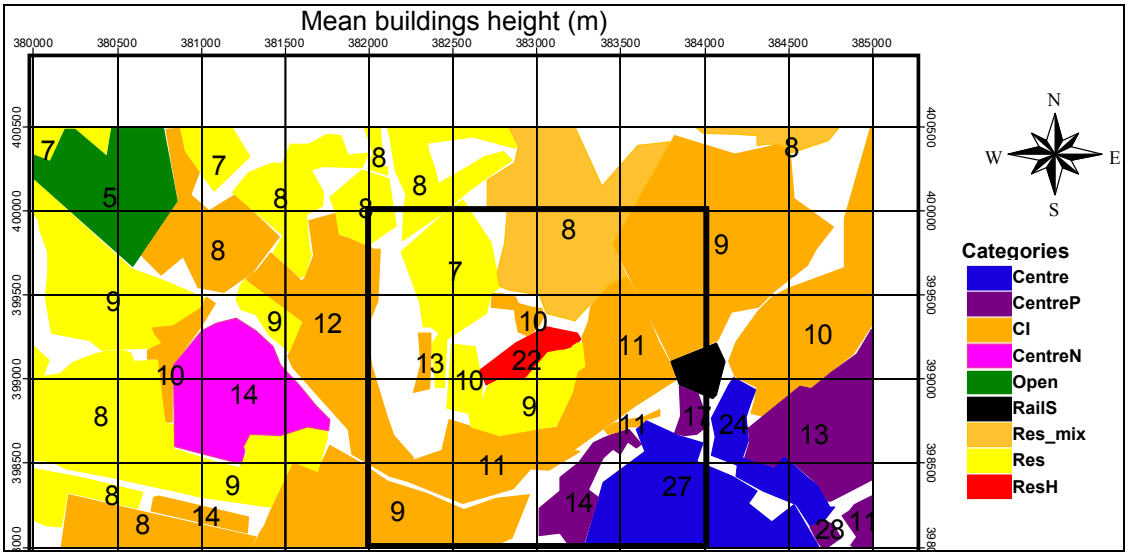

Figure 6.2 *- Preliminary mapping over Grid A. Mean buildings height (m) estimated for each tile of Grid A, indicated by the number placed over each tile. Different tile colours refer to different categories, as shown on the legend. The thin black lines indicate a grid of 500m resolution discussed later. Heavy black lines show the area covered by Grid B (**Figure 6.3**).*

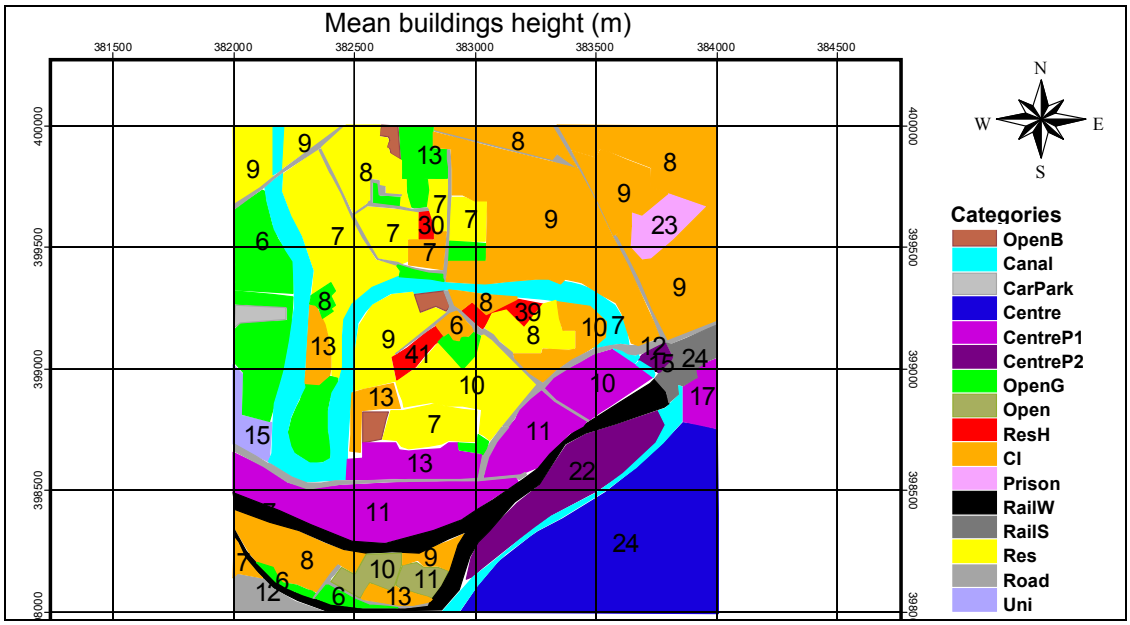

Figure 6.3 *- Preliminary mapping over Grid B. Mean buildings height (m) estimated for each tile of Grid B, indicated by the number placed over each tile. Different tile colours refer to different categories, as shown on the legend. The thin black lines indicate a grid of 500m resolution.*

Table 6.1 *- Preliminary land-use classifications for Greater Manchester. Land-use categories identified over Grid A and Grid B.*

Description	Grid A	Grid B
Manchester city centre. High density housing, rows, more then 2 levels, with some tall blocks.	**Centre**	**Centre**
Manchester city centre periphery. Medium density housing, rows, more then 2 levels.	**CentreP**	**CentreP1** **CentreP2**
New city centre (Salford precinct). Low density, tall blocks.	**CentreN**	
Low residential houses. Low density housing, 2 levels small houses with yards, equally spaced rows.	**Res**	**Res**
High residential apartments Low density residential tall blocks.	**ResH**	**ResH**
Low density housing, large low level commercial/ industrial buildings.	**CI**	**CI**
Mixture of low residential and commercial/ industrial buildings.	**Res_mix**	
University of Salford. Large buildings, parking lot, vegetated ground.		**Uni**
Prison		**Prison**
Railway Station	**RailS**	**RailS**
Rail way		**RailW**
Road		**Road**
Car park		**CarPark**
Open terrain, with few or no buildings.	**Open**	**OpenG** (Green) **OpenB** (Barren) **Open** (not well identified)
Canal		**Canal**

When delimitating the homogenous tiles, it is important to pay attention to the areas where high rise buildings might be surrounded by low construction. Also urban parks with tall trees must be considered. On the other hand, the presence of water layers has to be marked. Further analyses and improvements of this initial classification would lead to the final classification of land-use categories established over Greater Manchester, which is described in section 6.6 and **Table 6.3**.

6.4.2 A simple data analysis based on the tiles atributes, for a sample area

Having delimited the tiles it is necessary to assign numerical values to surface characteristics. Descriptive statistics of CR data for each tile of Grids A and B are

calculated and a characterisation of each tile in terms of some morphologic parameters is obtained, i. e., mean, maximum and standard deviation of the buildings height; mean, maximum, standard deviation of buildings plan area. The fraction of the built up area (plan area index) was also calculated.

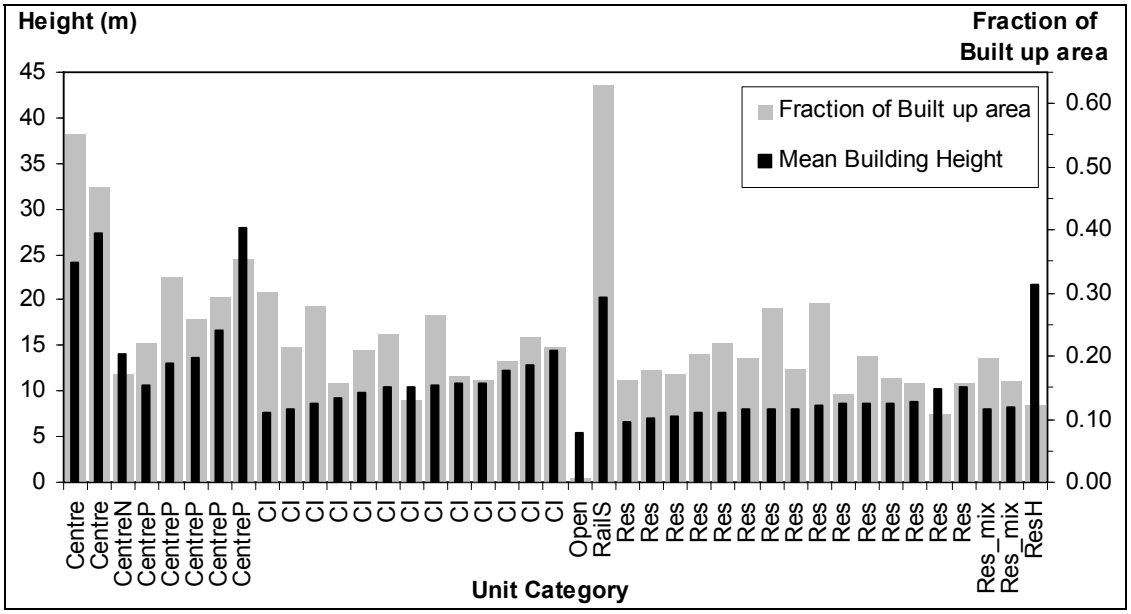

Figure 6.4 *- Statistics of CR data on each tile of Grid A: mean buildings height, and fraction of built up area (plan area index).*

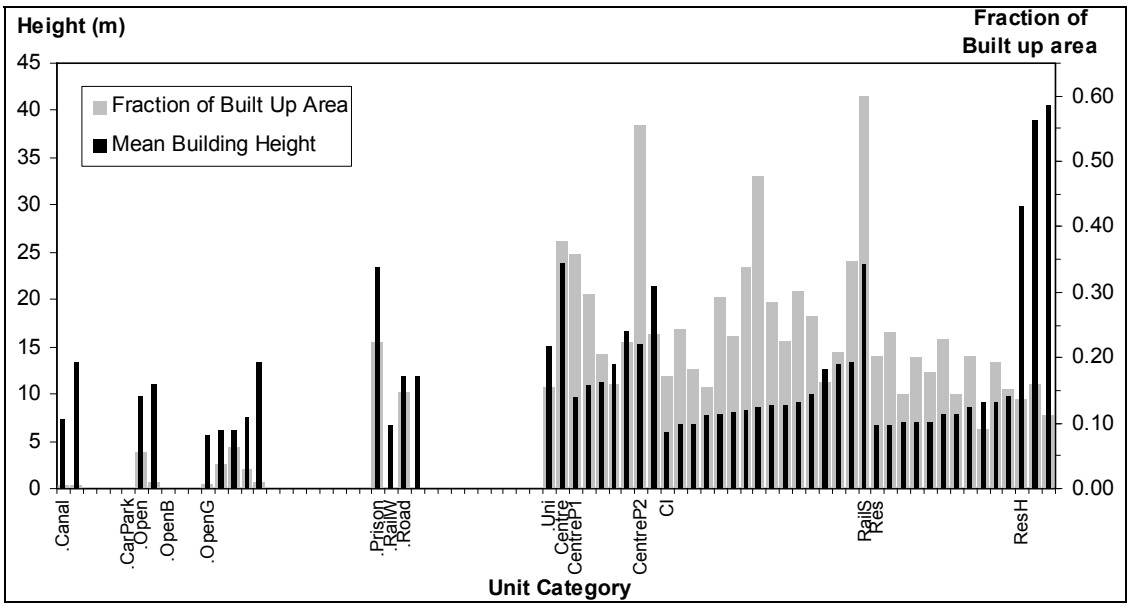

Figure 6.5 *- Statistics of CR data on each tile of Grid B: mean buildings height, and fraction of built up area (plan area index).*

Figure 6.4 and **Figure 6.5** show the results obtained for mean buildings height (also indicated in **Figure 6.2** and **Figure 6.3**) and fraction of the built up area (plan area index) over each tile. Note that, although some adjusts can to be done in the final mapping of tiles, in general this preliminary identification of homogeneous zones (tiles) and their classification into categories seems to be acceptable. In general, tiles grouped in the same category show similar values for the considered morphologic parameters. **Figure 6.6** maps the values of λ_P shown in **Figure 6.4** and **Figure 6.5.**

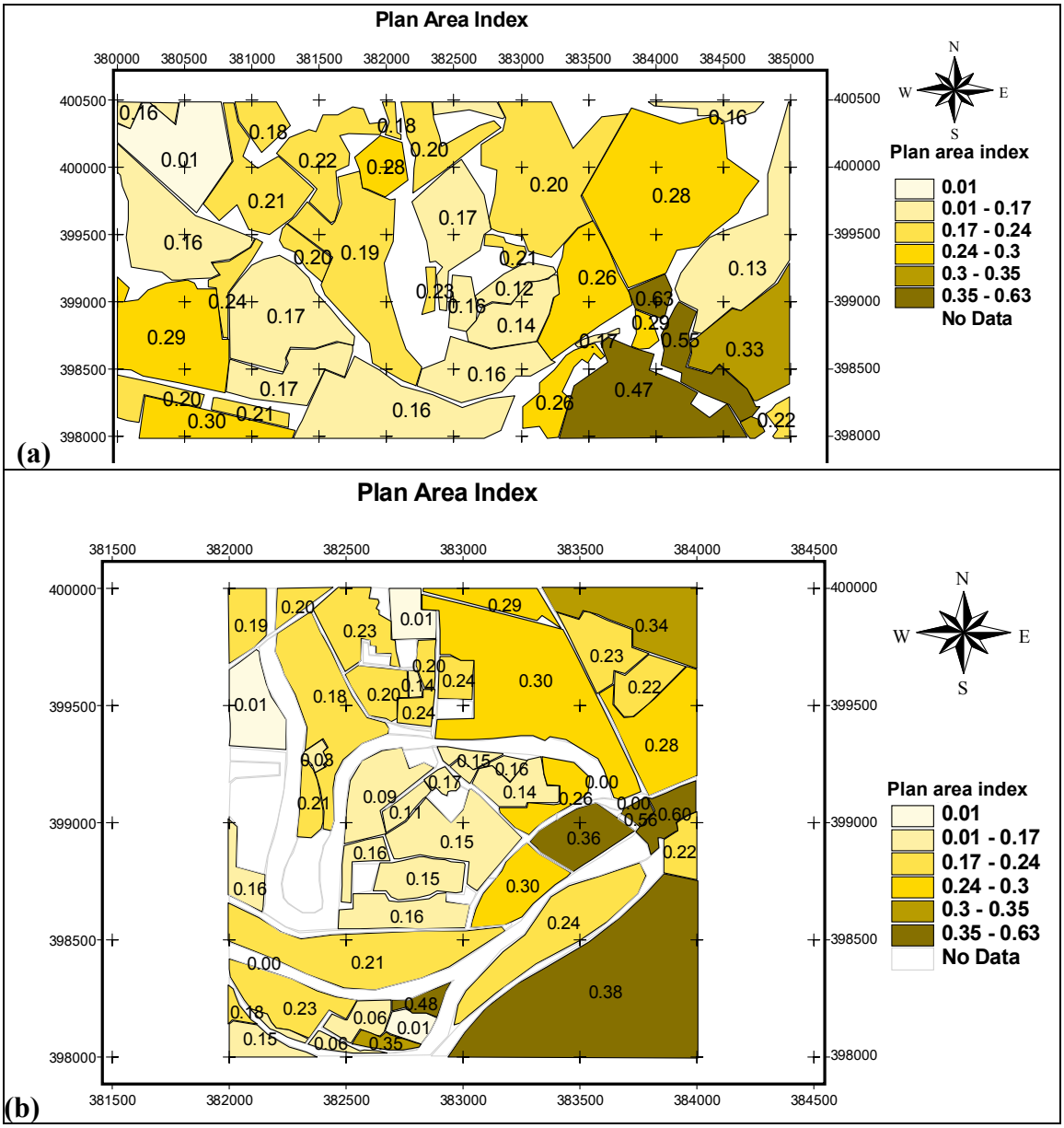

Figure 6.6 *- Fraction of built up area (Plan area index), λ_P, over (a) Grid A and (b) Grid B.*

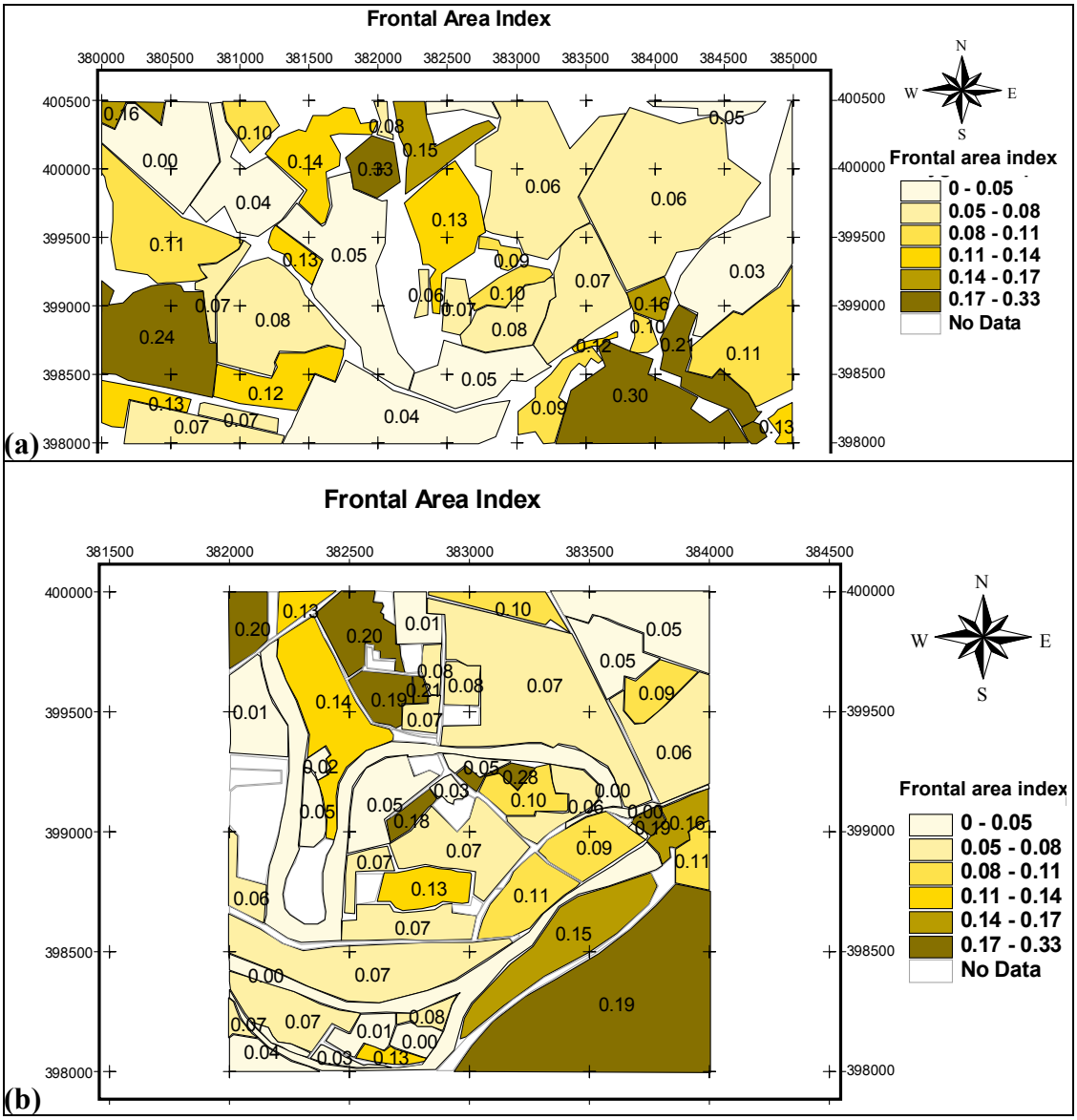

Figure 6.7 *- Frontal area index, λ_F, over (a) Grid A and (b) Grid B.*

Figure 6.6a and **Figure 6.6b** map the plan area index, λ_P, shown in **Figure 6.4** and **Figure 6.5**, for each tile of (a) Grid A and (b) Grid B, respectively. **Figure 6.7a** and **Figure 6.7b** map the frontal area index, λ_F, for each tile of Grids A and B. These values were obtained from CR data using the calculation described in section 6.3. The values of the plan area index and frontal area index are considerably high in the city centre and low in the typical residential zones, illustrating the roughness heterogeneity of the urban area (see also the maps of the mean buildings height in **Figure 6.2** and **Figure 6.3**). Note that other areas with high rise buildings are also evident, namely

Salford Precinct zone in **Figure 6.7a** (bottom, left hand side) and residential areas of high blocks (top, centre).

6.4.3 A simple data analysis by land-use category, for a sample area

A data analysis by land-use category has been carried out taking into consideration the global area of all tiles in each land-use category, and the categories have been characterised in terms of some morphologic parameters, such as mean buildings height, mean buildings area, and plan area index (**Figure 6.8 - Figure 6.10**, and **Table A2.1** in the Appendix 2).

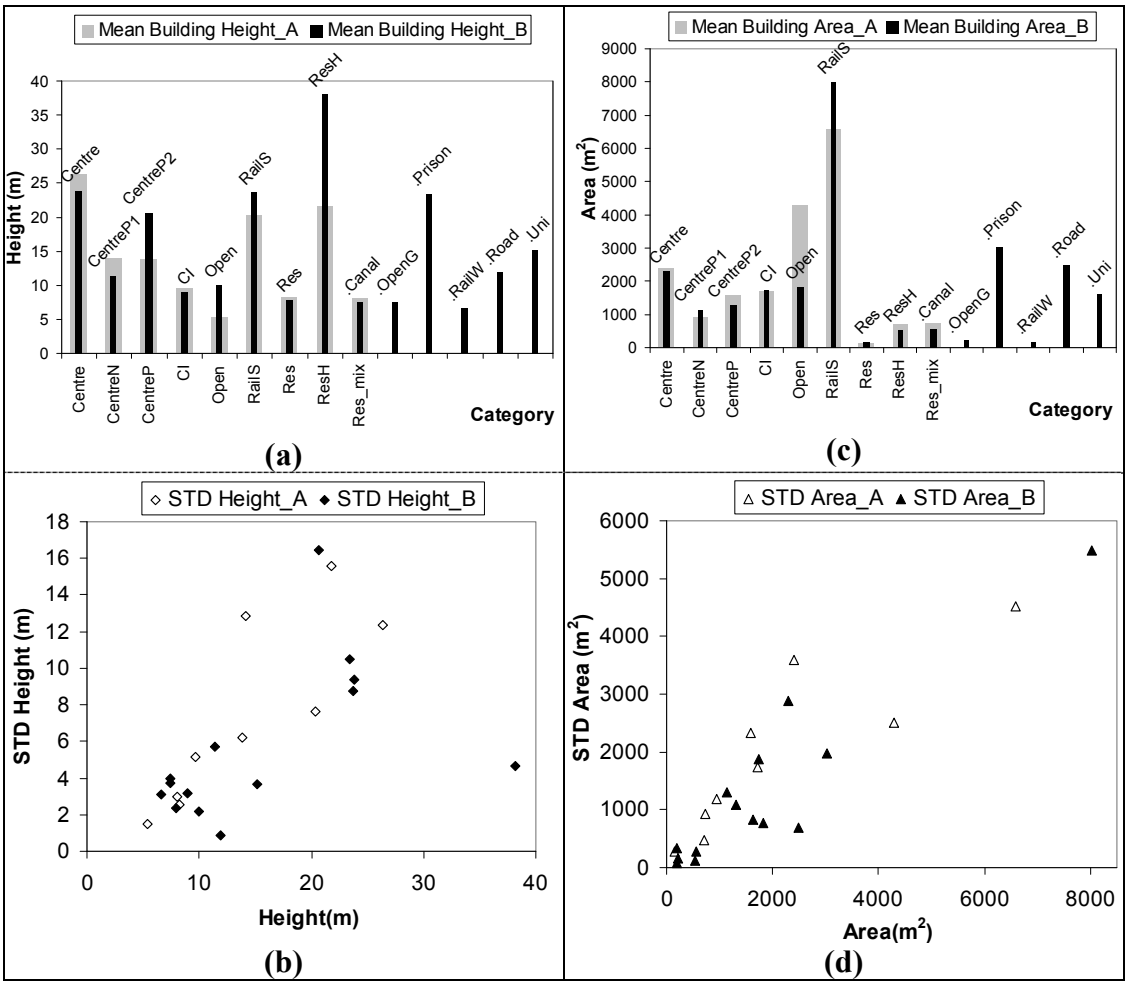

Figure 6.8 *- Statistics of CR data for each category derived for Grids A and B. (a) Mean buildings height (m), and (b) their standard deviations; (c) Mean buildings area (m^2), and (d) their standard deviations (see Appendix 2,* ***Table A2.1****). The labels placed above the black bars refer to the categories defined for Grid B, while the legends on the X axis refer to the categories defined for Grid A.*

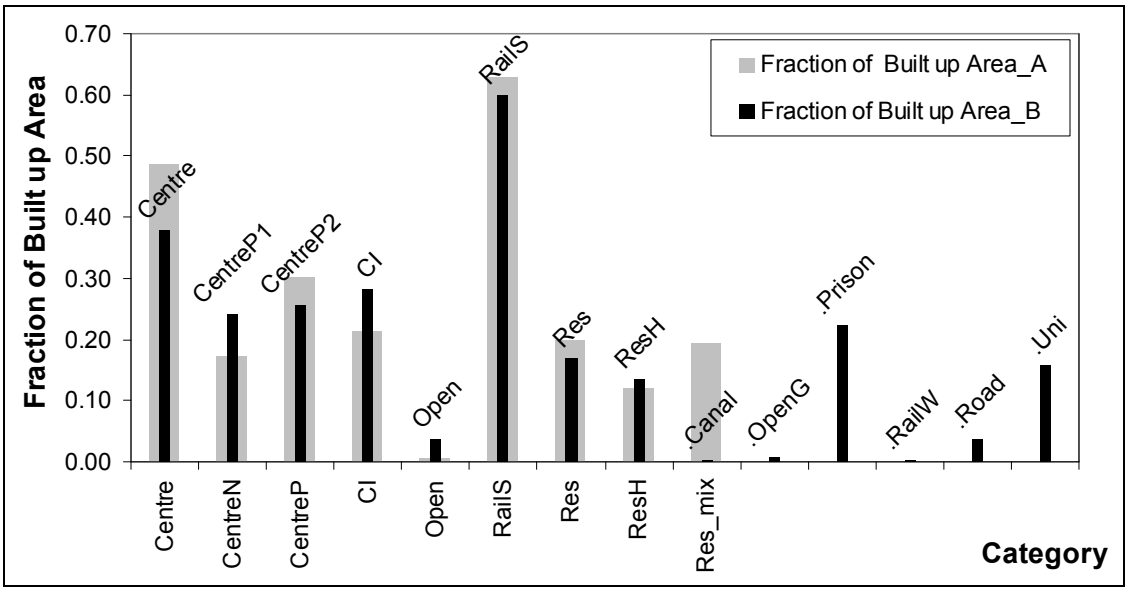

Figure 6.9 *- Fraction of built up area (plan area index) for each category. Estimates of the fraction of built up area performed over Grids A and B, based on the statistics of CR data for each category (see Appendix 2,* ***Table A2.1****). The labels placed above the black bars refer to the categories defined for Grid B, while the legends on the X axis refer to the categories defined for Grid A.*

Note the increase in the standard deviation of the buildings height as a function of buildings height shown in **Figure 6.8**. This indicates that zones of increasing high buildings tend to be more heterogeneous. **Figure 6.9** shows that the city centre has relatively high values of fraction of built up area, central zones are denser then others. Also an increase of the area of the buildings with increasing building height is suggested in **Figure 6.10**. On the other hand, the values of mean buildings height and area are not significant parameters for some categories since they correspond to averages over very few buildings. It is the case of the categories Open terrain, Canal, or Road, where the fraction of built up area is very low (**Figure 6.9**).

The values of the morphologic parameters associated to a certain category can be quite different depending on the grid that was used to make the data analyses (Grid A or Grid B). This reveals the importance of the size of the delimitated tiles and of the criteria for being homogeneous. It is necessary to consider not very large tiles, principally when there are high rise buildings, but on the other hand the size of the tiles should not be too small and must be adequate to the scale of the problem.

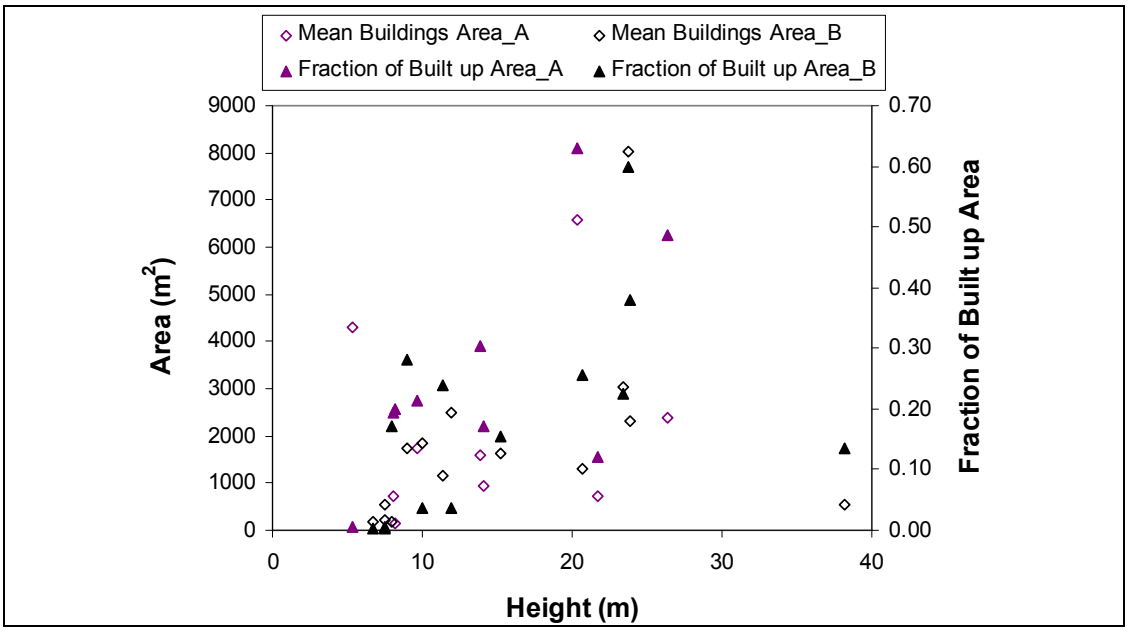

Figure 6.10 *- Mean buildings area and fraction of built up area (plan area index) versus mean buildings height for each category, based on Grid A (purple) and Grid B (black).*

Many of the tile properties are strongly related to, but not necessarily directly associated with, socio-economic activities. However, it was convenient to associate the tiles with some major land-use categories.

The most relevant categories in terms of their contribution to the urban surface roughness are those related to built areas. For certain categories over the study domain, such as *Road*, *Rail way*, *Canal*, *Open*, *Green* or *Barren*, the fraction of built up area is low, but in some cases they cover a considerable area which cannot be neglected in further studies. **Figure 6.11** shows the percentage of each land-use category for the sample area of Salford and Manchester.

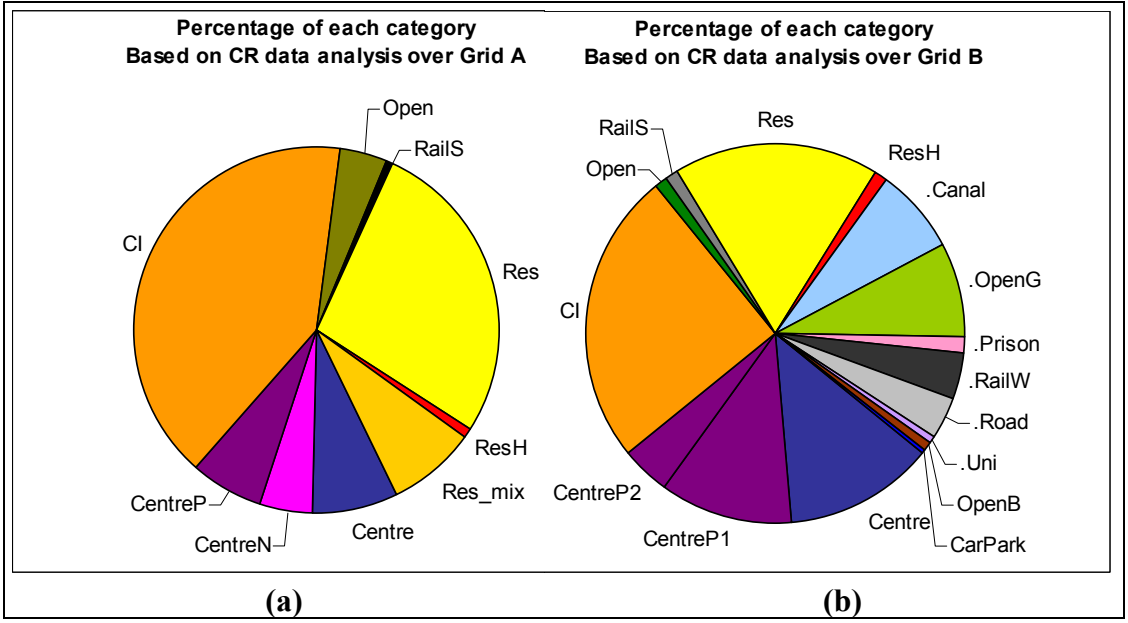

Figure 6.11 *- Categories distribution. Percentage of each category for a sample area covering a zone of Salford and Manchester over (a) a tile of 2.5km x 5km, using Grid A of* ***Figure 6.2*** *(b) a tile of 2 km x 2 km, using Grid B of* ***Figure 6.3****.*

6.5 Assessment of the frontal area index (λ_F) and of the derived height-normalized values of zero-plane displacement (z_D/z_H), for the sample area

6.5.1 Comparison between the estimates of frontal area index (λ_F) obtained from the CR data and values derived from Grimmond and Oke's (1999a) conceptual curve

As an alternative to the estimation of the frontal area index from the data set according to the formulation discussed in section **6.3** (and section **5.4**), the estimation of the frontal area index may be obtained from Grimmond and Oke (1999a) (reproduced in **Figure 5.3**), which shows a conceptual representation of the relation between height-normalized values of zero-plane displacement (z_D/z_H) and the packing density of roughness elements using (a) λ_P and (b) λ_F to describe density. The procedure adopted here to make this comparison is the following. Using the curve of the **Figure 5.3a**, the values of z_D/z_H are obtained from the observed values of λ_P. Then

the frontal area index, $\lambda_{F\_G\&O}$, is estimated using the curve of z_D/z_H *versus* frontal area index on **Figure 5.3b**. The comparison of these two approaches is based on the values of the frontal area index for Grid A.

Figure 6.12 shows the values of plan area index, λ_P, observed over each tile of Grid A and the values of frontal area index derived using both approaches, λ_F and λ_F_G&O. Also indicated are the mean buildings height, z_H, and the land-use category of each tile. The values of λ_F_G&O obtained from the Grimmond and Oke (1999a) curves tend to follow the same trend as the plan area index values λ_P. The lines corresponding to these two parameters are similar, and therefore there exists a good correspondence between the two parameters.

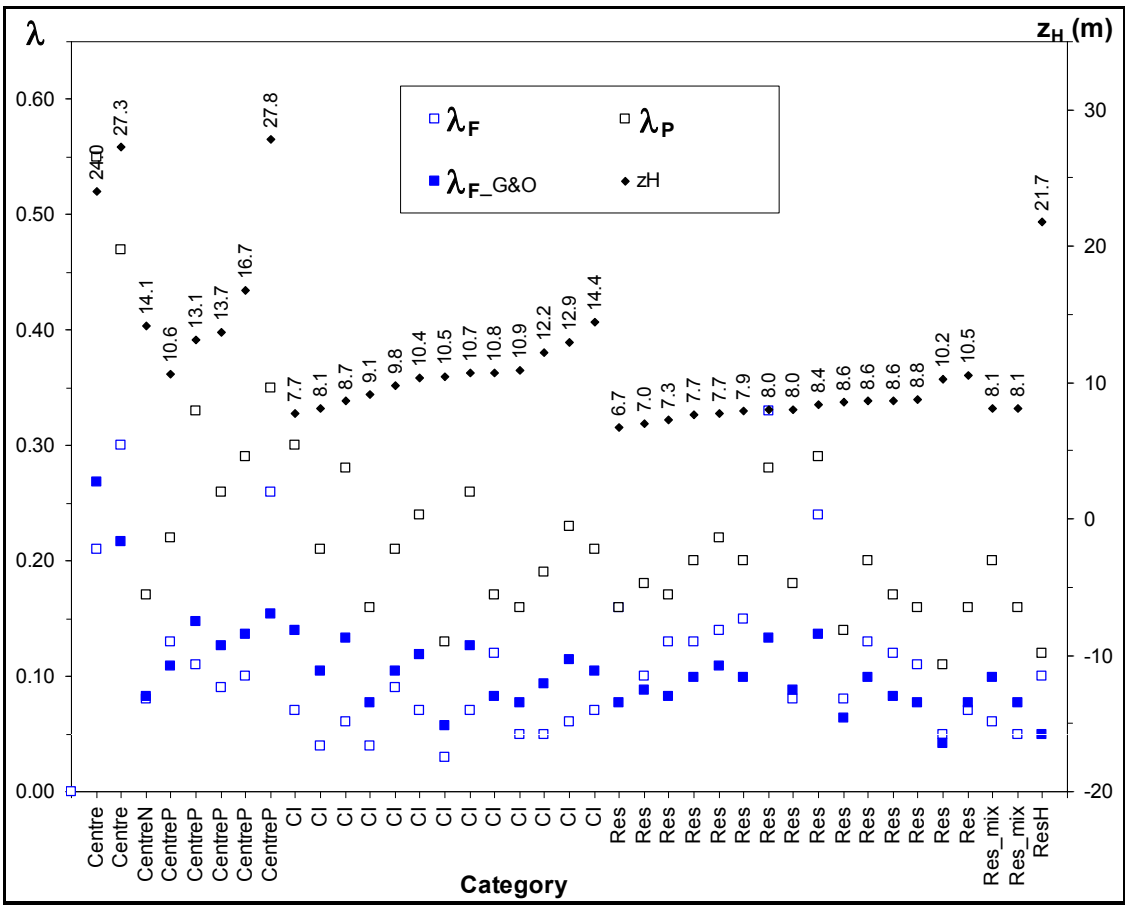

Figure 6.12 *- Frontal area index, plan area index and buildings height. Estimates of the frontal area index for each tile of Grid A,* ***[□ λ_F]*** *based on CR data set statistics and* ***[■ λ_F_G&O]*** *using the conceptual curves of Grimmond and Oke (1999a). Mean buildings height* ***[♦ z_H]*** *and plan area index* ***[□ λ_P]*** *for each tile of* ***Figure 6.2*** *and* ***Figure 6.6a*** *are also shown. The urban category associated to each tile is indicated by the label of the horizontal axis.*

Moreover, the graph of λ_F_G&O *versus* λ_P (**Figure 6.13**) supports the indication in the Grimmond and Oke conceptual curves that these two parameters might be correlated in a unique manner, which does not correspond to what might be expected to happen in real cities. In fact, a large plan area index doesn't necessarily leads to a large frontal area index. On the other hand, the representation of the observed values λ_F *versus* λ_P, in the same figure, shows that there is no evidence in this case of any trend curve corresponding closely to the λ_F_G&O curve (**Figure 5.3b**). Although there is a suggestion of a trend where small plan area index indicates small frontal area index, and vice-versa, there is a large variability.

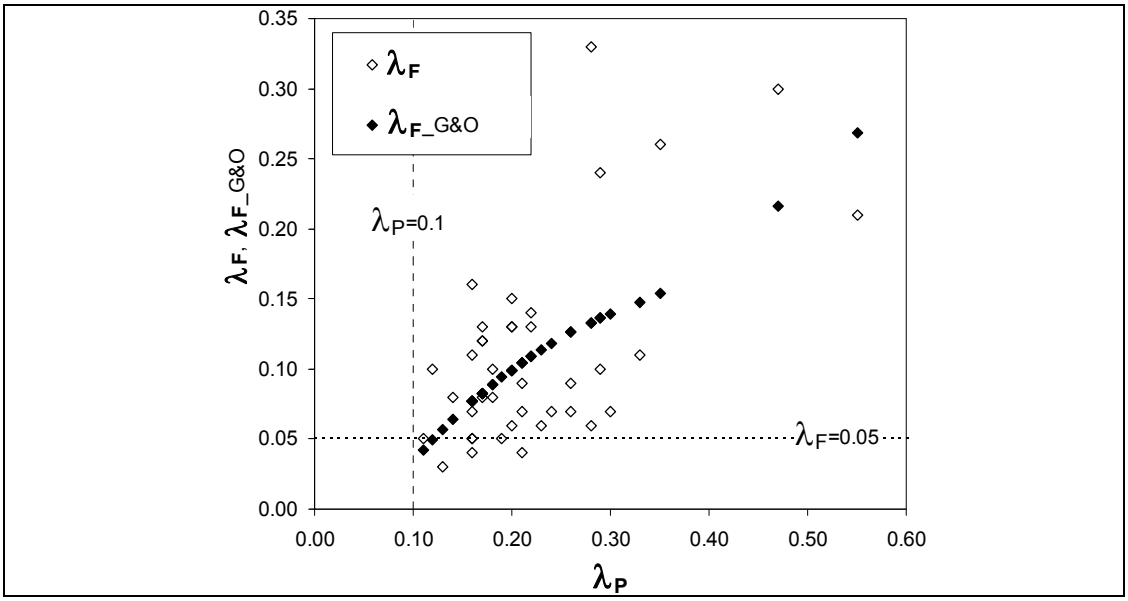

Figure 6.13 *- Frontal area index versus plan area index, λ_P, for Grid A. Estimates of λ_F are obtained from the CR data set and* ***λ_F_G&O*** *are given by the conceptual curves of Grimmond and Oke (1999a).*

Although, the values of λ_F_G&O obtained from the Grimmond and Oke curves do not match very well with the observed λ_F, the Grimmond and Oke points do represent the overall trend (see **Figure 6.12** and **Figure 6.13**). In cases where a more direct estimate of λ_F from a data set is not possible, the Grimmond and Oke curves can therefore be used to obtain "best guess" values of the frontal area index from λ_P.

6.5.2 Comparison between the estimates of height-normalized values of zero-plane displacement (z_D/z_H) obtained from Raupach's (1994, 1995) equation and from Grimmond and Oke's (1999a) conceptual curve

As discussed in section 5.4.2, the formulation proposed by Raupach (1994, 1995) (equation **5.4.4**) will be used to model the surface sensible heat flux, that is

$$\frac{z_D}{z_H} = 1 + \left\{ \frac{\exp\left[-\left(c_{d1} 2\lambda_F\right)^{0.5}\right] - 1}{\left(c_{d1} 2\lambda_F\right)^{0.5}} \right\}$$

where c_{d1} is a free parameter, with a typical value of $c_{d1} = 7.5$. Since it is possible to specify the height-normalized values of zero-plane displacement, z_D/z_H, as a function of λ_F, it is interesting to compare this relation with the equivalent curve in Grimmond and Oke (1999a) (**Figure 5.3b**). **Figure 6.14** shows z_D/z_H *versus* λ_F given by the Grimmond and Oke (1999a) curve (λ_F_G&O) and by the equation **5.4.4** (λ_F_Ra,model), for the range of λ_F values observed over the sample area (Grid A). As can be seen in the figure, there is a significant difference between both relations.

In fact the Grimmond and Oke (1999a) curve is a *conceptual* representation, as designated by the authors. **Figure 5.3b** illustrates their heuristic arguments that provide some quasi-physical reasoning to explain what happens when extra roughness elements are added to a surface. However these arguments are unable to give the exact shape of the curves so they are only sketched as shaded zones. However this approach is sufficient to suggest that it is reasonable to expect that these methods to predict z_D (and z_{0M}) should give estimates that track within them. These shaded areas are referred to by the authors as the ‘‘reasonable’’ zones or envelopes.

Figure 6.14 shows also that although the model values do not follow the Grimmond and Oke (1999a) curve, they lie inside the "reasonable" zone defined by the authors.

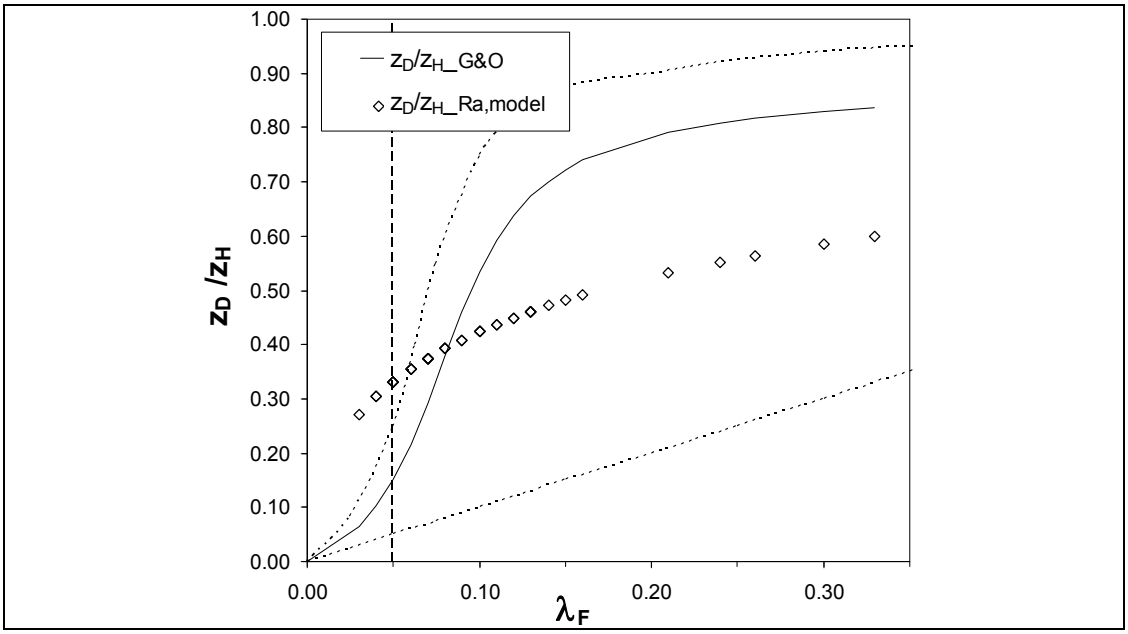

Figure 6.14 *- Height-normalized values of zero-plane displacement (z_D/z_H) versus frontal area index, for the range of λ_F values observed over the sample area (Grid A).* ***[z_D/z_H_G&O]*** *are given by the Grimmond and Oke (1999a) conceptual curve (**Figure 5.3b**), and* ***[z_D/z_H_Ra,model]*** *by the Raupach (1994, 1995) model equation 5.4.4. The vertical dashed line shows the lower limit of real-city frontal area index ($0.05 < \lambda_F < 0.47$) and envelopes contained by the curved dashed lines define the reasonable limits outlined in (**Figure 5.3b**), after Grimmond and Oke (1999a).*

6.6 Establishement of the land-use categories for Greater Manchester.

Considering the results previously obtained in section **6.4**, and after a re-examination of the data, the categories previously defined have been adjusted and a classification of 15 categories has finally been established. These categories are presented in **Table 6.2** and **Table 6.3** with some typical values for Greater Manchester. The values of the roughness parameters, such as mean surface elements height (z_H) and frontal area index (λ_F), necessary to model the surface sensible heat flux over the Greater Manchester study domain, are summarized in **Table 6.2**, for each land-use category. These include built-up areas, vegetated areas and water surfaces.

The attributes z_H, λ_P and λ_F for the first nine categories were obtained from the previous CR data analysis discussed in sections **6.2 - 6.4**. The letter (R) indicates the roughness parameters taken from the published literature, which have been used for the categories named as *Trees* (Grimmond *et al.*, 1998). For the rest of the categories very low values (*) for z_H and λ_F are assumed.

Note that, while for urbanized zones z_H and λ_F are estimated mainly from the geometric dimensions of the surface elements (buildings), for permeable-rough surfaces with vegetation and water surfaces these values are extrapolated from reference tables in the published literature. Although the definitions illustrated in **Figure 5.4** are general and apply to permeable-rough surfaces covered with vegetation, in this case it is not easy from geometric analyse to assign values to z_H and λ_F. Thus in our study the values of z_H=8.7 m and λ_F=0.18 are assumed for the land-cover category "trees", which are values presented by Grimmond *et al.* (1998) for urban parks with few trees. And the values of z_H=0.15 m and λ_F=0.01 are assigned to the category "green" (extrapolated from the roughness values of Pasquill (1950) for long grass; in Weiringa, 1993, and Brutsaert, 1982).

On the other hand in the Greater Manchester study domain the water surfaces are mainly small rivers, canals, and a reservoir, often surrounded by rows of trees. The reservoir sited some miles away from the city is quite big, occupying about two domain cells, but its environmental impact is beyond the scope of our study. In the present work, over water the values of z_H=0.001 m and λ_F=0.001 are assumed. It is expected that this will lead to results in agreement with parameterisations usually

considered over water: z_d= 0 and z_{0M} = 2 x 10^{-4} m (Brutsaert, 1982; Wieringa, 1993; Grimmond and Oke, 1999a).

It is assumed that the great variation in the surface heterogeneity over our study domain is mainly due to differences between urbanised and rural surface cover, and that over urban zones is due to the different types of the constructions. The rural vegetated zones in the Manchester region are relatively homogeneous (typically grass with a few scattered bushes and clumps of trees).

Table 6.2 *- Roughness parameters for each land-use category. Mean buildings height (z_H), plan area index (λ_P), frontal area index (λ_F), normalised zero plan displacement height estimated (z_D/z_H)(e) estimated from λ_F values shown on this table using equation 5.4.4, and mean horizontal plan area of the buildings, respectively.*

Category	z_H	λ_P	λ_F	z_D/z_H	H.Area
	(m)				(m^2)
Centre	26	0.51	0.26	0.56 (e)	2401
CentreN	14	0.17	0.08	0.39 (e)	942
CentreP	15	0.29	0.14	0.47 (e)	1581
CI	10	0.21	0.06	0.35 (e)	1718
RailS	20	0.63	0.16	0.49 (e)	6584
Res	8	0.19	0.13	0.46 (e)	142
Res_mix	8	0.18	0.06	0.35 (e)	736
ResH	22	0.12	0.10	0.42 (e)	715
Uni	15	0.16	0.06	0.35 (e)	1628
Trees	8.7 (R)	0.45 (R)	0.18 (R)		
Baren	0.05*		0.01*		
Green	0.15*		0.01*		
RailW	0.05*		0.01*		
Road	0.05*		0.01*		
Water	0.001*		0.001*		

The different categories have been compared with those presented by Ellefsen (1990/91) in **Table 6.3**. In general the Urban Terrain Zones (UTZ) identified by Ellefsen (1990/91) for U.S.A. cities can be significantly different from what is found in urbanised areas of United Kingdom. In the case of Salford and Manchester, for example, there are substantial green areas and the industrial and residential high rise buildings have important differences in their characteristics. However some of the UTZ are comparable to some urban categories present in our study area.

Table 6.3 - *Greater Manchester categories and Ellefsen (1990/91) UTZ. Categories defined for Salford and Manchester (first column) and Urban Terrain Zones (UTZ) of Ellefsen (1990/91). Mean buildings height (in storey and metre tiles, considering that one storey is about 3.5 m height); total of roof area in each UTZ; area of the UTZ; fraction of roof area. The values underlined refer to the Greater Manchester Categories (from* ***Table 6.2****); all the other values are for the UTZ of Ellefsen (1990/91).*

Greater Manchester Categories (Images adapted from *Google Earth-2006)*	**Ellefsen (1990/91) Urban Terrain Zones**	H (st.)	Hx3.5 (m)	Roof Area (ha)	U.T.Z. Area (ha)	F. of Roof Area
City Centre (Centre) High density housing, rows, more then 2 levels, with some tall blocks. 	**A1 Attached high-rise commercial** The core area. The old down town composed mainly of offices and stores. 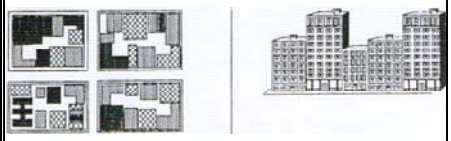	8.8	26/ 31 <u>26</u>	43	114	0.38 <u>0.51</u>
City Centre Periphery (CentreP) Medium density housing, rows, more then 2 levels.	**A2 Attached apartments & hotels**. Core periphery. 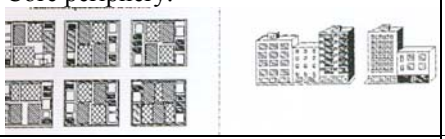	5.0	15/18 <u>15</u>	43	114	0.38 <u>0.29</u>
	A4 Attached buildings, Industrial/ Storage. Near the core.	3.9	12/14	58	162	0.36
	Dc1 Redeveloped core area.	28.4	85/99	20	105	0.19
New Centre (CentreN) Low density, tall blocks. 	**Dc8 Outer city**. 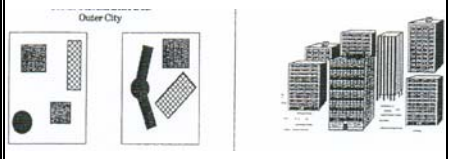	6.1	18/21 <u>14</u>	12	157	0.11 <u>0.17</u>
Residential High (ResH) Low density residential tall blocks. 	**Do2 Detached, open-set planned apartments.** 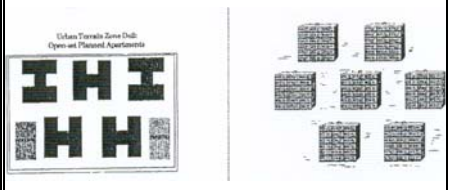	5.2	16/18 <u>22</u>	251	1090	0.23 <u>0.12</u>
	Dc2 Close-set apartments (blocks).	3.1	9/ 11	252	913	0.28

	Do3 Detached, open-set houses.	1.6	5/ 6	650	6530	0.10
Residential (Res) Low density housing, 2 levels small houses with yards, equally spaced rows. 	**A3 Attached houses.** Residential. Attached houses. The typical "row houses".  **Dc3 Close-set detached houses.** 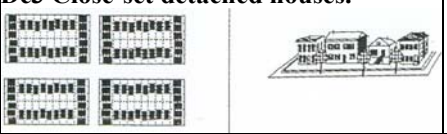	1.2 1.7	4/ 4 5/ 6 8	768 2766	2503 12893	0.31 0.21 0.19
Commercial/ Residential (Res_mix) Mixed of low residential and commercial/ industrial buildings. 			8			0.18
	A5 Attached commercial buildings on string streets outward from the core. Old commercial ribbons.	2.5	8/ 9	204	341	0.60
	Dc5 Close-set commercial string street Close-set commercial ribbons, along major arterials.	1.7	5/ 6	173	582	0.30
Commercial/ Industrial (CI). Low density housing, large low level buildings. 	**Do4 Open-set detached industrial/ storage.** 	2.0	6/ 7 10	366	1886	0.19 0.21
	Do5 Large unit commercial ribbon. Detached new buildings.	1.6	5/ 6	24	672	0.04
	Do1 Shopping centres (open-set).	2.4	7/ 8	20	312	0.06
Railway Station (RailS)	**Dc4 Railroad/dock related industrial storage**.	2.4	7/ 8 20	585	2813	0.36 0.63
University (Uni) Large buildings, parking lot, vegetated ground.	**Do6 Administrative/Cultural**. 	4.0	12/ 14 15	187	1170	0.16 0.16

6.7 Mapping the surface roughness parameters over a rectangular grid of 1x1km^2 resolution, for the Greater Manchester study area (24 x 24 km^2)

6.7.1 Tests of mapping morphologic surface parameters over a rectangular grid taking a sample area

As before, first a sample area has been considered in order to test the procedure that will be used later for the entire study area. Thus, a regular grid with square tiles of 500m x 500m has been placed over the sample area. The grid lines are also shown on **Figure 6.2** and **Figure 6.3**. The rectangular grid, designed Grid C, has been created because, in general, a characterisation of the study area in this regular base is more convenient for subsequent use with meteorological numerical models.

As for the non regular Grids A and B, also for the rectangular Grid C some descriptive statistics of CR data have been carried out over the same sample area, and the region has been characterised in this regular base in terms of height of the buildings, z_H, the plan area index (fraction of built up area), λ_P, and the frontal area index, λ_F.

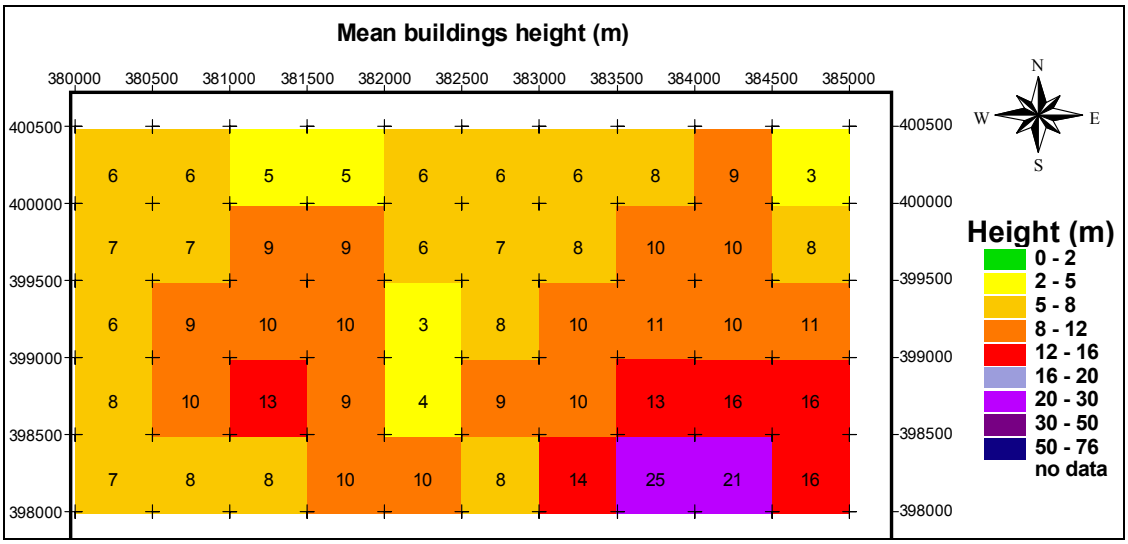

Figure 6.15 *- Mean buildings height over the sample area, using a rectangular grid. The mean buildings height (m) for each cell of the rectangular grid is indicated by the number placed over each cell. Different cell colours refer to different classes of mean building height (m), as shown on the legend.*

In this case, the values of the plan area index, λ_P, are directly obtained from the intersection of the CR data set layer with each cell of Grid C on the same way as it has been done for Grids A and B. The estimates of the height of the buildings, z_H, and of the frontal area index, λ_F, for each cell of the squared Grid C are area-weighted averages of the values previously obtained for each urban category, considering the percentage of each category present in the grid cell. The results thus obtained are mapped on **Figure 6.15** to **Figure 6.17**.

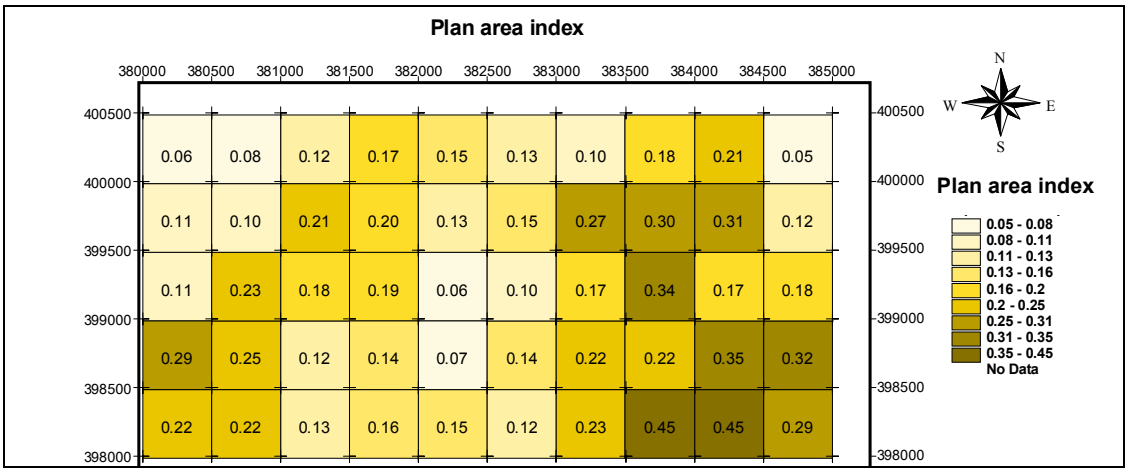

Figure 6.16 *- Plan area index over the sample area, using a rectangular grid. The plan area index,* λ_P*, for each cell is indicated by the number placed over each cell. Different cell colours refer to different classes of* λ_P*, as shown on the legend.*

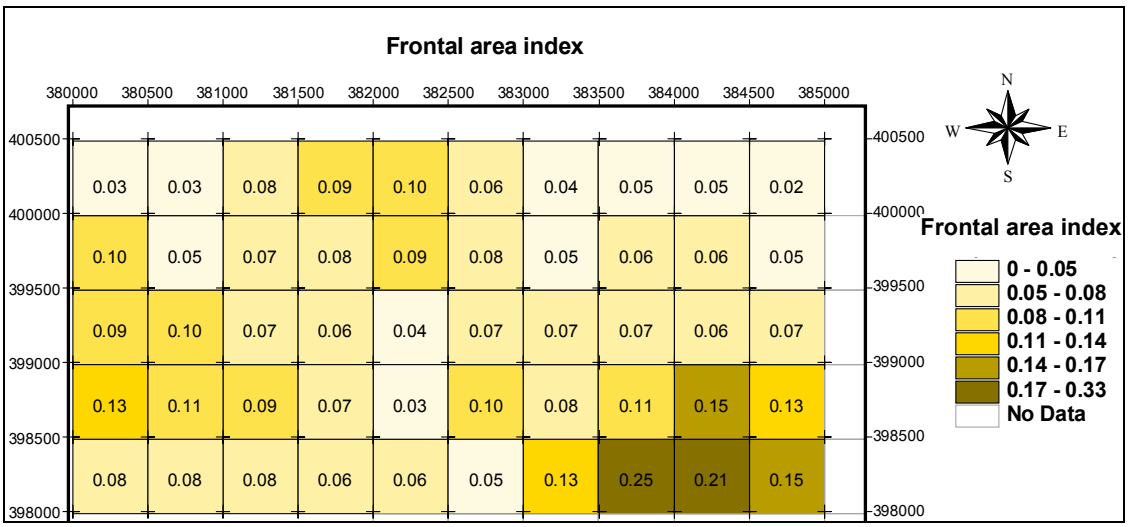

Figure 6.17 *- Frontal area index over the sample area, using a rectangular grid. The frontal area index,* λ_F*, for each cell is indicated by the number placed over each cell. Different cell colours refer to different classes of* λ_F*, as shown on the legend.*

6.7.2 Mapping the surface roughness parameters over a rectangular grid of 1x1km^2 resolution, for the Greater Manchester study area (24 x 24 km^2)

Based essentially on maps and aerial photographs [www.multimap.com, scale: 1/25000], the identification of the different land use categories has been extended to the entire study domain (24 x 24 km^2). The dimensions of the area of interest are based on the typical local scale of the convective processes (to ensure the area would embrace several convective cells). Tiles of similar morphology and surface cover are delimited forming a non regular polygonal grid over the study area. These tiles are classified according to the reference categories previously established in section **6.6**, and the respective roughness parameters are assigned according to **Table 6.2**. **Figure 6.18** illustrates the procedure used to identify and mark the different categories over the entire study area using ArcView software.

A regular grid with square cells of 1x1 km^2 has been placed over the study domain. The intersection of the polygonal and the squared grids enables estimation of the area of each category in each domain cell of 1x1 km^2. The sum of the areal percentages of the urban categories (Res, ResH, Res_mix, CI, Centre, CentreN, CentreP, RailS, Uni, and Road) in each domain cell gives the fraction of urbanised area. These estimates are shown in **Figure 6.19**, which reveals the spatial variation of the degree of urbanisation for the present Greater Manchester study area.

The values of the mean height of the surface elements, z_H, and frontal area index, λ_F, for each cell depend on the percent of each land-cover present, since they are area-weighted averages of the respective values assigned to each land-use category present (**Table 6.2**). The results for a particular cell will reflect the characteristics of the predominant land-use category. The estimates of z_H and λ_F obtained for Greater Manchester study area, over a rectangular grid of 1x1 km^2, are shown on **Figure 6.20a** and **Figure 6.20b**. Note the difference between the rural areas to the east and south compared to the urban areas. The area of high rise buildings is clearly evident.

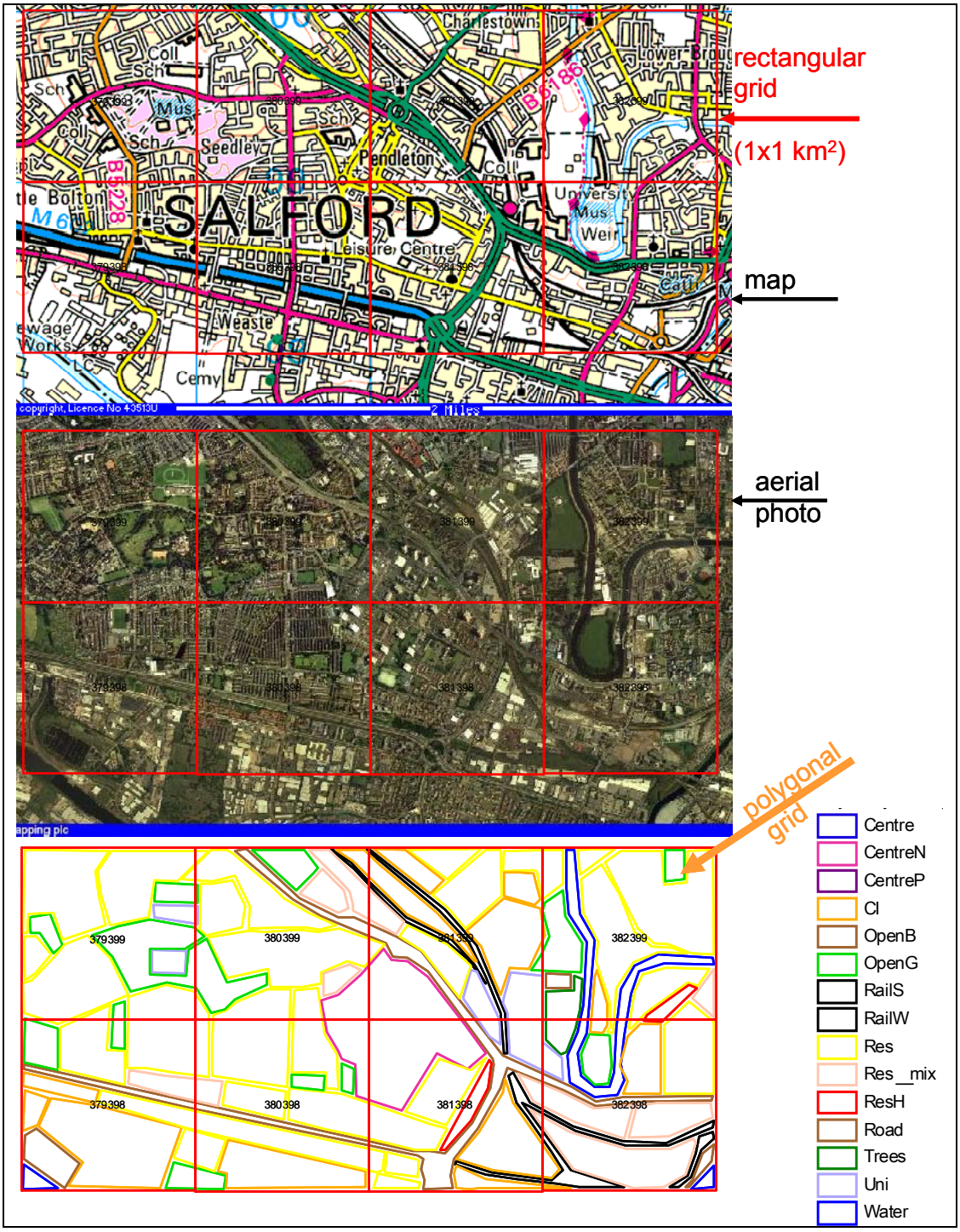

Figure 6.18 *- Illustration of the procedure used to identify and mark the different categories over the entire study domain. Arc View software is used, and based essentially on the map and aerial photograph layers (created from images available in www.multimap.com) it was possible to draw the polygonal grid. The number centred in each square cell (1x1 km²) gives the U.K. National grid coordinates (in km) of the cell inferior left corner; the first three digits are the latitudinal coordinate and the last three are the longitudinal coordinate.*

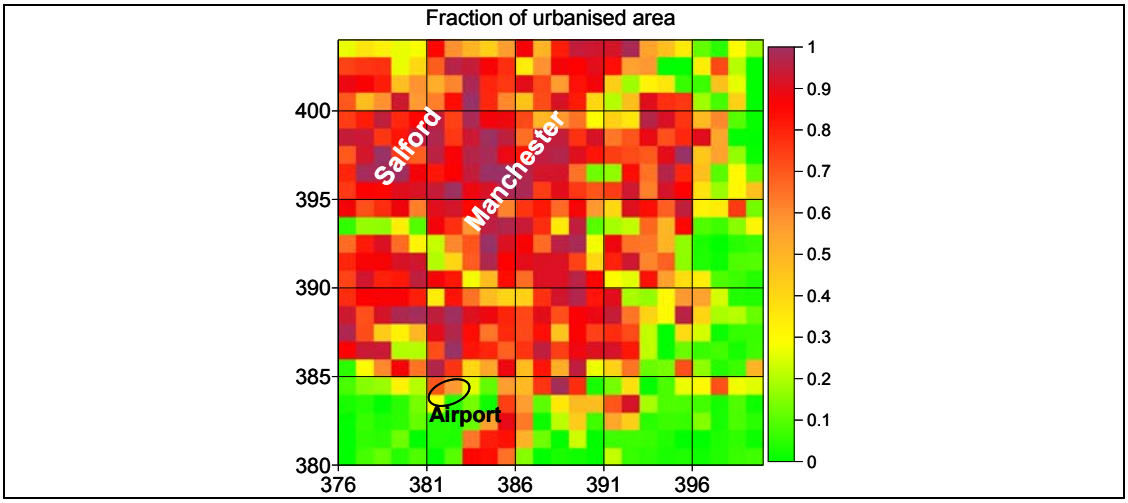

Figure 6.19 *- Fraction of urbanised area for the Greater Manchester study domain. The coordinates X and Y are the U.K. National Coordinates. The total study area is 24 x 24 km^2 and the area of each grid square 1x1 km^2. The legend on the right-hand side refers to the values of the fraction of urbanised area.*

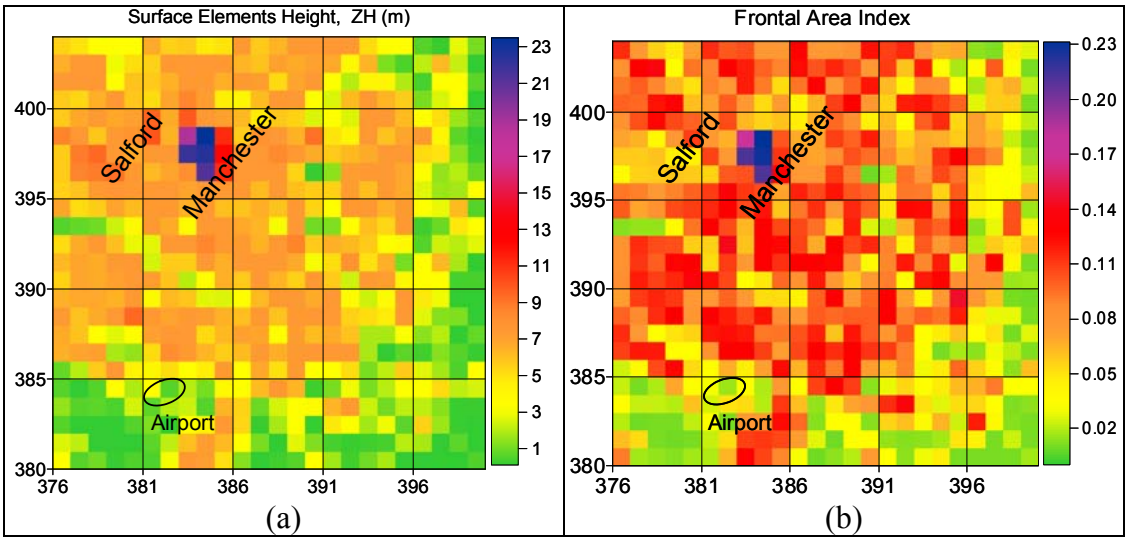

Figure 6.20 *- Roughness data for the Greater Manchester study domain shown in Figure 6.19. The coordinates X and Y are the U.K. National Coordinates. The total study area is 24 x 24 km^2 and the area of each grid square 1x1 km^2. (a) Mean building height, z_H, for each cell in the study domain. The legend on the right-hand side refers to the values of z_H expressed in m. (b) Mean frontal area index, λ_F, for the same study area. The legend on the right-hand side refers to the values of λ_F. Statistics of z_H and λ_F over the entire study domain are shown in* ***Table A2.2*** *of the Appendix 2.*

The roughness parameters z_H and λ_F mapped in **Figure 6.20** were used to model the spatial distribution of surface sensible heat flux over the Greater Manchester urban area. The formulation scheme discussed in Chapter 5 [Raupach's (1994, 1995) method, equations 5.4.4 to 5.4.6] to calculate the zero-plane displacement length, z_D, and roughness length for momentum, z_{0M}, was applied for all the cells of the study domain. **Figure 6.21a** and **Figure 6.21b** show the model estimates of the roughness parameters z_D and z_{0M}, over the study area, derived from the values of z_H and λ_F shown in **Figure 6.20**. These are surface roughness parameters characteristic of the Greater Manchester study area and considered to be the same for all study days.

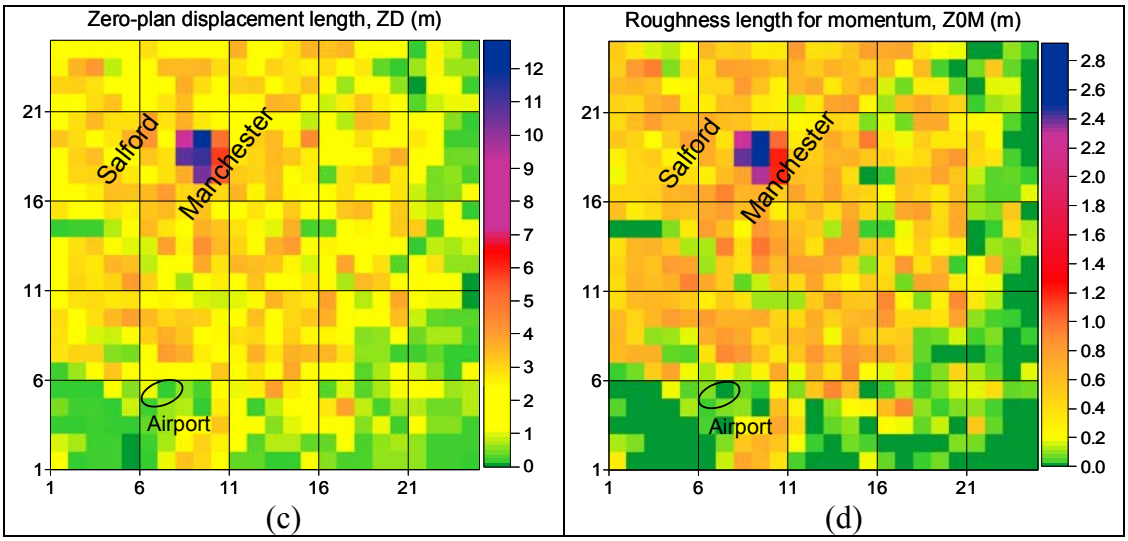

Figure 6.21 *- Model estimates of roughness parameters for the Greater Manchester study domain shown in* ***Figure 6.19****. The total study area is 24 x 24 km^2 and the area of each grid square 1 km^2. (a) Zero-plan displacement height, z_D, for each domain cell. The legend on the right-hand side refers to the values of z_D expressed in m. (b) Roughness height for momentum, z_{0M}, for each domain cell. The legend on the right-hand side refers to the values of z_{0M} expressed in m. Statistics of z_D and z_{0M} over the entire study domain are shown in* ***Table A2.2*** *of the Appendix 2.*

Note that taking all the roughness values over the entire study domain it was found that z_D=5z_{0M}, z_D=0.4z_H , z_{0M}= 0.08z_H (see **Figure 6.22**). These results are in agreement with published literature (see, for example, Grimmond and Oke 1999a).

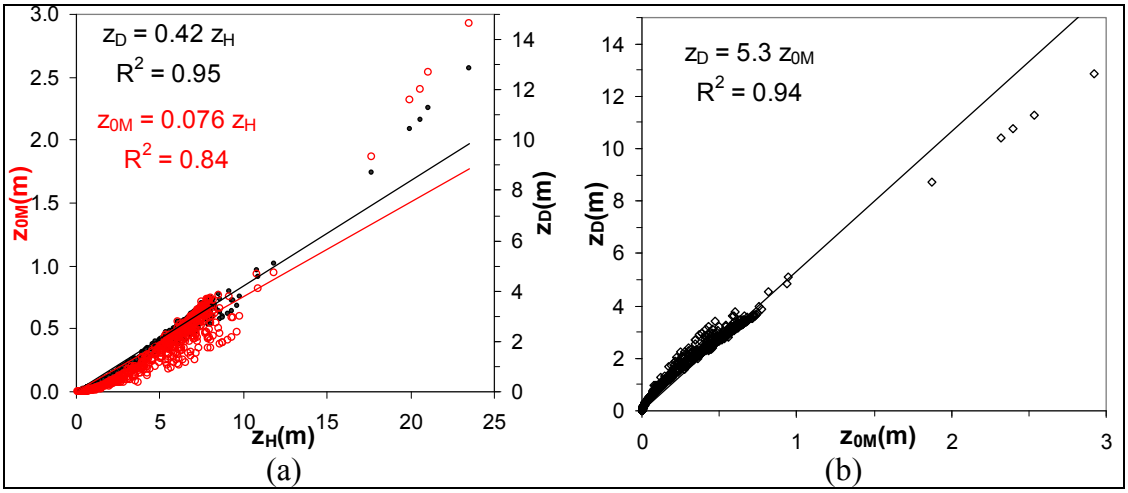

Figure 6.22 *- (a) Zero plan displacement length, z_D, and roughness length for momentum, z_{0m}, as functions of the surface roughness elements height, z_H. (b) Zero plan displacement length, z_D, versus roughness length for momentum, z_{0M}. Each line represents the fitted linear function between a pair of variables resulting from linear regression. R is the linear correlation coefficient.*

6.8 Concluding remarks

An approach to deriving key parameters used in modelling the urban atmospheric boundary layer, in particular to model the surface sensible heat flux, has been described and tested.

A classification of 15 land-use categories has been established for Greater Manchester and reference morphologic parameters, such as surface elements height, z_H, and frontal area index, λ_F, were attributed to each category. Comparisons with earlier published work revealed similarities to previous representations, but also some differences. These differences are probably due to the nature of the urban areas in the United Kingdom, for example the distribution and type of buildings and green spaces.

The surface elements height, z_H, and frontal area index, λ_F, were mapped over a rectangular grid of 1 x 1 km^2 resolution, for the Greater Manchester study domain. The estimates of z_H and λ_F for each grid cell are area-weighted averages of the values attributed for each land-use category, considering the percentage of each category present in the cell.

The model estimates of the zero-plane displacement length, z_D, and roughness length for momentum, z_{0M}, derived from the values of z_H and λ_F, were also presented for the study domain over a rectangular grid of 1 x 1 km^2 resolution. These estimates of the roughness parameters z_D and z_{0M} are comparable to previously published values. In addition, taking the roughness values obtained for the entire study domain it was found that $z_D=5z_{0M}$, $z_D=0.4z_H$, $z_{0M}=0.08z_H$. These results are in agreement with published literature (see, for example, Grimmond and Oke 1999a).

The 1 km^2 resolution maps of z_D, z_{0M}, z_H and λ_F for the study area (24x24 km^2) clearly show the Manchester city centre and surrounding urban area. Rural areas, presenting low roughess values, are shown on the borders of the study area to the south and east. Suburban areas such as Salford and Sale to the west, and Stockport to the south-southeast of Manchester. Also evident is the Mersey River Valley which runs from the west perimeter of the study area approximately 4-5 km south of Manchester city centre. The Valley is evident in the data for a length of approximately 10 km as it runs initially east and then southeast.

Note that, as it was discussed in (Wieringa, 1993), the effective roughness of heterogeneous terrain exceeds the area-weighted arithmetical average of the z_{0M} values of individual patches, $\overline{z_{0M}}$, because relatively rough patches contribute more than their area fraction to the integral effective roughness (see also Garrat, 1992, for a discussion about the effective roughness). Thus the area- weighted average used in the present study might not be the more adequate way to obtain mean roughness parameters representative of a certain area. This aspect deserves more investigation, and has to be taken into consideration in future works.

In the present study the study domain was described in a static sense. One description was used for all periods of measurements or modelling, which does not vary with wind direction or meteorological conditions (e.g., atmospheric stability). In reality surface properties are spatially heterogeneous and there are preferred wind directions. Consequently, the properties of the surface area contributing to a turbulent flux at any point are constantly changing. This suggests a dynamic approach, where the surface characteristics and changing meteorological conditions are taken into account, may be a more appropriate way to describe a site when measurements are

being conducted, especially if modelled data are to be evaluated against measured data to ensure spatial consistency (Grimmond, 1992; Grimmond and Souch, 1994).

The surface area contributing to a flux measurement, or source area (Schmid and Oke, 1990), is dependent on the process involved, the instrumentation used and the meteorological conditions under which the measurements occurred. The dimensions of the source area for the turbulent fluxes can be determined using the Schmid and Oke (1990) Source Area Model (SAM). The SAM outputs consists of weighted elliptically shaped source areas for each hour with dimensions that are a fairly sensitive function of the sensor height, and are further affected by stability and roughness, in that order of importance. Using the SAM ellipses with a GIS it is possible to determine the area influencing the measurements and objectively describe the site, or determine parameters for models which are to be evaluated against the measured data. However in the present study this approach was not adopted.

Chapter 7. Application of the model to Greater Manchester: simulations of surface sensible heat flux

In this Chapter, the model is applied to Greater Manchester for three case studies (on 2 May 2002, 14 and 21 June 2004). The objective is to generate fields of surface sensible heat flux over Greater Manchester in order to look for any patterns that may indicate areas of increased surface sensible heat flux, which might be related to downwind convective initiation.

Thus, in Section 7.1 and Section 7.2 the study domain and the selected study days are described. In Section 7.3 observations of air temperature and wind, at five weather stations located in the study domain, are analysed. Also the radiometric surface temperatures obtained from satellite imagery over the Greater Manchester study area are discussed. Some measurements of sensible heat flux from two ground based observational sites are presented. In Section 7.4 the values of the model input data over the entire study domain are specified for the three study cases. In Section 7.5 the results of the surface sensible heat flux model simulations over the study area for the three case studies are shown, and compared with observations. In Section (7.6) model estimates of the roughness length for sensible heat flux and excess resistance for heat are discussed. In Section 7.7 the impact of surface heterogeneity on the distribution of surface sensible heat flux is discussed. Some tests to evaluate the sensitivity of the modelled surface sensible heat flux to the surface roughness and surface temperature are carried out based on Greater Manchester conditions for the three study cases. The selection of the case studies proved difficult. It was necessary to select synoptic situations having westerly winds to limit any orographic effects over the city. The Pennines and the West Pennine Moors lie to the east and north of the city respectively. Also it was necessary to select days on which there was little or no cloud before convective cloud development as the model needed to operate with surface temperatures derived from satellite data. A further limitation was the lack of other meteorological data on specific days. All these difficulties limited the availability of

case study days. Even so one of the case studies (2 May 2002) was significantly restricted by the presence of cloud over the urban area. The author would have liked to undertake further case studies had the data been available for her.

7.1 The study domain

The model is implemented over Greater Manchester on a study domain of 24x24 km^2, using a grid of 1x1 km^2 resolution. The study area comprises Manchester city centre and some major suburbs, namely Salford and Stockport, Manchester International Airport and some non urbanised areas located mostly to the East and South. The terrain is quite flat; to the east it is bounded by the main Pennine chain of hills, and to the north by the West Pennine Moors, the most significant features in the region, but in the other directions, principally to the west, there are no significant relief features (**Figure 7.1**). The surface sensible heat flux model is applied to the Greater Manchester study area for three selected study days.

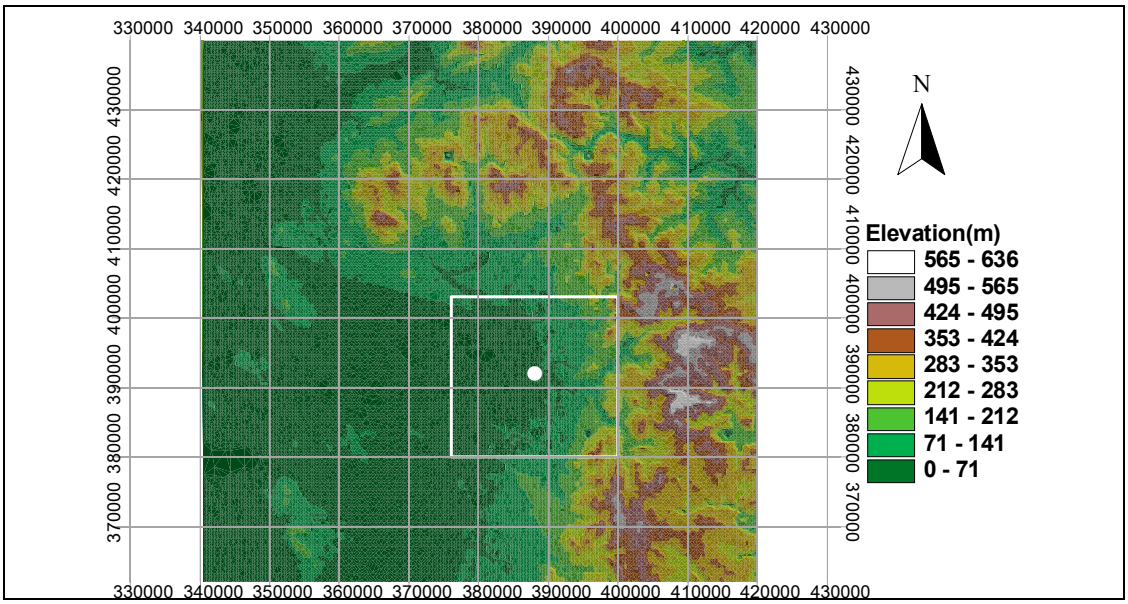

Figure 7.1 *- Relief in the Manchester region obtained from the Land-Form PANORAMA product provided by the Ordnance Survey, UK [http://www.ordnancesurvey.co.uk/]. The white square delimits the Greater Manchester study area of 24x24km^2. The coordinates X and Y are the U.K. National Grid Coordinates. The legend on the right-hand side refers to the values of the height above sea level expressed in metres.*

7.2 Study days

The main objective of our study is to apply the model to the Manchester urban area for convective daytime summer conditions for which the atmosphere is unstable and moist. These are conditions for which we anticipate that the urban morphology will modify the distribution of sensible heat flux and influence convective development.

The selection of the study days depends on the occurrence of synoptic convective conditions, with westerly winds and a cloud free sky, followed by rain events. Westerly wind conditions are required to avoid the effect of the presence of the Pennines, and the satellite radiometric surface temperature is only available when clouds are absent. The model is implemented for dry terrain conditions, at around 12 UTC when surface sensible heat flux is considerable and later convective showers are expected.

To meet all these criteria is not easy, and this represents a limitation to the application of the model to real study cases in the British islands, in particular because cloud free conditions are quite rare. However Shaw (1962) stated that a considerable proportion of the total precipitation (34–50%) is of convective origin in northern England.

Note that it is not likely to observe cloud free conditions before rain events! On the other hand the comparison of model estimates of Q_H and observations does not require the occurrence of later rain events.

In the present work surface sensible heat flux model estimates are compared with observations for three case studies, on 2nd May 2002, 14 and 21 June 2004 when observations *in situ* of surface sensible heat flux and radiometric surface temperature from satellite imagery are available, and the wind blows from the NW (see pressure maps and MODIS imagery in **Figure A3.1** of Appendix A3). On 21 June 2004, when rainfall radar data are available, the model is applied to a case for which convection is initiated (Chapter 8).

7.3 Observations

Air temperature, wind, and surface temperature

During the National Environment Research Council (NERC) funded Salford Experiment SALFEX on April-May 2002, some measurements were made in a residential area of Salford, Thursfield Street. For the 2nd May 2002, this campaign provided 10 min averages of the three wind components, air temperature and respective covariances, from a sonic anemometer at the height of 11 m (Dr. Janet Barlow, private communication). Some radiosonde observations at the same site at around midday are also available (Dr. Fay Davies, private communication).

During a field experiment at Salford University on May-June 2004, some weather instrumentation was installed on the top of the 20 m high Telford Building. An Automatic Weather Station (AWS) collected data on air temperature and wind speed (1/2 hour observations). A CSAT3 sonic anemometer provided measurements of the three wind components, temperature, and respective covariances. Also a fine wire thermocouple used by the author with the sonic anemometer operated during some no-rain days. The resulting processed data are 10 min averages of these measurements.

For the summer of 2004, 10 min averages of the air temperature and wind speed from sonic anemometers installed on the top of the 50m high Sackville Building in central Manchester were provided by the University of Manchester Atmospheric Science Research Group (private communication).

For both study periods of 2002 and 2004, hourly (or 1/2 hour) averages of the air temperature (T_a), wind speed (u), and wind direction, from the synoptic Automatic Weather Station at Manchester International Airport (Met Office) and a private AWS located in a residential area of Salford, are available on-line [www.metoffice.gov.uk, weather.noaa.gov, and www.wunderground.com, last accessed 2004]. These two AWS are the only operational observational weather stations over the study domain during the periods of interest.

Table 7.1 summarises the air temperature and wind data sources used in the present work.

***Table 7.1**- Summary of the observational of air temperature and wind data sources.*

Site		Source	Data	
Manchester International Airport-Ringway	Met Office, UK , (03334) EGCC Synoptic AWS	[www.metoffice.gov.uk, weather.noaa.gov, and www.wunderground.com, last accessed 2004]	T_a - air temperature at 2m u - wind speed at 10m Wind direction (hourly or 1/2 hour averages)	2002-2004
Salford - residential zone	Private AWS	[www.wunderground.com, last accessed 2004]	T_a - air temperature at 5m u -wind speed at 7m Wind direction (hourly averages)	2002-2004
Manchester - city centre (roof of Sackville Building)	University of Manchester Atmospheric Science Research Group	UMIST-ASRG, Ian Longley and Dr. Karen Bozier private communication	T_a - air temperature at 50m u - wind speed at 50m (10 min averages)	Summer 2004
Salford-residential zone (Thursfield Street)	SALFEX field campaign	Dr. Fay Davies and Dr. Janet Barlow private communications	T_a, u - radiosonde T_v, u , $<w' T_v'>$- Sonic anemometer at 11m (10 min averages)	2 May 2002
University of Salford (roof of Telford Building)	Field experiment organised by C.G. Collier, M.G.D. Carraça, Dr. Karen Bozier and Dr. Gavin Robins from Salford University research group	Dr. Karen Bozier and M.G.D. Carraça	T_a, u - AWS at 20m (1/2 hour averages) T_v, u,$<w' T_v'>$ - CSAT3D sonic anemometer at 20m (10 min averages) T_a, $<w' T_a'>$- Fine wire thermocouple at 20m (10 min averages)	May-June 04 with interruptions 14,21June 04 14 June 04

The location of the above mentioned observational urban sites, over a 6x5 km^2 area of the study domain, is shown in **Figure 7.2**, and a more detailed aerial view of the surroundings of the sites is shown in **Figure A4.1** of Appendix A4. Some photographs of the urban sites are presented in **Figures A4.2-A4.5** of Appendix A4. **Figure 7.3** shows the relative position of all observational sites over the entire study domain.

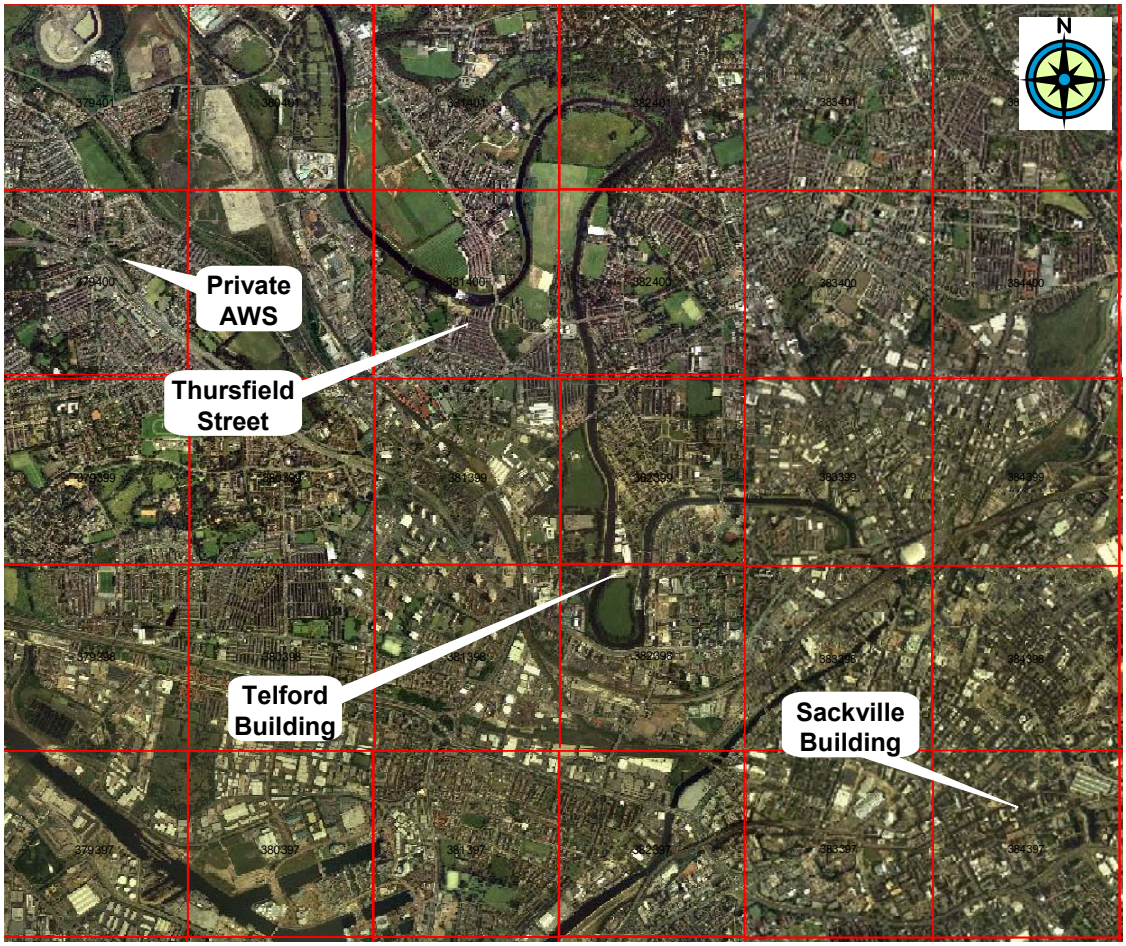

Figure 7.2 *- Location of the urban observational sites in the Greater Manchester study domain [adapted from the aerial photographs available in www.multimap.com]: (a) Private AWS in Salford, (b) Thursfield Street (SALFEX field campaign), (c) Telford Building (experiment at Salford University), and (d) Sackville Building in central Manchester (observations from the University of Manchester University Atmospheric Science Research Group). The red lines indicate the georeferenced grid used in the present study, with cells of 1km x 1km. The UK National Coordinates of the lower-left and upper-right corners of the 6x5 km^2 area represented in this figure are (379000, 397000) and (385000, 402000), respectively.*

The radiometric surface temperature, T_R, data used in the present work are derived from satellite imagery over Greater Manchester using the MODIS Terra/Aqua Land Surface Temperature/Emissivity [modis-land.gsfc.nasa.gov, last accessed 2004] (5 min, 1km), only available with cloud free sky conditions. The radiometric surface temperature, T_R, over Greater Manchester for the 24 x 24 km^2 area of interest, around midday, are shown in **Figure 7.3** for: (a) 2 May 2002, (b) 14 June 2004, and (c) 21

June 2004. In spite of the difficulty arising from the fact that the satellite surface temperature is available only in clear sky conditions, it is necessary to use these data because they do not exist from any other operational observational network at the surface providing a spatial distribution of surface temperature (either radiative or aerodynamic/ soil).

Figure 7.4 shows differences between MODIS radiometric surface temperature (T_R) and air temperature near the surface (T_a), and the wind speed (u) over Greater Manchester on some clear sky days. The data refer to a particular hour of the day, between 11:55 and 13:55 UTC, depending on the time of the satellite (Terra or Aqua) overpass available for each specific day. The values of T_R presented in this figure were extracted from images similar to the examples given in **Figure 7.3**.

The air temperature and wind speed observations of **Figure 7.4** are obtained from different sources (see **Table 7.1**). The observations from the synoptic AWS at Manchester airport are referred to as *Ta_MxAirport_2m* and *u_MxAirport_10m*. On the other hand, the values referred to as *Ta_Salford_5m* and *u_Salford_7m* are provided by a private AWS situated in Salford. The values referred to as *Ta_SalfordUni_20m* and *u_SalfordUni_20m* are given by the AWS installed at Salford University on the top of the 20 m high Telford building during an experiment on May-June 2004. Finally, *Ta_UMIST_50m* and *u_UMIST_50m are* air temperature and wind speed observations at the top of the 50m high Sackville Building in central Manchester.

The radiometric temperatures derived from satellite data represent the surface "skin" temperature and are, on average, about 7 C higher than the air temperatures. Note that the surface temperature is significantly lower at the Airport, situated in a rural area, than in the urban zones of Salford and Manchester. The values of the surface temperature in these urban observational sites are nearly the maximum ($T_R$max) observed over the entire study domain (24 x 24 km^2) (see also **Figure 7.3**).

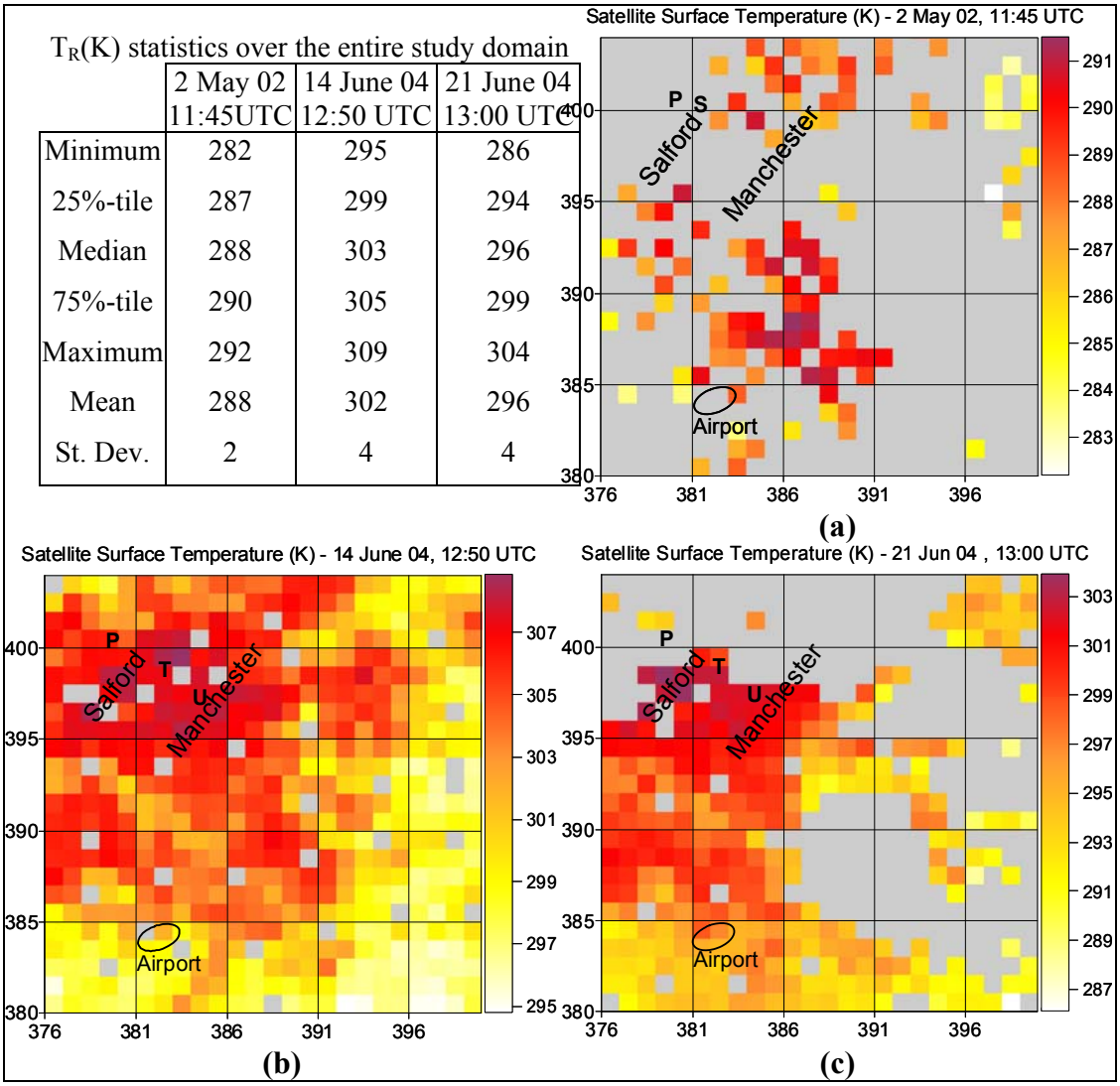

T_R(K) statistics over the entire study domain

	2 May 02 11:45UTC	14 June 04 12:50 UTC	21 June 04 13:00 UTC
Minimum	282	295	286
25%-tile	287	299	294
Median	288	303	296
75%-tile	290	305	299
Maximum	292	309	304
Mean	288	302	296
St. Dev.	2	4	4

Figure 7.3 *- Radiometric surface temperature, T_R, from satellite imagery (MODIS Terra/ Aqua) over Greater Manchester,* ***(a)*** *on the 2nd May 2002, at 11:45 UTC, under scattered cloud conditions,* ***(b)*** *on the clear sky day of 14th June 2004, at 12:50 UTC, and* ***(c)*** *on the 21st June 2004, at 13:00, under scattered cloud conditions. The total study area is 24 x 24 km^2 and the area of each grid square is 1 km^2. The grey areas are either missing data due to the mapping technique or areas of clouds. The legend on the right-hand side of each figure refers to the values of the temperature expressed in K. The coordinates X and Y are the U.K. National Coordinates, and the location of the* ***S****ALFEX site, the* ***P****rivate AWS at Salford,* ***T****elford Building at the University of Salford, the Sackville Building at the* ***U****niversity of Manchester, and the Manchester* ***Airport*** *are indicated. Also statistics of T_R (K) over the entire study domain are shown.*

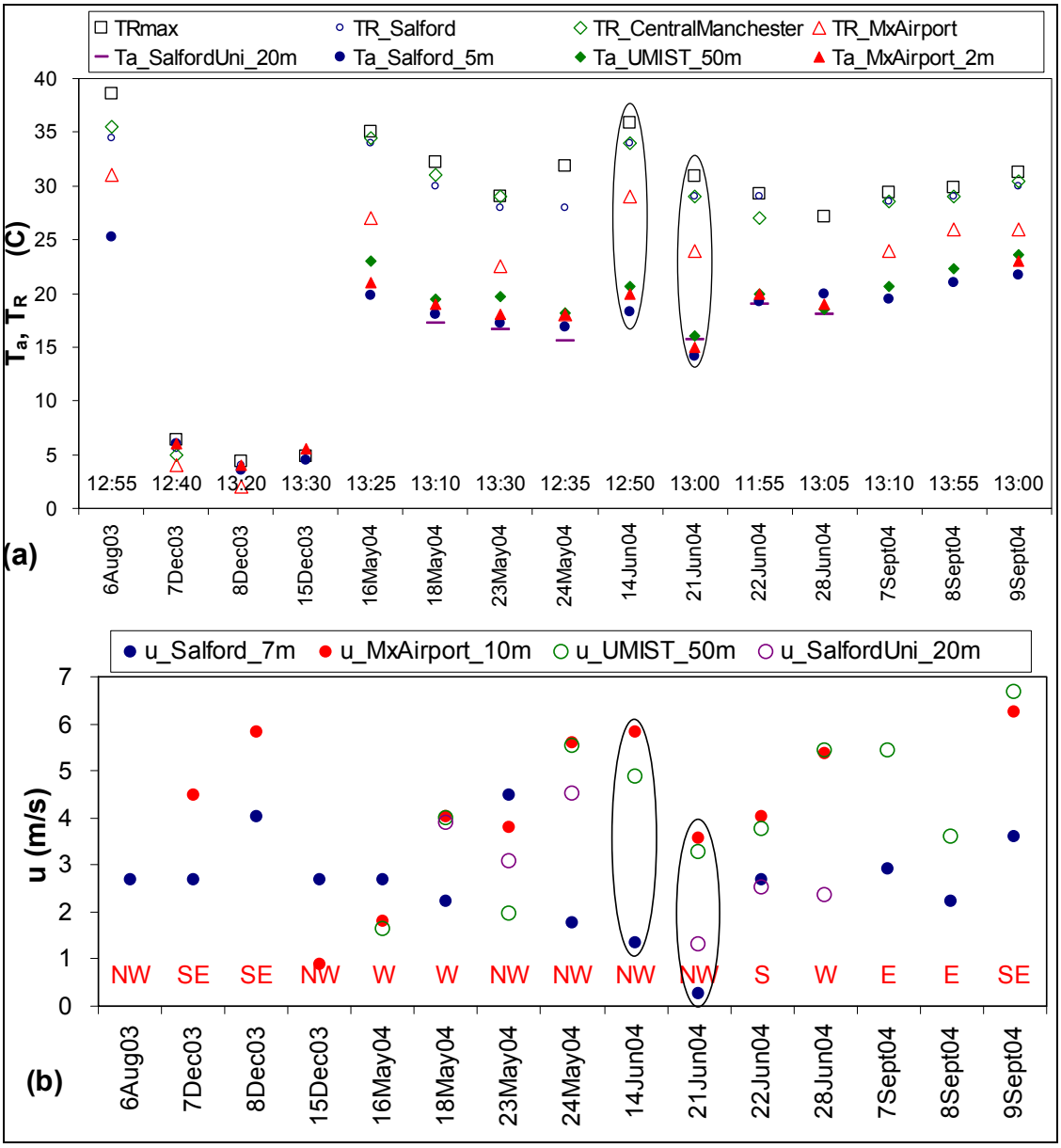

Figure 7.4 *- Radiometric surface temperature, T_R, air temperature, T_a, (a) and wind speed, u, (b) near the surface over Greater Manchester around 12 UTC on some clear sky days (dates on x-axis). T_R is derived from MODIS Terra/Aqua satellite data. T_a and u were obtained from several sources as indicated on the top legends. T_{Rmax} is the highest surface temperature value observed in a 1km^2 cell of the 24x24 km^2 Greater Manchester study domain. The data refer to a particular hour of the day (see* ***Figure 7.4a****) depending on the time of the satellite overpass available for each specific day. The values of T_R presented in this figure were extracted from images similar to the examples given in* ***Figure 7.3****.*

Although our study is not focused on the effects of the air temperature or wind, during the study situations, the spatial variation of surface temperature seems to be much more accentuated than the variation of air temperature. On the other hand **Figure 7.4a** and **Figure 7.4b** show that the air temperature values from the different observational sites fell in a quite narrow range, while in the case of the wind speed a wide range of values is obtained (see also **Figure 7.5** and **Figure 7.6**).

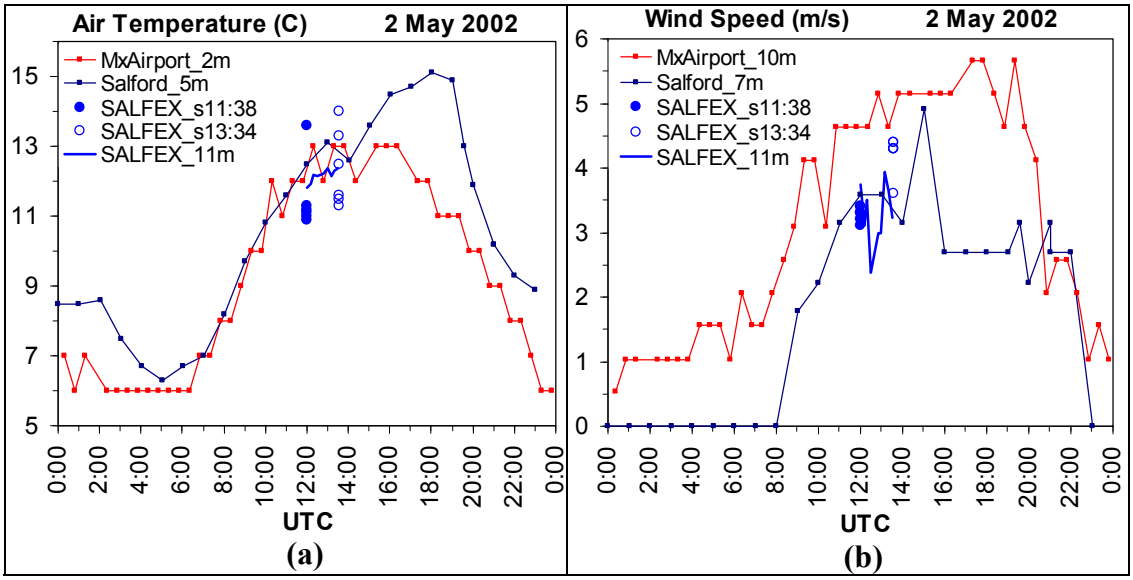

Figure 7.5 *- Air temperature (a) and wind observations (b) on the 2nd May 2002, from different sources over Greater Manchester: the synoptic AWS at Manchester airport (■), the private AWS situated in Salford (■), and the SALFEX campaign. The blue lines (—) represent 10min averages of the ultrasonic measurements at 11m during the SALFEX campaign. The figure also shows two sets of SALFEX radiosonde observations starting at 11:38 UTC (●) (at levels: 16, 20, 27, 37, 45 m) and 13:34 UTC (○) (at levels: 6, 14, 23, 31, 41 m); for each sounding, the highest temperature and the lowest wind speed shown are the values extrapolated for the 0 m level.*

Figure 7.5 shows the air temperature (a) and wind observations (b) on the 2nd May 2002, from different sources: the SALFEX campaign, the synoptic AWS at Manchester airport, and the private AWS situated in Salford.

Figure 7.6 shows the air temperature (a) and wind observations (b) on the 14th and 21st June 2004 from different sources as in **Figure 7.4**, except that for these days the AWS observations on the top of Telford Building at Salford University are not

always available. For the 14th June observations of the air temperature (*Ta_SalfordUni_20m*) from a fine wire thermocouple used with the CSAT3 located at this site are shown instead. Also 10 min averages of the CSAT3 sonic anemometer measurements of virtual temperature (*Tv_SalfordUni_20m*) and wind speed and (*u_SalfordUni_20m*), are presented for these two days.

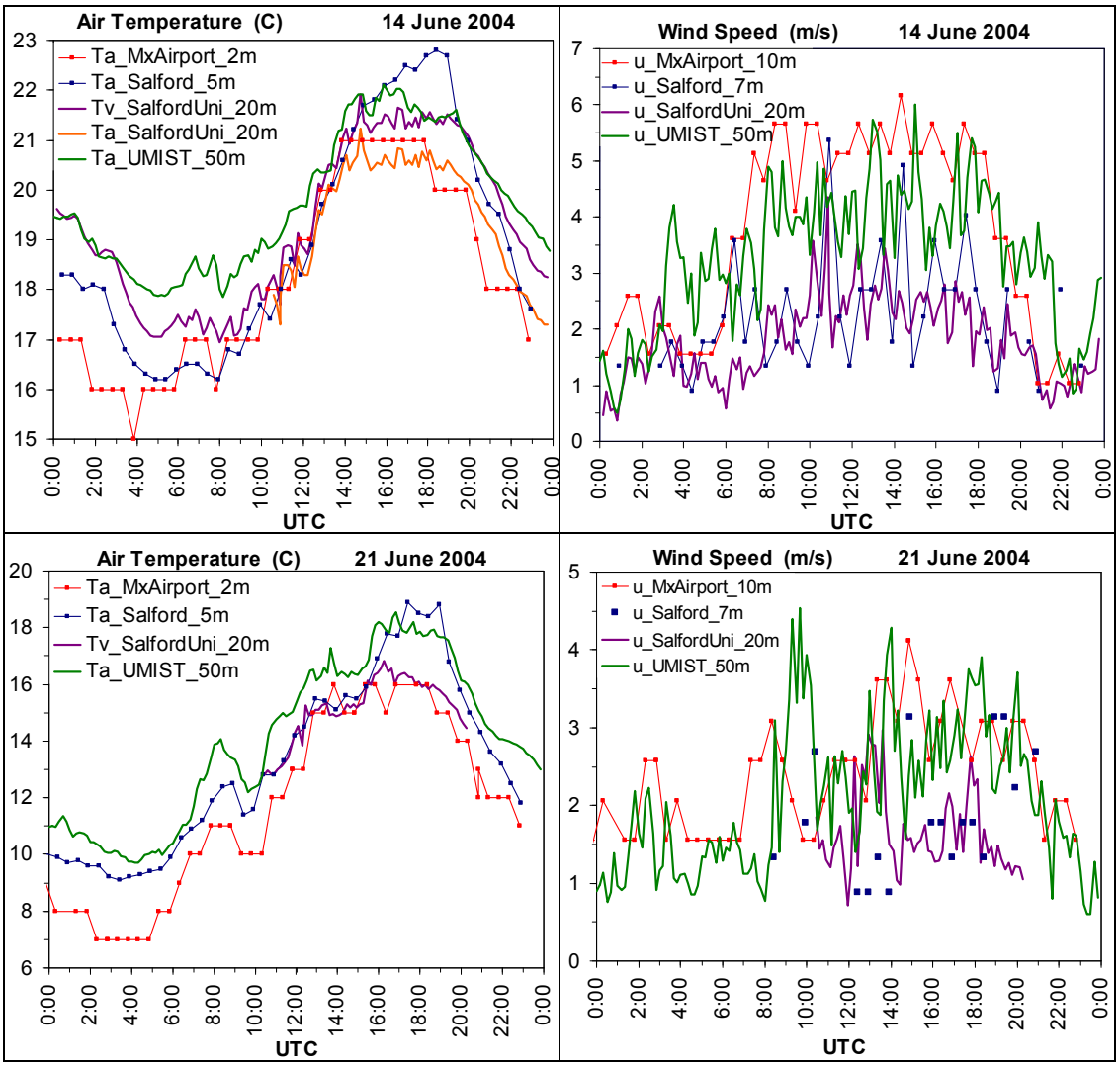

(a) **(b)**

Figure 7.6 *- Air temperature (a) and wind (b) observations on the 14 and 21 June 2004 from different sources over Greater Manchester: the synoptic AWS at Manchester airport (■), the private AWS situated in Salford (■), the experiment setup on the roof of the* Sackville Building, *from the University of Manchester Atmospheric Science Research Group (—), and the experiment setup on the roof of the Telford Building at the University of Salford- (— and —).*

Note on local versus satellite radiometric surface temperature observations

There is a lack of surface temperature data in the literature for Manchester or UK cities, and the existence of previous experiments is unknown to the author. During the period of the present study some *in situ* (instantaneous point) radiometric surface temperature measurements of walls and pavement have been made and compared with the MODIS satellite data (5min, 1km). The aim of this procedure is to get an approximate idea about the range of surface temperature values T_R that might be observed in urban areas, and is not to obtain a proper calibration of the satellite data.

On 2 May 2002 the measurements have been carried out at Thursfield Street (**Figure A4.4**) during the SALFEX campaign using a handheld infrared thermometer. On the 28 June 2004 an instrument borrowed from the Laser Laboratory of Salford University (infrared thermometer IMPAC IN5 Plus) has been used in front of the Peel Building at Salford University (**Figure A4.3**), and on 9 September 2004, at the same site, measurements have been made by the author using a handheld infrared thermometer (Raytek ST60 ProPlus).

The range of surface temperature values measured *in situ* on 2 May 2002 at around 12 UTC is 13C < T_R < 30C. These extremes have been observed on the pavement (SALFEX, Dr. Janet Barlow, private communication). There are no available satellite data for the 1km x 1km domain cell where the local measurements are made, but the nearest observation from MODIS satellite imagery at 11:45 UTC is 15 C.

On the 28 June 2004 the range of surface temperature values measured *in situ,* between 13:30-14:30 UTC, is 16C < T_R <34C. The lower value was observed at the soil surface (shade) and the higher value at the asphalt pavement (sun). In this case satellite observations in the neighbourhood of the in situ measurements are not available due to the scattered cloudy conditions, and the sparse values available for the $1km^2$ cells over the entire domain lie between 11 C and 27 C.

On the 9 September 2004 the range of surface temperature values measured *in situ,* between 12:20-13:00 UTC, is 21C < T_R < 38C. These extremes have been observed on the white cement pavement (shade) and asphalt pavement (sun). The surface temperature from MODIS satellite imagery, at 13 UTC for the $1km^2$ domain cell where the local measurements were made, is 30 C.

The satellite T_R values relate to the range of values obtained for the different

surface types (asphalt, red brick, cement, and ground) and observational conditions (shade/sun, surface orientation, etc). The satellite measurements lie between the maximum and the minimum values observed *in situ* using the infrared thermometers. It seems reasonable to accept that the satellite radiometric surface temperature may represent an average value over the 1km x 1km cell where the site is located. However satellite radiometric surface temperature data in general are affected by considerable uncertainty due to the combination of solar and surface geometries (Lagouarde *et al.*, 2004).

Sensible heat flux

The reference values of sensible heat flux (**Table 7.2** and **Figure 7.7**) for the 2nd May 2002, 14th and 21st June 2004, around midday are calculated from 10 min averaged covariances between the observed vertical wind component and the air temperature:

$$Q_H = \rho\, c_p\, \overline{w'T'} \qquad (7.1)$$

Where

$\rho \equiv$ air density (1.2 kg m^{-3})

$c_p \equiv$ air specific heat capacity at constant pressure (1004 J kg^{-1} K^{-1})

$w \equiv$ vertical wind component (measured with a sonic anemometer)

$T \equiv$ air temperature (measured with a fine wire thermocouple used with the sonic anemometer, T_a , or from the sonic anemometer, T_S).

$\overline{w'T'} \equiv$ 10 min averaged covariance between w and T.

Note that the sonic temperature is very similar to the virtual temperature T_v, according to the Instruction Manual of the three-dimensional sonic anemometer CSAT3 used in the present work.

The sensible heat flux observations of the 2nd May 2002 were carried out in Thursfield Street during the SALFEX field campaign (**Figure 7.2b** and **Figure A4.1**). The reference values of surface sensible heat flux (see **Table 7.2**) were estimated from 10 min average covariances between the vertical component of the wind and the temperature obtained with a sonic anemometer installed on a mast at 11 m height (Dr. Janet Barlow, 2003, private communication).

Table 7.2 *- Sensible heat flux observed on the 2nd May 2002, around 12 UTC, in Thursfield Street, Salford, using a sonic anemometer at 11m.*

UTC	11:20	12:00	13:00
Q_{H_Tv} (W/m^2)	104	128	229

On the 14th and 21st of June 2004 the sensible heat flux observations were carried out during a field experiment at Salford University. The instrumentation was installed at 20 m height on the roof of Telford Building (**Figure 7.2c** and **Figure A7.2**). As for the SALFEX experiment, the sensible heat flux (Q_{H_Tv}) is estimated from the observations using a CSAT3 sonic anemometer. However for the 14th of June it was also possible to estimate the sensible heat flux using the measurements of the air temperature from a fine wire thermocouple. The values so obtained (Q_{H_Ta}) are shown in **Figure 7.7** and are very close to the results using the sonic temperature (Q_{H_Tv}) (see also **Table 7.3**).

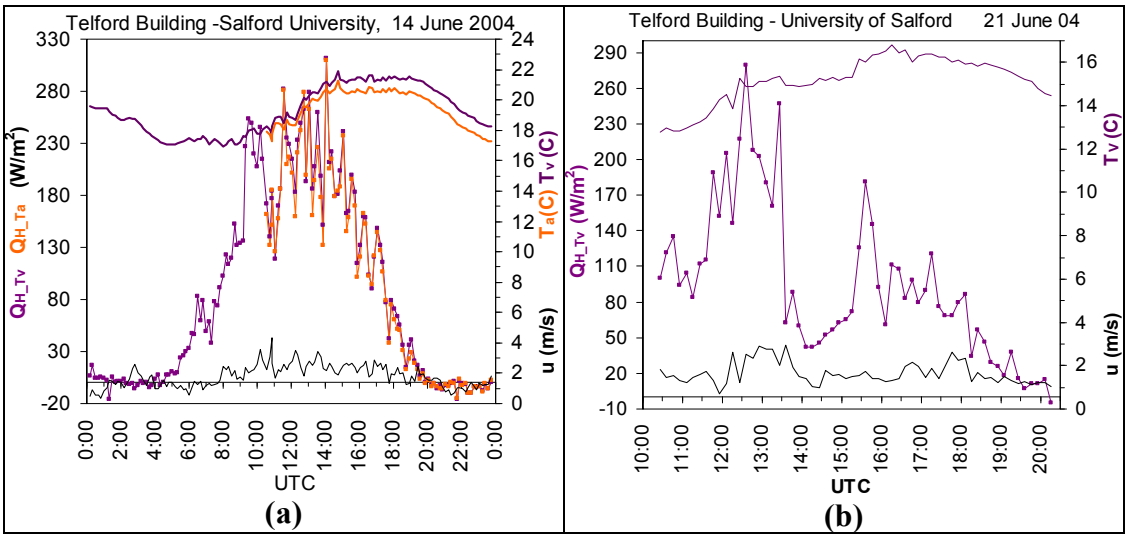

Figure 7.7 *- Observations on the 14th (a) and 21st (b) June 2004, at 20m height, on the roof of Telford building at the University of Salford (10 min averages): wind speed (u —) and virtual temperature (T_v —) from a CSAT3 sonic anemometer, and air temperature (T_a —) from a fine wire thermocouple. Q_{H_Tv} (■) and Q_{H_Ta} (■) are estimates of the sensible heat flux using 10 min averaged covariances between the observed vertical wind component and temperature. Q_{H_Tv} uses the virtual temperature values and Q_{H_Ta} the air temperature. These two estimates are similar.*

Table 7.3 *- Sensible heat flux observed on the 14 and 21 June 2004, around 13 UTC, on the roof of Telford Building at 20m, at the University of Salford (from* ***Figure 7.7*** *).*

14 June 2004	Q_{H_Ta} (W/m^2)	Q_{H_Tv} (W/m^2)	21 June 2004	Q_{H_Tv} (W/m^2)
12:35	249	242	**12:45**	208
12:45	263	279	**12:55**	203
12:55	193	199	**13:05**	180
13:05	279	262	**13:15**	161

7.4 Model input data over the entire study domain

The absence of more observations of the air temperature and wind, over Greater Manchester, is recognised as a limitation to the model application. The available observations over the study domain are very sparse, and their spatial distribution is not generally adequate for our study.

Because the air temperature and wind speed data provided by the different sources were taken under different conditions, different measurement heights and different morphologic characteristics of the surrounding area, it is not easy to relate them. It is not possible to interpolate the values in order to obtain an adequate spatial distribution at 1km steps over the study area, or extrapolate the values to the height, z_S, in order to have the input data required by the model. Therefore, in the absence of other data, it seems more reasonable to use the same values of air temperature (T_a) and wind speed (u), observed at Manchester International Airport, as model inputs over the entire domain. These measurements are carried out under standard conditions and provided by the UK Met Office. The model input values of T_a and u are the values observed at the Manchester airport at the same time as the MODIS satellite imagery. These data refer to a particular hour of the day (around midday) depending on the time of the satellite overpass available for each specific day.

The model input values of the radiometric surface temperature T_R, derived from MODIS Terra/Aqua satellite imagery, over Greater Manchester for the 24 x 24 km^2 area of interest, are shown in **Figure 7.3** for: (a) the 2nd May 2002 at 11:45 UTC, (b) 14th June 2004 at 12:50 UTC, and (c) 21st June 04 at 13:00 UTC.

The values of T_a and u observed at Manchester airport on these three occasions were: (a) T_a= 285 K, u= 4.6 m/s, (b) 293 K, 5.8 m/s, and (c) 288 K, 3.6 m/s, respectively. The mean wind direction in these cases is from the NW, which provides

quite good conditions for the model evaluation, since there are no significant orographic obstacles in this direction (see **Figure 7.1**).

Model input roughness parameters, building height (z_H) and the frontal area index (λ_F) obtained for the Greater Manchester study area are shown in **Figure 6.20a** and **Figure 6.20b** of Chapter 6, respectively. These roughness parameters were derived by the author from a surface morphologic database for Greater Manchester that has being developed from analysis of digitised georeferenced data of the surface elements provided by the Environment Agency and the Cities Revealed User Group, aerial photographs, maps and field surveys (for a detailed explanation see Chapter 6).

The model input values used in the three case studies, and described in the previous paragraphs, are summarised on **Table 7.4**.

Table 7.4 *- Model input data used over the entire study domain for the three case studies.*

2nd May 2002	14th June 2004	21st June 2004
T_a = 285K , u = 4.6m/s T_R from satellite imagery at 11:45 UTC (**Figure 7.3a**) z_H and λ_F spatial distributions of **Figure 6.20**.	T_a = 293K , u = 5.8m/s T_R from satellite imagery at 12:50 UTC (**Figure 7.3b**) z_H and λ_F spatial distributions of **Figure 6.20.**	T_a = 288K , u = 3.6m/s T_R from satellite imagery at 13:00 UTC (**Figure 7.3c**) z_H and λ_F spatial distributions of **Figure 6.20.**

7.5 Surface sensible heat flux model estimates versus observations

7.5.1 Case study 2 May 2004

Model results for the entire study domain

Model estimates of sensible heat flux, Q_H, for different measurement levels (z_S = 11, 16, ..., 45m) have been derived over the entire study domain (24 x 24 km^2). In this case (see **Table 7.4**), the air temperature, T_a, and the wind speed, u, are the values observed at 12:00 UTC, from the weather station at Manchester International Airport. T_R is the satellite surface temperature at 11:45 UTC (MODIS- Terra satellite imagery

of **Figure 7.3**a). The spatial distribution of the roughness parameters used is shown on **Figure 6.20** of Chapter 6.

The model estimates of sensible heat flux (Q_H) over the entire study domain, for the measurement level z_S= 11m, are shown on **Figure 7.8**. The figures obtained for the other measurement levels (not presented here) show the same spatial distribution pattern of Q_H, but since the rest of the input parameters remain the same, the values of Q_H decrease for higher levels (see **Table 7.5**, for example).

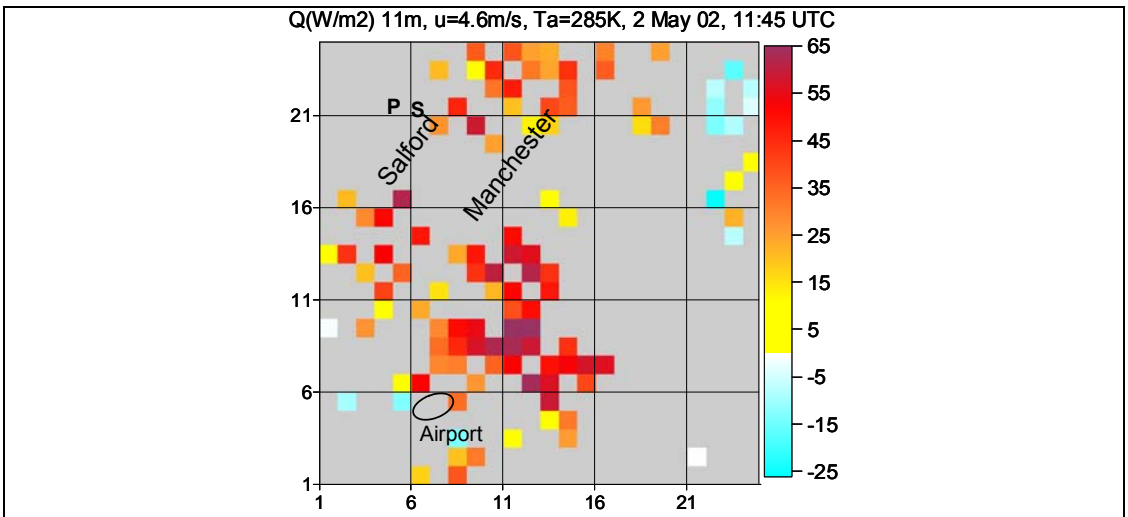

Figure 7.8 *- Model estimates of surface sensible heat flux, Q_H, on the 2nd May 2002, at 11:45 UTC, under scattered cloud conditions, for the Greater Manchester study area (24x24 km^2) shown in* ***Figure 7.3a****. The grey areas are either missing data due to the mapping technique or areas of clouds. The legend on the right-hand side of each figure refers to the values of Q_H expressed in W/m^2. The locations of the* ***S****ALFEX site, the* ***P****rivate AWS at Salford and the Manchester* ***Airport*** *are indicated by letters. Statistics over the entire study domain for the model estimates of Q_H (W/m^2) are shown on the bottom of the figure.*

Because of the scattered cloud conditions, the satellite imagery does not provide a value for the surface temperature for the cell of interest where SALFEX observational equipment is installed, and consequently a model estimate of sensible heat flux is not available for this place. The nearest model estimates are available for two domain cells at around 1 km southeast and 2 km east from the observational site

(see **Figure 7.8**). **Table 7.5** shows the model estimates of Q_H and respective input data sets, for the two domain cells in the nearer neighbourhood of the cell of interest where SALFEX observational equipment is installed. Also shown in the last columns of this table are the minimum and maximum values of Q_H found over the entire study domain.

Comparison of the observed values (>100 W/m^2, **Table 7.2**) with the model results (<50 W/m^2, **Table 7.5**) shows that the model seems to largely underestimate the surface sensible heat flux.

Table 7.5 *- Model results of sensible heat flux, Q_H, and respective input data sets, for two domain cells in the nearer neighbourhood (southeast/ east) of the cell of interest where SALFEX observational equipment was installed. Also shown in the last column are the minimum and maximum values of Q_H estimated over the entire study area. The values in bold are represented in* ***Figure 7.8****.*

		T_a = 285 K , u = 4.6 m/s (NW)	
	SALFEX cell z_H = 5.1 m, λ_F = 0.07 T_R = no data	southeast / east of SALFEX cell z_H = 6.5 / 8.5 m, λ_F = 0.10 / 0.07 T_R = 288 / 289 K	
	z_S(m)	Q_H (W/m^2) southeast / east	Q_H (W/m^2) min / max
1	**11**	**27 / 46**	**-26 / 65**
2	16	24 / 40	-20 / 58
3	20	22 / 37	-18 / 54
4	27	20 / 34	-14 / 55
5	30	20 / 33	-13 / 54
6	37	19 / 34	-10 / 53
7	45	19 / 33	-9 / 51

Other simulations

Due to the uncertainty in the values of the surface roughness and atmospheric conditions directly associated with the observed Q_H, model estimates of Q_H using different input data sets have been carried out, and compared with the observations.

The average roughness parameters for the 1km^2 domain cell (381000, 400000) where the instruments are located obtained from the georeferenced morphologic database (**Figure 6.20** of Chapter 6) are: z_H = 5.1m; λ_F= 0.07. The model estimates of sensible heat flux, Q_H, obtained when using these input values for the roughness parameters are shown in **Table 7.6**. **Table 7.7** shows the input data and the model

estimates of Q_H, obtained when using the average roughness parameters for the *residential* urban category (UTZ) in Greater Manchester (**see Chapter 6**): z_H = 8m; λ_F= 0.13 (λ_P=0.19).

Note that Rooney *et al.* (2005) consider z_H= 8m and λ_P= 0.4, around the anemometer location at Thursfield Street in the SALFEX field experiment. Using the "Cities Revealed" and "Environment Agency" digitised data, and considering a homogenous sample of this residential area of approximately 50000m^2 (5 ha) around the anemometer location, values of z_H= 7.8 m and a maximum of λ_F= 0.52 (λ_P= 0.45) are obtained. On the other hand, considering just the row of houses of Thursfield Street leads to a possible maximum and a minimum of λ_F depending on the wind direction namely: λ_F =0.39 (NNE) and λ_F =0.078 (WNW).

In both sets of model calculations (**Table 7.6** and **Table 7.7**), the sensible heat flux is estimated for different measurement heights, z_S. The air temperature, T_a, and the wind speed, u, are the measured values at 12:00 UTC using the sonic anemometer at 11m, and given by a local radiosonde ascent starting at 11:38 UTC (levels 2-6). These measurements of air temperature and wind are results from the SALFEX campaign on 2 May 2002.

In cases A1 and A2 of **Table 7.6** and **Table 7.7**, T_R is the satellite surface temperature at 11:45 UTC (**Figure 7.3a**). However, because T_R data are not available for the domain cell where the surface sensible heat flux measurements were made, the nearest available surface temperature data to the southeast, T_R= 288 K (A1), and to the east T_R= 289 K (A2), are used.

Since the model estimates of Q_H, when using the nearest satellite surface temperatures (cases A1 and A2 of **Table 7.6** and **Table 7.7**), are much lower than the observations (**Table 7.2**), and the range of surface temperature values measured in the street (walls, pavement) at around 12 UTC, using a handheld infrared thermometer, is 13C < T_R < 30C (SALFEX, 2002, Dr. Janet Barlow, private communication), the model has also been run using higher surface temperature values (cases B1, B2, and B3 of **Table 7.6** and **Table 7.7**). As expected for the higher surface temperatures much larger values of Q_H are obtained.

Table 7.6 *- Model estimates of surface sensible heat flux, Q_H, and respective input data sets. In all cases z_H=5.1m and λ_F= 0.07.*

				A1 T_R= 288 K (15 C)	A2 T_R=289 K (16 C)	B1 T_R=293 K (20 C)	B2 T_R=298 K (25 C)	B3 T_R=303 K (30 C)
	z_S(m)	T_a (K)	u (m/s)	Q_H (W m^{-2})				
1	11	285.0 (12C)	3.7 NW	25	33	66	118	167
2	16	284.5	3.2 NW	23	32	64	105	148
3	20	284.4	3.3 NW	25	33	64	105	147
4	27	284.3	3.3 NW	25	32	62	102	143
5	37	284.2	3.4 NW	25	32	62	101	142
6	45	284.0 (11C)	3.9 NW	28	35	67	109	152

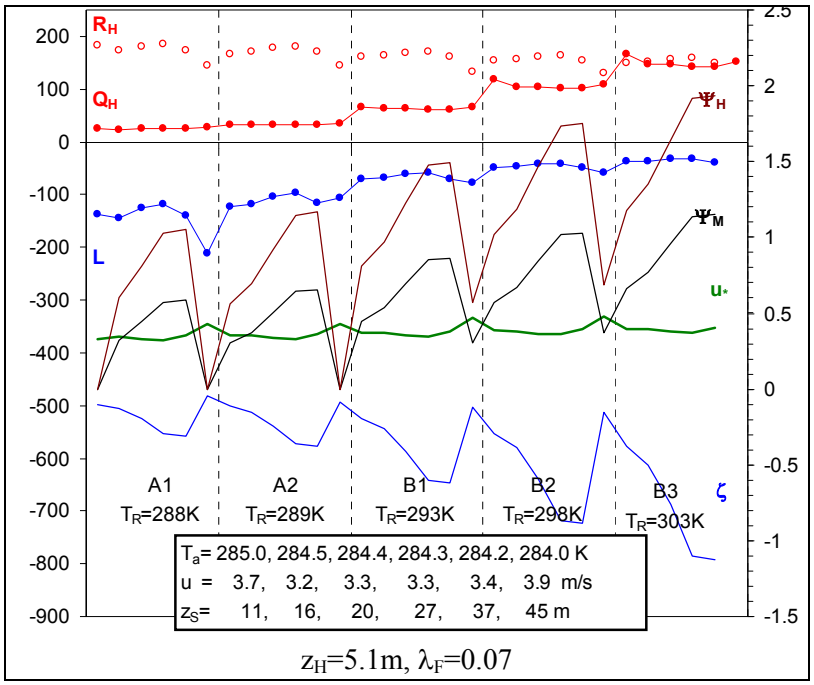

Figure 7.9 *- Model estimates of surface sensible heat flux, Q_H, using different input data sets (T_R, T_a, u, z_S, z_H and λ_F) as presented in* ***Table 7.6****. The corresponding model outputs for the Monin-Obukhov variable ζ, friction velocity u_*, the stability correction functions for momentum and sensible heat, Ψ_M and Ψ_H, the Monin-Obukhov length, L, and the resistance to heat transfer between the surface and the measurement level , R_H, are shown as well. In all model runs z_H=5.1m and λ_F= 0.07. The graph is divided in five parts, showing the model outputs for five different surface temperature input values, T_R. For each surface temperature six different situations have been considered; the values of the input variables (T_a, u, and z_S) for the six cases are shown on the bottom of the graph. The model estimates represented by single lines are read on the right-hand axis, and the estimates represented by dots on left-hand axis.*

Table 7.7 *- Model estimates of surface sensible heat flux, Q_H, and respective input data sets. In all cases z_H=8m and λ_F= 0.13.*

				A1 T_R= 288 K (15 C)	A2 T_R= 289 K (16 C)	B1 T_R= 293 K (20 C)	B2 T_R= 298 K (25 C)	B3 T_R= 303 K (30 C)
	z_S(m)	T_a (K)	u (m/s)	Q_H (W m^{-2})				
1	11	285.0 (12C)	3.7 NW	28	37	75	121	168
2	16	284.5	3.2 NW	25	32	60	105	148
3	20	284.4	3.3 NW	24	31	63	103	144
4	27	284.3	3.3 NW	22	31	60	98	137
5	37	284.2	3.4 NW	24	31	59	95	134
6	45	284.0 (11C)	3.9 NW	26	34	63	102	142

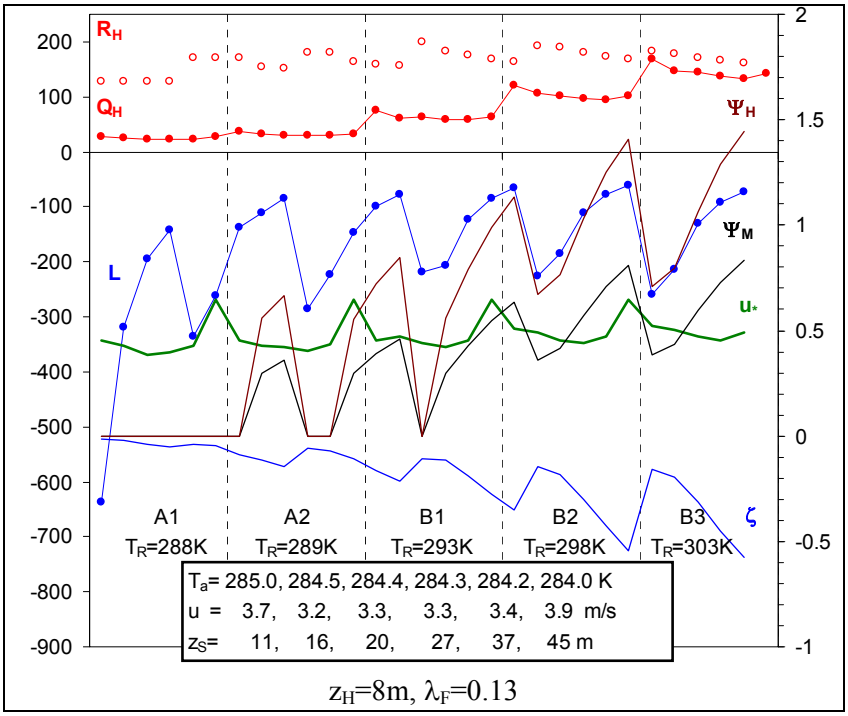

Figure 7.10 *- Model estimates of surface sensible heat flux, Q_H, using different input data sets (T_R, T_a, u, z_S, z_H and λ_F), as presented in* ***Table 7.7****. The corresponding model outputs for ζ, u_*, Ψ_M, Ψ_H, L, and R_H, are shown as well. Here the model runs are similar to those shown in the* ***Figure 7.9****, except that now the input roughness parameters are z_H=8m and λ_F= 0.13. The model estimates represented by single lines are read on the right-hand axis, and the estimates represented by dots on left-hand axis.*

Figure 7.9 and **Figure 7.10** show the model estimates of surface sensible heat flux, Q_H, using different input data sets (T_R, T_a, u, z_S, z_H and λ_F) as presented in **Table 7.6** and **Table 7.7**, respectively. The corresponding model outputs for the Monin-Obukhov variable ζ, friction velocity u_*, the stability correction functions for momentum and sensible heat, Ψ_M and Ψ_H, the Monin-Obukhov length, L , and the resistance to heat transfer between the surface and the measurement level , R_H, are shown as well. Notice that for moderately-stable conditions, $0.1<\zeta<1$, and for unstable conditions, $\zeta< -0.1$; for near neutral conditions, $|\zeta| < 0.1$, the stability correction functions for momentum and for heat are null, $\Psi_M(\zeta) = \Psi_H(\zeta) = 0$. The values of L lie roughly between -50 and -200 m, this corresponding to the typical order of magnitude (1 - 200m) presented in the published literature (Stull, 1988).

Comparison of the measured values with the model results, for the study case of 2 May 2002, shows that the model underestimates the surface sensible heat flux.

Since the observed wind direction is NW, the upwind source area contributing to the Q_H seen by the instruments is quite green, non-urbanised, and is crossed by a river (**Figure 7.2**). It is reasonable to expect that the estimated Q_H is higher then the observed value of Q_H. The surface temperature and the model roughness inputs refer to the characteristics of urbanised areas which include a percent of housing higher then the source area, but even so the model results are lower then the measurements.

Moreover, the model seems to be more sensitive to the vertical temperature gradient than to the roughness expressed by the parameters z_H and λ_F (see **Figure 7.9** and **Figure 7.10**), although locally the effects of the roughness maybe of central importance.

7.5.2 Case studies of 14 and 21 June 2004

Model results for the entire study domain

Figure 7.11 shows the model results for the spatial distribution of surface sensible heat flux Q_H, at z_S=45m , over the entire study domain, on the (a) 14th June 2004 at 12:50 UTC and (b) 21st June 2004 at 13:00 UTC. The input values used in these case studies are described in the previous subsection, and summarised in **Table 7.4**.

Although in the present case studies the observations of sensible heat flux (**Figure 7.7**) were made at a level z_S = 20m, **Figure 7.11** presented here refers to estimates for the level z_S=45m. This is because a few situations of non-convergence of the model are more likely to occur for lower values of z_S, and the correspondent figures (not presented here) for the spatial distribution of Q_H show more holes. Also the model is not valid for values of $z_S > z_H$, *i. e.*, the measurement level considered must be above the average surface elements height, and values of z_H > 20m occur in Manchester city centre in three domain cells (**Figure 6.20a**). The maximum value over the entire domain is z_H = 23.5 m.

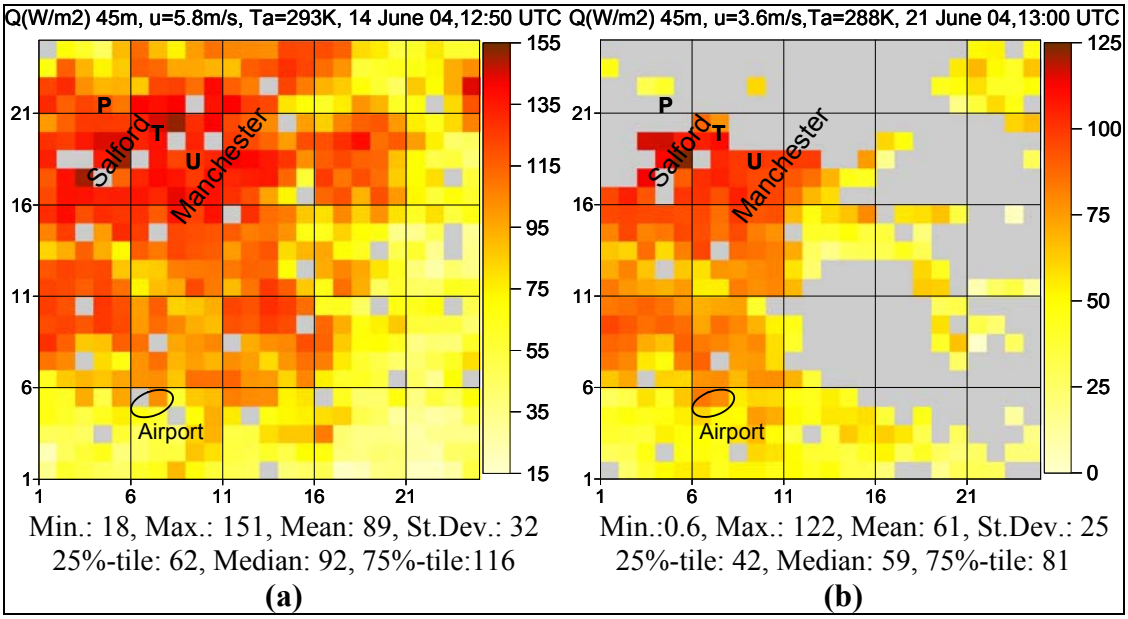

Figure 7.11 *- Model estimates of surface sensible heat flux, Q_H, around 13 UTC, (a)on the clear sky day of 14th and (b) on the 21st June 2004, under scattered cloud conditions, for the Greater Manchester study area (24x24 km^2) shown in* ***Figure 7.3****. The grey areas are either missing data due to the mapping technique or areas of clouds. The legend on the right-hand side of each figure refers to the values of Q_H expressed in W/m^2. The locations of the Private AWS at Salford* ***P****, the Telford Building at Salford University* ***T****, University of Manchester* ***U****, and Manchester* ***Airport*** *are indicated. Statistics over the entire study domain for the model estimates of Q_H (W/m^2) are shown on the bottom of the figure.*

The figures obtained for other measurement levels, z_S = 20m and z_S = 30m, for example (not presented here), show the same spatial distribution pattern of Q_H, but since the rest of the input parameters remain the same, the values of Q_H decrease for higher levels. **Figure 7.12** compares the model estimates taking z_S = 20m and z_S = 30m, with the model results from **Figure 7.11** for z_S = 45m. For the domain cell (382000, 398000) in the neighbourhood of the observational instruments, the estimates are Q_H (20m) =153 W/m^2 and Q_H (45m) =137 W/m^2, in the case of 14 June 2004. For the 21 June 2004, the estimates are Q_H (20m) =120 W/m^2 and Q_H (45m) =109 W/m^2. Thus the differences do not exceed 10% of Q_H (20m).

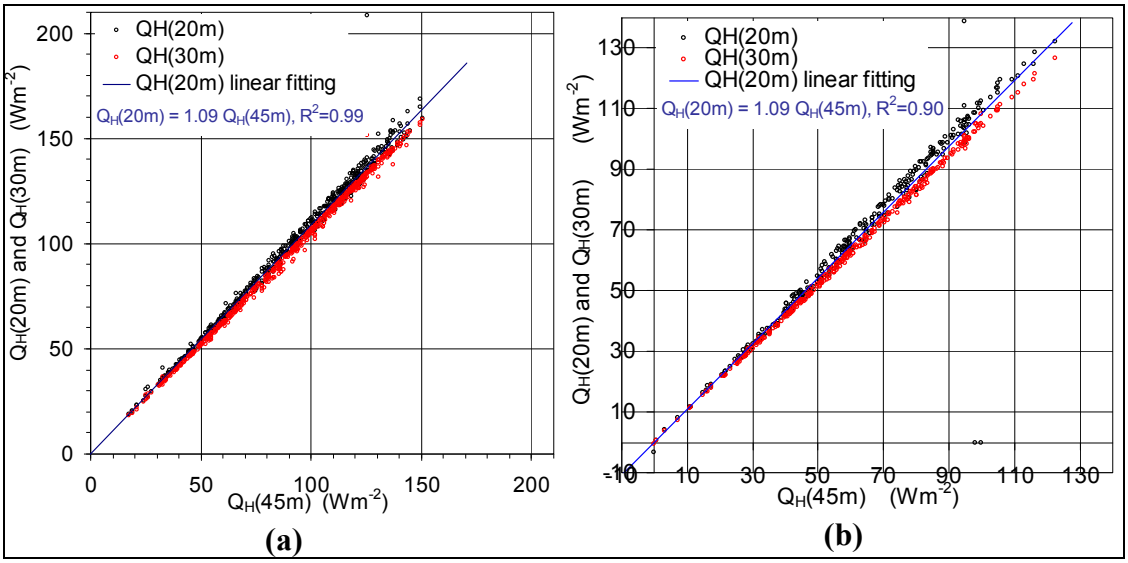

Figure 7.12 *- Model estimates of surface sensible heat flux, Q_H, around 13 UTC, on (a) 14th and (b) 21st June 2004, for z_S=20 m and z_S=30m versus the same model estimates for z_S=45m shown in* ***Figure 7.11****. The statistical parameter R is the Pearson linear correlation coefficient.*

Comparison of the model results of **Figure 7.11a** and **Figure 7.11b** [Q_H (20m) =153 W/m^2 and Q_H (20m) =120 W/m^2, at around 13 UTC], against the observations from **Figure 7.7a** and **Figure 7.7b** [Q_H ~200 W/m^2 and Q_H ~180 W/m^2, from **Table 7.3**, respectively] shows that the model underestimates the surface sensible heat flux, for the case studies of 14 and 21 June 2004.

However the pattern of the modelled spatial distribution of Q_H is similar for different atmospheric/ weather conditions. Although on the 21 June 2004 the figure is

not complete due to the scattered cloud conditions, for the area available the pattern is the same as that for 14 June 2004. Also for some other cases of cloud free conditions, not shown here (6 August 2003 and 7 December 2003, for example), the model has been run and the resulting patterns of sensible heat flux are similar (see **Figure A5.3** of Appendix 5).

As expected we found higher values of sensible heat flux over urbanised zones than over rural zones. The spatial distribution of the model estimates of sensible heat flux follows the same pattern as the surface temperature (**Figure 7.3**) and roughness, expressed by the parameters z_H, z_D, z_{0M}, and λ_F (**Figure 6.20** and **Figure 6.21**).

7.6 Model estimates of the roughness length for sensible heat flux, z_{0H}, and excess resistance for heat $kB^{-1} = \ln(z_{0M}/z_{0H})$

Momentum and heat transfer from vegetation and rigid obstacles are significantly different. The transfer of heat to, or from, a surface encounters more aerodynamic resistance than does momentum. The excess resistance for heat is expressed commonly in terms of the dimensionless parameter kB^{-1} which is a term of equation 5.1.2:

$$kB^{-1} = \ln\left(\frac{z_{0M}}{z_{0H}}\right) \qquad (7.2)$$

Figure 7.13 shows model estimates of the roughness length for sensible heat flux, z_{0H}, for the three case studies of 2 May 2002, and 14 and 21 June 2004, around midday, for the study area of Greater Manchester. These values are related to the model results of sensible heat flux shown on **Figure 7.11**.

Also **Figure 7.14** shows model results of $kB^{-1} = \ln(z_{0M}/z_{0H})$, for the three case studies. According to the model formulation, these values are calculated from the values of roughness length for momentum, z_{0M}, shown in **Figure 6.21b** and the model estimates of z_{0H} shown in **Figure 7.13**.

Taking into consideration the three case studies, it is found that z_{0H} values range between $\sim 10^{-21}$ and $\sim 10^{-2}$, with the lower values sited over urbanised zones and the highest values over rural areas. Values between 10^{-9} and 10^{-15} occur in the urbanised zones, except for the city centre where extremely low values ranging from

~10^{-15} to ~10^{-21} can be found. The corresponding model estimates of kB^{-1} in urbanised zones lie within a range of values of 15 - 30 over the urbanised zones, but for the city centre these values can be very high, around 50. The lowest values of kB^{-1} are found over the rural zones.

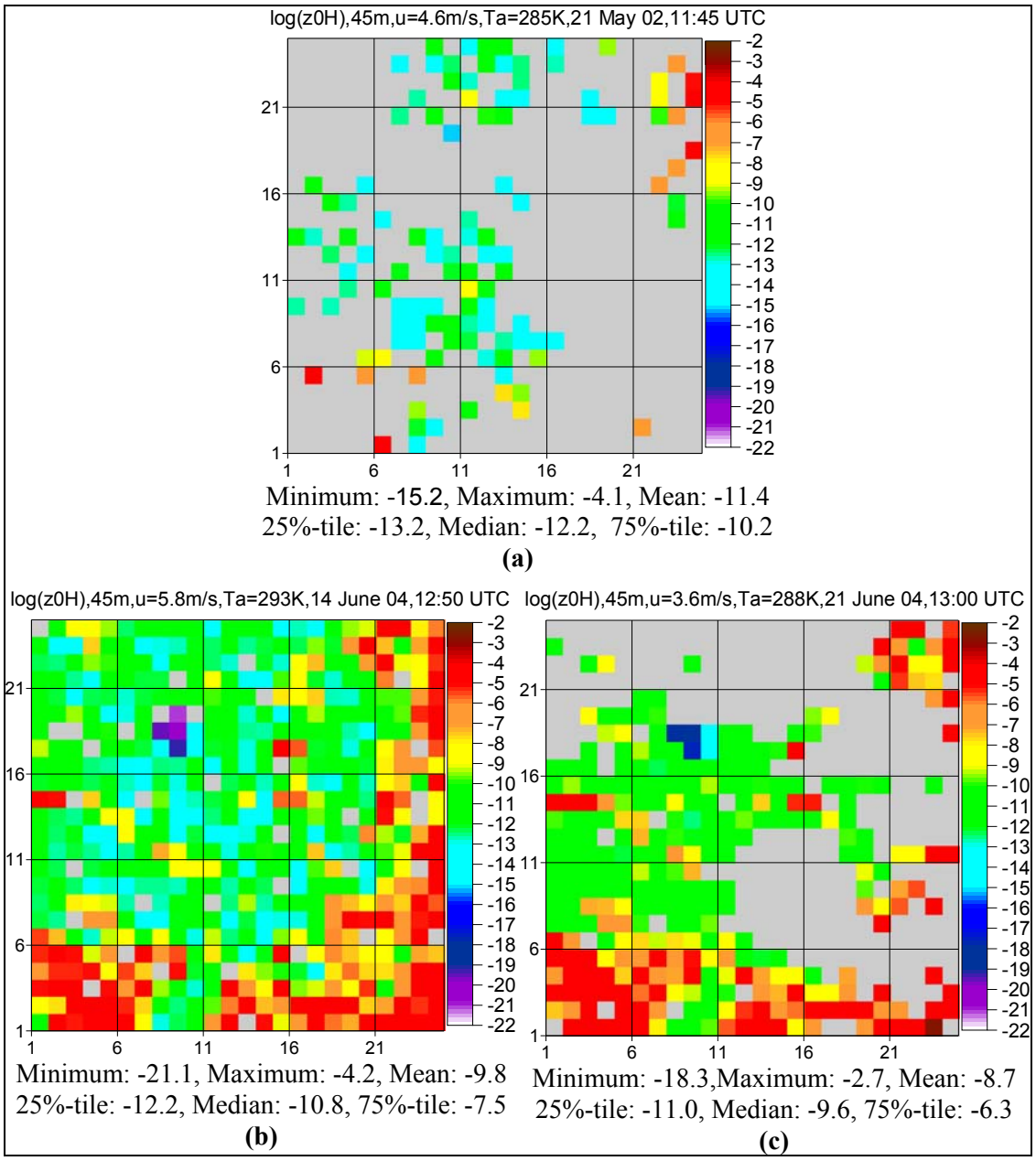

Figure 7.13 *- Model estimates of log(z_{0H}) for the case studies, on the (a) 2nd May 2002, and (b) 14th and (c) 21st June 2004, around midday, for the Greater Manchester study area (24x24 km^2). These estimates are related to the model results of sensible heat flux shown on* ***Figure 7.11****. Grey areas are as in* ***Figure 7.11****. . Statistics over the entire study domain, for the model estimates of log(z_{0H}) are shown on the bottom of the figures.*

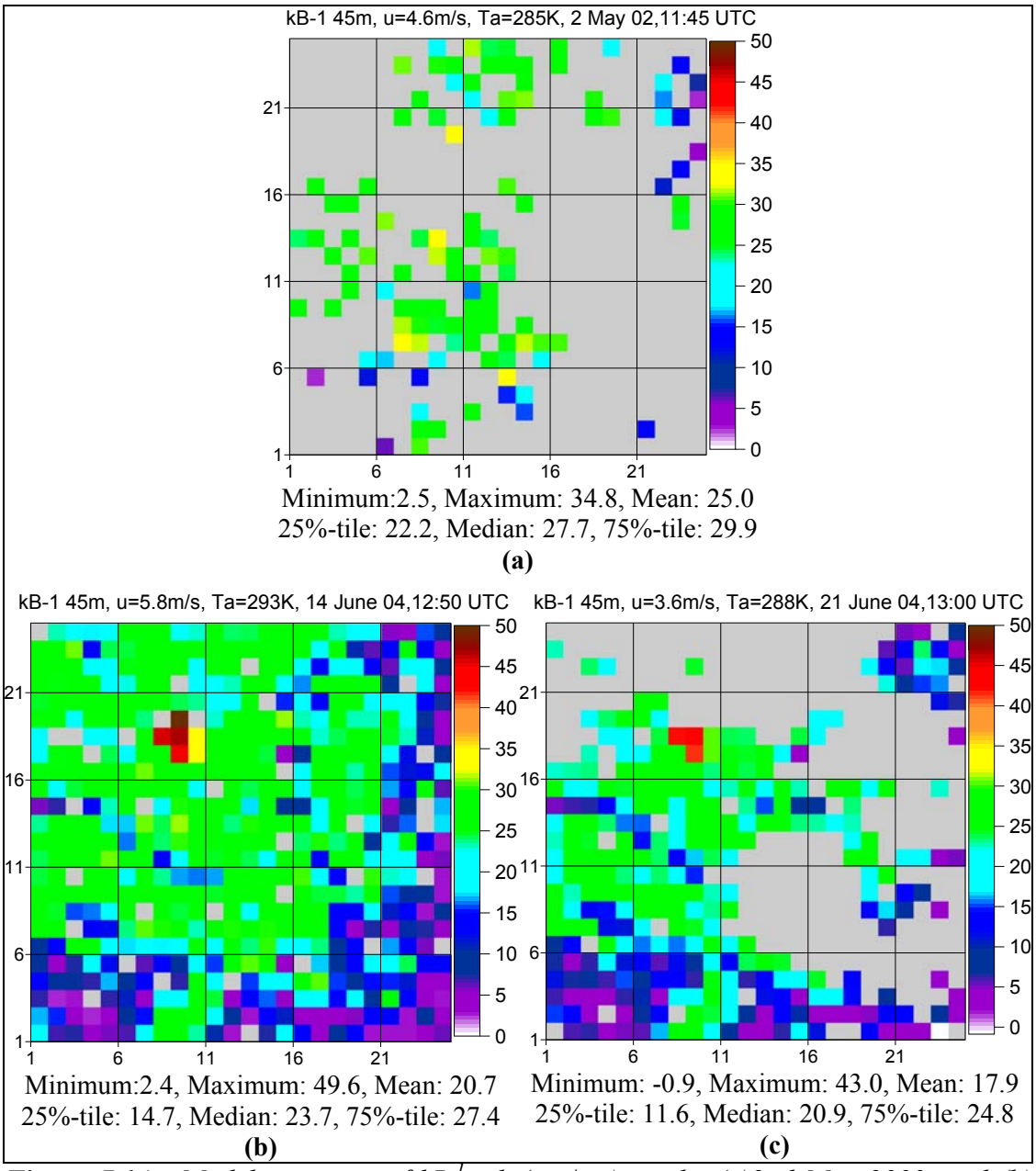

Figure 7.14 *- Model estimates of* $kB^{-1} = \ln(z_{0M}/z_{0H})$ *on the (a)2nd May 2003, and (b) 14th and (c) 21st June 2004, around midday, for the Greater Manchester study area (24x24 km*^{2}*). These values are related with the model results of sensible heat flux shown on* ***Figure 7.11****. Grey areas are as in* ***Figure 7.11****. Statistics over the entire study domain, for the model estimates of* kB^{-1} *are shown on the bottom of the figures.*

The model estimates of z_{0H} and kB^{-1} obtained in the present study are comparable to the values indicated on the published literature (e.g., Brutsaert, 1982, Voogt and Grimmond, 2000). However, for urban areas with high rise buildings, such

as the city centre, extremely high momentum to heat roughness lengths ratios (and very low z_{0H}) were found, but no values to compare the present model results against to were found in the published literature. As recognised by many authors (e. g., Voogt and Grimmond, 2000; Piringer and Joffre, 2005) there is a lack of studies in complex urban environments and more research is needed. For vegetated surfaces most reported values of kB^{-1} range from 1 to 10, and frequently a value of 2 is attributed to natural surfaces (see, e.g., Brutsaert, 1982; Stewart *et al.,* 1994; Verhoef *et al*., 1997).

Voogt and Grimmond (2000), in a study for a simple urban area, a light industrial site with little vegetation, determined values for kB^{-1} of about 20–27, which are larger than those estimated over vegetated surfaces. This range of values were obtained by three independent methods, and the values determined for the bluff-rough curve of Brutsaert (1982), provided the largest values. However the authors conclude that, for this kind of urban environment with little vegetation, an appropriate kB^{-1} value could be obtained by using the Brutsaert (1982) method. Note that this is the formulation used in the present study (see section 5.4, equation 5.4.7).

Large values of kB^{-1} imply very small z_{0H} values. For the studied urban environment, Voogt and Grimmond (2000) determined radiometric roughness lengths for heat (z_{0H}) ranging from 10^{-4} to 10^{-12} m, which were also found in other published works [e.g., Sugita and Brutsaert, 1990, and Malhi, 1996]. The authors suggest that the results in their study are likely to be close to the extreme because of the lack of vegetation at the site, however they too recognise that there is a lack of studies for urban areas and more research is needed.

Evidence of diurnal variations in kB^{-1} have been reported in many studies, with higher values observed in the afternoon, generally rising later in the day (see Verhoef *et al*., 1997, and Voogt and Grimmond, 2000). The larger values of kB^{-1} (smaller z_{0H}) are associated with the largest difference between surface and air temperatures (T_R - T_a) but not the higher value of sensible heat flux, Q_H. It is also documented that the value of kB^{-1} depends on the method used to determine the surface radiometric temperatures, which are affected by the combination of solar and surface geometries..

The large momentum to heat roughness lengths ratio z_{0M}/z_{0H} is a typically urban feature and is caused by the presence of bluff elements, i.e., solid rather than permeable obstacles (Garratt, 1992). This question is discussed in Piringer and Joffre, 2005. The authors note that sensitivity studies performed using the Advanced Regional

Prediction System (ARPS) mesoscale meteorological model to evaluate the impact of the roughness parameters on the urban Surface Energy Balance (SEB) lead to the conclusion that the large ratio of the roughness length for momentum *versus* heat (small z_{0H}) characterising cities may be the main cause of the observed high values for the heat storage flux. The extremely small values of z_{0H}, combined with relatively low wind speeds generally observed over urban surfaces (due to the high momentum roughness), lead to a very high resistance for sensible heat flux, thus strongly inhibiting this flux. As a consequence, cities tend to store incoming radiant energy in the ground and building substrate during the day, which is released to the atmosphere during the night. Thermal inertia, though often cited as a cause of the observed large values of the storage heat flux in cities, is less important in this respect as urban and rural thermal admittance values (Appendix 1) do not differ by much (Piringer and Joffre, 2005).

The very small values for the radiometric roughness lengths for heat (z_{0H}) have no direct physical meaning because they are many orders of magnitude smaller than any actual roughness surface element. The extremely small values of z_{0H} can indicate that Monin-Obukhov similarity theory is predicting physically unrealistic values to compensate for the inadequacy of the stability dependence of the aerodynamic resistance (see section 5.2, equation 5.2.10). The extremely small values represent an adjustment of the roughness height values to compensate for the unsuitability of the stability functions with use of the radiometric surface temperature, so that Monin-Obukhov Similarity Theory correctly predicts the surface fluxes [for a detailed discussion see Sun and Mahrt, 1995, Verhoef *et al*., 1997, Voogt and Grimmond, 2000].

The surface layer temperature and humidity profiles are defined in equation 4.2.47 and equation 4.2.48, respectively, with scalar lengths z_{0H} and z_{0E} replacing z_{0M} in the wind profile relation. Surface temperature and humidity are thus assumed to apply at heights $z= z_{0H}$ and $z= z_{0E}$, respectively. In fact with surface temperature defined as the radiative temperature using an airborne infrared radiometre, equation 4.2.47 is consistent with observations over a number of different surfaces only if z_{0H} is allowed to differ from z_{0M} (Garratt, 1992). Conceptually the large difference between roughness lenghts z_{0M} and z_{0H} (or z_{0E}), for rough surfaces with bluff obstacles, is a manifestation of the dissimilarity between the transfer mechanisms of momentum and

those of scalar properties, such as air temperature and water vapour, right at the surface. While momentum transfer is a result of viscous shear and also form drag involving local pressure gradients, generated by the roughness of obstacles, the transfer of the passive properties at the surfaces is controlled primarily by molecular diffusion (Brutsaert, 1982; Garratt, 1992; see also Verhoef *et al*., 1997).

According to Fisher *et al.* (2005) momentum to heat roughness lengths ratio z_{0M}/z_{0H} reveals the most significant differences of behaviour between urban and rural types of surface. Current knowledge regarding this ratio is insufficient, with different alternative formulations in the literature (e.g., Brutsaert, 1975; Joffre, 1988; Cahill *et al.*, 1997; Hasager *et al.*, 2003) and more research on this topic is required.

7.7 Testing the impact of surface heterogeneity - Model sensitivity tests to changes in the surface roughness and surface temperature

In order to evaluate the impact of the roughness differences on the spatial distribution of sensible heat flux, Q_H, the model has been run using the same input parameters over the entire study domain, except for the roughness which takes the spatial distribution found for the Greater Manchester study area (**Figure 6.20**, Chapter 6). Here the model input for T_R is the mean satellite radiometric surface temperature observed over the study domain which, as for the wind speed u and the air temperature T_a, is now considered to be the same in all the domain cells (see columns (a) of **Table 7.8**). Three examples are presented based on the conditions observed in Greater Manchester on the 2nd May 2002 at 11:45 UTC, 14th June 2004 at 12:50 UTC, and 21st June 2004 at 13:00.

Similarly, the effects of the surface temperature spatial distribution are evaluated using the same input parameters over the entire domain, except for the surface temperature T_R which has the spatial distribution obtained from satellite imagery over Greater Manchester on the two study days (**Figure 7.3)**. In these simulations the input roughness parameters for all the domain cells are z_H=8m and λ_F=0.13, which are found to be typical values for residential areas in Greater Manchester (see Chapter 6).

The summary, the input data used in the model sensitivity tests described above is shown on **Table 7.8** and the respective results for the spatial distributions of sensible heat flux, Q_H, are shown in **Figure 7.15** and **Figure 7.16** and **Figure 7.17.**

Table 7.8 *- Summary of the model input data used over the entire study domain for the model sensitivity tests to the surface roughness and surface temperature.*

Simulations based on Greater Manchester conditions					
2 May 2002		**14 June 2004**		**21 June 2004**	
(a)	**(b)**	**(a)**	**(b)**	**(a)**	**(b)**
T_a =285K u =4.6m/s	T_a =285K u =4.6m/s	T_a =293K u =5.8m/s	T_a =293K u =5.8m/s	T_a =288K u =3.6m/s	T_a =288K u =3.6m/s
T_R=289 K	z_H=8m λ_F=0.13	T_R=302 K	z_H=8m λ_F=0.13	T_R=296 K	z_H=8m λ_F=0.13
z_H and λ_F spatial distributions of **Figure6.20**	T_R spatial distribution of **Figure 7.3a**	z_H and λ_F spatial distributions of **Figure6.20**	T_R spatial distribution of **Figure 7.3b**	z_H and λ_F spatial distributions of **Figure6.20**	T_R spatial distribution of **Figure 7.3c**

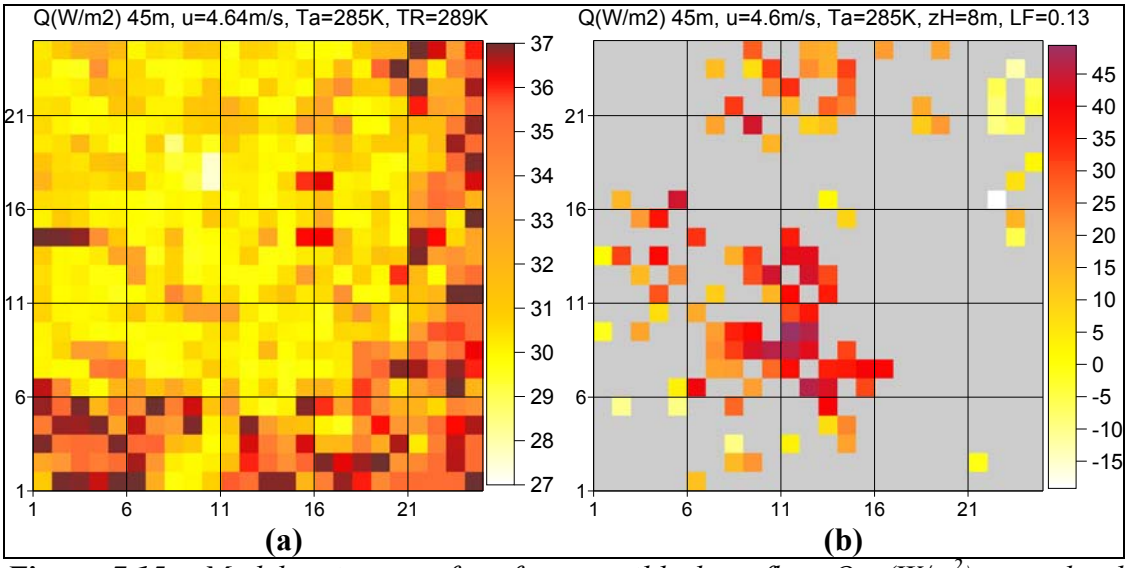

Figure 7.15 *- Model estimates of surface sensible heat flux, Q_H (W/m^2), at a level z_S=45 m, using for all the domain cells the input values presented on the top of each figure, and (a) the spatial distributions of the roughness parameters z_H and λ_F for Greater Manchester shown in* ***Figure 6.20****, and (b) the spatial distribution of the surface temperature T_R from the satellite imagery over Greater Manchester on 2May 2002 at 11:45 UTC shown in* ***Figure 7.3a****.*

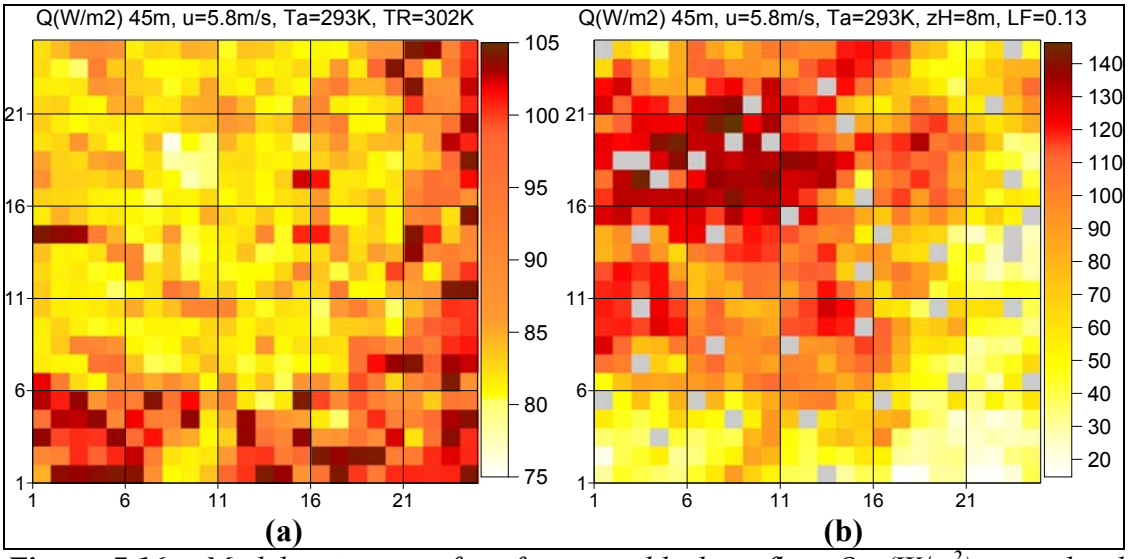

Figure 7.16 *- Model estimates of surface sensible heat flux, Q_H (W/m^2), at a level z_S=45 m, using for all the domain cells the input values presented on the top of each figure: (a) using the spatial distributions of the roughness parameters z_H and λ_F for Greater Manchester shown in* ***Figure 6.20****, and (b) using the spatial distribution of the surface temperature T_R from the satellite imagery over Greater Manchester on 14 June 2004 at 12:50 UTC shown in* ***Figure 7.3b****.*

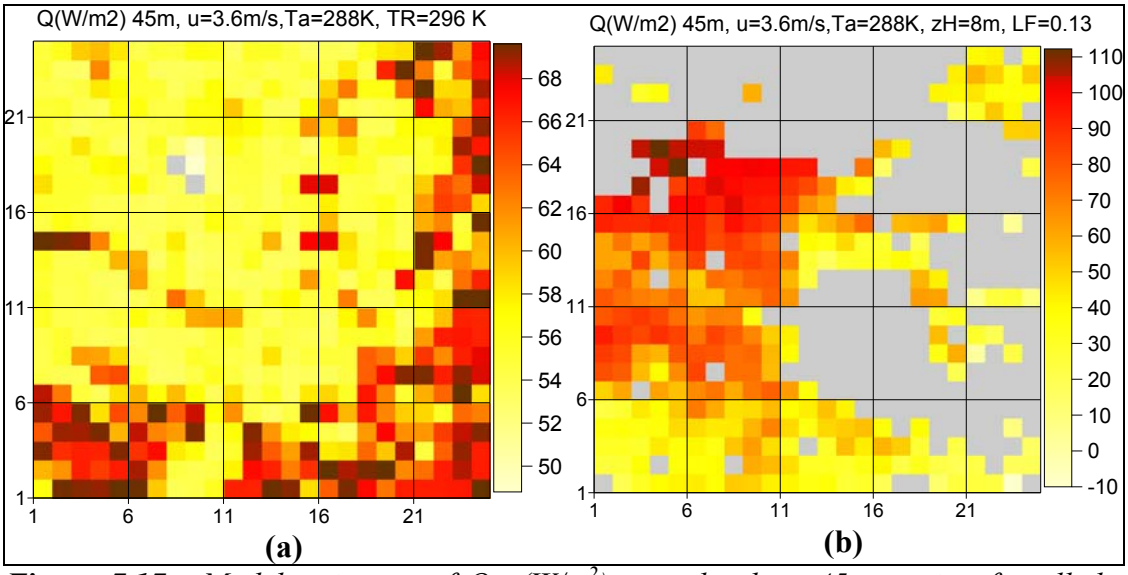

Figure 7.17 *- Model estimates of Q_H (W/m^2), at a level z_S=45 m, using for all the domain cells the input values presented on the top of each figure: (a) using the spatial distributions of the roughness parameters z_H and λ_F for Greater Manchester shown in* ***Figure 6.20****, and (b) using the spatial distribution of T_R from the satellite imagery over Greater Manchester on 21 June 2004 at 13:00 UTC shown in* ***Figure 7.3c****.*

The test performed to evaluate the impact of roughness on the spatial distribution of Q_H (compare **Figure 7.15a** or **Figure 7.16a** with **Figure 6.21a** and **Figure 6.21b**) shows that although the patterns of Q_H and z_{0M} (or z_D) are similar, the values of Q_H are lower where the roughness is higher.

A comparison of **Figure 7.15a** or **Figure 7.16a** with **Figure 6.20b** reveals that the fields shown have a similar pattern. However higher values of the surface sensible heat flux, Q_H, occur in the urban sectors with relatively lower surface roughness, λ_F, and vice-versa. This result is in agreement with the basic model equations, and with the model test results presented in **Chapter 5**. This is due to the fact that the λ_F values over all the study area are less than the threshold value of 0.29. As pointed out in section **5.5** (see **Figure 5.8**), when $\lambda_F < 0.29$, z_{0H} and Q_H decrease as λ_F increases. However, there is different behaviour of the roughness parameter z_{0M} for values of $\lambda_F >$ 0.29. The physical meaning of this threshold was mentioned in section **5.5**, namely that above this value "over sheltering" occurs (Raupach, 1994). Note that z_{0H} has been calculated as a function of z_{0M} and thus of λ_F. According to the model formulation, for values of λ_F >0.29 the roughness length for heat z_{0H} will increase, the resistance to heat R_H will decrease and thus Q_H is expected to increase.

For the surface temperature test based on the case study of 2 May 2002, the comparison between the spatial distributions of the sensible heat flux and the surface temperature is inconclusive, because of the lack of data (see **Figure 7.15b** and **Figure 7.3**). Because the T_R values over the domain are very sparse, it is not impossible to clearly identify a distribution pattern for Q_H. However, as expected, the surface temperature tests for the 14 and 21 June 2004 reveal that the patterns of sensible heat flux Q_H and T_R are similar, and that increased surface temperature corresponds to an increase in heat flux (compare **Figure 7.16b** with **Figure 7.3b,** and **Figure 7.17b** with **Figure 7.3c**).

7.8 Concluding remarks

The model of surface sensible heat flux, Q_H, was implemented over the Greater Manchester study area for three study days (on 2 May 2002, 14 and 21 June 2004). The surface sensible heat flux fields were examined in order to look for any patterns that may indicate areas of increased heat flux, which might be related to convective initiation downwind the urban area. It was found that the urban area produces considerable spatial variation in surface sensible heat flux, with particularly high values in the city centre, and the lowest values in rural areas. The pattern of the modelled spatial distribution of Q_H seems to be similar for the different study days.

Comparison of the model results against the observations for the three studied cases shows that, for the limited measurements available, the model results are acceptable, although they tend to underestimate the sensible heat flux Q_H, by approximately 10%.

Although derived from different data sources, the patterns of the surface temperature T_R and roughness (expressed by the parameters z_H, λ_F, z_D and z_{0M}) are similar; they reveal the presence of the city and the variations of the building density and urban morphology.

The spatial distribution of the model estimates of sensible heat flux Q_H follows the same pattern as the urban fraction, the surface temperature T_R, the buildings height z_H (z_D, z_{0M}), and λ_F (z_{0H}). However higher values of the surface sensible heat flux, Q_H, occur in the urban sectors with relatively lower surface roughness expressed by λ_F, and vice-versa. This result is in agreement with the basic model equations, and with the model test results presented in Chapter 5. This is due to the fact that the λ_F values over all the study area are less than the threshold value of 0.29. As pointed out in section **5.5** (see **Figure 5.8**), while $\lambda_F < 0.29$, z_{0M} and Q_H decreases as λ_F increases. However, there is different behaviour of the roughness parameter z_{0M} for values of $\lambda_F > 0.29$. The physical meaning of this threshold was mentioned in section **5.5**, namely that above this value "over sheltering" occurs (Raupach, 1994).

Sensitivity tests to evaluate the impact of the spatial variations of roughness surface temperature on the modelled spatial distribution of sensible heat flux, Q_H, for some typical values in Greater Manchester, indicate that the surface temperature field

seems to dominate the sensible heat flux, with the impact of the roughness being much less.

Model estimates of roughness length for sensible heat flux, z_{0H}, and excess resistance for heat expressed in terms of the dimensionless parameter $kB^{-1} = \ln(z_{0M} / z_{0H})$, for the studied cases, are comparable to the values indicated in the published literature (e.g., Brutsaert, 1982, Voogt and Grimmond, 2000). However, for urban areas with high rise buildings, such as the city centre, extremely high momentum to heat roughness length ratios (and very low z_{0H}) were found but no values to compare these model results against to were found in the published literature. As recognised by many authors (e. g., Voogt and Grimmond, 2000, Piringer and Joffre, 2005), more research in complex urban environments is needed.

Chapter 8. Applications of the model in Greater Manchester to imply convective initiation.

In this chapter, the surface sensible heat flux model results for Greater Manchester are used to imply convective initiation. The hypothesis is that the increased surface sensible heat flux over urban areas relative to its surroundings can be related to the initiation of convection.

In order to demonstrate that our hypothesis is well founded, we relate the differences of diurnal surface sensible heat flux, between the Greater Manchester urban area and its rural surroundings, to values of thermal forcing, which may eventually trigger convective initiation (Section 8.1). The procedure adopted here is comparable to that of Baik e*t al.* (2001), used to evaluate the impact of the nocturnal excess of surface radiative flux over an urban area, compared with its rural surroundings, on convective initiation downwind the city.

The spatial distribution of surface sensible heat flux derived in Chapter 7 is compared with integrated rainfall rate fields derived from a C-band radar for the 21 June 2004 study day. Convective cells are observed to initiate downwind of the centre of the city. The initiation of convective cells by the sensible heat flux input generated by the high-rise buildings in the city centre is discussed (Section 8.2).

8.1 Relationship of sensible heat flux to thermal forcing

In unstable conditions updrafts are associated with an increase in temperature and sensible heat flux associated with the upward movement of buoyant thermals. The sensible heat flux is a measure of the vertical gradient of temperature and the lapse rate given the equivalent thermal forcing on the atmosphere (e.g. Oke, 1987). Hence, the field of sensible heat flux relates to the occurrence of upward moving thermals in unstable conditions and therefore the likely initiation of rainfall in near saturated conditions.

In previous chapters the impact of the urban area on the distribution of surface sensible heat flux, Q_H, has been examined. Our hypothesis is that the increased surface sensible heat flux over urban areas relatively to its surroundings is related to the initiation of convection. Previous numerical studies by Baik *et al*. (2001) and Han and Baik (2006) using a complex mesoscale numerical atmospheric model, including microphysics, have examined dry and moist convection thermally forced by the presence of an urban heat island, and consequent downwind precipitation enhancement.

In what follows we relate values of surface sensible heat flux to thermal forcing in order to demonstrate that our hypothesis is well founded.

To represent the urban heat island in the numerical model, the following thermal forcing has been used in the thermodynamic energy equation adopted by Baik *et al*. (2001) (see also section 2.1.4):

$$\rho Q = \frac{\rho q_0}{c_p} \frac{a^2}{(x-c)^2 + a^2} e^{-\frac{z}{h}} \tag{8.1}$$

where ρ is the air density, q_0 is the heating amplitude, c_p is the specific heat of air at constant pressure, a is the half-width of a bell-shaped function, c is the horizontal location of the heating centre from the left boundary of the model, and h is the *e*-folding height. The specified heating (ρQ) decreases horizontally in a bell shape from the heating centre and decreases exponentially with height. According to the authors, this heating structure roughly imitates the observed spatial temperature deviation pattern over cities. The heating centre is located at a distance $x = c$ away from the left boundary of the model grid. The parameters a and h are specified as 10 km and 700 m, respectively. The physical domain sizes are 150 km in the horizontal and 12 km in the vertical. The horizontal and vertical grid intervals are 1 km and 150 m, respectively.

The parameter q_0 represents the intensity of the heat island and varies from 0.2 to 2 J kg^{-1} s^{-1}. The peak heating would be given by q_0/c_p, which corresponds to a heating rate of 0.7 to 7.1 K h^{-1} for a heating amplitude of 0.2 to 2 J kg^{-1} s^{-1}:

$$\left(\frac{\Delta T}{\Delta t}\right)^{urban} - \left(\frac{\Delta T}{\Delta t}\right)^{rural} = \frac{q_0}{c_p} \tag{8.2}$$

A typical maximum difference in heating/cooling rate between urban and rural areas in mid-latitudes under "ideal" (calm, clear) weather conditions is of the order of a few degrees per hour (Oke, 1982).

In our case we are interested in the thermal forcing on the atmospheric boundary layer due to the increased sensible heat input from below, during day time, associated with the presence of urban areas. Hence differences between the surface sensible heat flux over urban and rural surfaces must be considered.

Atmospheric heating/cooling occurs as a result of horizontal and vertical divergence in the transport of heat by radiation and turbulence. The heating/cooling rate for air within the canopy layer associated with the divergence of sensible heat flux from the canopy layer can be expressed by

$$\frac{\partial T}{\partial t} = \frac{\nabla . Q_H}{\rho c_p} \tag{8.3}$$

Neglecting the horizontal divergence, this equation can be re-written in its finite difference form as

$$\frac{\Delta T}{\Delta t} \cong \frac{1}{\rho c_p} \frac{\Delta Q_H}{\Delta z} \tag{8.4}$$

Where ΔQ_H is the difference between the flux at bottom (z=0) and at the top of the canopy layer, and Δz is the depth of the canopy layer. Using the control volume approach for the urban canopy, whose top is set above the roof level, and its base at the depth of zero net ground heat flux over the chosen time scale or period (see Chapter 4), one can consider only the sensible heat flux through its top. Moreover adjacent to the canopy layer is the inertial sublayer, where the turbulent fluxes vary by less than 10% with the height, and therefore one can consider that the flux through the top of the canopy layer is approximately that measured at a level z_S within the inertial sublayer, i.e.,

$$\frac{\Delta T}{\Delta t} \cong \frac{1}{\rho c_p} \frac{Q_H}{z_s} \tag{8.5}$$

Hence, there is a possible relation between the sensible heat flux estimated in previous chapters and the thermal forcing of the atmospheric boundary layer due to

urbanisation. The difference between the heating rate of the urban area and its surroundings is

$$\left(\frac{\Delta T}{\Delta t}\right)^{urban} - \left(\frac{\Delta T}{\Delta t}\right)^{rural} \cong \frac{1}{\rho c_p z_s}\left(Q_H^{urban} - Q_H^{rural}\right) \tag{8.6}$$

Comparison of equations (8.2) and (8.6) leads to

$$\left(\frac{\Delta T}{\Delta t}\right)^{urban} - \left(\frac{\Delta T}{\Delta t}\right)^{rural} \cong \frac{1}{\rho c_p z_s}\left(Q_H^{urban} - Q_H^{rural}\right) = \frac{q_0}{c_p} \tag{8.7}$$

$$\left(Q_H^{urban} - Q_H^{rural}\right) = \rho z_s q_0 \tag{8.8}$$

Now we are able to relate the differences between our estimates of sensible heat flux for urban and rural areas $\left(Q_H^{urban} - Q_H^{rural}\right)$ to the thermal forcing expressed by q_0, and consequently compare our results with the results of Baik *et al*. (2001) and Han and Baik (2006) in order to evaluate the possible impact of the sensible heat flux on convective initiation.

8.2 Case study 21 June 2004

Figure 8.1 shows the surface pressure field and frontal positions over the UK and surrounding areas at 12:00 UTC on 21st June 2004. Convective cells are seen to be moving across North West England in the MODIS visible satellite image during late morning on 21st June 2004 (**Figure 8.2**).

In order to examine the rainfall from the convective cells, data from the C-band Hameldon Hill radar located some 24km north of the city centre are displayed in **Figure 8.3**. This figure shows a sequence of radar images compared to the field of surface sensible heat flux, Q_H, at 13:00 on 21st June 2004 (from **Figure 7.11 (b)**). The white box over the radar images shows the area corresponding to the area for which Q_H is evaluated shown in the first frame. Note that a rainfall cell is generated downwind of the large values of Q_H over the city centre. **Figure 8.4** shows Hövmoller diagrams. In these diagrams distance is plotted against time for a direction corresponding to the low wind level direction (westerly in this case), see the legend to **Figure 8.4**.

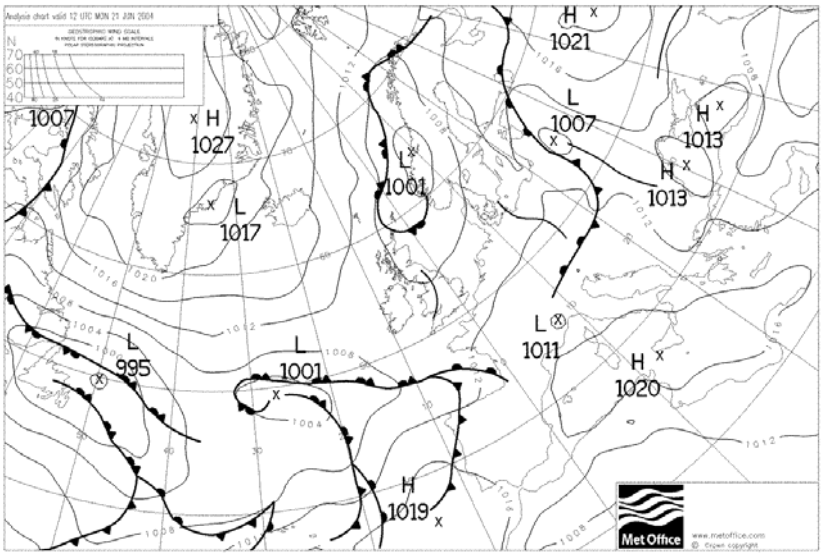

Figure 8.1 *- The synoptic pressure field and frontal positions over the UK and surrounding area at 12:00 UTC on 21st June 2004.*

(a)

(b)

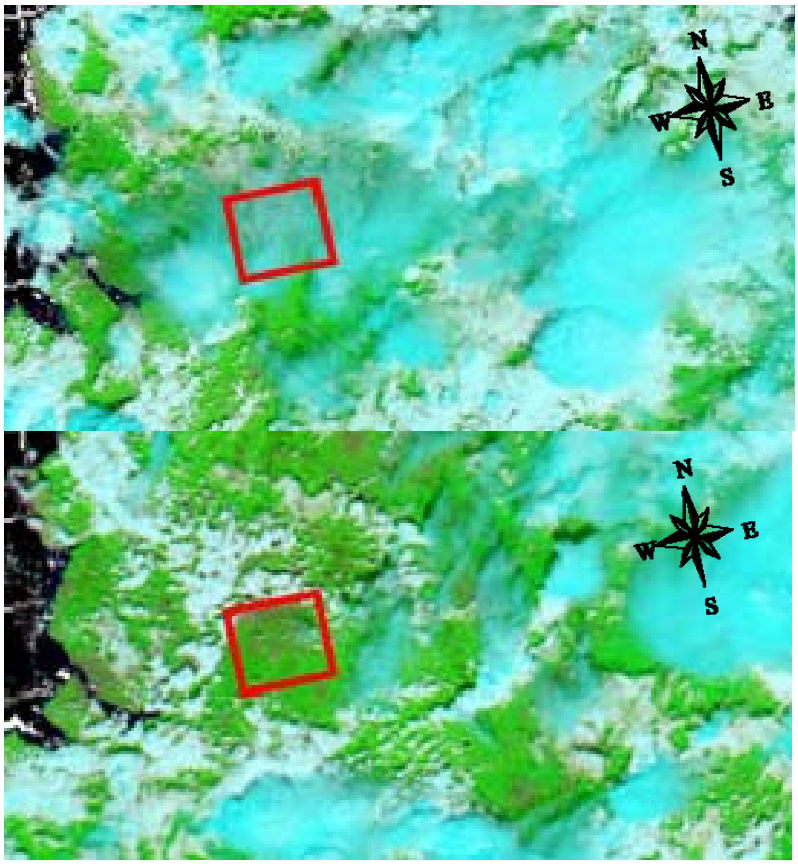

Figure 8.2 *- Satellite images over North West England on 21st June 2004 (MODIS, Bands 7-2-1, 5min, 500m) (a) Terra/ MODIS, 11:15 UTC (b) Aqua/MODIS, 13:00 UTC. The red line delimits the Greater Manchester study area of 24x24km^2. Note there are slight differences in projection between (a) and (b). The Mersey and Dee estuaries can just be seen on the left-hand side of the images.*

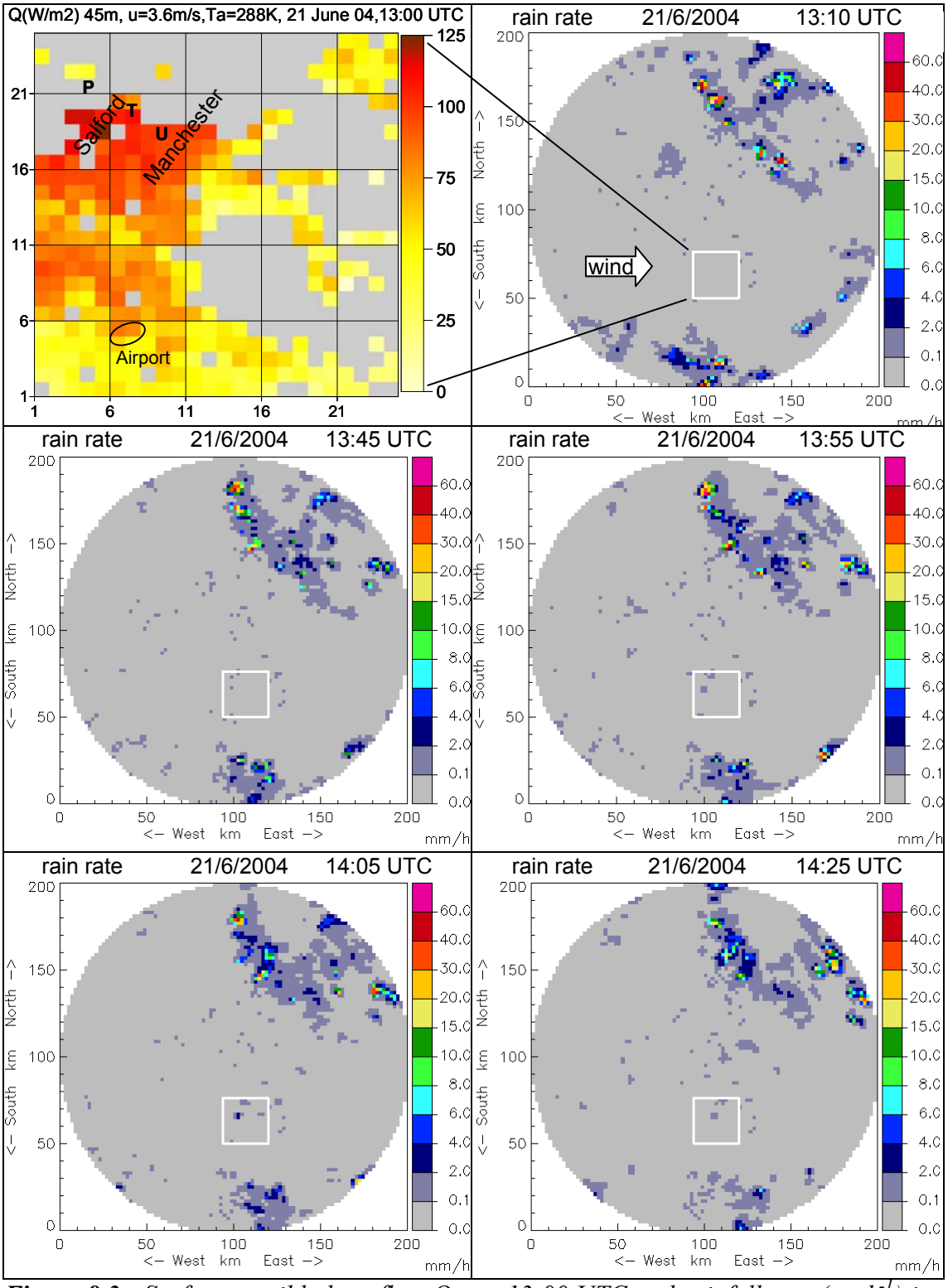

Figure 8.3 *- Surface sensible heat flux, Q_H, at 13:00 UTC and rainfall rate (mmh^{-1}) in the afternoon, on 21st June 2004, shown in a sequence of five images from the Hameldon Hill C-band radar located some 24km north of the centre of Manchester, North West England. These images are an example of the radar product used in this work (instantaneous rainfall rate image, every 5 min, with 2x2 km^2 spatial resolution).*

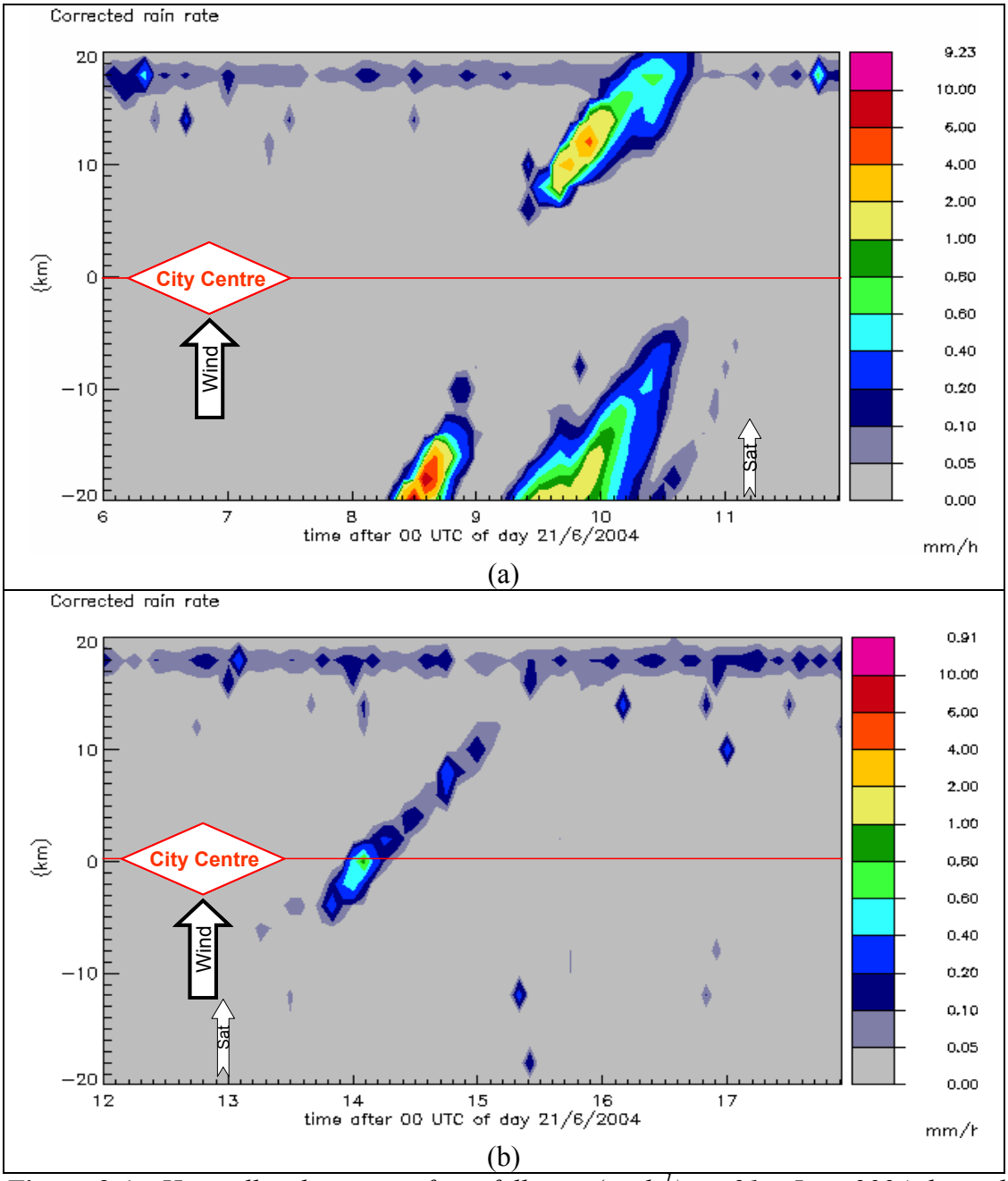

Figure 8.4 *- Hovmoller diagrams of rainfall rate (mmh^{-1}) on 21st June 2004 derived from the Hameldon Hill C-band radar located some 24km north of the centre of Manchester, North West England (a) 06:00-11:00 UTC and (b) 12:00-17:00 UTC. The coordinates represent distance along a 7km wide swath running through the city centre in the direction of the westerly cell movement and the abscissa represents time. Some small spurious areas of rain remain where the removal of radar ground clutter echoes has been incomplete. The time of the satellite images shown in* ***Figure 8.2*** *are indicated by the vertical arrows next to the time axis. These diagrams were produced using IDL (Interactive Data Language) software.*

Figure 8.4a shows the diagram constructed for the period 06:00 to 11:00 UTC on 21st June 2004, **Figure 8.4b** shows the same format for the period 12:00 to 17:00 UTC on this day. The colours indicate the rainfall rates in mmh^{-1}, and the centre of each box (y= 0 km) corresponds to the centre of the urban area of Greater Manchester.

During the morning (**Figure 8.4a**) a convective rain cell is generated just downwind of Manchester city centre moving in an easterly direction. In addition, cells are also seen to form on the western edge of the urban area dissipating as they move over to the east of the city towards the upland area. In the afternoon (**Figure 8.4b**) a cell forms to the west of Manchester city centre over Salford moving eastwards and dissipating. The areas associated with the cell generation seem to be those areas in which the sensible heat flux is largest (**Figure 7.11**) brought about by the existence of high rise buildings.

The simulations of Baik *et al*. (2001) and Han and Baik (2006), using various heating amplitudes and uniform basic-state wind speeds, show that downwind upward motion induced by the urban heat island can initiate moist convection and result in downwind precipitation under favourable thermodynamic conditions. They found that the distance downwind where rain formed depended upon the strength of the surface heating amplitude, the wind speed and the relative humidity.

In the two-dimensional numerical model simulations described by Baik et al. (2001) the basic-state temperature profile follows that of the standard atmosphere, which is stable through the atmosphere. The relative humidity (RH) is constant from the surface to z=1 km, thereafter decreasing linearly with height up to z=11 km, and is constant above, with RH=10%. The relative humidity in the layer between the surface and z= 1 km (RH_L) is set to 50%, 60%, 70%, 80%, and 90%. The basic-state wind speed in the numerical simulations is considered to be uniform in the vertical and is set to 2, 3, 4, and 5 m s^{-1}.The physical domain sizes are 150 km in the horizontal and 12 km in the vertical. The horizontal and vertical grid intervals are 1 km and 150 m, respectively. The model is integrated forward in time up to 6 h.

Consider for example the simulation for a relative humidity of RH_L=90% and a wind speed of u=5m/s, using a thermal forcing of q_0=1.2 J kg^{-1} s^{-1}. In this case, the calculated convective available potential energy, CAPE (Tsonis, 2002), for the basic-state thermodynamic soundings is 101 J kg^{-1}. Model results for the fields of the

perturbation in the vertical velocity, cloud water mixing ratio and rainwater mixing ratio, show that after less than 1 hour, the updraft cell induced by thermal forcing moving in the downstream direction initiates moist convection downstream, with cloud water forming at 13 km from the heating centre. After 2 h the cloud has moved further downwind, to approximately 24 km from the heating centre, and precipitation reaching the ground has all ready started. However, Han and Baik (2006) concluded that the first cloud water and rainwater formation occur earlier and closer to the heating centre than in the two-dimensional moist simulations of Baik *et al.* (2001), since the maximum downwind updraft in three-dimensional moist simulations develops more rapidly at the early stage.

Indeed, in **Figure 8.4** we see rain first occurring some 10 km downwind of Salford in the morning of the 21st June 2004. In the afternoon the rain first occurred over Salford implying that the convection may be first initiated over the upwind rural-urban boundary, or the high rise buildings lead to significant upward vertical velocities.

We consider that the effect of the forcing (q_0=1.2 J kg^{-1} s^{-1}) used in the simulation carried out by Baik *et al*. (2001), would be equivalent to that due to a difference of sensible heat fluxes of 65 W m^{-2}, given by

$$\left(Q_H^{urban} - Q_H^{rural}\right) = \rho z_s q_0 \qquad (8.9)$$

taking ρ = 1.2 kg m^{-3} and z_S = 45m.

The modelled spatial distribution of surface sensible heat flux, Q_H, over Greater Manchester for the case study of 21 June 2004 (see **Figure 7.11b**), shows that differences of sensible heat flux of 65 W m^{-2}, between the urban area and its rural surroundings, necessary for a forcing of 1.2 J kg^{-1} s^{-1}, may occur for relatively extensive areas. Therefore it is acceptable to conclude that the presence of the city may have triggered convection.

Note that in our case study the observed low-level air temperature was 288K, the wind speed 3.6 m/s (from NW), and high values of relative humidity have been observed in the morning. A CAPE of approximately 200 J kg^{-1} (and a small value for the convective inhibition energy, CIN (Tsonis, 2002), of -2 J kg^{-1}) has been calculated based on the soundings at 12 UTC, from the operational upper-air station of Castor Bay, Northern Ireland, located at about 300 km (NW) from Greater Manchester. These

conditions are not far from the values associated with the simulation Baik *et al*. (2001) that we have been considering.

8.3 Concluding remarks

The surface sensible heat flux fields obtained in Chapter 7 were examined in order to look for any patterns that may indicate areas of increased heat flux, which might be related to convective initiation downwind the urban area. It was found that the urban area produces considerable spatial variation in surface sensible heat flux, with particularly high values in the city centre, and the lowest values in rural areas.

Here a case study on 21 June 2004 is described in which the model-generated distributions of surface sensible heat flux over Greater Manchester are compared with rainfall fields derived from C-band radar. Convective cells are observed to initiate downwind of the centre of the city occupied by high rise buildings.

When differences of surface sensible heat flux between the Greater Manchester urban area and its rural surroundings are related to values of thermal forcing, and the results for the 21 June 2004 study day are compared with the simulation results of Baik *et al*. (2001) and Han and Baik (2006), it is possible to conclude that the presence of the Manchester urban area may trigger convective initiation.

The procedure adopted here is comparable to that of Baik e*t al.* (2001), used to evaluate the impact of the nocturnal excess of surface radiative flux over an urban area, compared with its rural surroundings, on convective initiation downwind the city. However, in our case we are concerned with the impact of a diurnal excess of surface sensible heat flux over an urban area compared with its rural surroundings. It has been found that spatial variations of about 65 W m^{-2} of surface sensible heat flux are related to values of thermal forcing that might trigger convective initiation. The modelled spatial distribution of surface sensible heat flux for Greater Manchester shows that these differences of surface sensible heat flux may occur between the urban area and its rural surroundings over extensive areas.

Note that the atmospheric conditions of wind speed, relative humidity and CAPE in our case study are comparable to the values of the simulation of Baik *et al*.

(2001), and the distance from the city centre at which the rain cells appear is similar to the simulation results of Baik *et al*. (2001).

As discussed in Chapter 4, it would appear that the area of Salford (high rise buildings close together) has a similar impact to medium height buildings over a larger area as predicted by the experiments reported. Which of these areas leads to convective cell generation depends upon the details of the wind and temperature fields.

Although spatial variations of sensible heat flux for Greater Manchester may act as a forcing to convective initiation, the up-lift effect due to the presence of high rise buildings should not be neglected. The relative importance of these two factors must be taken into consideration in future studies.

In this study we tried to relate surface sensible heat flux fields (spatial distribution) to convective initiation and the occurrence of downwind clouds and precipitation. Other factors impacting the development of these convective phenomena, such as humidity, uplift, cloud condensation nuclei, etc., were not taken into consideration, and this constitutes the main limitation of the numerical model used in this work to study the impact of urbanisation on clouds ands and precipitation.

Chapter 9. Summary, conclusions and future work

9.1 Formulation for a model of surface sensible heat flux for Greater Manchester

The model

The aim of the work described in this thesis was to study the influence of an urban area on convective precipitation, namely how the urban surface roughness, temperature and sensible heat flux affect the precipitation over and downwind of a city. Of particular interest is the degree to which spatial variations of surface heterogeneity, notably from high-rise buildings, impact these phenomena, and whether the processes involved can be represented appropriately within a single-column model of surface energy balance applied on a rectangular grid.

A simple model was used to highlight the physical processes involved in coupling between the atmosphere and urban morphology. More complex models, such as the NCAR Weather Research and Forecasting (WRF) model and the Met Office Unified Model, even at very high resolutions, for example 1km, can not be initialised accurately and reliably enough for detailed studies of the interactions of buildings with the atmosphere over neighbourhood scales. However the results from simple model studies can provide useful information on how to parameterise urban processes in these more complex models.

A simple model of the surface sensible heat flux (described in Chapters 4 and 5) was used to explore the impact of urban canopy heterogeneity. The numerical scheme, based upon several published systems, principally Voogt and Grimmond (2000) and Grimmond and Oke (1999a), was developed to derive fields of surface sensible heat flux for a range of wind and temperature over an urban area. The model estimates the sensible heat flux at a level z_S, above the surface within the atmospheric inertial sub layer, where the Monin-Obukhov similarity theory (MOST) is valid.

The surface sensible heat flux, Q_H, was calculated from the MOST based bulk equation (5.2.1)

$$Q_H = \rho\ c_p \frac{(T_0 - T_a)}{r_{ah}} = \rho\ c_p \frac{(T_0 - T_a)}{r_{am} + r_b} \tag{5.2.1}$$

where ρ is the air density, c_p the specific heat capacity for the air, T_a the air temperature at level z_S in the surface layer, T_0 the aerodynamic surface temperature, and r_{ah} is the aerodynamic resistance for heat transfer between the surface level z_{0H} (at $T=T_0$) and the level z_S (at $T=T_a$); r_{am} is the areodynamic resistance for momentum (between z_S and z_{0M}) and r_b, the bulk aerodynamic excess resistance (or laminar resistance), represents the resistance between the level z_{0M} and the surface level z_{0H} (at $T=T_0$).

As discussed in Section 5.2, the sensible heat flux can be calculated using remotely sensed surface temperature, such as the radiometric surface temperature T_R obtained from satellite imagery (equation 5.2.5).

$$Q_H = \rho\ c_p \frac{(T_R - T_a)}{r_H} = \rho\ c_p \frac{(T_R - T_a)}{r_{am} + r_T} \tag{5.2.5}$$

Where r_H is the resistence to heat transfer between the surface (at $T=T_R$) and a atmospheric level z_S (at $T=T_a$); r_{am} is the areodynamic resistance for momentum (between z_S and z_{0M}) and r_T represents the resistance between the level z_{0M} and the surface.

The resistances are defined (section 5.2) in terms of the von Karman's constant (k), the wind speed (u) at a level z_S in the surface layer, the roughness parameters zero-plan displacement length (z_D) and roughness lengths for momentum and heat (z_{0M} and z_{0H}, respectively), and the stability correction functions for momentum and heat, $\Psi_M(\zeta)$ and $\Psi_H(\zeta)$ (Table 5.1). The resistance to heat transfer is given by

$$r_H = \frac{1}{k\,u_*}\left[\ln\left(\frac{z_s - z_D}{z_{0M}}\right) - \Psi_H\right] + \frac{1}{k\,u_*}\ln\left(\frac{z_{0M}}{z_{0H}}\right) \tag{5.2.10}$$

and the value of the excess of resistance for heat expressed in terms of

$$kB^{-1} = \ln\left(\frac{z_{0M}}{z_{0H}}\right) \tag{5.2.11}$$

depends on the use of the radiometric temperatures and the method for calculating the resistance.

The meteorological variables used as input to the model were the satellite radiometric surface temperature, T_R, the air temperature, T_a, and the wind velocity, u. T_a and u are typically measured several metres above the surface, at the measurement height, z_S, in the inertial sub-layer.

Model input roughness parameters are the building height, z_H, and the frontal area index, λ_F. Over built areas z_H and λ_F are derived from analysis of surface form according to the Grimmond and Oke (1999a) methodology, while for natural surfaces these roughness parameters are estimated using reference tables shown in the literature (for example, Grimmond and Oke, 1999a, Wieringa, 1993, Brutsaert, 1982, Grimmond *et al.*, 1998). The zero-plane displacement length, z_D, and roughness length for momentum, z_{0M}, were estimated as a function of building height, z_H, and frontal area index, λ_F, using Raupach's (1994, 1995) method (equations 5.4.4 -5.4.6). The roughness length for heat, z_{0H}, is determined as a function of z_{0M} and roughness Reynold's number indicating atmospheric stability, using the formulation proposed by Brutsaert (1982) for bluff-rough surfaces (equation 5.4.7 -5.4.8).

The main objective of our study was to apply the model to the Manchester urban area in atmospheric convective conditions, which occur during daytime, typically in springtime and summer. These are conditions for which we anticipated that the urban morphology will modify the distribution of sensible heat flux and influence convective development.

The relationship of sensible heat flux to convective initiation was discussed, and the sensible heat flux fields thus derived were compared with integrated rainfall fields derived from C-band radar data.

Model limitations

The implementation of this formulation, can be considered the most straightforward method to obtain the sensible heat flux Q_H at the surface-atmosphere interface (Piringer and Joffre, 2005). However there are a number of limitations.

A major limitation of this approach is that it is only applicable under clear-sky conditions, when remotely sensed measurements are available, consequently restraining the temporal continuity of its implementation, at best providing sporadic results.

On the other hand, applying this approach is problematic, especially for cities. Namely, because this method is susceptible to large errors mainly induced by inaccuracies on the input parameters required in the equations (Piringer and Joffre, 2005).

The surface temperature is a relatively ambiguous quantity. In equation (5.2.1), T_0 represents the aerodynamic temperature, i.e., the temperature of the first air molecules immediately above the land surface. However, the radiative temperature as observed from remote sensors looking down at cities may be quite different (Piringer and Joffre, 2005).

Land surface temperatures obtained from satellite-based measurements involve two main errors related to the atmospheric absorption and emission and surface emissivity effects. Even after applying corrections for these effects, the remaining error is of the order of a few degrees (Vazquez *et al*., 1997). The estimation of the land surface temperature from remote sensors involves the correct interpretation of measurements of the radiation emissions from the surface. This is particularly difficult when it concerns the urban surface, due to its complex three-dimensional form and the different thermal, radiative and moisture properties of its numerous surface elements. The geometric structure creates shade patterns in combination with the solar beam and obscures portions of the surface from the sensor, depending on where it is pointing and its field-of-view (Soux *et al*., 2004).

In addition, due to the remarkable heterogeneity of the cities, over urban surfaces the definition of the "surface" is not unique. For example, Roth *et al*. (1989) emphasize the difference between the "active" urban surface, which includes horizontal and vertical solid surfaces exchanging heat with the atmosphere, and the "satellite-sensed" surface that tends to over-emphasize the role of roofs and tree tops, while in meso-scale atmospheric models the "surface" may be a roughly horizontal immaterial surface above the canopy.

Also, it is important to mention that one of the main problems when retrieving the land surface temperature for a city from space is the lack of appropriate ground - based measurements to validate a given approach. Due to the spatial heterogeneity of the cities, it is difficult or even impossible to compare ground-based measurements, which are representative of relatively small areas, with satellite-based measurements containing pixels covering areas of the order of about one square kilometre or more

(Piringer and Joffre, 2005). This is a general difficulty when retrieving the surface energy balance of a city from space.

On the other hand there are also problems related to the incomplete knowledge of the appropriate surface layer values of the wind speed and air temperature, u and T_a, both required in the model formulation. Usually, it is necessary to use measurements of these variables from routine meteorological observations from a nearby weather station. However, due to the large spatial heterogeneity typical of the urban environment, an error of several degrees is to be expected in the air temperature and a relative error of up to several tens of percent in the wind speed. Especially this last error will induce an error of a similar magnitude on the heat flux (Piringer and Joffre, 2005). An additional problem is caused by the fact that wind speed and temperature measurements are often carried out within the roughness sub-layer or in sheltered locations, hence invalidating similarity theory.

Finally, a very serious problem in applying the present approach is the insufficient knowledge of the excess resistance, expressed by $kB^{-1}= \ln(z_{0M}/z_{0H})$, especially for cities (Piringer and Joffre, 2005). Typically, the roughness lengths ratio z_{0M}/z_{0H} for cities is considerably larger than for homogenous vegetated surfaces. However, although some studies (e. g., Voogt and Grimmond, 2000) provide estimates for this parameter for cities, the available information is insufficient.

Results of preliminary model simulations

Before implementing the model over the Greater Manchester study area, sensitivity experiments for a range of typical input values were carried out to test the validity of the numerical model, and experiments with a schematic urban morphology are used to investigate the impact of different types of building arrays (Chapter 5). Model output values for z_D, z_{0M}, z_{0H},..., L, u_*, and Q_H were derived.

The sensitivity of Q_H to the different model parameters, z_H, u, T_R, T_a, and λ_F, was investigated (Chapter 5), for a range of synthetic typical input values: $0.01 \leq \lambda_F \leq 0.47$; $0.5\text{m} \leq z_H \leq 12\text{m}$; $0.5\text{m/s} \leq u \leq 12\text{m/s}$; $274\text{K} \leq T_R \leq 320\text{K}$; $280\text{K} \leq T_a \leq 303\text{K}$, with z_s=20m. For the range of typical input values used, the model behaves reasonably for slightly stable to unstable conditions. However, as expected, the model fails for stable conditions, where $z_S >> L$, and does not converge in the cases where there is a discontinuity of the stability functions. These discontinuities are a consequence of the

established criteria for being near neutral stability: $|\zeta=(z_S-z_D)/L| < 0.1$, where $\Psi_M = \Psi_H = 0$. A discontinuity is also observed for cases where $\lambda_F \geq 0.29$ due to the different behaviour of the roughness parameter z_{0M} for values of $\lambda_F > 0.29$. The value λ_{Fmax} (=0.29) can be interpreted as the onset of "over-sheltering", the point at which adding further roughness elements merely shelters one another (Raupach, 1994). After this point the roughness z_{0M} is seen to decrease, yet the heat flux (Q_H) increases.

In order to more clearly identify the comparative impact of surface roughness versus local heating effects, some experiments using a stylised representation of the urban area have been carried out, for a range of typical values of z_H, λ_F, T_a , u, and T_R (Chapter 5). The results of these experiments on spatial variations of urban roughness show that an area of uniform low buildings has a lower sensible heat flux than those areas which have higher roughness. However, interestingly, an area of high rise buildings close together produces almost the same sensible heat flux as the area having lower buildings covering a much larger area than the high rise buildings.

9.2 Application of the model of surface sensible heat flux to Greater Manchester

Application of the model

The model was formulated for Greater Manchester, over a study area of 24x24 km^2 and on a grid of 1x1 km^2 resolution. The bulk equations were used and the model parameters were specified as averages over each grid square. The dimensions of the area of interest were based on the typical local scale of the convective processes. The study area comprises Manchester city centre and some major suburbs, namely Salford and Stockport, Manchester International Airport and some non urbanised areas located mostly to the East and South. The terrain is quite flat; to the east it is bounded by the Pennines, the most significant feature in the region, but in the other directions, principally to the west, there are no significant relief features (Figures 5.1 and 7.1).

The model was applied to the Greater Manchester study area, at different seasons of the year (for example, 2 May 2002, 14 June 2004, 21 June 2004, 6 August 2003 and 8 December 2003), for clear sky conditions and for westerly wind, which provided good conditions for the model evaluation, since there are no significant

orographic obstacles in this direction. The model was implemented for dry terrain conditions, at around midday when surface sensible heat flux is considerable and later convective showers might be expected.

The surface sensible heat flux model estimates were compared with observations in three case studies, on 2nd May 2002, 14 and 21 June 2004 when ground-based observations of surface sensible heat flux are available (Chapter 7). On 21 June 2004, when also rainfall radar data are available, the model is applied to convective initiation (Chapter 8).

The radiometric surface temperature, T_R, data used in the present work were derived from MODIS Terra/Aqua (1 km, 5 min) satellite imagery over Greater Manchester at around midday. The model input values of air temperature, T_a, and wind speed, u, are the hourly values observed at the Manchester airport at the same time as the MODIS satellite imagery. These data refer to a particular hour of the day (around midday) depending on the time of the satellite overpass available for each specific day. Model input roughness parameters, surface elements height (z_H) and the frontal area index (λ_F) were derived by the author from a surface morphologic database for Greater Manchester that has being developed from analysis of digitised georeferenced lidar data of the surface elements provided by the Environment Agency and the Cities Revealed User Group, aerial photographs, maps and field surveys (Chapter 6).

The surface temperature, air temperature and wind data

The spatial distribution of surface temperatures, T_R, at 1x1 km^2 resolution over Greater Manchester study area showed that, as expected, higher values of surface temperature are found over urbanised zones than over rural zones. The surface temperature is significantly lower at the Airport, situated in a rural area, than at the urban zones of Salford and Manchester. The values of the surface temperature in these urban observational sites are nearly the maximum (T_{Rmax}) observed over the entire study domain (Chapter 7).

Comparison of the satellite imagery for different days, at around midday, showed that under clear sky conditions the pattern of the spatial distribution of the radiometric surface temperature T_R is essentially the same for all study days; it does not seem to depend significantly on the season of the year.

The spatial variation of surface temperature T_R seems to be much more accentuated than the variation of air temperature T_a. Differences between T_R observations in the city centre and at the Airport (rural zone) can be more than 10C, while for the T_a are around 2C (Chapter 7).

Note that an obstacle to implementation of the model is the lack of observations of air temperature and wind data over the study domain. This is a common problem, since in general observational networks with 1km step, or so, are not available. Thus investigation must be carried out on how to extrapolate the measurements at the airport for use in urban studies (see for example Wit *et al.*, 2002), and eventually some field campaigns for the area of interest are needed.

Although some local measurements of surface temperature have been carried out during the present study they are not sufficient to evaluate the data derived from satellite imagery. Some investigation of procedures to evaluate the quality of the land surface temperature datasets from satellite imagery should be carried out. The possibility of estimating the surface temperature from other sources or empirical methods should also be investigated.

The surface morphologic database, and model estimates of the roughness parameters zero-plane displacement length, z_D, and roughness length for momentum, z_{0M}.

A classification of 15 land-use categories (9 UTZ) has been established for Greater Manchester and reference morphologic parameters, such as building mean height (z_H), plan area index (λ_P) and frontal area index (λ_F), were attributed to each category (Chapter 6). Comparisons with earlier published work (e.g., Ellefsen, 1990/91, for U.S.A. cities) revealed similarities to previous representations, but also some differences. These differences are probably due to the nature of the urban areas in the United Kingdom, for example the distribution and type of buildings and green spaces.

The model surface morphologic parameters, surface elements height (z_H) and frontal area index (λ_F), were estimated and mapped over a rectangular grid of 1 x 1 km^2 resolution, for the Greater Manchester study domain (Chapter 6). The estimates of the height of the buildings, z_H, and of the frontal area index, λ_F, for each cell were

weighted averages of the values attributed for each urban category, considering the percentage of each category present in the grid cell.

The resulting spatial distributions of surface element heights (z_H) and frontal area index (λ_F) reveal the difference between the rural areas to the east and south compared to the urban areas. The area of high rise buildings is clearly evident (Figure 6.20).

The model estimates of the zero-plane displacement length, z_D, and roughness length for momentum, z_{0M}, derived from the values of z_H and λ_F, were also presented (in Figure 6.21) for the study domain. These estimates of the roughness parameters z_D ,and z_{0M} are comparable to previously published values. In addition, taking the roughness values obtained for the entire study domain it was found that $z_D=5z_{0M}$, $z_D=0.4z_H$, $z_{0M}= 0.08z_H$. These results are in agreement with published literature (see, for example, Grimmond and Oke 1999a).

Note that, although derived from different data sources, the patterns of the surface temperature T_R and roughness expressed by the parameters z_H, λ_F, z_D, and z_{0M} are similar; they reveal the presence of the city and the variations of the building density and urban morphology.

The surface roughness parameters characteristic of the Greater Manchester study area were considered to be the same for all study days, and have been used to model the spatial distribution of surface sensible heat flux, Q_H, over the Greater Manchester urban area.

In fact, for the construction of the present surface morphology database, it has been assumed that the roughness surface elements such as buildings are rigid parallelepipeds and that the roughness effects do not vary with the wind direction. A more realistic approach must take into consideration the orientation and shape of the buildings. Further improvements on the data base should involve a dynamic approach, where roughness parameters such as the frontal area index may assume different values depending on the wind direction.

The modelling of the urban atmospheric boundary layer in both process studies and operational meteorological models requires specific representations of the urban morphology. The database for the roughness parameters developed here can be used for many urban studies in the future. The development of the present database was slow and arduous because most of the roughness parameters of interest were not

derived automatically from the digitised georeferenced dataset of surface elements height. Computational research should be carried out to improve the process of construction of this type of database, in order to construct them faster, allow for an easy update (for example Manchester has been changing very fast in the last few years and our database needs to be updated for the city centre and its neighbourhoods quite often), and calculate roughness parameters for different wind directions.

9.3 Model results of surface sensible heat flux for Greater Manchester. Model estimates of roughness length for heat, z_{0H}, and roughness lengths ratio (z_{0M}/z_{0H})

The model estimates of sensible heat flux, Q_H, around midday, have been mapped for the 24 x 24km^2 Greater Manchester study area at 1 x 1km^2 resolution for the three study days of 2 May 2002, and 14 and 21 June 2004. The pattern of the modelled spatial distribution of Q_H seems to be similar for the different study days. As expected higher values of sensible heat flux were found over urbanised zones than over rural zones (Chapter 7). Comparison of the model results against the observations for the case studies shows that the model results are acceptable although they tend to underestimate the sensible heat flux Q_H.

Model estimates of roughness length for sensible heat flux, z_{0H}, and excess resistance for heat expressed in terms of the dimensionless parameter kB^{-1}, $kB^{-1} = \ln(z_{0M} / z_{0H})$, were presented for the three study cases (Figures 7.13 and 7.14). Taking into consideration all the values obtained for the three cases, it is found that z_{0H} values range between $\sim 10^{-21}$ and $\sim 10^{-2}$, with the lower values sited over urbanised zones and the highest values over rural areas. Values between 10^{-9} and 10^{-15} occur in the urbanised zones, except for the city centre where extremely low values ranging from $\sim 10^{-15}$ to $\sim 10^{-21}$ were found. The corresponding model estimates of kB^{-1} over urbanised zones lie on a range of values of 15 - 30 over the urbanised zones, but for the city centre these values can be very high, around 50. The lowest values of kB^{-1} are found over the rural zones. These values of z_{0H} and kB^{-1} are in the range of the values referred on the published literature (e.g., Brutsaert, 1982; Voogt and Grimmond, 2000).

The spatial distribution of the model estimates of sensible heat flux Q_H follows the same pattern as the urban fraction, T_R, z_H, and λ_F, but for λ_F (λ_F <0.29) the Q_H decreases as this parameter increases to the threshold of λ_F , thereafter Q_H is expected to increase.

Tests to evaluate the impact of the roughness differences on the spatial distribution of sensible heat flux, Q_H, for Greater Manchester reveal that the spatial distributions of Q_H and z_H and λ_F have a similar pattern (Chapters 6 and 7). However higher values of the surface sensible heat flux, Q_H, occur in the urban sectors with relatively lower surface roughness, expressed by λ_F, and vice-versa. This result is in agreement with the basic model equations, and with the previous model test results (section 5.5). This is due to the fact that the λ_F values over all the study area are less than the threshold value of 0.29. As pointed out, while $\lambda_F < 0.29$, z_{0H} and Q_H decrease as λ_F increases. However, there is a different behaviour of the roughness parameter z_{0M} for values of $\lambda_F > 0.29$. The physical meaning of this threshold relates to "over sheltering".

As expected, the model sensitivity tests to the surface temperature reveal that the patterns of the spatial distribution of sensible heat flux, Q_H, and surface temperature, T_R, are similar, and that increases in surface temperature correspond to increased heat flux. Thus, it seems that, for the three study conditions in Greater Manchester, the surface temperature dominates the distribution of sensible heat flux, with the impact of the roughness being much less.

9.4 Applications of the model in Greater Manchester to convective initiation

A case study on 21 June 2004 was described in which the model-generated distribution of sensible heat flux over Greater Manchester was compared with rainfall fields derived from C-band radar. The surface sensible heat flux values were interpreted as values of thermal forcing (Chapter 8). Convective cells are observed to initiate downwind of the centre of the city occupied by high rise buildings, the exact impact of the building configuration depending upon the details of the wind and

temperature fields. The eventual initiation of convective cells by the sensible heat flux input generated by the high-rise buildings in the city centre was discussed (Chapter 8).

Radar imagery showed that during the morning a convective rain cell is generated just downwind of Manchester city centre moving in an easterly direction. In addition, cells are also seen to form on the western edge of the urban area dissipating as they move over to the east of the city towards the upland area. In the afternoon a cell forms to the west of Manchester city centre over Salford moving eastwards and dissipating. The areas associated with the cell generation seem to be those areas in which the sensible heat flux is largest brought about by the existence of high rise buildings.

The impact of the urban area on the distribution of surface sensible heat flux, Q_H, has been examined. Our hypothesis is that the increased surface sensible heat flux over urban areas relative to its surroundings is related to the initiation of convection. Previous numerical studies by Baik *et al*. (2001) and Han and Baik (2006), using a complex mesoscale numerical atmospheric model, have examined dry and moist convection thermally forced by the presence of an urban heat island, and consequent downwind precipitation enhancement. We relate values of surface sensible heat flux to thermal forcing in order to demonstrate that our hypothesis is well founded.

In our case we are interested in the thermal forcing on the atmospheric boundary layer due to the increased sensible heat input from below, during day time, associated to the presence of urban areas. Hence we related the differences between our estimates of sensible heat flux Q_H for rural and urban areas to the thermal forcing (q_0), and compared our results with the results of Baik *et al*. (2001) and Han and Baik (2006) in order to evaluate the possible impact of the sensible heat flux on convective initiation.

We estimated that the effect of the forcing on convective initiation (q_0=1.2 J kg^{-1} s^{-1}) used in the simulation carried out by Baik et al. (2001), would be equivalent to that due to a difference of sensible heat fluxes of 65 J kg^{-1} s^{-1}. The modelled spatial distribution of surface sensible heat flux, Q_H, over Greater Manchester for the case study of 21 June 2004, shows that differences of sensible heat flux, between the urban area and its rural surroundings, necessary for a forcing of 65 J kg^{-1} s^{-1}, may occur.

Therefore it is acceptable to conclude that the presence of the city may have triggered convection.

It is observed rain first occurring some 10 km downwind of Salford during the morning of the 21st June 2004. In the afternoon the rain first occurring over Salford implying that the convection may be first initiated over the upwind rural-urban boundary, or the high rise buildings lead to strong upward vertical velocities.

The observed atmospheric conditions in our case are not far from the values associated to the simulation Baik *et al*. (2001). The distance from the city at which the rain cells appear is comparable to the simulation results of Baik *et al*. (2001).

Note that in this study we tried to relate surface sensible heat flux fields (spatial distribution) with convective initiation and the occurrence of downwind clouds and precipitation. Other factors impacting the development of these convective phenomena, such as humidity, uplift, cloud condensation nuclei, etc., were not taken into consideration, and this constitutes a main limitation of the model to study the impact of urbanisation on precipitation.

9.5 Implications for city development

Comparison of the two average annual rainfall maps covering NW England for 1941-1970 and 1961-1990 (Met. Office, UK), suggests an increase of precipitation over some south west suburbs of Greater Manchester. Considering the expansion of urbanisation during the past fifty years or so, with a significant increase of high rise buildings in the early 1970s, it is reasonable to consider whether or not these differences in rainfall may be due to the urban development, noting that it may be due to some other reason such as different rainfall regimes, or even global climate change.

However it is clear that urbanisation and regeneration in cities will influence the distribution of surface heating leading to changes in the urban heat island, and if conditions are appropriate increases in rainfall in the suburbs and rural areas downstream of the urban area. Such changes will require modifications to building design and city planning in order to mitigate the occasional detrimental impacts on human health through adverse weather conditions and poor air quality.

Further developments in central Manchester with the eventual construction of high-rise buildings, either on open spaces or by replacement of old buildings, are expected to modify significantly the city microclimate, and increase the impact of the city on regional weather, through the enhancement of convective developments.

These changes will arise through significant alteration of the surface balances of energy, momentum and humidity. For example, the surface sensible heat flux, Q_H, may increase due to the enhancement of the vertical temperature gradient and turbulence.

The increase in the total area of the buildings surface means an increase in the area of the materials used (absorbing more radiation) and the consequent enhancement of the surface and air temperatures, with an increase on the vertical temperature gradient and on the atmospheric turbulence. Also the change of the building materials used in the urban area can contribute to this effects.

On the other hand, the enhancement of the volume of buildings leads not only to increased buildings height z_H, but also to increases in the frontal area index λ_F and plan area index λ_P. This will affect the airflow, through increased uplift and turbulence, and also intensifies the surface heat fluxes. The frontal area index may increase and eventually reach values in excess of the threshold of 0.29, leading to increases in Q_H.

9.6 Future work

As discussed recently by many authors, further studies are necessary to investigate urban effects on convective precipitation in cities located in different geographic and climatic conditions, and to characterise the physical processes involved in urban-induced precipitation.

The present work is a contribution to this field, however an important limitation of this study relates to the fact that the model has been implemented for few cases in Greater Manchester, consequently the model should be evaluated for more case studies of convective conditions in order to confirm the results reported here.

Also the model estimates should be compared with measurements of sensible heat flux from the Salford Doppler lidar. The lidar provides measurements over a wide

area from a single location, and therefore is an ideal tool with which to investigate model and observational values of sensible heat flux.

On the other hand, the model should be applied to urban areas with different urban fabric, with different vegetation, and percentage of green areas. The impact of buildings materials, e.g., green roofs, has to be investigated. Also the urban sea side locations require study. The importance of the latent heating must be investigated, and the Bowen ratio should be determined.

It is also an objective of future studies to introduce orographic effects into the model.

Finally, since the author is affiliated to the University of Évora and to the Centre of Geophysics of Évora, in Portugal, it is important to consider the possibility of carry out further studies in a Mediterranean climate, which might involve the following tasks:

- Investigate the relationship of urban areas in Portugal to the generation of convective rainfall and other weather phenomena using where possible remote sensing data and modelling.

- Establish an observational network within and around Evora, or other suitable urban area, to investigate the impact of the city on local weather (heat island, rainfall, local winds, etc.).

- Obtain (or gain access to) a mesoscale model for stand-alone operation to support field campaigns (US MM5, WRF, MESO-NH, for example), case studies and comparisons with simple models.

Appendix 1. Thermal properties of common materials

Table A1.1 *- Thermal properties of natural materials (after Oke, 1987).*

Material	Remarks	ρ Density ($kg\ m^{-3} \times 10^3$)	c Specific heat ($J\ kg^{-1}\ K^{-1} \times 10^3$)	C Heat capacity ($J\ m^{-3}\ K^{-1} \times 10^6$)	k Thermal conductivity ($W\ m^{-1}\ K^{-1}$)	κ Thermal diffusivity ($m^2\ s^{-1} \times 10^{-6}$)	μ Thermal admittance ($J\ m^{-2}\ s^{-1/2}\ K^{-1}$)
Sandy soil (40% pore space)	Dry	1·60	0·80	1·28	0·30	0·24	620
	Saturated	2·00	1·48	2·96	2·20	0·74	2550
Clay soil (40% pore space)	Dry	1·60	0·89	1·42	0·25	0·18	600
	Saturated	2·00	1·55	3·10	1·58	0·51	2210
Peat soil (80% pore space)	Dry	0·30	1·92	0·58	0·06	0·10	190
	Saturated	1·10	3·65	4·02	0·50	0·12	1420
Snow	Fresh	0·10	2·09	0·21	0·08	0·10	130
	Old	0·48	2·09	0·84	0·42	0·40	595
Ice	0°C, pure	0·92	2·10	1·93	2·24	1·16	2080
Water*	4°C, still	1·00	4·18	4·18	0·57	0·14	1545
Air*	10°C, still	0·0012	1·01	0·0012	0·025	20·50	5
	Turbulent	0·0012	1·01	0·0012	~125	~10 × 10^6	390

* Properties depend on temperature, see Appendix A3.
Sources: van Wijk and de Vries (1963), List (1966).

Table A1.2 *- Thermal properties of materials used in building and urban construction (after Oke, 1987).*

Material (dry state)	Remarks	ρ Density ($kg\ m^{-3} \times 10^3$)	c Specific heat ($J\ kg^{-1}\ K^{-1} \times 10^3$)	C Heat capacity ($J\ m^{-3}\ K^{-1} \times 10^6$)	k Thermal conductivity ($W\ m^{-1}\ K^{-1}$)	κ Thermal diffusivity ($m^2\ s^{-1} \times 10^{-6}$)	μ Thermal admittance ($J\ m^{-2} s^{-1/2}\ K^{-1}$)
Asphalt		2·11	0·92	1·94	0·75	0·38	1205
Concrete	Aerated	0·32	0·88	0·28	0·08	0·29	150
	Dense	2·40	0·88	2·11	1·51	0·72	1785
Stone	Av.	2·68	0·84	2·25	2·19	4·93	2220
Brick	Av.	1·83	0·75	1·37	0·83	0·61	1065
Clay tiles		1·92	0·92	1·77	0·84	0·47	1220
Wood	Light	0·32	1·42	0·45	0·09	0·20	200
	Dense	0·81	1·88	1·52	0·19	0·13	535
Steel		7·85	0·50	3·93	53·3	13·6	14475
Glass		2·48	0·67	1·66	0·74	0·44	1110
Plaster	Gypsum	1·28	1·09	1·40	0·46	0·33	795
Gypsum board	Av.	1·42	1·05	1·49	0·27	0·18	635
Insulation	Polystyrene	0·02	0·88	0·02	0·03	1·50	25
	Cork	0·16	1·80	0·29	0·05	0·17	120

Source: van Straaten (1967), Goward (1981).

Appendix 2. Surface morphologic parameters for a sample area and for the entire study domain

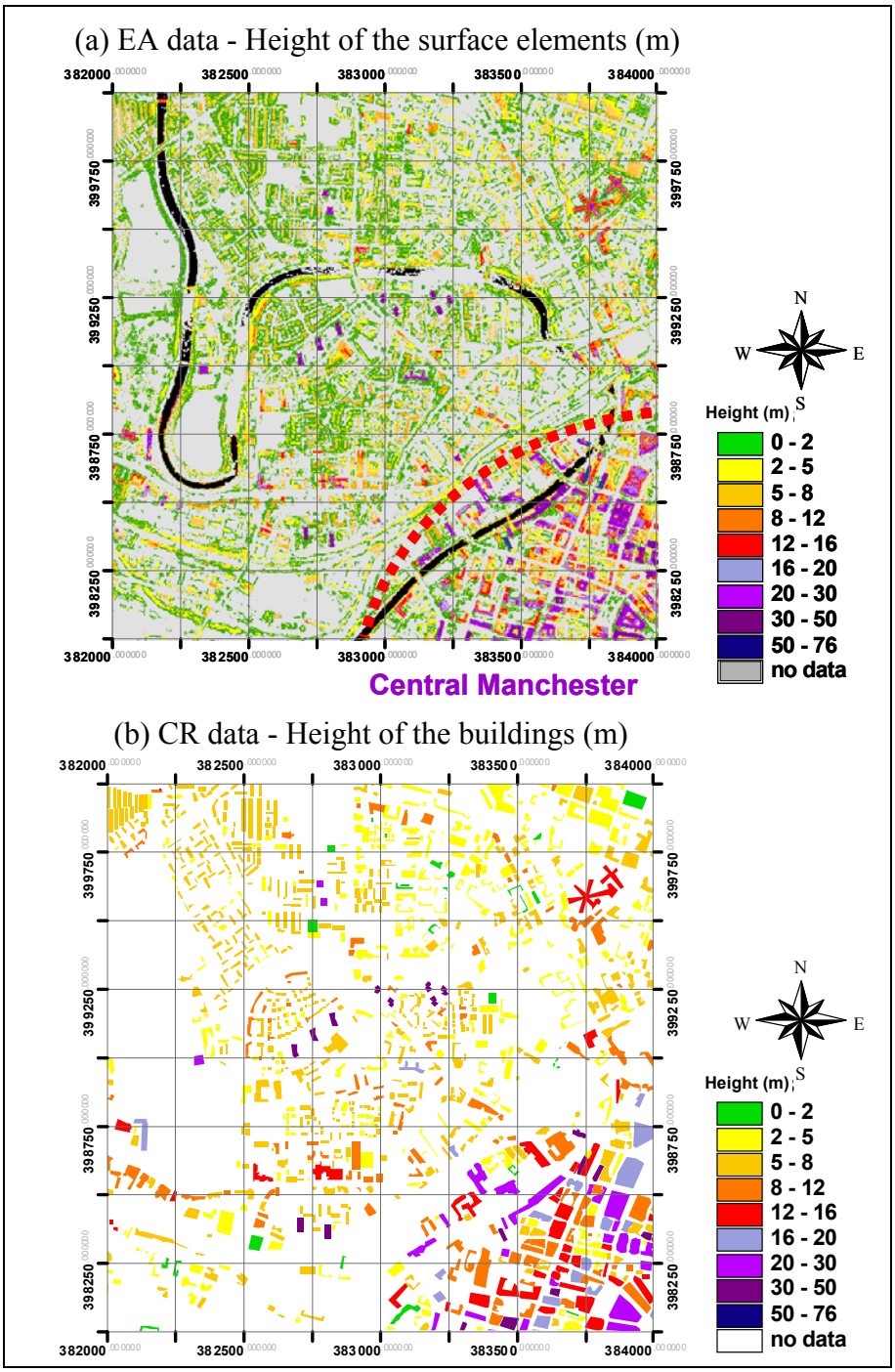

Figure A2.1 *- Comparison of two surface data products. Samples (2x2 km^2) of digitised georeferenced data over the same area of Greater Manchester from (a) Environment Agency, EA, and (b) Cities Revealed Building Height Data, CR. The axes labels represent the U. K. National Grid co-ordinates. The legend shows the values of the surface elements height associated with the different colours.*

Table A2.1 - *Data analysis results. Statistics of CR data for each category performed over grids A and B (build up area, buildings height, buildings area, and total area for each category). The estimates of the fraction of built up area for each category are based on the values of the total area and the build up area of each category.*

Grid A

	Built Up	Buildings Height (m)				Buildings Area (m^2)					Total Area	
Category	**Area (m^2)**	MIN	MAX	Mean	STD	MIN	MAX	Mean	STD	**Category**	**(m^2)**	**Fraction Built Area**
Centre	371791	4.0	108.0	26.4	12.4	1	18147	2401	3587	Centre	762613	0.49
CentreN	84761	2.5	60.6	14.1	12.9	8	4868	942	1181	CentreN	496488	0.17
CentreP	196655	3.0	57.5	13.9	6.2	2	10257	1581	2332	CentreP	648343	0.30
CI	898140	2.6	108.0	9.7	5.2	1	10063	1718	1739	CI	4196194	0.21
Open	2175	3.1	7.8	5.4	1.5	30	5874	4301	2510	Open	433024	0.01
RailS	42248	10.8	31.1	20.3	7.7	21	12690	6584	4520	RailS	67173	0.63
Res	559403	1.8	44.4	8.2	2.6	1	5471	142	272	Res	2795390	0.20
ResH	10677	3.1	40.8	21.7	15.6	8	1525	715	473	ResH	88142	0.12
Res_mix	154300	2.3	30.2	8.1	3.0	0	3774	736	937	Res_mix	793212	0.19

Grid B

	Built Up	Buildings Height (m)				Buildings Area (m^2)					Total Area	
Category	**Area (m^2)**	MIN	MAX	Mean	STD	MIN	MAX	Mean	STD	**Category**	**(m^2)**	**Fraction Built Area**
Centre	186468	4.2	51.9	23.8	9.4	1	18147	2304	2875	Centre	491712	0.38
CentreP1	105889	3.1	41.5	11.4	5.7	6	4981	1142	1308	CentreP1	441489	0.24
CentreP2	39353	3.9	83.7	20.7	16.4	1	3027	1304	1076	CentreP2	154136	0.26
CI	271549	2.3	22.6	9.0	3.2	1	7189	1740	1868	CI	961540	0.28
Open	1960	4.2	11.0	10.0	2.2	56	2212	1826	764	Open	52268	0.04
RailS	22404	6.2	31.1	23.7	8.8	27	12690	8019	5483	RailS	37345	0.60
Res	115546	3.1	20.3	7.9	2.4	1	1581	188	335	Res	677803	0.17
ResH	5301	3.1	40.8	38.1	4.6	8	667	534	111	ResH	39333	0.13
.Canal	949	3.0	15.2	7.5	3.9	15	1003	560	285	.Canal	275350	0.00
.OpenG	2143	3.0	13.3	7.4	3.7	5	1110	217	149	.OpenG	317310	0.01
.Prison	9963	4.6	64.2	23.4	10.5	73	5274	3037	1983	.Prison	44577	0.22
.Rail	487	3.1	13.0	6.7	3.1	8	309	193	80	.Rail	156183	0.00
.Road	4829	10.8	12.6	11.9	0.8	62	2977	2481	697	.Road	133476	0.04
.Uni	4502	6.9	27.0	15.2	3.7	52	2579	1628	821	.Uni	28856	0.16
										Barren	26760	0.00
										CarPark	12986	0.00

Table A2.2 *- Statistics over the entire study domain for the roughness parameters* z_H*(m),* λ_F *,* z_D *(m) and* z_{0M} *(m), shown in* ***Figure 6.20*** *and* ***Figure 6.21****.*

	z_H (m)	λ_F	z_D (m)	z_{0M} (m)
Minimum	0.1	0.01	0.02	0.001
25%-tile	2.2	0.03	0.70	0.078
Median	5.4	0.06	2.08	0.326
75%-tile	6.9	0.10	2.85	0.505
Maximum	23.5	0.23	12.8	2.924
Mean	4.8	0.06	1.91	0.326
Standard Deviation	3.0	0.04	1.44	0.303

Appendix 3. Pressure maps and satellite images for the study days

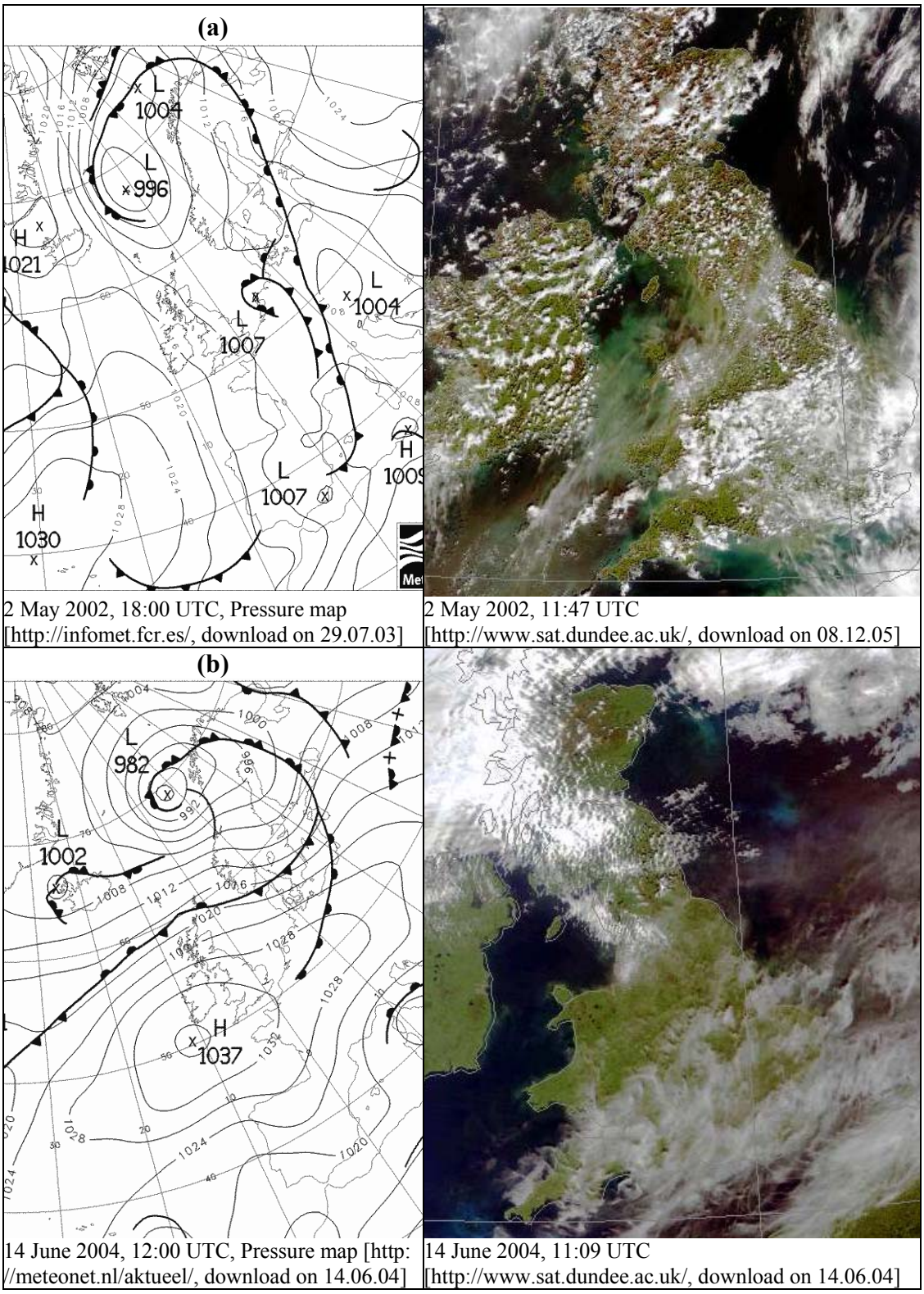

2 May 2002, 18:00 UTC, Pressure map [http://infomet.fcr.es/, download on 29.07.03]

2 May 2002, 11:47 UTC [http://www.sat.dundee.ac.uk/, download on 08.12.05]

14 June 2004, 12:00 UTC, Pressure map [http://meteonet.nl/aktueel/, download on 14.06.04]

14 June 2004, 11:09 UTC [http://www.sat.dundee.ac.uk/, download on 14.06.04]

Figure A3.1 *- The synoptic pressure field and frontal positions, and satellite images, over the UK and surrounding area, for three study days. (Continued on the next page.)*

(c)

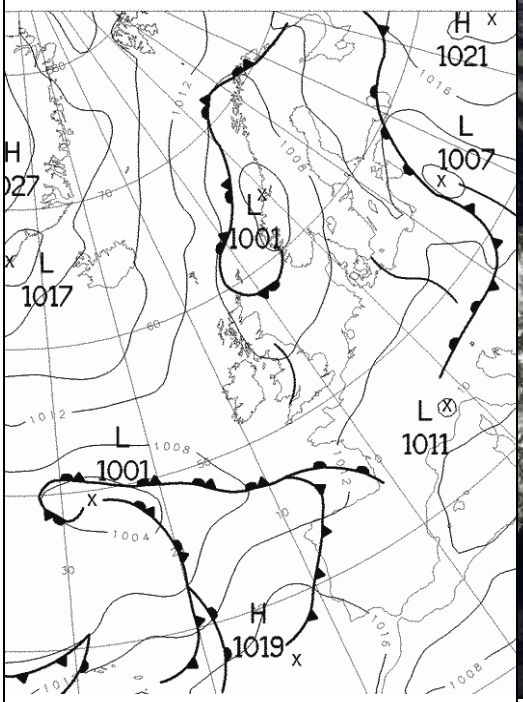

21 June 2004, 12:00 UTC, Pressure map, [http://meteonet.nl/aktueel/, download on 21.06.04]

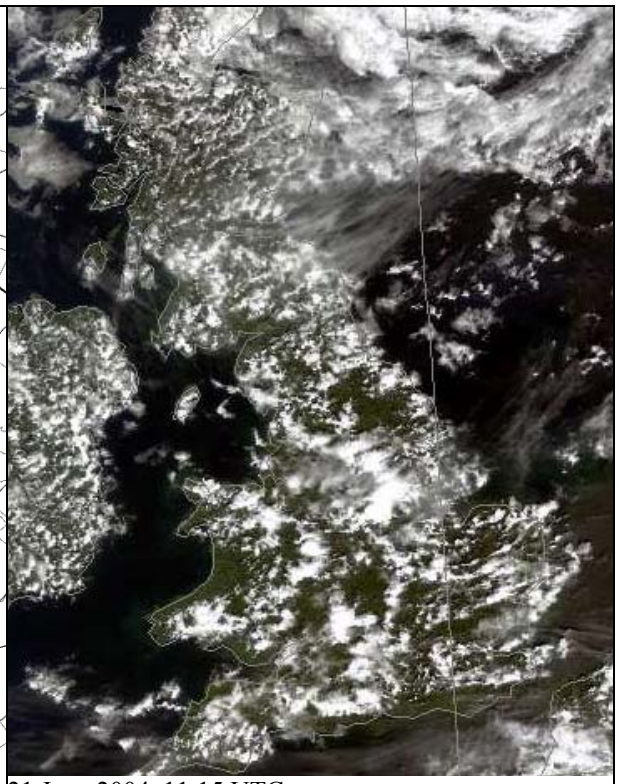

21 June 2004, 11:15 UTC [http://www.sat.dundee.ac.uk/, download on 22.06.04]

Figure A3.1 *- The synoptic pressure field and frontal positions, and satellite images, over the United Kingdom and surrounding area, for three study days:* ***(a)*** *2 May 2002,* ***(b)*** *14 June 2004, and* ***(c)*** *21 June 2004. (Left- hand side) Analysis chart from MetOffice, UK, Crown Copyright. (Right- hand side) Imagery received from Satellite Terra [Satellite Receiving Station, University of Dundee, Channel 1, 4, 3, Natural Environment Research Council (NERC) Copyright. The dates are indicated below each image. (Continued from the previous page.)*

Appendix 4. Photographs from the observational sites

Figure A4.1 *- Location of the urban observational sites (yellow mark) in the Greater Manchester study domain [Adapted from Google Earth]. (a) Personal AWS in Salford, (b) Thursfield Street (SALFEX field campaign), (c) Telford Building (Experiment at Salford University, (d) Sackville Building in central Manchester (Experiment from the University of Manchester University Atmospheric Science Research Group). Each photograph shows an area of 1x1 km^2.*

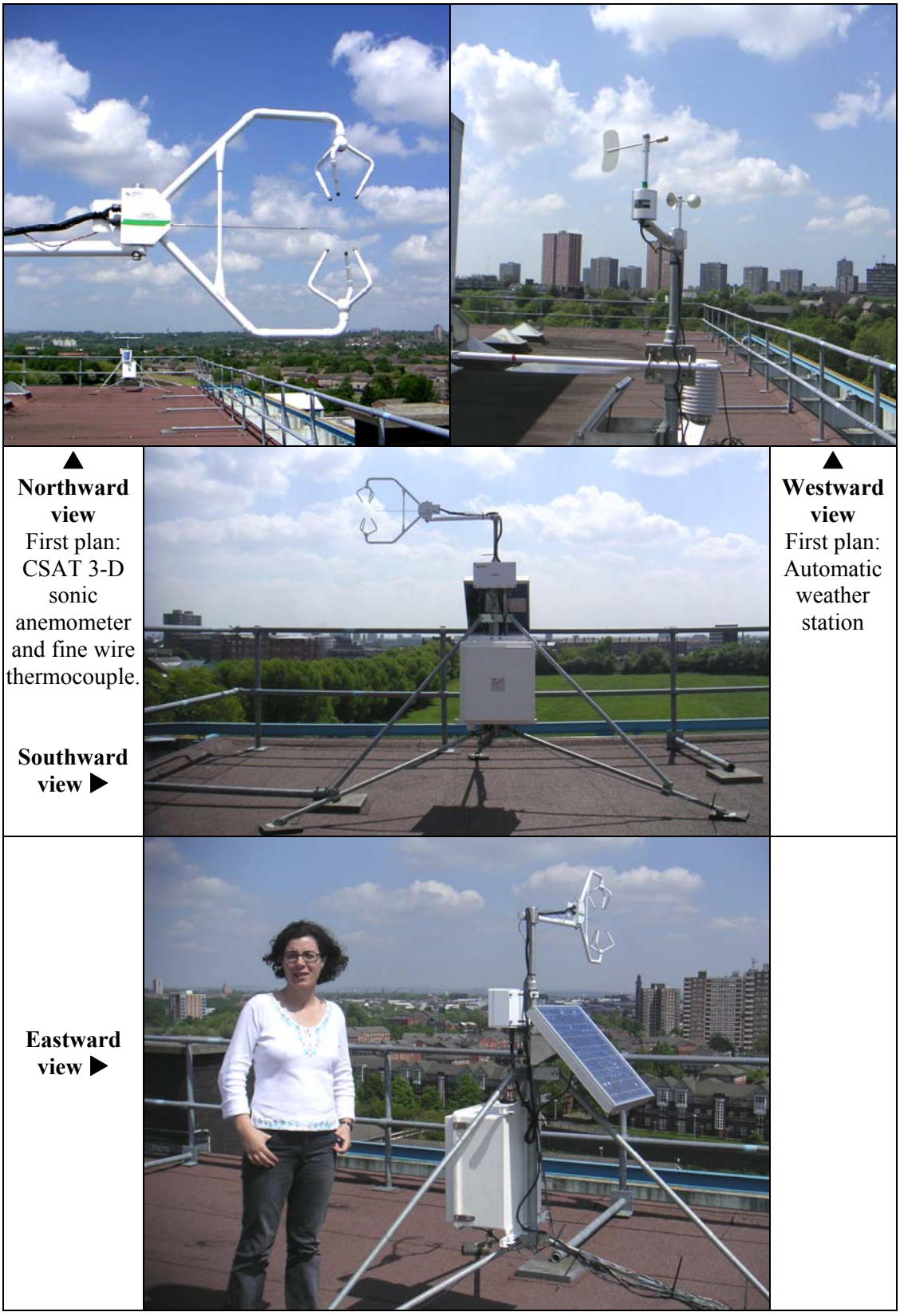

Figure A4.2 - *Photographs taken in the afternoon, on the roof of Telford Building at Salford University, during the experiment of May - June 2004 (by Karen Bozier and M.G.D. Carraça).*

Figure A4.3 - *Photograph taken on 28 June 2004, at Salford University, front of Peel Building (by Karen Bozier). It shows the infrared thermometer (IMPAC IN5 Plus) and respective equipment used to measure the surface temperature.*

Figure A4.4 *- SALFEX site at Thrusfield Street in Salford (Northwestward view). [From fttp://cloudbase.phy.umist.ac.uk/people/longley/salfex_experimental_site.htm, last accessed on May 2007.]*

Figure A4.5 *- Sackville Building in Central Manchester, seen from Portland Tower. [From http://cloudbase.phy.umist.ac.uk/field/cityflux/, last accessed on May 2007.]*

Appendix 5. The 6 August 2003 and the 7 December 2003

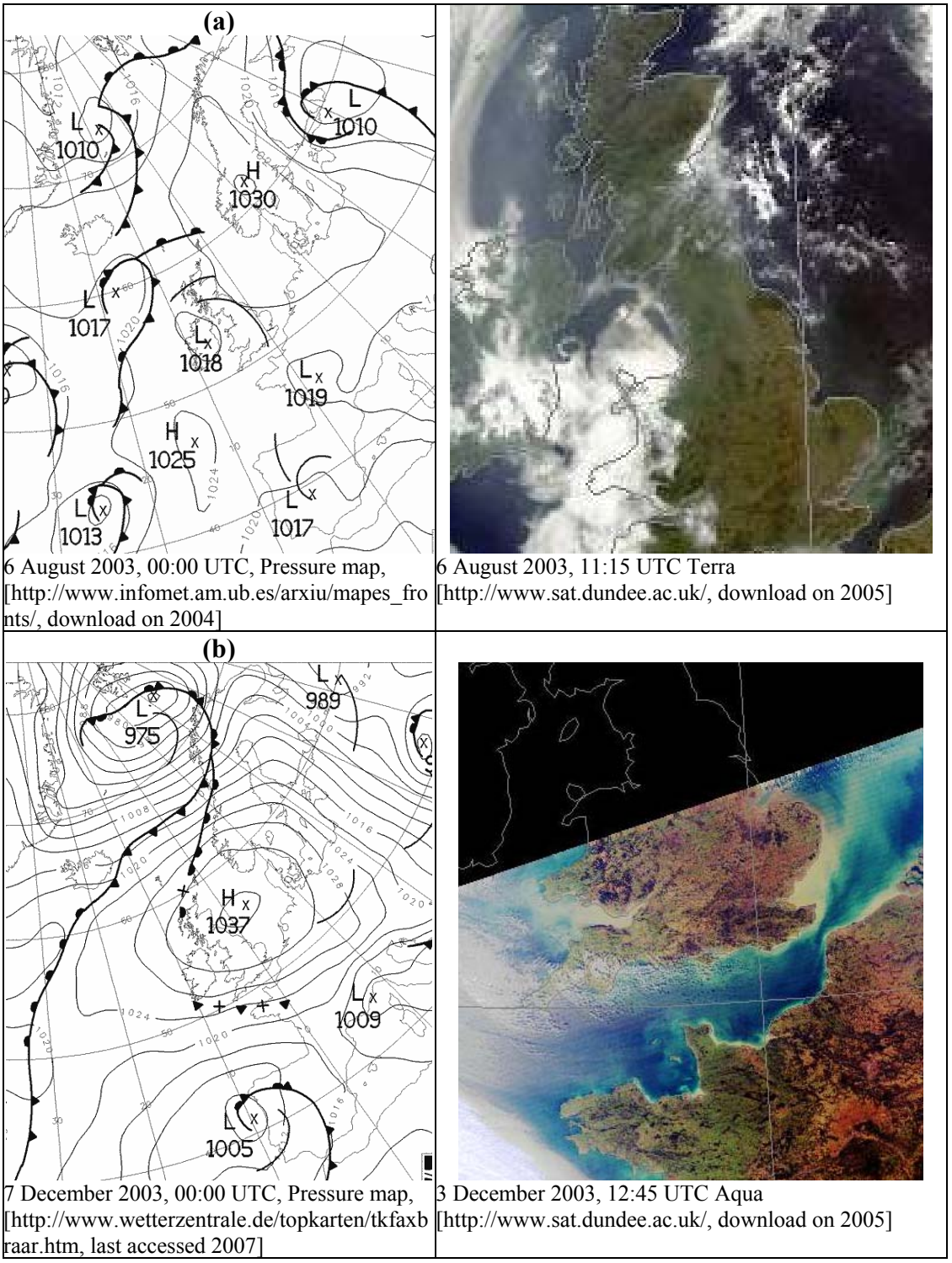

6 August 2003, 00:00 UTC, Pressure map, [http://www.infomet.am.ub.es/arxiu/mapes_fronts/, download on 2004]

6 August 2003, 11:15 UTC Terra [http://www.sat.dundee.ac.uk/, download on 2005]

7 December 2003, 00:00 UTC, Pressure map, [http://www.wetterzentrale.de/topkarten/tkfaxbraar.htm, last accessed 2007]

3 December 2003, 12:45 UTC Aqua [http://www.sat.dundee.ac.uk/, download on 2005]

Figure A5.1 *- The synoptic pressure field and frontal positions, and satellite images, over the United Kingdom and surrounding area, for two days:* ***(a)*** *6 August 2003 and* ***(b)*** *7 December 2003. (Left- hand side) Analysis chart from MetOffice, UK, Crown Copyright. (Right- hand side) Imagery received from Satellite Terra/Aqua [Satellite Receiving Station, University of Dundee, Channel 1, 4, 3, Natural Environment Research Council (NERC) Copyright. The dates are indicated below each image.*

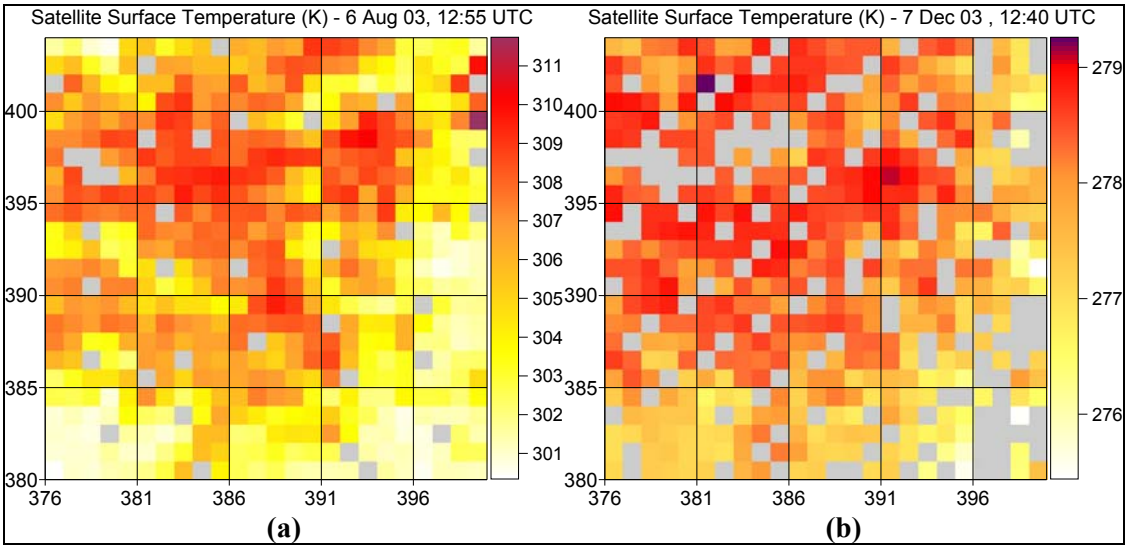

Figure A5.2 *- Radiometric surface temperature, T_R, from satellite imagery (MODIS Aqua) over Greater Manchester,* ***(a)*** *on the clear sky day of the 6 August 2003, at 12:55 UTC, and* ***(b)*** *on the 7 December 2003, at 12:40, under scattered cloud conditions. The total study area is 24 x 24 km^2 and the area of each grid square is 1 km^2. The grey areas are either missing data due to the mapping technique or areas of clouds. The legend on the right-hand side of each figure refers to the values of the temperature expressed in K. The coordinates X and Y are the U.K. National Coordinates.*

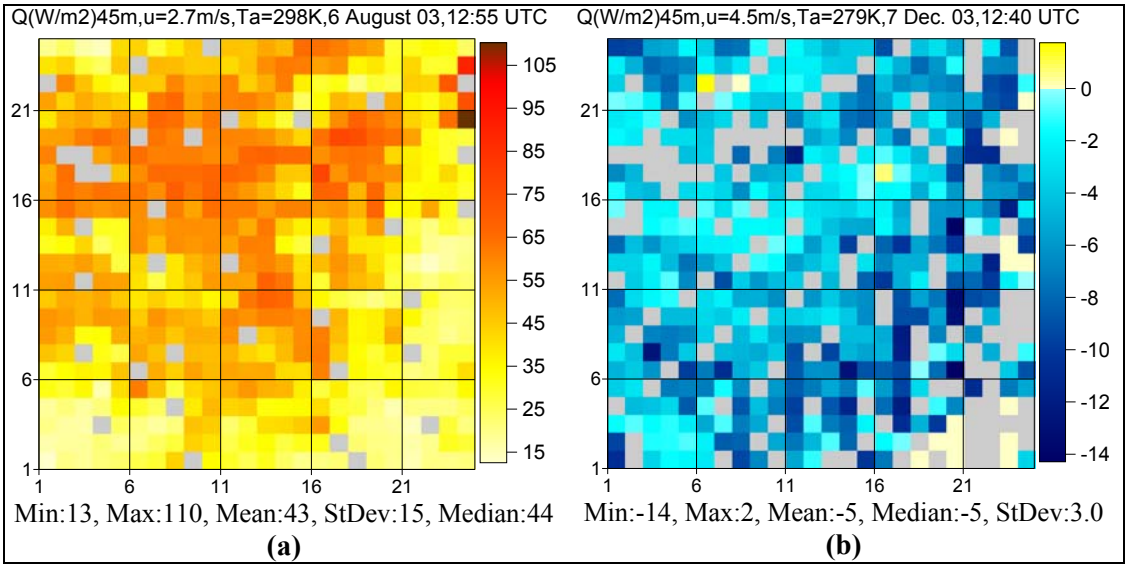

Figure A5.3 *- Model estimates of surface sensible heat flux, Q_H, around 13 UTC,* ***(a)*** *on the clear sky day of 6 August 2003 and* ***(b)*** *on the 7 December 2003, under scattered cloud conditions, for the Greater Manchester study area (24x24 km^2) shown in* ***Figure 6.19****. The grey areas are either missing data due to the mapping technique or areas of clouds. The legend on the right-hand side of each figure refers to the values of Q_H expressed in W/m^2. Also statistics over the entire study domain for the model estimates of Q_H (W/m^2) are shown.*

References

Andreae, M.O., Rosenfeld, D., Artaxo, P., Costa, A.A., Frank, G.P, Longo, K.M., and Silva-Dias, M.A.F., 2004. Smoking rain clouds over the Amazon. *Science,* 303, 1337–1341.

Andreas, E.L, Claffey, K.J., Jordan, R.E., Fairall, C.W., Guest, P.S., Persson, P.G., and Grachev, A.A., 2006. Evaluations of the von Kármán constant in the atmospheric surface layer. *J. Fluid Mech*., 559, 117–149.

Angell, J.K., Hoecker, W.H., Dickson, C.R., and Pack, D.H., 1973. Urban influence on a strong daytime air flow as determined from tetroon flights. *J. Appl. Meteor.*, 12, 924–936.

Arnfield, A.J., 2003. Two decades of urban climate research: A review of turbulence, exchanges of energy and water, and the urban heat island. *Int. J. Climatol.*, 23, 1–26.

Arnfield, A.J., and Grimmond, C.S.B., 1998. An urban canyon energy budget model and its application to urban storage heat flux modeling. *Energy Build*., 27, 61-68.

Auer Jr., A.H., 1981. The urban boundary layer. *Amer. Meteor. Soc. Monographs*, No.40, 41–62.

Arya, S.P., 1999. *Air Pollution, Meteorology, and Dispersion*. New York: Oxford University Press, 310 pp.

Arya, S.P., 2001. *Introduction to Micrometeorology*. 2nd ed., London: Academic Press Inc. (International Geophysics Series, 79), 420 pp.

Baik, J.-J., Kim, Y.-H., and Chun, H.-Y., 2001. Dry and moist convection forced by an urban heat island. *J. Appl. Meteor.*, 40, 1462–1475.

Baik, J.-J., Kim, Y.-H., and Chun, H.-Y., 2002. Modeling dry and moist convection forced by an urban heat island. *In: 4th Symposium on the Urban Environment, Norfolk, Virginia, USA, 20-24 May 2002*. Amer. Meteor. Soc..

Balling, R., and Brazel, S., 1987. Recent changes in Phoenix summertime diurnal precipitation patterns. *Theor. Appl. Climatol.,* 38, 50–54.

Balling Jr., R.C., and Cerveny, R.S., 1987. Long- term associations between wind speeds and the urban heat island of Phoenix, Arizona. *J. Clim. Appl. Meteor.*, 26, 712-716.

Beljaars, A., 1992. The parametrization of the planetary boundary layer. *Meteorological Training Course Lecture Series,* European Center for Medium range Weather Forecasting ECMWF, 2002. [http://www.ecmwf.int/newsevents/training/rcourse_notes/pdf_files/Boundary_layer.pdf, last accessed on July 2008]

Beljaars, A., and Holtslag, A.A.M., 1991. Flux parameterization over land surfaces for atmospheric models. *J. Appl. Meteorol*., 30, 327-341.

Bennett, L.J., Browning, K.A., Blyth, A.M., Parker, D.J., and Clark, P.A., 2006. A review of the initiation of precipitating convection in the United Kingdom. *Quart. J. Roy. Meteor. Soc.*, 132, 1001–1020.

Best, M.J., and Clark, P.A., 2002. The influence of vegetation on the urban climate. *In: 4th Symposium on the Urban Environment, Norfolk, Virginia, USA, 20-24 May 2002.* Amer. Meteor. Soc., 88-89.

Bornstein, R.D., and Craig, K.J., 2002. Survey of the history of the urbanization of numerical mesoscale models. *In: 4th Symposium on the Urban Environment, Norfolk, Virginia, USA, 20-24 May 2002*. Amer. Meteor. Soc..

Bornstein, R.D., and LeRoy, M., 1990. Urban barrier effects on convective and frontal thunderstorms. *In: 4th AMS Conference on Mesoscale Processes*, Boulder, CO, USA, 25–29 June 1990, Amer. Meteor. Soc., 120-121.

Bornstein, R.D., and Lin, Q., 2000. Urban heat islands and summertime convective thunderstorms in Atlanta: three case studies. *Atmos. Environ.*, 34, 507-516.

Borys, R.D., Lowenthal, D.H., and Mitchell, D.L., 2000. The relationships among cloud microphysics, chemistry and precipitation rate in cold mountain clouds. *Atmos. Environ.,* 34, 2593–2602.

Borys, R.D., Lowenthal, D.H., Cohn, S.A., and Brown, W.O.J., 2003. Mountaintop and radar measurements of anthropogenic aerosol effects on snow growth and snowfall rate. *Geophys. Res. Lett.,* 30, 1538, doi:10.1029/2002GL016855.

Bottema, M., 1995a. *Aerodynamic roughness parameters for homogeneous building groups—Part 1: Theory*. Document SUBMESO 18, Ecole Centrale de Nantes, France, 40 pp.

Bottema, M., 1995b. *Aerodynamic roughness parameters for homogeneous building groups—Part 2: Results*. Document SUB-MESO 23, Ecole Centrale de Nantes, France, 80 pp.

Bottema, M., 1995c. Parameterisation of aerodynamic roughness parameters in relation to air pollutant removal efficiency of streets. *In: Air Pollution Engineering and Management*. Power, H., Moussiopoulos, N. and Brebbia, C.A., (Eds). Computational Mechanics Publications, 235–242.

Bottema, M., 1997. Urban roughness modelling in relation to pollutant dispersion. *Atmos. Environ.*, 31, 3059–3075.

Bottyán, Z., and Unger, J., 2002. The role of land-use parameters in the spatial development of urban heat island in Szeged, Hungary. *In: 4th Symposium on the Urban Environment, Norfolk, Virginia, USA, 20-24 May 2002*. Amer. Meteor. Soc., 48-49.

Braham, R.R., Semonin, R.G., Auer, A.H., Changnon Jr., S.A. , and Hales, J.M., 1981. Summary of urban effects on clouds and rain. *In: METROMEX: A Review and Summary*. Changnon, S.A., Jr., (Ed.)., *Amer. Meteor. Soc. Monographs*, No. 40, Amer. Meteor. Soc., 141–152.

Brutsaert, W., 1975. The roughness length for water vapor, sensible heat, and other scalars. *J. Atmos. Sci.*, 32, 2028-2031.

Brutsaert, W.H., 1982. *Evaporation into the Atmosphere.* 2nd ed., Doordrecht, Holland: D. Reidel, 299 pp.

Burian, S.J., and Shepherd, J.M., 2005. Effect of urbanization on the diurnal rainfall pattern in Houston. *Hydrol. Process*., 19, 1089–1103.

Businger, J.A., Wyngaard, J.C., Izumi, Y., and Bradley, E.F., 1971. Flux-profile relationships in the atmospheric surface layer. *J. Atmos. Sci.*, 28, 181-189.

Cahill, A.T., Parlange, M.B., and Albertson, J.D., 1997. On the Brutsaert temperature roughness length model for sensible heat flux estimation. *Water Resour. Res.*, 33, 2315-2324.

Carraça, M.G.D., and Collier, C.G., 2007. Modelling the impact of high-rise buildings in urban areas on precipitation initiation. *Meteorol. Applications*, 14, 149-161.

Cermak, J.E., Davenport, A.G., Plate, E.J., and Viegas, D.X., Eds., 1995. *Wind Climate in Cities*. Kluwer Academic, 772 pp.

Changnon, S.A., 1979. Rainfall changes in summer caused by St. Louis. *Science,* 205, 402–404.

Changnon, S.A., 1992. Inadvertent weather modification in urban areas: Lessons for global climate change. *Bull. Amer. Meteor. Soc.,* 73, 619–627.

Changnon, S.A., 2003. Urban modification of freezing-rain events. *J. Appl. Meteor.,* 42, 863–870.

Changnon, S.A., Huff, F.A., Schickedanz, P.T., and Vogel, J.L., 1977. Weather anomalies and impacts. *In: Summary of METROMEX Vol. I*. Illinois State Water Survey Bulletin 62, 260 pp.

Changnon, S.A., Jr., (Ed.); Changnon, S.A., Semonin, R.G., Auer, A.H., Braham, R.R., and Hales, J., 1981. METROMEX: A Review and Summary. Meteor. *Amer. Meteor. Soc. Monographs*, No.18, Amer. Meteor. Soc., 181 pp.

Changnon, S.A., Shealy, R.T., and Scott, R.W., 1991. Precipitation changes in fall, winter, and spring caused by St. Louis. *J. Appl. Meteor.,* 30, 126–134.

Chow, W.T.L., and Roth, M., 2006. Temporal dynamics of the urban heat island of Singapore. *Int. J. Climatol*., 26, 2243–2260.

Christen, A., Vogt, R., Rotach, M.W., and Parlow, E., 2002a. First Results from BUBBLE I: Profiles of fluxes in the urban roughness sublayer. *In: 4th Symposium on the Urban Environment, Norfolk, Virginia, USA, 20-24 May 2002*. Amer. Meteor. Soc., 105-106.

Christen, A., Vogt, R., Rotach, M.W., and Parlow, E., 2002b. First Results from BUBBLE II: Partitioning of turbulent heat fluxes over urban surfaces. *In: 4th Symposium on the Urban Environment, Norfolk, Virginia, USA, 20-24 May 2002*. Amer. Meteor. Soc., 137-138.

Christen, A., and Vogt, R., 2004. Energy and radiation balance of a central European city. *Int. J. Climatol.,* 24, 1395-1421.

Christen, A., Bernhofer, C., Parlow, E., Rotach, M.W., and Vogt, R., 2003a. Partitioning of turbulent fluxes over different urban surfaces. *In: 5th International Conference on Urban Climate, 1-5 September 2003, Lodz, Poland*, [http://www.geo.uni.lodz.pl/~icuc5/text/O_10_4.pdf]

Christen, A., Vogt, R., and Rotach, M.W., 2003b. Profile measurements of selected turbulence parameters over different urban surfaces. *In: 4th International*

Conference on Urban Air Quality, Prague, Czech Republic, 25-27 March 2003, 408-411.

Cleugh, H.A., and Oke, T.R., 1986. Suburban-rural energy balance comparisons in summer for Vancouver, B.C. *Bound.- Layer Meteor*., 36, 351–369.

Climate Change Science Program and Subcommittee on Global Change Research, 2003. *Strategic plan for the U.S. Climate Change Science Program. Final Rep.*, 221 pp. [http://climatescience.gov.]

Coakley Jr., J.A., Bernstein, R.L., and Durkee, P.A., 1987. Effects of ship-stack effluents on cloud reflectivity. *Science*, 237, 1020-1022.

Collier, C.G., 2006. The impact of urban area on weather. *Quart. J. Roy. Meteor. Soc.,* 132, 1-25.

Cotton, W.R., Pielke Sr., R.A., Walko, R.L., Liston, G.E., Tremback, C.J., Jang, H., McAnelly, R.L., Harrington, J.-Y., Nicholls, M.E., Carrio, G.G., and McFadden, J.P., 2003. RAMS 2001 Current status and future directions. *Meteorol. Atmos. Phys*., 82, 5-29.

Craig, K.J., and Bornstein, R.D., 2002. MM5 Simulations of urban induced convective precipitation over Atlanta. *In: 4th Symposium on the Urban Environment, Norfolk, Virginia, USA, 20-24 May 2002*. Amer. Meteor. Soc.. [http://www.met.sjsu.edu/faculty/bornstein/atlanta/mm5-ken-atlanta-2002.pdf]

Dabberdt, W.F., Hales, J., Zubrick, S., Crook, A., Krajewski, W., Doran, J.C., Mueller, C., King, C., Keener, R.N., Bornstein, R., Rodenhuis, D., Kocin, P., Rossetti, M.A., Sharrocks, F., and Stanley Sr., E.M., 2000. Forecast Issues in the Urban Zone: Report of the 10th Prospectus Development Team of the U.S. Weather Research Program. *Bull. Amer. Meteor. Soc.,* 81, 2047-2064.

Davenport, A.G., 1965. The relationship of wind structure to wind loading. *In: Conference on Wind Effects on Structures*, Sympos. 16, Vol.1, National Physical Laboratory, London, HMSO, 53-102.

Deardorff, J.W., 1974. Three-dimensional numerical study of the height and mean structure of a heated planetary boundary layer. *Bound.- Layer Meteor*., 7, 81–106.

Diem, J.E., and Brown, D.P., 2003. Anthropogenic impacts on summer precipitation in central Arizona, U.S.A.. *Prof. Geogr.,* 55, 343–355.

Dixon, P.G., and Mote, T.L., 2003. Patterns and causes of Atlanta's urban heat island-initiated precipitation. *J. Appl. Meteor.,* 42, 1273–1284.

Draxler, R.R., 1986. Simulated and observed influence of the nocturnal urban heat island on the local wind field. *J. Clim. Appl. Meteor.*, 24, 1125–1133.

Dupont, E., Menut, L., Carissimo, B., Pelon, J., and Flamant, P., 1999. Comparison between the atmospheric boundary layer in Paris and its rural suburbs during the ECLAP experiment. *Atmos. Environ.*, 33, 979-994.

Dyer, A.J., 1974. A review of flux-profile relationships. *Bound.-Layer Meteor.*, 7, 363-372.

Ellefsen, R., 1990–91. Mapping and measuring buildings in the canopy boundary layer in ten U.S. cities. *Energy Build.*, 15–16, 1025–1049.

Ellis, N.L., and Middleton, D.R., 2000a. *Field measurements and modelling of urban meteorology in Birmingham.* UK Met Office Turbulence and Diffusion Note No. 268.

Ellis, N.L., and Middleton, D.R., 2000b. Field measurements and modelling of surface uxes in Birmingham, U.K. *In: Surface energy balance in urban areas. COST-715 Expert Meeting, Antwerp, Belgium, 12 April 2000.* Piringer, M., (Ed.). Report EUR 19447, 66-75.

Ellis, N.L., and Middleton, D.R., 2000c. Field measurements and modelling of urban meteorology in Birmingham, U.K.. *In: 3rd AMS Symposium on Urban Environment, Davis, California, 14-18 August 2000.* Amer. Meteor. Soc., 108-109.

Environment Agency (EA), U.K.. [http://www.environment-agency.gov.uk/yourenv/eff/land/213950/landuse/ , last accessed on September 2004).

Fisher, B., Schatzmann, M., and Brechler, J., 2001. Preparation of Meteorological Input Data for Urban Site Studies. *In: 7th International Conference on Harmonization within Atmospheric Dispersion Modelling for Regulatory Purposes, May 28-31, 2001, Belgirate, Italy*, 286-290 [http://aqm.jrc.it/harmo7/ or http://www2.dmu.dk/atmosphericenvironment/cost/docs/COST715_Belgirate.pdf , 2008].

Fisher, B., Joffre, S., Kukkonen, J., Piringer, M., Rotach, M.W., and Schatzmann, M., (Eds), 2005. *Meteorology Applied to Urban Air Pollution Problems, Final report COST Action 715*. Bulgaria: Demetra Ltd Publishers, 276 pp.

Fox, N.I., 1998. *Estimation of catchment flood potential using satellite data*. Thesis (Ph.D.), University of Salford, UK.

Fujibe, F., 1987. Weekday-weekend Difference of Urban Climates-Part 1. Temporal Variation of Air Temperature and Other Meteorological Parameters in the Central Part of Tokyo. *J. Meteor. Soc. Japan*, 65, 923-929.

Fujibe, F., 1988a. Weekday-weekend Difference of Urban Climates-Part 2. *J. Meteor. Soc. Japan*, 66, 373-376.

Fujibe, F., 1988b. Weekday-weekend Difference of Urban Climates-Part 3. *J. Meteor. Soc. Japan*, 66, 377-385.

Fujibe, F., 2003. Long-term surface wind changes in the Tokyo Metropolitan area in the afternoon of sunny days in the warm season. *J. Meteor. Soc. Japan,* 81, 141–149.

Garratt, J.R., 1992. *The Atmospheric Boundary Layer*. Cambridge, UK: Cambridge University Press, 316 pp.

Givati, A., and Rosenfeld, D., 2004. Quantifying precipitation suppression due to air pollution. *J. Appl. Meteor.,* 43, 1038–1056.

Gordon, A.H., 1994. Weekdays warmer than weekends?. *Nature*, 367, 325–326.

Grimmond, C.S.B., 1992. The suburban energy balance: Methodological considerations and results from a mid-latitude west coast city under winter and spring conditions. *Int. J. Climatol.*, 12, 481-497.

Grimmond, C.S.B., 2006. Progress in measuring and observing the urban atmosphere. *Theor. Appl. Climatol.* 84, 3-22.

Grimmond, C.S.B., and Cleugh, H.A., 1994. A simple method to determine Obukhov lengths for suburban areas. *J. Appl. Meteor*., 33, 435–440.

Grimmond, C.S.B., and Oke, T.R., 1995. Comparison of heat fluxes from summertime observations in the suburbs of four North American cities, *J. Appl. Meteor*., 34, 873-889.

Grimmond, C.S.B., and Oke, T.R., 1999a. Aerodynamic properties of urban areas derived from analysis of surface form. *J. Appl. Meteor*., 38, 1262–1292.

Grimmond, C.S.B., and Oke, T.R., 1999b. Heat storage in urban areas. Local-scale observations and evaluation of a simple model. *J. Appl. Meteor*., 38, 922–940.

Grimmond, C.S.B., and Oke, T.R., 2000. A Local-scale Meteorological Pre-processing Scheme (LUMPS). *In: Workshop Preparation of Meteorological Input Data for*

Urban Site Studies, Prague Czech Republic 15 Jun 2000. COST Action 715, 87-97.

Grimmond, C.S.B., and Oke, T.R., 2000. A local-scale urban meteorological pre-processing scheme (LUMPS). *Proceedings of the COST 715 Workshop, Preparation of Meteorological Input Data for Urban Site Studies (Ed.: M. Schatzmann, J. Brechler, B. Fisher), Prague, Czech Republic, June 15, 2000*, 73-83.

Grimmond, C.S.B., and Oke, T.R., 2002. Turbulent Heat Fluxes in Urban Areas: Observations and a Local-Scale Urban Meteorological Parameterization Scheme (LUMPS). *J. Appl. Meteor.*, 41, 792–810.

Grimmond, C.S.B., and Souch, C., 1994. Surface description for urban climate studies: a GIS based methodology. *Geocarto International*, 1, 47-59.

Grimmond, C.S.B., King, T.S., Roth, M., and OKE, T.R., 1998. Aerodynamic Roughness of Urban Areas Derived from Wind Observations. *Bound.- Layer Meteor.*, 89, 1–24.

Grimmond, C.S.B., Salmond, J., Offerle, B.D. and Oke, T.R., 2002. Local-Scale Surface Flux Measurements at a Downtown Site in Marseille during the ESCOMPTE Field Campaign. *In: 4th Symposium on the Urban Environment, Norfolk, Virginia, USA, 20-24 May 2002*. Amer. Meteor. Soc..

Guilloteau, E., and Dupont, S., 2002. A new modelling of heat exchange between urban soil and atmosphere. *In: COST Action 715, Surface energy balance in urban areas. Extended abstracts of an expert meeting, 12 April 2000, Antwerp, Belgium*. European Commission, Report EUR 19447, 76-91.

Guo, X., Fu, D., and Wang, J., 2006. Mesoscale convective precipitation system modified by urbanization in Beijing City. *Atmos. Res.*, 82, 112–126.

Hage, K.D., 1975. Urban-rural humidity differences. *J. Appl. Meteorol.*, 14, 1277-1283.

Han, J-Y, and Baik, J.-J., 2006. A Theoretical and Numerical Study of Urban Heat Island-Induced Circulation and Convection. *In: 6th Symposium on the Urban Environment, 28 January- 2 February 2006, Atlanta, USA*. Amer. Meteor. Soc. [http://ams.confex.com/ams/pdfpapers/100301.pdf].

Han, J-Y, and Baik, J.-J., 2008. A Theoretical and Numerical Study of Urban Heat Island-Induced Circulation and Convection. *J. Atmos. Sci.,* 65, 1859–1877.

Hand, W.H., 2005. Climatology of shower frequency in the British Isles at 5 km resolution. *Weather*, 60, 153–158.

Hand, W.H., Fox, N.I., and Collier, C.G., 2004. A study of twentieth-century extreme rainfall events in the United Kingdom with implications for forecasting. *Meteorol. Appl.*, 11, 15–31.

Hanna, S.R., Ramsdell, J.V., and Cramer, H.E., 1987. Urban Gaussian diffusion parameters. *In: Modelling the Urban Boundary Layer*. Amer. Meteor. Soc., 337-379.

Hasager, C.B. Nielsen, N.W., Boegh, E., Jensen, N.O., Christensen, J.H., Dellwik, E., and Soegaard, H., 2003. Effective roughnesses calculated from satellite-derived land cover maps and hedge information and used in a weather forecasting model. *Bound.- Layer Meteor*., 109, 227-254.

Högström, U., 1988. Non-dimensional wind and temperature profiles in the atmospheric surface layer: A re-evaluation. *Bound.-Layer Meteor.*, 42, 55–78.

Holmer, B., and Eliasson, I., 1999. Urban-rural vapour pressure differences and their role in the development of urban heat island, *Int. J. Climatol.*,19, 989–1009.

Holton, J.R., 1992. *An Introduction to Dynamic Meteorology*. 3rd ed., London, UK: Academic Press (International Geophysics Series, 48), 511 pp.

Honjo, T., Sugawara, Mikami, T., H., Narita, K., Kimura, K., and Kuwata N., 2002. Observation of thermal effect of Shinjuku Gyoen park. *In: 4th Symposium on the Urban Environment, Norfolk, Virginia, USA, 20-24 May 2002*. Amer. Meteor. Soc., 84-85.

Houze Jr., R.A., 1993. *Cloud Dynamics*. San Diego: Academic Press (International Geophysics Series, 53).

Huff, F.A., 1986. Urban hydrological review. *Bull. Amer. Meteor. Soc.,* 67, 703–712.

Huff, F.A., and Vogel, J.M., 1978. Urban, topographic and diurnal effects on rainfall in the St. Louis region. *J. Appl. Meteor.,* 17, 565–577.

Hunt, J., Orr, A., Rottman, J., and Capon, R., 2004. Coriolis effects in mesoscale flows with sharp changes in surface conditions. *Quart. J. Roy. Meteor. Soc.,* 130, 2703-2731.

Ichinose, T., Shimodozono, K., and Hanaki, K., 1999. Impact of anthropogenic heat on urban climate in Tokyo. *Atmos. Environ.*, 33, 3897-3909.

Inoue, T., and Kimura, F., 2004. Urban effects on low-level clouds around the Tokyo metropolitan area on clear summer days. *Geophys. Res. Lett.,* 31, L05103, doi:10.1029/2003GL018908.

Instruction Manual of the three-dimensional sonic anemometer CSAT3 [http://www.campbellsci.com/documents/manuals/csat3.pdf, last accessed March 2007].

Jauregui, E., and Romales, E., 1996. Urban effects on convective precipitation in Mexico City. *Atmos. Environ.,* 30, 3383–3389.

Jauregui, E., Moreno, M.C., and Tejeda, A., 2002. The energy balance of central Barcelona (Spain). *In: 4th Symposium on the Urban Environment, Norfolk, Virginia, USA, 20-24 May 2002*. Amer. Meteor. Soc., 100-1002.

Jin, M., and Shepherd, J.M., 2005. Inclusion of urban landscape in a climate model: How can satellite data help? *Bull. Amer. Meteor. Soc.,* 86, 681–689.

Jin, M., Shepherd, J.M, and King, M.D, 2005. Urban aerosols and their interaction with clouds and rainfall: A case study for New York and Houston. *J. Geophys. Res.*, **110**, D10S20, doi:10.1029/2004JD005081.

Joffre, S.M., 1988. Modelling the dry deposition velocity of highly soluble gases to the sea surface. *Atmos. Environ*., 22, 1137-1146.

Kaimal, J.C., and Finnigan, J.J., 1994. *Atmospheric Boundary Layer Flow. Their structure and measurement*. New York, USA: Oxford University Press, Inc., 289pp.

Kanda, M., 2006. Progress in the scale modeling of urban climate: Review. *Theor. Appl. Climatol.*, 84, 23-34.

Kanda, M., 2007. Progress in Urban Meteorology :A Review. *J. Meteor. Soc. Japan*, 85B, 363-383.

Kanda, M., Kanega, M., Kawai, T., Sugawara, H., and Moriwaki, R., 2007. Roughness lengths for momentum and heat derived from outdoor urban scale models, *J. Appl. Meteor. Climatol.*, 46, 1067-1079.

Kanda, M., Moriwaki, R., and Kimoto, Y., 2005. Temperature profiles within and above an urban canopy. *Bound.- Layer Meteor*., 115, 499-506.

Katsoulis, B.D., and Theoharatus, G.A. 1985. Indications of the urban heat island in Athens, Greece. *J. Clim. Appl. Meteor.*, 24, 1296-1302.

Kim, Y.-H., and Baik, J.-J., 2002. Maximum urban heat island intensity in Seoul. *J. Appl. Meteor.,* 41, 651–659.

Kim, Y.-H., and Baik, J.-J., 2004. Daily maximum urban heat island intensity in large cities of Korea. *Theor. Appl. Climatol*., 79, 151–164.

Klysik, K., 1996. Spatial and seasonal distribution of anthropogenic heat emissions in Lodz, Poland. *Atmos. Environ*., 30, 3397-3404.

Klysik, K., and Fortuniak, K., 1999. Temporal and spacial characteristics of the urban heat island of Lodz, Poland. *Atmos. Environ*, 33, 3885-3895.

Kusaka, H., Kimura, F., Hirakuchi, H., and Mizutori, M., 2000. The effects of land-use alteration on the sea breeze and daytime heat island in the Tokyo metropolitan area. *J. Meteor. Soc. Japan,* 78, 405–420.

Lagouarde, J.-P., Moreau, P., Irvine, M., Bonnefond, J.-M., Voogt, J., and Solliec, F., 2004. Airborne experimental measurements of the angular variations in surface temperature over urban areas: case study of Marseille (France). *Rem. Sens. of Environ.*, 93, 443-462.

Landau, L.D., and Lifshitz, E.M., 1959. *Fluid Mechanics*. London: Pergamon Press, 536 pp..

Landsberg, H.E., 1981. *The Urban Climate.* New York: Academic Press, 275 pp.

Loose, T., and Bornstein, R.D., 1977. Observations of mesoscale effects on frontal movement through an urban area. *Mon. Wea. Rev.,* 105, 563–571.

Lowry, W.P., 1967. *The climate of cities*. Sci. Am., 217, 15-23.

MacDonald, R.W., Griffiths, R.F., and Hall, D.J., 1998. An improved method for the estimation of surface roughness of obstacle arrays. *Atmos. Environ.,* 32, 1857-1864.

Malhi, Y., 1996. The behaviour of the roughness length for temperature over heterogeneous surfaces. *Quart. J. Roy. Meteor. Soc.*,122, 1095–1125.

Martilli, A., Clappier, A., and Rotach, M.W., 2002. An urban surface exchange parameterisation for meso-scale models. *Bound.- Layer Meteor*., 104, 261-304.

Masson, V., 2000. A physically-based scheme for the urban energy budget in atmospheric models. *Bound.-Layer Meteor.*, 94, 357–397.

Masson, V., 2006. Urban surface modeling and the meso-scale impact of cities. *Theor. Appl. Climatol*., 84, 35–45.

McIlveen, R., 1992. *Fundamentals of Weather and Climate*. London: Chapman & Hall, 497 pp.

McIlveen, R., 1998. *Fundamentals of weather and climate*. 2nd ed., Cheltenham, UK: Stanley Thornes Publishers Ltd., 497 pp.

McNider, R.T., and Kopp, F.J., 1990. Specification of the scale and magnitude of thermals used to initiate convection in cloud models. *J. Appl. Meteor.,* 29, 99-104.

Mestayer P., Durand, P., Augustin, P., Bastin, S., Bonnefond, J.M., Bénech, B., Campistron, B., Coppalle, A., Delbarre, H., Dousset, B., Drobinsk, P., Druilhet, A., Fréjafon, Grimmond, C.S.B., Groleau, D., Irvine, M., Kergomard, C., Kermadi, S., Lagouarde, J.P., Lemonsu, A., Lohou, F., Long, N., Masson, V., Moppert, C., Noilhan, J., Offerle, B., Oke, T., Pigeon, G., Puygrenier, V., Roberts, S., Rosant, J.M., Saïd, F., Salmond, J., Talbaut, M., and Voogt, J., 2005. The urban boundary layer field experiment over Marseille UBL/CLU-ESCOMPTE: Experimental Set-up and First Results. *Bound.- Layer Meteor*., 114, 315-365.

Meteorological Office, 1983. *The Climate of Great Britain, Lancashire and Cheshire and Isle of Man.* Meteorological Office, Bracknell: Crown. Climatological Memorando 130.

Middleton, D.R., 1995. Modelling air pollution transport and deposition. Pollution of Land, Sea and Air: An Overview for Engineers. *In: IEE Colloquium on 10 Oct. 1995*, 11/1 - 11/7.

Middleton, D.R., Morrison, N.L., Rooney, G.G., and Thomson, D.J., 2002. A comparison of dispersion model met pre-processing with urban flux measurements from Birmingham U.K.. *In: 8th International Conference on Harmonisation Within Atmospheric Dispersion Modelling For Regulatory Purposes, Sofia, Bulgaria, 14-17 October 2002*, 226.

Middleton, D.R., and Thomson, D.J., 2002. *Uncertainties in met pre-processing for dispersion models*. (Presented to the Atmospheric Dispersion Modelling Liaison Committee- ADMLC. *In: Workshop on Reliability of Atmospheric Dispersion Models. NRPB, 22-23 October 2001*). Met Office: Crown., 14 pp. [http://www.admlc.org.uk/pdfs/workshop/doug_middleton.pdf]

Molders, N., and Olson, M.A., 2004. Impact of urban effects on precipitation in high latitudes. *J. Hydrometeor.,* 5, 409–429.

Monin, A.S., and Obukhov, A.M., 1954. Basic laws of turbulent mixing in the ground layer of the atmosphere. *Tr. Geofiz Inst. Akad. Nauk SSSR*, 151, 163-187.

Moriwaki, R., and Kanda, M., 2006. Scalar Roughness Parameters for a Suburban Area. *J. Meteor. Soc. Japan*, 84, 1063-1071.

Moriwaki, R., and Kanda, M., 2004. Seasonal and diurnal fluxes of radiation, heat, water vapor, and CO_2 over a suburban area. *J. Appl. Meteor.*, 43, 1700–1710.

Musk, L.F., 1988. *Weather Systems*. Cambridge: Cambridge University Press, 160 pp.

Narita, K., Mikami, T., Honjo, T., Sugawara, H., Kimura, K., and Kuwata, N., 2002. Observations about cool-island phenomena in urban park. *In: 4th Symposium on the Urban Environment, Norfolk, Virginia, USA, 20-24 May 2002*. Amer. Meteor. Soc., 86-87.

Noilhan, J., and Planton, S., 1989. A simple parameterization of land surface processes for meteorological models. *Mon. Weather Rev.*, 117, 536–549.

Offerle, B., Grimmond, C.S.B., and Fortuniak, K., 2005. Heat storage and anthropogenic heat flux in relation to the energy balance of a central European city center. *Int. J. Climatol*., 25, 1405–1419.

Offerle, B., Grimmond, C.S.B., Fortuniak, K., Kłysik, K., and Oke, T.R., 2006. Temporal variations in heat fluxes over a central European city centre. *Theor. Appl. Climatol.,* 84, 103-115.

Ohashi, Y., and Kida, H., 2002. Local circulations developed in the vicinity of both coastal and inland urban areas: a numerical study with a mesoscale atmospheric model. *J. Appl. Meteor.,* **41,** 30–45.

Oke, T.R., 1982. The energetic basis of the urban heat island. *Quart. J. Roy. Meteor. Soc.*, 108, 1-24.

Oke, T.R., 1987. Boundary *layer climates*. 2nd ed ., London: Routledge, 435 pp.

Oke, T.R., 1988. The urban energy balance. *Progr. Phys. Geogr.,* 12, 471–508.

Oke, T.R., 1995. The heat island of the urban boundary layer: Characteristics, causes and effects. *In: Wind Climate in Cities*. Cermak, J.E., Davenport, A.G., Plate, E.J., and Viegas, D.X., (Eds.). Dordrech, The Netherlands: Kluwer Academic Publishing, 81-107, 772 pp.

Oke, T.R., 1997. Urban environments. In: *Surface Climates of Canada.* Bailey, W.G., Oke, T.R., and Rouse, W.R., (Eds). Montréal: McGill-Queen's University Press, 303-327.

Oke, T.R., 2006. *Initial guidance to obtain representative meteorological observations at urban sites*. Instruments and Observing Methods, Report No. 81, WMO/TD-No. 1250, Geneva: World Meteorol. Organiz. [http://www.wmo.ch/web/www/IMOP/publications/IOM-81/IOM-81-UrbanMetObs.pdf].

Oke, T.R., Cleugh, H.A., Grimmond, S., Schnid, H.P., Roth, M., 1989. Evaluation of spatially-averaged fluxes of heat, mass and momentum in the urban boundary layer. Weather and Climate 9, 14}21.

ONS Office for National Statistics of UK [http://www.statistics.gov.uk/downloads/theme_population/regional_snapshot/LA_KeyStats_population.xls]

Orville, R.E., Huffines, G., Nielsen-Gammon, J., Zhang, R., Brandon, E., Steiger, S., Phillips, S., Allen, S., and Read, W., 2001. Enhancement of cloud-to-ground lightning over Houston Texas. *Geophys. Res. Lett.*, 28, 2597–2600.

Pasquill, F., 1950. The Aerodynamic Drag of Grassland. *Proceedings of the Royal Society of London. Series A, Mathematical and Physical Sciences*, 202, 143-153.

Paulson, C.A., 1970. The mathematical representation of wind speed and temperature profiles in the unstable atmospheric surface layer. *J. Appl. Meteor*., 9, 857-861.

Pearlmutter, D., Berliner, P., and Shaviv, E., 2005. Evaluation of urban surface energy fluxes using an open-air scale model. *J. Appl. Meteor*., 44, 532-545.

Pielke Sr., R.A., 2001. Influence of the spatial distribution of vegetation and soils on the prediction of cumulus convective rainfall. *Rev. Geophys.* 39, 151–177.

Pielke Sr., R.A., Beltrán-Przekurat, A., Hiemstra, C.A., Lin, J., Nobis, T.E., Adegoke, J., Nair, U.S., and Niyogi, D., 2006. Impacts of Regional Land Use and Land Cover on Rainfall: An Overview. *Climate Variability and Change—Hydrological Impacts. In: 5th FRIEND World Conference, Havana, Cuba, November 2006*. International Association of Hydrological Sciences (IAHS) Publ., 308, 2006.

Pielke Sr., R.A., Adegoke, J., Beltrán-Przekurat, A., Hiemstra, C.A., Lin, J., Nair, U.S., Niyogi, D., and Nobis, T.E., 2007. An overview of regional land-use and land-cover impacts on rainfall. *Tellus*, 59B, 587-601.

Piringer, M. (Ed.), 2002. Surface energy balance in urban areas. *Extended abstracts of an Expert Meeting. Working Group 2, COST Action 715, Antwerp,* Belgium, 12 April 2000. European Commission. Report EUR 19447, 103 p.

Piringer, M., and Joffre, S., (Eds.); Baklanov, A., Burzynski, J., Christen, A., Deserti, M., De Ridder, K., Emeis, S., Joffre, S., Karppinen, A., Mestayer, P., Middleton, D., Piringer, M., and Tombrou, M., 2005. *The urban surface energy budget and mixing height in European cities: data, models and challenges for urban meteorology and air quality. - Final Report of Working Group 2 of COST-715 Action*. Sofia, Bulgaria: Demetra Ltd Publishers, 239 pp.

Piringer, M., Grimmond, C.S.B., Joffre, S.M., Mestayer, P., Middleton, D.R., Rotach, M.W., Baklanov, A., De Ridder, K., Ferreira, J., Guilloteau, E., Karppinen, A., Martilli, A., Masson, V., and Tombrou, M., 2002. Investigating the surface energy balance in urban areas - Recent advances and future needs. *Water Air and Soil Poll.: Focus*, 2, 1-16.

Prandtl, L., 1932. Meteorologische Anwendungen der Strömungslehre. *Beitr. Phys. Fr. Atmosph.*, 19, 188-202.

Pruppacher, H.R. and Klett, J.D., 1997. *Microphysics of Clouds and Precipitation*. Dordrecht, Netherlands: Kluwer Academic Publishers, Atmospheric and Oceanographic Sciences Library, 18.

Radke, L.F., Coakley Jr., J.A., and King, M.D., 1989. Direct and remote sensing observations of the effects of ships on clouds. *Science*, 246,1146-1149.

Raupach, M.R., 1994. Simplified expressions for vegetation roughness length and zero-plane displacement as functions of canopy height and area index. *Bound.-Layer Meteor*., 71, 211-216.

Raupach, M.R., 1995. Corrigenda. *Bound.-Layer Meteor.,* 76, 303-304.

Raupach, M.R., Antonia, R.A., and Rajagopalan, S., 1991. Rough wall turbulent boundary layers. *Appl. Mech. Rev.*, 44, 1-25.

Rooney, G.G., Longley, I.D., and Barlow, J.F., 2005. Variation of urban momentum roughness length with land use in the upwind source area, as observed in two U.K. cities. *Bound.- Layer Meteor*., 115, 69–84.

Rosenfeld, D., 1999. TRMM observed first direct evidence of smoke from forest fires inhibiting rainfall. *Geophys. Res. Lett.*, 26 , 3105–3108.

Rosenfeld, D., 2000. Suppression of rain and snow by urban and industrial air pollution, *Science*, 287, 1793-1796.

Rosenfeld, D., Rudich, Y., and Lahav, R., 2001. Desert dust suppressing precipitation: A possible desertification feedback loop. *Proc. Natl. Acad. Sci. USA*, 98 (11), 5975-5980.

Rotach, M.W., 1999. On the influence of the urban roughness sublayer on turbulence and dispersion. *Atmos. Environ.*, 33, 4001- 4008.

Rotach, M.W., 2002. Overview on the Basel Urban Boundary Layer Experiment—BUBBLE. *In: 4th Symposium on the Urban Environment, Norfolk, Virginia, USA, 20-24 May 2002*. Amer. Meteor. Soc., 25-26.

Rotach, M.W., Vogt, R., Bernhofer, C., Batchvarova, E., Christen, A., Clappier, A., Feddersen, B., Gryning, S.-E., Mayer, H., Mitev, V., Oke, T.R., Parlow, E., Richner, H., Roth, M., Roulet, Y.-A., Rufeux, D., Salmond, J., Schatzmann, M., Voogt, J.A., 2005. BUBBLE - an Urban Boundary Layer Project. *Theor. Appl. Climatol.,* 81, 231-261.

Roth, M., 2000. Review of atmospheric turbulence over cities. *Quart. J. Roy. Meteor. Soc.*, 126, 941-990.

Roth, M., 2002. Effects of Cities on Local Climates. *In:Workshop of IGES/APN Mega-City Project, Kitakyushu, Japan, 23-25 January 2002.* Institute for Global Environmental Strategies (IGES), [http://www.iges.or.jp/en/ue/pdf/megacity02/data/PDF/08-1(Roth).pdf].

Roth, M., and Oke, T.R., 1995. Relative eficiencies of turbulent transfer of heat, mass and momentum over a patchy urban surface, *J. Atmos. Sci*., 52, 1864-1870.

Roth, M., Oke, T.R., and Emery, W.J., 1989. Satellite-derived urban heat islands from three coastal cities and the utilization of such data in urban climatology. *Intern. J. Remote Sensing*, 10, 1699-1720.

Rozoff, C.M., Cotton, W.R., and Adegoke, J.O., 2002. Simulated thunderstorms over St. Louis, MO. *In: 4th Symposium on the Urban Environment, Norfolk, Virginia, USA, 20-24 May 2002*. Amer. Meteor. Soc., 3-4.

Rozoff, C.M., Cotton, W.R., and Adegoke, J.O., 2003. Simulation of St. Louis Missouri, land use impacts on thunderstorms. *J. Appl. Meteor.*, 42, 716–738.

Schmid, H.P., and Oke, T.R., 1990. A model to estimate the source area contributing to surface layer turbulence at a point over a patchy surface. *Quart. J. Roy. Meteor. Soc*, 116, 965- 988.

Segal, M., and Arrit, R.W., 1992. Nonclassical mesoscale circulations caused by surface sensible heat flux gradients. *Bull. Amer. Meteorol. Soc.*, 73, 1593-1604.

Segal, M., Garratt, J.R., Kallos, G., and Pielke, R.A., 1989. The impact of wet soil and canopy temperatures on daytime boundary-layer growth. *J. Atmos. Sci*., 46, 3673–3684.

Seinfeld, J.H., and Pandis, S.N., 1998. *Atmospheric Chemistry and Physics: From Air Pollution to Climate Change*. New York: John Wiley & Sons, Inc. 1326 pp.

Selover, N., 1997. Precipitation patterns around an urban desert environment topographic or urban influences? *In: Association of American Geographers Convention, Fort Worth, TX, USA, 25–29 May 1997*. Assoc. Amer. Geographers.

Shaw, E.M., 1962. An analysis of the origins of precipitation in Northern England, 1956-1960. *Quart. J. Roy. Meteor. Soc.*, 88, 539-547.

Shepherd, J.M., 2002. An investigation of the influence of urban areas on rainfall using a cloud-mesoscale model and the TRMM satellite. *In: 4th Symposium on the Urban Environment, Norfolk, Virginia, USA, 20-24 May 2002*. Amer. Meteor. Soc., 1-2.

Shepherd, J.M., 2005. A review of current investigations of urban-induced rainfall and recommendations for the future. *Earth Interactions*, 9, 1-27.

Shepherd, J.M., and Burian, S.J, 2003. Detection of urban-induced rainfall anomalies in a major coastal city. *Earth Interactions*, 7, 1-17.

Shepherd, J.M., and Jin, M., 2004. Linkages between the urban environment and Earth's climate system. *Eos, Trans. Amer. Geophys. Union,* 85, 227–228.

Shepherd, J.M., Pierce, H., and Negri, A.J., 2002. Rainfall modification by major urban areas: Observations from spaceborne rain radar on the TRMM satellite. *J. Appl. Meteor.,* 41, 689–701.

Shepherd, J.M., Taylor, L., and Garza, C., 2004. A dynamic multi-criteria technique for siting NASA-Clark Atlanta rain gauge network. *J. Atmos. Oceanic Technol.,* 21, 1346–1363.

Simmonds, I., and Keay, K., 1997. Weekly cycle of meteorological variations in Melbourne and the role of pollution and anthropogenic heat release. *Atmos. Environ.*, 31, 1589–1603.

Soux, A., Voogt, J.A., and Oke, T.R., 2004. A model to calculate what a remote sensor "sees" of an urban surface. *Bound.-Layer Meteor.*, 111, 109–132.

Steiger, S.M., and Orville, R.E., 2003. Cloud-to-ground lightning enhancement over southern Louisiana. *Geophys. Res. Lett.,* 30, 1975, doi:10.1029/2003GL017923.

Stewart, J.B., Kustas, W.P., Humes, K.S., Nichols, W.D., Moran, M.S., and Bruin, H.A.R. de, 1994. Sensible heat flux–radiometric temperature relationship for eight semiarid areas. *J. Appl. Meteor*., 33, 1110–1117.

Stewart, J.B., 1984. Measurement and prediction of evaporation from forested and agricultural catchments. *Agric. For. Manag*., 8, 1– 28.

Stull, R.B., 1988. *An introduction to boundary layer meteorology.* Dordrech, The Netherlands: Kluwer Academic Publishers, 666 pp.

Sugawara, H., 2001. Heat exchange between urban structures and the atmospheric boundary layer. Ph.D. dissertation, Tohoku University, 140 pp.

Sugita, M., and Brutsaert, W., 1990. Regional fluxes from remotely sensed skin temperature and lower boundary layer measurements. *Water Resour. Res.*, 26, 2937–2944.

Sun, Y., and Mahrt, L., 1995a. Relationship of surface heat flux to microscale temperature fluctuations. *Bound.-Layer Meteor*., 76, 291–301.

Sun, Y., and Mahrt, L., 1995b. Determination of surface fluxes from the surface radiative temperature. *J. Atmos. Sci*., 52, 1096–1106.

Sutton, O.G., 1953. *Micrometeorology*. New York: McGraw-Hill, 333pp.

Szeicz, G., 1974. Gaseous wastes and the vegetation. Unpublished manuscript given at *Symposium on Waste Recycling and the Environment*, Royal Society of Canada, Ottawa, ON, Canada, 12 pp. [Available from Royal Society of Canada, 225 Metcalf St., Ottawa, ON K2P 1P9 Canada.].

Takahashi, H., 2003. Secular variation in the occurrence property of summertime daily rainfall amount in and around the Tokyo Metropolitan area (in Japanese with an English abstract). *Tenki,* 50, 31–41.

Thielen, J., and Gadian, A., 1996. Influence of different wind directions in relation to topography on the outbreak of convection in Northern England. *Annales Geophysicae*, 14, 1078-1087.

Thielen, J., and Gadian, A., 1997. Influence of topography and urban heat island effects on the outbreak of convective storms under unstable meteorological conditions: a numerical study. *Meteor. Applic.*, 4, 139- 149.

Thielen, J., Wobrock, W., Gadian, A., Mestayer, P.G., and Creutin, J.-D., 2000. The possible influence of urban surfaces on rainfall development: a sensitivity study in 2D in the meso-γ-scale. *Atmos. Res.*, 54, 15–39.

Toon, O.B., 2000. How Pollution Suppresses Rain. *Science*, 287, 1763-1765.

Tsonis, A.A., 2002. *An Introduction to Atmospheric Thermodynamics*. Cambridge, UK: Cambridge University Press, 171pp.

Tumanov, S., Stan-Sion., A., Lupu, A., Soci, C., and Oprea, C., 1999. Influences of the city of Bucharest on weather and climate parameters. *Atmos. Environ.*, 33, 4173-4183.

Ulden, A.P. van, and Holtslag, A.A.M., 1985. Estimation of atmospheric boundary layer parameters for diffusion applications. *J. Climate Appl. Meteor.*, 24, 1196–1207.

Unger, J., Sumeghy, Z., and Zoboky, J., 2001. Temperature cross-section features in an urban area. *Atmos. Res.*, 58, 117-127.

United Nations, Department of Economic and Social Affairs/Population Division, 2004. *World Urbanization Prospects: The 2003 Revision (Data Tables and Highlights)*, New York: United Nations [www.unpopulation.org or http://www.un.org/esa/population/unpop.htm, last accessed on September 2004].

Vazquez, D.P., Reyes, F.J.O. and Arboledas, L.A., 1997. A comparative study of algorithms for estimating land surface temperature from AVHRR Data. *Remote Sens. Environ*., 62, 215-222.

Verhoef, A., Bruin, H.A.R. de, and Hurk, J.J.M. van den, 1997. Some practical notes on the parameter kB^{-1} for sparse vegetation. *J. Appl. Meteor.*, 36, 560–572.

Verma, S.B., 1989. Aerodynamic resistances to transfers of heat, mass and momentum. *In*: *Estimation of Areal Evapotranspiration*, Black, T.A., Spittlehouse, D.L., Novak, M.D., and Price, D.T., (Eds.). International Association of Hydrological Sciences (IAHS), 13–20.

Voogt, J.A., 2002. Urban Heat Island. *In: Encyclopedia of Global Environmental Change* (Ed. T. Munn), Vol. 3: Causes and Consequences of Global Environmental Change. (Ed. I. Douglas). Chichester: John Wiley & Sons, Ltd., 660-666.

Voogt, J.A., and Grimmond, C.S.B., 2000. Modeling surface sensible heat flux using surface radiative temperatures in a simple urban area. *J. Appl. Meteor*., 39, 1679-1699.

Voogt, J.A., and Oke, T.R., 1997. Complete urban surface temperatures. *J. Appl. Meteor*., 36, 1117–1132.

Voogt, J.A., and Oke, T.R., 2003. Thermal remote sensing of urban climates. *Remote Sens. Environ*. 86, 370-384.

Walko, R.L., Band, L.E., Baron, J., Kittel, T.G.F., Lammers, R., Lee, T.J., Ojima, D., Pielke, R.A., Taylor, C., Tague, C., Tremback, C.J., and Vidale, P.L., 2000. Coupled atmosphere–biophysics–hydrology models for environmental modeling. *J. Appl. Meteor.*, 39, 931–944.

Wallace, J.M., and Hobbs, P.V., 1977. *Atmospheric Science, an introduction survey*. London: Academic Press, 467 pp.

Wieringa, J., 1993. Representative roughness parameters for homogeneous terrain. *Bound.- Layer Meteor*., 63, 323-363.

Wilby, R.L., 2001. Downscaling summer rainfall in the UK from North Atlantic ocean temperatures. *Hidrol. Earth. Syst. Sc.*, 5, 245–257.

Wit, M.H., Stathopoulos, T., and Wisse, J.A., 2002. Airport wind speeds used for the design in urban environments: the Eindhoven case. *J. Wind Eng. Ind. Aerod.* 90, 1289–1298.